AD-A133 958   EXPERIMENTAL AND ANALYTICAL STUDIES OF SHIELDING
               CONCEPTS FOR POINT SOURC..(U) TORONTO UNIV DOWNSVIEW
               (ONTARIO) INST FOR AEROSPACE STUDIES R L WONG MAY 83

UNCLASSIFIED   UTIAS-266 AFOSR-TR-83-0838 AFOSR-75-2808   F/G 20/1

1/2

NL

MICROCOPY RESOLUTION TEST CHART

NATIONAL BUREAU OF STANDARDS-1963-A

INSTITUTE

for

AEROSPACE STUDIES

UNIVERSITY OF TORONTO

AFOSR-TR- 83-0838

EXPERIMENTAL AND ANALYTICAL STUDIES OF
SHIELDING CONCEPTS FOR POINT SOURCES AND JET NOISE

by

Raymond Lee Man Wong

DTIC
ELECTE
OCT 2 4 1983
D

May, 1983

83 10 17 161

REPORT DOCUMENTATION PAGE		READ INSTRUCTIONS BEFORE COMPLETING FORM
1. REPORT NUMBER AFOSR-TR- 83-0838	2. GOVT ACCESSION NO. AD·A133958	3. RECIPIENT'S CATALOG NUMBER
4. TITLE *(and Subtitle)* EXPERIMENTAL AND ANALYTICAL STUDIES OF SHIELDING CONCEPTS FOR POINT SOURCES AND JET NOISE		5. TYPE OF REPORT & PERIOD COVERED INTERIM
		6. PERFORMING ORG. REPORT NUMBER UTIAS Report No. 266
7. AUTHOR(s) RAYMOND LEE MAN WONG		8. CONTRACT OR GRANT NUMBER(s) AFOSR-75-2808
9. PERFORMING ORGANIZATION NAME AND ADDRESS UNIVERSITY OF TORONTO, INSTITUTE FOR AEROSPACE STUDIES, 4925 DUFFERIN ST, DOWNSVIEW, ONTARIO, CANADA, M3H 5T6		10. PROGRAM ELEMENT, PROJECT, TASK AREA & WORK UNIT NUMBERS 61102F 2307/A3
11. CONTROLLING OFFICE NAME AND ADDRESS AIR FORCE OFFICE OF SCIENTIFIC RESEARCH/NA BOLLING AFB, DC 20332		12. REPORT DATE May 1983
		13. NUMBER OF PAGES 266
14. MONITORING AGENCY NAME & ADDRESS(*if different from Controlling Office*)		15. SECURITY CLASS. *(of this report)* Unclassified
		15a. DECLASSIFICATION/DOWNGRADING SCHEDULE

16. DISTRIBUTION STATEMENT *(of this Report)*

Approved for Public Release; Distribution Unlimited.

17. DISTRIBUTION STATEMENT *(of the abstract entered in Block 20, if different from Report)*

18. SUPPLEMENTARY NOTES

19. KEY WORDS *(Continue on reverse side if necessary and identify by block number)*
JET NOISE
ACOUSTICS
NOISE REDUCTION
BARRIERS
SHIELDING

20. ABSTRACT *(Continue on reverse side if necessary and identify by block number)*

This analytical and experimental study explores concepts for jet noise shielding. Model experiments centre on solid planar shields, simulating engine-over-wing installations and 'sugar scoop' shields. Tradeoff on effective shielding length is set by interference 'edge noise' as the shield trailing edge approaches the spreading jet. Edge noise is minimized by (i) hyperbolic cutouts which trim off the portions of most intense interference between the jet flow and the barrier and (ii) hybrid shields - a thermal

DD FORM 1473 EDITION OF 1 NOV 65 IS OBSOLETE

83 10 17 161

refractive extension (a flame); for (ii) the tradeoff is combustion noise.

In general, shielding attenuation increases steadily with frequency, following low frequency enhancement by edge noise. Although broadband attenuation is typically only several decibels, the reduction of the subjectively weighted perceived noise levels is higher. In addition, calculated ground contours of peak PN dB (perceived noise level) show a substantial contraction due to shielding: this reaches 66% for one of the 'sugar scoop' shields for the 90 PN dB contour.

The experiments are complemented by analytical predictions. They are divided into an engineering scheme for jet noise shielding and more rigorous analysis for point source shielding. The former approach combines point source shielding. The former approach combines point source shielding with a suitable jet source distribution. The results are synthesized into a predictive algorithm for jet noise shielding: the jet is modelled as a line distribution of incoherent sources with narrow band frequency $\sim$ (axial distance)$^{-1}$. The predictive version agrees well with experiment (1 to 1.5 dB) up to moderate frequencies. The insertion loss deduced from the point source measurements for semi-infinite as well as finite rectangular shields agrees rather well with theoretical calculations based on the exact half plane solution and the superposition of asymptotic closed-form solutions. An approximate theory, the Maggi-Rubinowicz line integral, is found to yield reasonable predictions for thin barriers including cutouts if a certain correction is applied. The more exact integral equation approach (solved numerically) is applied to a more demanding geometry: a half round sugar scoop shield. It is found that the solutions of the integral equation derived from the Helmholtz formula in normal derivative form show satisfactory agreement with measurements.

Accession For

NTIS GRA&I	☒
DTIC TAB	☐
Unannounced	☐
Justification	

By

Distribution/

Availability Codes

Dist	Avail and/or Special
A	

EXPERIMENTAL AND ANALYTICAL STUDIES OF

SHIELDING CONCEPTS FOR POINT SOURCES AND JET NOISE

by

Raymond Lee Man Wong

ACKNOWLEDGEMENTS

The author wishes to express his gratitude to Professor H. S. Ribner, his thesis supervisor, for suggesting this project and a number of the shielding concepts; his guidance, warmth and easy accessibility are very much appreciated.

The author also expresses his sincere appreciation and thanks to Professor W.G. Richarz, his co-supervisor, for much fruitful advice and unending interest throughout this project. Furthermore, thanks are extended to Mr. Zhangwei Hu for many discussions throughout an enjoyable association at this Institute.

Finally, the author would like to thank his sister Christine for preparing the manuscript in her spare time.

ABSTRACT

This analytical and experimental study explores concepts for jet noise shielding. Model experiments centre on solid planar shields, simulating engine-over-wing installations and 'sugar scoop' shields. Tradeoff on effective shielding length is set by interference 'edge noise' as the shield trailing edge approaches the spreading jet. Edge noise is minimized by (i) hyperbolic cutouts which trim off the portions of most intense interference between the jet flow and the barrier and (ii) hybrid shields - a thermal refractive extension (a flame); for (ii) the tradeoff is combustion noise.

In general, shielding attenuation increases steadily with frequency, following low frequency enhancement by edge noise. Although broadband attenuation is typically only several decibels, the reduction of the subjectively weighted perceived noise levels is higher. In addition, calculated ground contours of peak PN dB (perceived noise level) show a substantial contraction due to shielding: this reaches 66% for one of the 'sugar scoop' shields for the 90 PN dB contour.

The experiments are complemented by analytical predictions. They are divided into an engineering scheme for jet noise shielding and more rigorous analysis for point source shielding. The former approach combines point source shielding with a suitable jet source distribution. The results are synthesized into a predictive algorithm for jet noise shielding: the jet is modelled as a line distribution of incoherent sources with narrow band frequency $\sim$ (axial distance) $^{-1}$. The predictive version agrees well with experiment (1 to 1.5 dB) up to moderate frequencies. The insertion loss deduced from the point source measurements for semi-infinite as well as finite rectangular shields agrees rather well with theoretical calculations based on the exact half plane solution and the superposition of asymptotic closed-form solutions. An approximate theory, the Maggi-Rubinowicz line integral, is found to yield reasonable predictions for thin barriers including cutouts if a certain correction is applied. The more exact integral equation approach (solved numerically) is applied to a more demanding geometry: a half round sugar scoop shield. It is found that the solutions of the integral equation derived from the Helmholtz formula in normal derivative form show satisfactory agreement with measurements.

1. INTRODUCTION

Ever since the Wright brothers launched the age of aviation in 1903, transportation by aircraft has had a major influence on our way of life. With the coming of the jet age in the 1950's, noise from turbojet-powered commercial aircraft has become a public nuisance, particularly for people living in communities near airports. Typical examples of commercial turbojets of the 1960's are the Boeing 707, and DC-8. The total acoustic power radiated into the air during takeoff is typically several thousand watts. In comparison, the acoustic power produced by one person speaking is about 10^{-5} watt, and only the latest outdoor multi-kilowatt sound systems come close to that of the jet engines.

The innovation of the turbofan engine for modern commercial jet aircraft (Boeing 747, DC-10, Lockheed L-1011) has alleviated the jet noise problem to a substantial extent. However, the noise problem has intensified as aircraft size increases, and as the number of flyovers multiply due to the ever increasing volume of air traffic. Reactions from neighbors of major airports have shown greater awareness of aircraft noise. This has led to stringent noise regulations, such as the FAR-36; this imposes noise limits for certification of aircraft. Still, the hostile reactions of people around some major airports has clearly indicated that the generated noise is well above the annoyance level. Acceptability of aircraft noise in a community thus has become a challenging problem that requires disciplines from diverse fields such as science and environmental studies.

The thrust of a jet engine scales with diameter and jet velocity about as D^2U^2, whereas the noise power scales (for subsonic U) as U^8D^2. For constant thrust, then, the noise scales as U^6 (or as D^{-6}); thus jet velocity is a very powerful parameter. This suggested the tradeoff of reduced jet velocity against increased engine diameter as a major means of noise reduction. The modern high bypass ratio turbofan engines have exploited this. These new engines with low exhaust velocity and ever-increasing diameter have resulted in the development of modern aircraft that are some 20 PN dB (perceived noise level) quieter than the earlier turbojet aircraft.

Noise suppression can also be achieved by modifying the turbulent mixing of the flow. The first innovation made was the introduction of the multi-tube or corrugated nozzles. These supposedly achieve noise reduction by allowing maximum entrainment of surrounding air. The aerodynamic mechanism is complicated and somewhat controversial. These nozzles were used in early years. The observed noise reduction is typically some 8-10 dB in the overall sound level, but only 2-3 PN dB in perceived noise level (which is a better measure of ear response).

Modern aircraft have carried these jet noise suppression concepts to the point of diminishing returns. An alternative to suppression at the source is the concept of reflective shielding. Here the radiation of the jet noise is redistributed such that the noise intensity is reduced in the 'shadow' zone. For example, by relocating engines above the wing, the latter can be used to deflect a significant portion of the jet noise skyward, so that what reaches the ground is reduced. Less

practical, perhaps, underwing engines could use add-on shields to partly
block downward radiation. The shields may be 'hard', such as a plate, or
'soft', such as a reflective thermal layer. These and combinations that
form composite shields are explored herein.

A number of studies of jet noise shielding have been undertaken in the
past (Refs. 1,2) . A shielding-flap jet noise suppressor as indicated
in Ref. 1 is seen to provide a maximum reduction of about 17 dB on the
shielded side of a slit jet flowing over the upper surface of a wing.
However, this is achieved with a very long shield length equal to 190
times the slit height. This causes a high thrust loss owing to 'wall
jet' drag on the wing which makes the idea unattractive. Nevertheless,
the arrangement bears resemblance to the externally-blown-flap blowing
concept used on the STOL airplanes of the future.

The recent German-Dutch VFW-614 airplane features an EOW (engine-over-
wing) design. This configuration exhibits a noise reduction averaging 5
PN dB over a wide range of downward directions in the shadow zone
(Ref. 3). This is an effect that is apparently due to shielding.

The engine-over-wing noise research has also been carried out exten-
sively in both model and full scale tests by NASA and Boeing for both
powered and conventional lift applications (Refs. 4, 5, 6, 7). For some
full scale powered lift configurations, a reduction of 10 dB in overall
sound pressure level is possible. This and other studies have shown that
tne concept is a promising one for reducing jet noise. Thus further
investigation of this effect is considered desirable.

1.1 Present Investigation

The present study is in part an experimental study of further concepts of
jet shielding by reflective barriers. This is coupled - for aspects
accessible to theory - with analytical developments and comparisons. In
addition, an 'engineering' approach is developed to provide reasonable
estimates of the expected jet noise shielding.

The experimental aspects are directed at conventional as well as
unorthodox configurations. The emphasis is placed on the concept,
feasibility being of secondary importance for now. The model
experiments center on solid planar shields (simulating EOW install-
ations), half round sugar scoop shields, and hybrid configurations com-
bining solid barriers and hot refractive gas layers. This hot gas layer
can play much the same role as a solid plate barrier. The gradient in
sound speed of the heated medium along the underside of the jet can cause
the sound waves to bend upward. The net effect is largely equivalent to
reflection.

The solid planar shield consisting of a simple planar baffle acts simply
as a reflective barrier. The half round scoop shield is motivated by the
expectation of better shielding to the side than that with flat shields
of a limited span. Moreover, they are expected to provide a comparable
degree of downward shielding for a minimum expenditure of barrier
material.

One of the problems encountered in jet noise shielding arises on extending the barrier length in an attempt to shield more and more of the jet: the trailing edge eventually runs into the spreading jet. As the edge approaches the 'conical' jet boundary, an interference effect generates intense 'edge noise'. This produces an augmentation of the levels at low frequencies. In fact there can be an increase in overall sound pressure level (OASPL). To this end, an interference probe is used to delineate the boundary of closest approach to the jet for negligible edge noise. In addition, an attempt is also made to quantify the extent of influence of the edge-induced interference noise to the shielded jet noise spectrum in terms of ▲ dB.

The adverse influence of the edge noise is reduced if 'hyperbolic cutouts' are used. A hyperbolic cutout is defined by the intersection of the shield and the cone of threshold interference mentioned above. This allows one to extend the effective barrier depth without encroaching on the boundary of closest approach for acceptably low edge noise. The hyperbolic cutout is also supplemented by strategic removal of much additional material elsewhere. This is a more practical implementation of the hyperbolic cutout. It turns out that this configuration attains similar noise suppression even if most of the material is removed.

A scaling law is also examined. This is used to give an estimate of the shielding performance of the shielding configurations at 'operational' frequencies. Its validity is examined via model testing of two different size nozzles.

The perceived noise level measured in PNdB is a subjective measure of hearing response: it weights the spectral bands in accordance with the annoyance caused by noise in each frequency band. It may differ much from the corresponding change in sound pressure level, measured in dB. Herein an indication of the effect of the shielding devices on the annoyance levels is calculated in terms of 'footprints' of peak intensity in PN dB, for an assumed airplane takeoff.

A series of experiments and analyses is also carried out to illuminate the mechanism of shielding of a jet by a barrier. The jet noise emitters are modeled as a distribution of point sources along a line (jet axis). The shielding of a single point source is determined as a function of position and frequency. These results are applied to synthesize the jet noise shielding. In addition, the shielding of point sources also allows one to assess by difference the jet-shield aeroacoustic interference. Measurements utilizing the point source are performed on all major shielding configurations. These are carried out by a variety of methods, including cross spectral measurements using broad-band source excitation, signal-averaged pulses, direct measurement via pure tone excitation, warbled tone, and 1/3 octave filtered noise.

The experiments are complemented by a variety of analytical methods. Their suitability to problems of the prediction of jet noise shielding is also examined and tested. This includes the exact half plane solution, Rubinowicz's line integral theory, various asymptotic and approximate schemes, and the more exact integral equation methods for complex shapes.

2. EXPERIMENTAL INVESTIGATIONS

2.1 Introduction

Consider a stream of particles impinging on an obstacle, such as a plate. Those portions incident on the plate will be intercepted or reflected, and the remaining portion will propagate without any disturbance. Hence one would expect the plate to cast a sharply defined shadow. However, wave motion is characterized by a phenomenon associated with the bending of the wave front around any obstacle known as 'diffraction'. The diffraction effect is more pronounced when a wave interacts with a finite obstruction which has dimensions comparable to the wavelength of the wave. With light, the wavelength is usually very small compared with the dimensions of the obstruction. One can not observe diffraction with the naked eye in ordinary situations, since the effect is observable only in regions comparable with a wavelength (10^{-7} m). In this case, there exists a sharply defined shadow behind the obstacle.

On the other hand, the wavelengths for audible sound waves are in general of the same order of magnitude as the dimension of common obstacles (i.e. approximately 2 cm at 15 kHz at the high frequency end to 7 m at 50 Hz at the low frequency end). Thus diffraction impairs the sound shadow in virtually all situations dealing with interaction between sound waves and shielding surfaces. Quantitatively, the effectiveness of a shield is a function of the ratio of the wavelength of the incident sound waves

and the typical dimensions. The performance of a shielding configuration also depends on the relative positions of the shield, the source, and the observer.

Fig. (2-1) shows a typical configuration. As a first approximation a barrier casts a 'sharp' shadow, which is 'filled in' to some extent, by diffracted waves. Thus, for a given effective barrier height 'h', the attenuation becomes 'more perfect' as the shadow angle 'τ' increases. This is equivalent to placing the observer closer to the barrier. A similar effect is also observed in reverse if the source appoaches the barrier while the observer remains at a fixed distance from it. In this sense, the relative position of the sound source and the observer can be interchanged while maintaining identical sound reduction. From geometrical considerations, the situation illustrated in Fig. (2-2) for elevated and depressed source and observer positions are identical in character as far as the diffraction effect of sound waves is concerned.

A similitude parameter for barriers, as defined in accordance with the usage in the literature, is the Fresnel number

$$N \quad = \quad \text{Path Difference} / (\lambda /2) \qquad (2\text{-}1)$$
$$= \quad 2 \, \delta / \lambda$$

Here, the variable ℓ is the difference in length between the shortest path diffracted over the edge and the straight line path from the source to the observer (Fig. 2-3).

Insertion loss is a measure of the local attenuation of sound waves due to a barrier. It is usually defined as the difference in the sound pressure level as measured by a precision sound level meter, in decibels, at a particular point in space with and without the insertion of the barrier. In principle, the measurement of insertion loss, or attenuation is not difficult, especially in the laboratory. Since the effectiver of a shield is governed by the ratio of wavelength to dimension, it is helpful to measure power spectral densities of the received signals. This allows one to assess the shielding of narrow frequency bands. Before the experimental results are presented, an overview of the facilities and instrumentation is given.

2.2 Experimental Facilities

2.2.1 Anechoic Rooms

All measurements were performed in two of the anechoic rooms at the University of Toronto, Institute for Aerospace Studies. The initial phase of the investigation was conducted in the acoustic wind tunnel facility. It has a test section surrounded by an anechoic chamber. The tunnel is capable of air speeds of 12 to 92 m/s. This facility thus allows simulation of forward flight effects, although such effects were not studied here. The anechoic room has dimensions $4.1 \times 5.9 \times 2.1 \ m^3$ between the tips of the fibreglass absorptive wedges. Acoustically, the anechoic chamber around the test section has a cutoff frequency of 150 Hz (defined by deviation from inverse square law for far field acoustic intensity). The background noise level is less than 25 dBA.

A second anechoic room became available in the later stages of the investigation. More than two-thirds of the relevant measurements were carried out there. This anechoic room is slightly smaller than the one in the acoustic wind tunnel facility. It has dimensions $4.2 \times 2.9 \times 2.1 \ m^3$ and a wedge depth of 20 cm. The walls have 3.2 mm thick lead sheet to insulate the chamber against exterior noise from the outside. The cutoff frequency of this room is approximately 300 Hz, and the background noise is also acceptably low (28 dBA).

2.2.2   Model Air Jet

The two model air jets used in the experiement are of identical design. The nozzles have circular exit diameters of 1.91 cm (3/4 in.) and an area ratio of 110. They can be operated over a range of flow speeds from 10 m/sec to 300 m/sec. The nozzle contour has been designed to produce a uniform velocity profile at the orifice (Ref. 8). A 1 m section of .2 m circular steel pipe is used as a settling chamber.

A silencer in the control room is connected to the model air jet via a flexible air hose. A continuously operating compressor supplies 4.8×10^5 to 6.9×10^5 N/m^2 (70 to 100 psi) air to the system. It is regulated down by a two stage regulator to provide any desirable flow velocity; the second of these is a Fisher Governor Type 99 precision pressure regulator. Any water in the air supply is collected in a filter prior to reaching the regulators. The static pressure in the settling chamber is monitored by a mercury manometer. The jet, settling chamber, and other equipment were wrapped in fibreglass to reduce reflections. Additional details may be found in Refs. [8, 9].

2.2.3   Microphone System

The sound pressure measurements were made with either a Bruel and Kjaer (B & K) Type 4135 ¼" (0.635 cm) or a Type 4133 ½" (1.27cm) condenser microphone cartridge coupled to a B & K preamplifier. This is connected to a B & K microphone power supply Type 2801 that provides the necessary polarizing voltage. The frequency response of the microphone is essentially flat between 20 Hz and 40 kHz and 100 kHz for ½" (1.27 cm) and ¼" (0.635 cm) diameters respectively. A Keithley model 102 B decade amplifier with amplification factors of 20, 40 and 60 dB was used to amplify the low level microphone signal. Further signal conditioning was provided by an Ithaco variable electronic filter with a broadband frequency range from 0.01 Hz to 1 MHz. A block diagram of the instrumentation for the shielding measurements is shown in Fig. (2-4).

A microphone boom supports the microphone in the horizontal plane of the jet at a distance of 1.63 m from the jet orifice. The boom allows rotation about an axis aligned with the jet centre line and the nozzle exit plane. Insertion loss measurements are performed with the shield interposed between the jet and the microphone. They are held in place by a specially constructed mounting. The arrangement allows the investigation of the shielding effectiveness in the sideline plane as well as the flyover plane and in-between (Fig. 2-5).

2.2.4 Signal Processing Instrumentation

In a laboratory, determination of shielding effects of a barrier for noise reduction involves measurement of overall sound pressure level or power spectral density, depending on the specific application. The analysis might be accomplished with either analog or digital equipment, or a combination of both. A Bruel and Kjaer Heterodyne Analyzer and a Spectral Dynamics Digital Signal Processor (DSP 360) were utilized throughout the investigation. Both types of analyzer cover the frequency range from near DC to an upper limit of 150 kHz, which is well above the frequency range of interest.

The B & K Heterodyne Analyzer Type 2010 is a constant bandwidth narrowband frequency analyzer. It utilizes the swept analysis technique. This instrument was used in conjunction with a B & K level Recorder Type 2307, which provides hard copies of frequency spectra on frequency calibrated strip-chart paper.

The Spectral Dynamics DSP 360 is a two channel real time analyzer incorporating a small dedicated computer. It has a fast Fourier transform capability, and can perform spectral analysis, cross-correlation, and other signal processing operations. This flexibility made possible alternative methods of insertion loss measurement, some of which will be discussed later on in the appropriate sections.

2.3 Planar Shield Configurations

2.3.1 Introduction

An uninterrupted barrier placed between the noise source and the observer will provide noise reduction in the geometric shadow. With this in mind, imagine a jet exhaust, the principle source of aircraft noise, placed above some structure such as a wing or some shielding configuration. It follows that an observer on the ground will be partially shielded from the noise sources. Jet noise shielding by these means is similar to the methods used for environmental noise control on the ground. Here, the erection of a solid barrier blocks any direct transmission between the noise source and recipient. The principal differences in the present investigation are the nature of the noise sources (i.e. convected field of random quadrupoles) and the relative disposition of sources, shield, and observer.

Under conditions of close proximity of the turbulent jet flow to the shielding surface, the edge will interact with the dynamics of the unsteady fluid flow; this will give rise to 'edge noise'. Edge noise (Ref. 10) is the additional noise produced by an interference effect when the separation between the jet boundary and the shield edge is reduced below a certain minimum. This and other factors peculiar to jets increase the complexity of the analysis as compared with that for a mathematical point noise source at a finite distance from a screen.

2.3.2. Mechanism of Edge Noise

The mechanism of surface effects in flow noise has been discussed extensively in the literature (See, e.g., Ffowcs Williams, Ref. 10 and Crighton, Ref. 11). An overview is given below, together with further references.

It is shown in Ref. 11 that if a source is placed closer than a wavelength to the edge of the plate, the scattered field can be found from incompressible flow arguments (Ref. 12) (i.e. solving the Laplace equation that results on assuming the Laplacian operator $(\frac{\partial^2}{\partial x_1^2} + \frac{\partial^2}{\partial x_2^2}) \gg k^2$ in the original Helmholtz equation, subject to the rigid surface boundary condition on the plate).

With the source at distance y normal to the axis (Fig. 2-8) in the close vicinity of a half plane, for a monopole of radian frequency $\omega = kc$, the field potential at a field point x takes the form (Ref. 11 , Eq. 7.15, P. 62).

$$\phi_m' = \frac{e^{ikx}}{x} e^{-iky_3 \sin\psi} (\cos\psi)^{1/2} (ky)^{1/2} \sin\frac{\theta}{2} \sin\frac{\theta_o}{2} \qquad (2-2a)$$

where ψ is the complement of the angle between $\hat{x}$ and the 3 axis.

In the absence of the half plane, the direct (incident) field at the observer takes the form

$$\phi_m = \frac{e^{ik|\bar{x}-\bar{y}|}}{|\bar{x}-\bar{y}|} \sim \frac{e^{ikx}}{x} e^{-ik_\perp(y\cos\theta+y_3\sin\theta)-iky_3\sin\psi} \qquad (2-2b)$$

where $k = k\cos\psi$ (component of the wave vector normal to the plate edge)

Using the above expression for the scattered monopole field, the fields due to quadrupoles can be found by suitable differentiation with respect to source position (Ref. 13). For a quadrupole with both axes normal to the plate near the edge[*] (YY quadrupole), the scattered field is given as

$$\phi_{q_1}' = \frac{\partial^2}{\partial y^2} \phi_m' \sim k^0 y^{-2} \phi_m' \qquad (2-3)$$

Similarly, the scattered field for quadrupoles with one axis in a plane normal to the plate edge and the other parallel to the edge (YY_3 quadrupole) is

$$\phi_{q_2}' = \frac{\partial^2}{\partial y \partial y_3} \phi_m' \sim k y^{-1} \phi_m' \qquad (2-4)$$

While for quadrupoles with both axis parallel to the plate edge ($Y_3 Y_3$ quadrupole)

$$\phi_{q_3}' = \frac{\partial^2}{\partial y_3^2} \phi_m' \sim k^2 y^0 \phi_m' \qquad (2-5)$$

Since the direct field potential of a quadrupole is

$$\phi_q \sim k^2 \phi_m \qquad (2-6)$$

and from Eq. (2-2) $\qquad \phi_m'/\phi_m \sim (ky)^{1/2}$

[*] Hereinafter the short phrase 'plate edge' will be used to signify the plane of the plate near the edge.

it follows that the ratio of diffracted sound to direct sound (no shield) for the differently oriented quadrupoles near an edge is:

(i) For the YY quadrupole

$$\frac{\phi_{f_i}'}{\phi_{m'}} \cdot \frac{\phi_m}{\phi_f} \sim (ky)^{-2}$$

$$\therefore \ \sigma_1 = \frac{\phi_{f_i}'}{\phi_f} \sim (ky)^{-2}(ky)^{1/2} = (ky)^{-3/2} \qquad (2\text{-}7)$$

(ii) For the YY_3 quadrupole

$$\frac{\phi_{f_2}'}{\phi_{m'}} \cdot \frac{\phi_m}{\phi_f} \sim (ky)^{-1}$$

$$\therefore \ \sigma_2 = \frac{\phi_{f_2}'}{\phi_f} \sim (ky)^{-1}(ky)^{1/2} = (ky)^{-1/2} \qquad (2\text{-}8)$$

(iii) For the Y_3Y_3 quadrupole

$$\frac{\phi_{f_3}'}{\phi_{m'}} \cdot \frac{\phi_n}{\phi_f} \sim (ky)^0$$

$$\therefore \ \sigma_3 = \frac{\phi_{f_3}'}{\phi_f} \sim (ky)^{1/2} \qquad (2\text{-}9)$$

Since y is assumed to be less than a wavelength from the edge, there is no enhancement of the sound from the Y_3Y_3 quadrupole, and the radiated sound field of the YY_3 quadrupole is weaker than that for the YY quadrupole: the dominant contribution will come from the latter. The amplification factor* is equal to $(ky)^{-3/2}$; this result was first obtained by Ffowcs Williams and Hall (Ref. 10).

* The factor may be less than unity.

From a dimensional argument, one can show that the power output from unit volume of jet is proportional to U^3M^5 (M^5 is characteristic of quadrupoles, Ref. 14). Due to the presence of an edge near the flow, the scattered field of a free quadrupole is amplified by the factor $(ky)^{-3/2}$. Since the wavelength of the emitted sound wave scales as

$$\lambda = c/f = c/(U/\ell) = \ell M^{-1} \qquad (2\text{-}10)$$

where ℓ is the length scale of a typical eddy, the above similarity gives

$$\sigma^2 \sim (ky)^{-3} \sim (y/\lambda)^{-3} = (M\ell^{-1}y)^{-3} \qquad (2\text{-}11)$$

for the ratio of diffracted power/unshielded power for a quadrupole. The corresponding sound power radiated from a jet near an edge will scale as

$$U^3M^5M^{-3}(\ell/y)^3 = M^2U^3(\ell/y)^3 \qquad (2\text{-}12)$$

Therefore, the power output from unit volume near the edge is amplified by a factor of

$$A \sim M^{-3}(\ell/y)^3 \qquad (2\text{-}13)$$

This indicates that for subsonic, unheated jets there is a larger increase in the edge noise generated as the Mach number of the jet decreases.

An alternative formulation of interaction noise is based on the behaviour of a pressure field convecting past an edge. The edge may be regarded as a pressure release region where the impedance presented to the turbulent pressure field abruptly changes from almost infinite (perfectly reflecting) to that of the characteristic value of the medium (ρc). As the unsteady pressure field convects over the plate, the associated acoustic signals will tend to cancel, as the net force on the plate is nearly zero. However, near the edge the cancellation is imperfect, and regions of high/low pressure will tend to accelerate the fluid around the edge. These unsteady forces give rise to an acoustic field similar to that due to a distribution of dipoles (Ref. 14   ).

Exploratory measurements during this investigation have shown that the edge-induced extra noise increases as the shield is moved closer to the jet, more nearly simulating the hypothesized situation. Some of the fundamental aspects and empirical prediction techniques for flow past an edge have been discussed in some details by Hayden (Ref. 15) and Grosche (Ref. 2) for slot nozzles.

19

2.3.3   Noise Characteristics of Jet Flow/Shield Surface Interaction Effect

The presence of interaction noise due to shielding makes it necessary to identify various mechanisms which influence the acoustic shielding characteristics. Therefore, extensive experimental studies have been performed to obtain quantitative information about the additional sound field generated along the edge. Far field measurements of a shielded jet show that these additional sources of noise tend to enhance the spectral components below the peak frequency of the jet (Fig. 2-7). This result is to be expected, since the edge of the shield is downstream of the jet nozzle. Here the turbulent eddies exhibit lower characteristic frequencies than in the source region close to the nozzle. Thus low frequency noise is observed. The peak intensity of the edge noise is found to have a U^5 scaling law (Fig. 2.8) for the velocity dependence. (see also Eq. 2 - 12). This result is based upon experimental finding, it is also consistent with prediction from theory of trailing edge noise (Ref. 16).

Spectra of the near field pressure measured by a microphone placed near the edge of the shield show a one to one correspondence between the near field peak frequency and the frequency of maximum augmentation of the far field spectra (Fig. 2-9a). The augmentation peak frequency is also a function of microphone position(Fig. 2-9b). This suggests that the phenomenon of edge interaction noise is a local one; in other words, interaction between the local near field acoustic pressure and the shield surface. This leads support to the not uncommon notion that 'edge noise' is generated by stationary dipoles at the shield trailing edge.

20

2.3.4 Definition of the Cone of Threshold Interference

We wanted to identify the boundary of closest approach for negligible edge noise without sacrificing appreciable shielding. To this end an interference probe was used (Fig. 2-10a), with dimensions as shown in the figure. The small width and thickness of the probe were chosen to minimize both its own shielding effect and the generation of strong aeolian tones.

The far field spectrum of the jet noise was monitored at $\theta = 90^0$ as the probe was moved in radially. The point of closest approach, or the threshold of interference, is arbitrarily defined herein to be the distance from the jet centre line at which the peak of the spectrum shows a (barely perceptible) rise of 1 dB. The results suggest that this limit is essentially a truncated cone (Fig. 2-10b).

There is uncertainty in the above measurement of the boundary of closest approach. The recent results of Fisher & Head (Ref. 18), as well as our own experience indicate, that the above boundary may be optimistic: too close to the jet. Fluid mechanical effects for a shield much larger than our probe may lead to generation of edge noise well before the above boundary is reached. For instance, some of the flow entrained by the jet would be incident on the shield. In addition the jet will tend to be drawn towards the shield due to higher entrained flow velocity in the confined region between the shield and the jet. This has the effect of increasing the wetted width along the shield edge.

Fig. 2-10b shows the measured threshold of interference cone (solid line) in relation to the jet. The jet boundary is imprecise: we show the $\alpha = 10^0$; 15^0, 20^0 'boundaries'. The truncated interference cone cuts across these: it has a virtual origin much further upstream of the nozzle.

2.3.5   Semi-Ininite Planar Shields

The simplest geometric configurations tested were rectangular shields. This concept is based on reflective shielding. It involves essentially redirecting a portion of the radiated acoustic energy in a particular direction. In this way, the shield can simulate the engine-over-wing configurations. Furthermore, it has the attraction of appearing amenable to theoretical prediction of the shielding attenuation. From the experimental point of view, the shields can be easily constructed. This simple shielding geometry also allows precision measurements to be carried out easily. In addition, large extensions can be added to the shield so that it approximates a semi-infinite barrier in the anechoic room. This is useful for deriving base-line data for diffraction problems.

The relative position of the jet exhaust and the shield is important since it determines the extent of the shadow zone, as well as the intensity of the noise generated by the jet flow/shield surface interaction. In order to achieve significant shielding, the barrier must be long and close to the jet boundary so as to increase the angle of diffraction ' Υ ' (Fig. 2-1). It is argued that a planar barrier is most effective as a jet noise suppressor at high frequencies. This is plausible, for higher frequency radiation comes from the region close to the nozzle exit. Furthermore, diffraction into a shadow zone decreases with increasing frequency, for fixed geometry.

If a barrier is moved or lengthened so that it penetrates the cone of interference, then edge noise will increase the overall noise radiated significantly at the larger angles. This induced low frequency noise has, in effect, increased the overall noise level radiated above that of an unshielded jet at large angles ($\Theta > 50^{0}$) with respect to the jet axis (Fig. 2 - 11a). The direction of the maximum intensity being normal to the plane of the barrier, thus the shielding effectiveness suffers most in the deep shadow zone. Moreover, a planar semi-infinite shield extending just to the cone of interference shows virtually no attenuation in the vertical plane. (Fig. 2 - 11b).

2.3.6   Hyperbolic Cutouts

According to some of the measurements on source strength distribution of jets (Ref. 19), it seems that any shielding device should extend 15 to 20 jet diameters downstream of the nozzle in order to shield the bulk of the noise sources. However, if the shield length is extended in the downstream direction, then it will ultimately intercept the cone of threshold interference. This will cause significant edge noise, which could be avoided by setting the nozzle high enough above the shield. This solution is not attractive on practical grounds due to aerodynamic and structural requirements. Alternatively, a hyperbolic cutout defined by the intersection of the extended flat plate shield and the cone of threshold interference should afford further noise reduction, at least in oblique planes, without a significant increase of the edge noise. The cutout section is that which would be within the zone of aeroacoustic interference with the jet.

A series of cutout configurations were examined with the nozzle placed above at different heights 'h'. The half angle of ' α ' , the cone of closest approach, was varied from 5 to 20 degrees in 5 degree intervals.

It is clear that some of those configurations will give rise to edge noise, particularly if the shield-jet separation and the cutout cone half angle are small. For the particular configuration, $h/D = 1.5$, $\alpha = 5^\circ$, 10°,

the jet noise shielding obtained at high frequencies is, as expected, accompanied by a low frequency noise augmentation over that of the un-shielded spectrum (Fig. 2-12). On the other hand, if a cone of 15° is used a considerable reduction in the edge noise is achieved at the expense of a reduction in shielding effectiveness at high frequencies. The vertex of the hyperbolic cutout section for $h = 1.5$ D and a cone half angle of 15° is at about 12 D upstream from the trailing edge of the shield (Fig. 2-10b). From the geometry, one can see that a large portion of the jet sources is not shielded from the observer. It thus appears that for a nozzle height of 1.5 D above the shield, there is no suitable 'hyperbolic cutout' which can provide adequate shielding with reduced jet-surface interaction noise.

However, considerable improvement was found by increasing the nozzle height 'h' to 3 D where, by suitable choice of α , the maximum level of the low frequency augmentation is less than the unshielded peak spectrum level at most observer angles. Fig. (2-13) shows the shielding char-acteristics for various cutout configurations at $h = 3$ D. It can be seen that a cutout section corresponding to $\alpha = 10^\circ$ is slightly more effective (inconsistent with the barrier theory) in the 1.5 to 10 kHz range than the corresponding straight-edged shield with no cutout. This behaviour appears to be associated with the edge interaction noise. Generally speaking, although the extra edge noise generated has a dominant low frequency noise spectrum, nevertheless, the noise increase is sufficiently broadband to exert influence on the levels in the mid and

high frequencies, but to a lesser extent. This can reduce the jet noise shielding benefit at the high frequencies. In this sense the shielding configurations should be sought for best mutual accommodation between two conflicting requirements: aerodynamic (ventilation) and acoustic shielding (blockage). For this particular configuration (i.e. $\alpha = 10^0$), the shield with a cutout section reduces the interference effect, so that this smaller shield is actually more effective. This net beneficial effect is less evident when the cutout area is large ($\alpha = 15^0, 20^0$), due to reduced shielding effect.

The low frequency levels in the 200 to 500 Hz range decrease rapidly when the apex of the hyperbolic cutout is moved in the upstream direction (i.e. as α increases). This indicates that the augmentation in this portion of the spectrum is strongly associated with the trailing edge interaction, and hence depends on the shield proximity to the jet. In the 'transition region' there is a balance between shielding and edge noise. This occurs within the 1 to 2 kHz range for the cases examined. The frequency of the cross-over point where shielding becomes dominant increases with decreasing jet/shield separation (Fig. 2 - 13). This is due to increased interference effects as the shield is moved closer to the jet.

Strictly speaking, one cannot estimate the shielding effectiveness of a cutout configuration on a Fresnel number basis since a portion of the shield edge consists of a hyperbola. As a first approximation, one would expect the frequency of the cross-over point where shielding occurs to

decrease as the cutout cone half angle α is decreased or vice versa. At large observation angles ($\theta \sim 90^0$), the cross-over frequency appears to be invariant with α (that is, with cutout size); this indicates that the noise from jet/surface interaction is well above the shielded nozzle spectral levels in this 'transition region'.

It can be seen that a cutout section corresponding to $\alpha = 15^0$ and h = 3 D is a good compromise between the favorable shielding and adverse interference effects (Fig. 2-13b). Here the maximum level of the low frequency augmentation is less than or comparable to the unshielded peak spectrum level at most observation angles θ . Fig. 2-14 shows that the 16 D plate with hyperbolic cutout provides more attenuation on an overall sound level basis than a comparable rectangular shield with identical shield length at the vertex of the cutout (9 D).

It may be argued that it would be more meaningful to compare the shielding of the same 16D plate with and without the cutout. For the latter configuration the edge noise generated by interference is seen to severely limit the effective shielding that can be obtained beyond $\theta = 50^0$ (Fig. 2-14).

2.3.7 Localized Extensions

Although the sources of noise in a jet are distributed over a considerable length downstream from the nozzle, the cross sectional spread is rather limited in extent. It can be argued that the shielding effectiveness of a barrier is governed by the barrier performance nearest the source region (Ref. 20). Thus a more practical implementation of the hyperbolic cutout would be a localized extension (Fig. 2-15). Such a scheme can also include the possibility of a retractable design. This configuration is seen to provide virtually identical noise suppression with a small shield area compared with the non-localized design (Fig. 2-15).

2.4 Half Round Configurations

There is no doubt that direct overflights generate the most intense noise levels. Nevertheless, sideline noise levels are quite high as well. In fact, it is standard practice to measure the maximum sideline noise level at low grazing incidence at a fixed distance to the side of the runway during aircraft takeoff. The ability of an aircraft to meet the noise standard in Federal Air Regulation FAR 36 sideline requirement (Fig. 2-16) is an important consideration in noise shielding.

The planar configurations provide variable noise reduction at points below the shield. A more efficient sideline noise suppression is desirable. Consider a planar wing shield with side fence in the chordwise direction, it should provide some reduction of sideline noise. In order to provide sufficient shielding, the side fence should be as least as high as the jet center line. A structure with such a large area attached to the wing undoubtedly imposes aerodynamic and structure problems. An alternative is to use a half cylinder whose axis is is collinear with the jet axis, extending downstream from near the nozzle. Such shields are referred to herein as 'sugar scoop' shields. The scoop shields approximately the bottom half of the sources, when viewed at side line elevations (i.e. small ψ). Thus these shields can offer better shielding to the sides than flat shields of limited span. For underwing engines, the half round scoop shields can be used to block downward as well as sideline radiation.

The effectiveness of a series of half round 'sugar scoop' shields of diameters 5 D, 10 D, 15 D have been studied. The shields were made from

galvanized steel sheets of 0.43 mm thickness rolled into a cylindrical shape. Variable shield length can be obtained by sliding a concentric piece which extends the trailing edge (Fig. 2-17).

All tests were conducted with the shield axis collinear with the jet axis. Owing to the limited length to avoid running into the spreading jet, the 5 D diameter provides negligible shielding (Fig. 2-18). A contributing reason is the small lateral dimensions of this shield relative to the dominant wavelength of the radiated jet noise. Furthermore, short shield lengths do not shield a sufficient portion of the source region of the jet. The shielding capability of longer shield length (above 6 D in length) is nullified by interference edge noise at large angles. The maximum shield length of this particular half round configuration for negligible interference is about 7 D (Fig. 2-18). This is consistent with the boundary of closest approach as determined by using a narrow probe (cf. Fig. 2-10)

The 10 D shield achieved a reduction of the peak broadband noise by at least three decibels for moderate lengths (12 to 15 D) (Fig. 2-19a). In the direction of peak jet noise (30 degrees), no appreciable gain in reduction can be achieved beyond 20 D in length. Fig.(2-19b) indicates that increases in shield length cause an increase in edge noise. Up to shield length of 22 D, there is increased edge noise; thereafter a decrease is observed. Thus although the longer shields give a greater broadband (or spectral average) attenuation, the lower frequencies are enhanced.

Figure 2-19c shows the expected advantage of the half-round shields over planar shields in attenuating sideline noise. The planar shield shows no lateral attenuation whatsoever: in fact, a slight enhancement.

For the 15 D diameter shield, the jet is at sufficiently large distance from the shield surface so that interaction between jet flow and shield surface is decreased considerably for fixed lengths. In spite of this, overall improvement is exceedingly small as compared with the smaller diameter shields of equal length. This is due to the decrease of effective barrier height as the shield moves away from the jet sources.

2.5 Hybrid Configurations

2.5.1 Introduction

In principle, the problem with the noise generated by the interference between jet flow/shield surface could be alleviated if the shield were replaced by a hot slit jet. This ignores the introduction of other noise sources. The concept stems from the principle that an acoustic wave suffers reflection at a boundary of change of acoustic impedance, such as a layer of hot gas which possesses a higher sound speed than the noise-producing jet (Appendix A). As a sound barrier, the hot gas can only have a limited effective downstream length, for entrainment of colder air progressively weakens the reflective/refractive capability. Consider, however, a hot jet emanating from the trailing edge of a shield: the combination would be effectively longer than either alone. The trailing edge jet should form a reflective extension of the shield that is free of interference edge noise.

In the past, theoretical and experimental studies of reflection and refraction of sound at an interface have been carried out. Of these, a comprehensive treatment of the theory of transmission and reflection of plane acoustic waves at an interface of layered media can found in Brekhovskikh's book (Ref. 22). Earlier works published in this area in the 1940's and 1950's for relatively moving fluid layers were found to err in applying the incorrect boundary condition to the wave equation (Refs. Rudnick[23] (1946), Keller[24] (1955), Franken and Ingard[25] (1956)).

Ribner (Ref. 26)and Miles (Ref. 27) were the first one to solve the problem of a moving fluid medium with the correct boundary condition applied at the interface of the discontinuity. (Continuity of normal velocity component is replaced by continuity of particle displacement.)

Experimental studies of the impedance layer shielding phenomenon have been carried out by I.S.F. Jones (Ref. 28), Norum (Ref. 29), and Cowan and Crouch (Ref. 30). Of these studies, both Jones and Cowan and Crouch used a heated sheet of gas as the shielding layer. Jones used a sheet of acetylene flame lying on an arc to shield a subsonic jet, and obtained a maximum attenuation of about 9 dB over a broad range of frequencies at 30 degrees to the jet axis. Cowan and Crouch made a more extensive experimental study of the shielding characteristics. They used a pure tone sound source located sufficiently far away to obtain quasi-plane sound waves incident on the planar slit jet gaseous shield. Reasonable agreement between the measured transmission loss and that calculated from a theoretical model for plane waves (Ref. 31) was obtained. A high speed air jet was also used as a broadband and distributed noise source to evaluate the effectiveness for practical application to jet noise problem. The results of Cowan and Crouch show an attenuation of 10 to 15 dB across the spectrum at 25 degrees to the jet axis. However, to achieve this the slit jet shield was enormously larger than the round jet it was shielding.

Norum used a low speed helium jet to create an impedance layer. Shielding obtained for pure tones emitted by a point source were in the order of 12 dB for frequencies between 4 and 12 kHz. Thus, these earlier

investigations suggest that substantial attenuations can be obtained from a high sound-speed gas layer, albeit when the layer cross-section is large compared with the jet cross-section and well removed. Subject to this limitation, the concept may have application for reducing jet noise.

2.5.2 Sugar Scoop Plus Thermal Layer Extension

Although the gaseous layers appear to provide a considerable degree of transmission loss, if extensive enough, it has been pointed out herein that a combination of a solid shield and a trailing hot gas layer might be more effective. Some relatively crude experimental tests of this new concept are reported below.

One of the hybrid configurations tested utilizes a thermal layer combined with a half round sugar scoop shield. The composite shield is constructed by attaching a specially modified acetylene burner to the trailing edge of a scoop shield. The burner is made of a 6 mm inside diameter copper tubing drilled with holes and bent into an arc to hug the trailing edge of the scoop shield. A 1.13 m^3 capacity tank supplies acetylene to the burner. The acetylene is passed through a pressure regulator and flexible tubing to a tee which is then connected with additional tubing to the two ends of the burner by means of 90 degree elbows. Some difficulty was experienced in obtaining a uniform sheet of flame. Through trial and error, a final design shown in Fig.(2-20a) evolved. It consists of forty five holes, each hole is 1.4 mm in diameter and adjacent holes are 6.4 mm apart. Although the overall flame sheet may be varied in size, allowance for the adjustment of individual flames has not been made. The length of the luminous core of the flame is about 3.8 cm without the jet on. The individual flames merge and give the appearance of an uninterrupted sheet which extends about 5 cm from the burner.

For conical flames, Jost (Ref. 32) develops a simple formula for the effective flame speed from geometrical considerations. Assuming the velocity of combustion is normal to the cone (flame surface) he obtains the flame speed as (Fig. 2-20b)

$$V_f = \frac{V_n}{\sin \phi}$$

where V_n is the normal velocity of combustion (1.35 m/sec for acetylene C_2H_2 in mixture with air) and ϕ the cone half-angle.

In the experimental set-up, the inner cone of the flame was estimated to be about 0.64 cm.

Therefore
$$\phi = \tan^{-1} (r/h)$$
$$= \tan^{-1} (0.7/6.4)$$
$$= 6.24^{\circ}$$

Thus, the speed of the hot gas close to the proximity of the burner can be estimated as:

$$V_f = V_n / \sin \phi$$
$$= 1.35 / \sin (6.24^{\circ})$$
$$= 12.4 \text{ m/sec}$$

The noise spectrum was measured for the gaseous shield (flame) alone. The flame noise is dominated by low frequencies. (Fig. 2-21). At 150 Hz there is a spectrum level comparable to that of the unshielded jet noise followed by a rapid decay at a rate of 16 dB/dec.

With this solid-gaseous combination, a 10 D diameter shield of length 14 D with a burner attached to the trailing edge provides a total of 4 to 5 dB insertion loss for frequencies above 1 kHz (Fig. 2.22). The visible length to the tip of the flame is about 15.5 D. This is comparable with or better than the attenuation provided at these higher frequencies by a 24 D long shield without a flame. The price is extra 'combustion noise' below 1 kHz.

Further investigations were also carried out with a burner attached to smaller diameter (5 D) shields of 7 D and 10 D in length. In this case, the flame is closer to both the jet axis and the nozzle than with the 10 D configuration just discussed. As expected, the jet/flame inter-action noise increases when the flame is moved closer to the jet (Fig. 2-23). At the same time, the composite shield shows considerably more improvement in shielding over the solid shield alone as compared with the bigger (10 D) shield (Fig. 2-22). This is consistent with expectation since the high frequency sources in the jet, i.e. those in a zone near the nozzle -now lie closer to the hot shielding layer. A layer of hot gas is more effective in blocking the short wave lengths. On the average, a flame attached to the trailing edge of the 5 D shields provides an additional effective length equivalent to a 3 D long extension of the solid material alone for shielding at high frequencies.

The effect of the hot gas layer is more evident as the observation angle θ is decreased (towards the peak intensity direction). At a particular observation angle, the observer's direct line of sight that intersects the shield edge is now interposed by a layer of flame. The sound waves (generated by the turbulent flow) that travel through the impedance layer at small θ to reach the observer are mostly from the high frequency source region (Fig. 2-24). Also, sound waves incident on the interface at a more grazing angle for small θ ($20^{\circ} \rightarrow 40^{\circ}$) are more likely to fall within the 'cut off' region of the layer in which an exponentially decaying wave occurs within the shielding layer instead of a propagating wave.

On the whole, these far-from-exhaustive model tests indicate that some increase in noise reduction can be achieved with the composite shield. The relatively small dimensions of the hot layer together with the jet/flame interaction noise caused the attenuation to fall short of expectation. Analysis of sound transmission through a layered medium (Appendix A) shows that the transmission loss increases with both sound speed ratio, and more strongly with layer thickness. Thus, much higher attenuation should be attainable by means of substantial increase in mass flow. This could be accomplished, for example, by installing cascades of burners. Hotter flames may be one other solut'on, but to be free of jet/flame interaction noise, it might be better to utilize preheated air.

As discussed, previous results in the literature (by Jones and by Cowan and Crouch) have shown attenuation over a broad range of frequencies of order 8 to 12 dB at 30° to the jet axis: these referred to a

gas layer shield alone. This is considerably higher than values measured in the present investigation for a hybrid shield: 'sugar scoop' plus hot gas layer. However, their thermal layers were relatively massive compared with the jet they were shielding, unrealistically so for practical implementation for real jets.

2.5.3. Hyperbolic Cut-outs Plus Sugar Scoops

Another hybrid configuration examined was the combined planar and half round shield. A hyperbolic cutout allows the barrier height to be increased without unduly enhancing the edge noise. At the same time, some of the source region remains exposed. This reduces the effectiveness of the reflective barrier. Accordingly, a scoop shield was installed below the cutout area to shield the exposed region. This provides an additional reduction over the simple planar configuration (Fig. 2-25). On the whole, however, a lighter scoop shield alone is seen to provide the same degree of downward shielding as this hybrid configuration.

3. SUMMARY OF SHIELDING EXPERIMENTS

A variety of shielding concepts has been examined in the laboratory (Fig. 3-1). Several factors appear to limit the effectiveness of the shields. First, the finite size of the shield in conjunction with the extended length of the source region in a turbulent jet allows direct sound radiation from part of the region to be received at most observer positions. Second, the decreasing frequency of noise sources with distance downstream of the nozzle, coupled with the fundamental property of barriers, permits significant noise reduction only at moderate and high frequencies. Third, when the barrier is made sufficiently large to approach the jet boundary -- as it must for significant shielding -- intense low frequency 'edge noise' may mask the shielding effect. In several cases a rise in the overall sound pressure level has been observed.

Among the configurations tested, the half round 'sugar scoop' shield was found to be the most cost effective, providing a good insertion loss in the order of 4 dB for a minimum expenditure of barrier material. The effectiveness of the shielding can be enhanced by the use of a hot gas layer; however careful attention must be paid to the problem of secondary noise sources such as combustion noise and flame/flow interactions. In our tests a longer scoop shield (L=24 D) provides comparable attenuation at the high frequencies (and produced less spurious low frequency noise) than the hybrid shield of visible length 15.5 D.

Overall insertion loss obtained is in the order of 3 to 4 dB, depending on the particular configuration. As the high frequencies suffer more attenuation, the change in the perceived noise level will most certainly differ from the corresponding change in physical sound pressure level. Owing to the increased sensitivity of the ear at high frequencies, the subjective loudness of the received signal ought to decrease. This will be examined in some detail in the ground contour calculations (Section 5).

4. ESTIMATE OF SCALING EFFECTS

The noise data from the model jet must scaled up to a full size jet in order to give estimates of barrier performance at 'operational' frequencies. Thus, scaling laws are required to convert the experimentally measured insertion loss and frequency data of the model up to a full scale system.

It is well known that to a first approximation the jet noise can be scaled to jet velocity U and diameter D by a $U^8 D^2$ power law. Further, it is characterized by a universal spectrum whose peak frequency 'f' occurs at a Strouhal number ($S=fD/U$) of the order of 0.3 . Based on Fresnel number considerations, for a fixed source and observer configuration the effectiveness of a barrier increases with the ratio of a typical dimension L ($=nD$, say) to the wavelength of the incident sound, λ . It is desirable to reduce the noise level at the peak frequency ($f = 0.3 \ U/D$): this in turn determines the typical dimension of the shielding configuration (nD/λ). The parameter D/λ is called the Helmholtz number, H; it can be expressed in terms of S and Mach number M ($H = D/\lambda = (fD/U)(U/C) = SM$). The criterion for similarity in jet noise shielding is to match both the Helmholtz and the Strouhal number between model and full scale. In general, it is not possible to match both, so we match $H = D/\lambda$, which governs the insertion loss at a given frequency. The resultant mismatch in S distorts the scaled model scale spectrum from the correct full-scale spectrum. This is handled by the following argument.

For shielding at any frequency 'f' to be invariant, the ratio D/λ is to be held constant for the model (m) as well as the full scale configuration (j) (Fig. 4-1).

$$D_j/\lambda_j = D_m/\lambda_m \qquad (4-1)$$

Since

$$\lambda = c/f$$

where c = sound speed,

therefore $\quad D_j/\lambda_j = f_j D_j/c_j \quad$ and $\quad D_m/\lambda_m = f_m D_m/c_m \qquad (4-2)$

For the case $\quad c_j = c_m \qquad (4-3)$

the above reduces to

$$f_j D_j = f_m D_m \qquad (4-4)$$

However, this requires that

$$f_j D_j/U_j = f_m(D_m/U_m)(U_m/U_j) \qquad (4-5)$$

or equivalently, $\quad S_j = S_m U_m / U_j \qquad (4-6)$

This implies that if at a certain model frequency f_m, the shielding data yields an insertion loss of say Δ dB, then the full scale should experience the identical Δ dB at a different frequency f_j defined by Eq.(4-5).

To test the validity of the above conclusion, the original 3/4" nozzle was considered to be the 'full scale' jet. A 1/4" nozzle was constructed and used as the 'model'. Flow speeds were varied from M = .3 to .9 so as to provide a variety of U_m / U_j ratios.

In principle, if the scaling law as stated was obeyed, then shielding should be invariant for both model and full scale at properly scaled Strouhal numbers (see Eq. 4-6). Thus, if the attenuation as measured is plotted against this modified Strouhal number, the data should collapse onto a single curve. However, it can be seen from Fig. (4-2) that the experimental data do not quite collapse on a single curve.

At first, the deviation was thought to be due to interference trailing edge noise arising from the shield being close to the jet, which modifies the jet spectrum in addition to the shielding effect. Several tests were then carried out with shields placed further away from the jet axis with negligible interference with the jet flow. However, this does not resolve the dilemma (Fig. 4-3). After further investigation, it was discovered that the jet spectrum of the small nozzle (1/4") did not exhibit the expected Strouhal scaling. This is illustrated by the normalized dimensionless jet noise spectra (Fig. 4-4).

A factor that could contribute to the failure to collapse is as follows. The assumption that insertion loss in dB for model and full scale is the same when D/λ is invariant underlies the analysis. This is based on the geometric similarity assumption that the location x of sources of wave

length λ along the jet axis scales with jet diameter D. But x/D is a function of Strouhal number S = fD/U. Since S is not invariant by (4-5) or (4-6) unless $U_m = U_j$, then x/D is not invariant. This alteration of x/D will have a more serious effect on diffraction for some shield length spacing geometries than others. Without further quantitative analysis, it is not known how this might relate to Figs. (4-2) and (4-3). However, one can see that the small model data points do lie indeed quite close to the large nozzle curve for $U_m = U_j$.

Another reason for the failure of the curves to collapse is believed to be the altered Strouhal scaling of the 1/4" jet. This in turn is believed to be related to the dependence upon Reynolds number (based on jet diameter) where transition from laminar to turbulent flow takes place. It could be that, because of the low turbulence level in the air supply, the boundary layer on the nozzle walls was laminar for the smaller diameter nozzle (1/4"). For larger nozzles, the Reynolds number increases accordingly. It should be pointed out that sound from low Reynolds number jet flows has been observed to behave differently from noise radiated by jets at Reynolds number in excess of 100000 (Ref. 33).

5. GROUND CONTOURS (Noise "Footprints")

On average, 3 or 4 dB reduction of the overall noise level has been achieved. 3 dB represents a redistribution of about 50% of the incident acoustic energy away from the microphone; on a linear scale, this is a considerable amount. However, the human ear does not respond linearly, but approximately as the one-third power of the intensity over a wide range (Ref. 65). Thus the loudness reduction is only about $1 - (.5)^{1/3}$ or 20.6%: not very much. A 1 dB reduction in intensity (7.4% in loudness) is about the minimum variation detectable by the human ear.

To put this in perspective, a 10 dB change in noise level (10-fold in intensity) is close to the hearing sensation of either two times or one-half the loudness, according to the 1/3 power law. The following table shows the subjective response to change in noise levels corresponding to perceived changes in loudness.

Change in Physical Sound Level	Subjective Effect (Change in Loudness)	
1 dB	Minimum detectible	
3 dB	Just perceptible	
5 dB	Clearly perceptible	
10 dB	Factor of two	
15 dB	Factor of three	approximately
20 dB	Factor of four	

Thus an aircraft noise reduction of only 3 dB is barely detectable. A 10 dB reduction is substantial. A 20 dB reduction is very substantial: it corresponds to a hundred fold diminution in the acoustic intensity at the microphone. To achieve an aircraft noise reduction of this magnitude by noise shielding alone is thought to be quite impracticable using present technology.

However, in assessing the effectiveness of shielding, the non-uniform frequency response of the human ear must be taken into account. It is especially helpful if components of the signal that are most annoying can be suppressed. To this end, an appropriate qualifier used in aircraft noise assessment is the perceived noise level (PNL), which provides a measure of the ear's response. PNL accounts for amplitude and frequency with an associated decibel rating: the PN dB.

The PN dB is a measure of the noisiness of a complex acoustic signal. The loudness of a noise is a function of frequency (Fig. 5-1); thus, signals with equivalent overall sound pressure level may not be judged equally loud or equally annoying. The total noisiness of a compound noise is calculated by assigning a level of perceived noisiness (NOYS) to each octave band from 63 Hz to 8000 Hz (Fig. 5-2). The total noisiness N_T is calculated by using the relationship.

$$N_T = N_m + 0.3 (\Sigma N - N_m)$$

where N_m = NOY value of the most noisy bands
and ΣN = sum of the noys values for all eight octave bands (This equation reflects the masking effect of the noisiest band over the others.)

N_T is then converted to a logarithmic measure of the perceived noise by the relation

$$PN\ dB = 40 + 33.3 \log_{10} N_T .$$

There are several methods by which one can implement the PN dB calculation procedure with a computer. The one described in Appendix B is taken from Ref. (35). The present algorithm was validated and was used to facilitate all such calculations.

Aircraft operations have the greatest impact on the population during take-off and landing. It is evident that an observer near the path of the aircraft will be exposed to a higher sound pressure level. As the aircraft moves along its flight path, so does the radiated sound pattern, a portion of which intercepts the ground. Thus 'footprints' of equal peak sound intensity can be defined. If a reduction of jet noise is realized, then the respective footprint areas will be reduced. The footprint will give a more complete picture of the effect of the shielding devices.

We will consider a single aircraft take-off. The maneouver is taken to be as close to the real life situation as possible. A procedure have been developed to compute the peak intensity level at points on the ground.

49

The computer results are used to estimate the effectiveness of the addition of various shielding devices for aircraft noise reduction.

Contours of these footprints are calculated on a PN dB basis. The model data consist of frequency spectra of the basic and shielded jet noise measured at discrete points over a hemispherical surface (Fig. 2-5). To calculate the perceived noise level, the measured noise spectra are analysed in octave bands. The noise radiated above the shield cannot be heard in the community, it is not considered here. The model data have been scaled to simulate a single jet engine delivering a thrust of 11000 Newtons (about 2600 lb). The full scale exhaust velocity and temperature are taken equal to those of the model configuration (see last paragraph on page 46 and Eq. 4-3). Furthermore, the frequency of the jet noise is scaled by the inverse of the geometric scale factor (Eq. 4.4).

The aircraft follows a flight path of 12^0 and climbs at a constant angle and velocity. The flight path and the system of grid points on the ground plane where the noise level is calculated are shown in Fig. 5-3 . We start with a spherical polar coordinate system attached to the aircraft and later make two coordinate transformations to ground-fixed coordinates. As the aircraft flies along the track, the instantaneous coordinates of the ground grid points (i.e. radial separation and polar angles) relative to the aircraft are calculated. The levels at points intermediate to the data 'points' are estimated by means of a two dimensional cubic spline interpolation scheme. Other effects such as

geometric spreading $(I \sim 1/r^2)$ and atmospheric absorption (Ref. 38) of sound are also considered. However, the effects of sound propagation over the ground at shallow angles is ignored: this provides additional absorption.

A computer program was developed to calculate the sound intensity at grid points on a ground plane. The rather complex sequence of operations is indicated schematically in Figure 5-4 . The intensity at the grid points is calculated as function of time for the given flight path. The maximum level is then selected to give the maximum PN dB level at each grid point. Contours of constant PN dB are then interpolated from the maxima calculated at each grid point.

Comparative footprints with and without the various shielding devices are shown in Fig (5-5). The rectangular shields are placed at a shield-jet separation h/D = 3, and the half round shield to be coaxial with the jet. In all cases, the shielding achieves a significant reduction in footprint area. As a basis of comparision, the 90 PN dB contour was considered. The ratio of areas within the 90 PN dB contour for different shields of equal length (L/D = 16)are as follows:

Shield	Relative area within 90 PN dB contour
None (Jet alone)	1.00
Rectangular Wing	.63
Localized Extension	.57
Rectangular Wing with Cut-Out	.46
Localized Extension + Scoop Shield	.40
Scoop Shield (10 D diameter)	.34

It can be seen from Fig. (5-5) that the general shape of the footprint has not been considerably altered; the scoop shield has, however, a significant influence on the width. This reflects the improvement in sideline noise reduction in section 2.4.

It should be pointed out that the extent of the reduction of the enclosed area by a certain PN dB ground coutour as calculated, involved a simplified approximation to simulate full scale flight. Complex and still controversial procedures allow inclusion of the effects of airplane motion relative to a ground observer and forward flight effect on the radiated noise field. The former will give rise to the familiar Dopper shift, the latter not only alters the effective source strength and directivity (Ref. 37) but also appears to have a measurable influence on the shielding effectiveness (Ref. 38). All this is beyond the scope of the present investigation.

6. AN ENGINEERING SCHEME FOR JET NOISE SHIELDING PREDICTION

6.1 Introduction

Scaling laws describing the radiated sound field of a turbulent jet can be derived from the self preservation properties of the turbulence in the mixing region (about 4.5 diameters long) and in the fully developed flow. The turbulent quantities are approximately self-similar in these regions, changing only in scale. As one proceeds in the downstream direction along the jet axis, the jet velocity decrees es and the length and time scales increase. Hence one would anticipate that high frequencies are preferentially generated near the nozzle and low frequencies further downstream. A turbulent jet can be considered as a broad band noise source, where narrow band spectra emitted from short segments of a jet exhibit a characteristic peak frequency that is a function of axial position. One can simplify the picture by letting a given slice of jet emit a single characteristic frequency.

Based on the theoretical formalisms relating certain turbulence properties to the radiated sound, various analytical and experimental diagnostic techniques have been devised; they deduce effective acoustic source strength per unit length as well as the approximate location of the sound sources in the jet. These strength measurements are in essence a means of linking the far field noise field with the flow turbulence

that generates it. Major source location schemes have been proposed by Grosche (19), and Fisher, Harper-Bourne and Glegg (Ref. 40).

In practice, solutions for the diffracted field are sought for relatively clearcut situations where the nature of the sources is well defined, usually a monopole source emitting a pure tone. Even if a reasonable estimate of the behaviour of the barrier can be made, one is still faced with the problem of adapting the information to a jet noise prediction scheme. The difficulty arises from the nature of the sources of jet noise, being a collection of 'correlation volumes' of random instantaneous strength, radiating much like acoustic quadrupoles of random orientation. It has been shown that the diffraction behaviour of the higher order sources is expected to yield poorer shielding as compared with simple monopoles (Ref. 41).

In the present investigation, the sources at different axial locations are treated as statistically independent radiators. This facilitates an approximate prediction scheme for jet noise shielding. It is assumed that it is reasonable to construct an effective far-field spectrum by summing over all possible source positions and frequencies, while accounting for any insertion loss due to shielding. This is in effect an engineering approach. The performance of such a scheme is examined below.

The scheme is based on modelling the jet sources as a distribution of point sources along a line (jet axis). The shielding of point sources is determined (by theory and experiment) as a function of position and frequency. In order to synthesize the jet source shielding from the shielding of point sources, the frequency and intensity distribution along the jet axis must be known. For a given source intensity distribution of a particular frequency, the attenuation due to shielding can be subtracted from the unshielded level separately for each position. The total attenuation for a particular frequency can then be added logarithmically. In this way, a 'shielded' spectrum can be built up (Appendix D).

There are several factors that influence the accuracy of this 'first cut' prediction scheme. However, reasonable predictions are possible if the principal features of flow noise generation and diffraction are accounted for. Aircraft noise shielding involves both diffraction by the solid boundary of the shield as well as the effect of sound-flow interaction, such as refraction by the mean velocity gradient and scattering by turbulence in a flow field. To simplify matters, the sound-flow interaction effect will be considered separately: an experiment was performed to assess whether or not the simplifying assumption that diffraction with no flow present is applicable; this will be discussed later.

As opposed to an omnidirectional source, the amplitude of the incident wave front from a jet that is being diffracted by a shield edge is different from the corresponding unshielded level in a particular direction due to the associated nonuniform directivity of the convected jet noise pattern. This directional pattern peaks strongly at an oblique

angle in the downstream direction. At $90°$ the basic unshielded jet noise is dominated by high frequencies. When a shield is introduced, the incident field in the neighborhood of, and thus diffracted by, the edge will be mainly the low frequency noise component in the peak noise direction. In this analysis, special consideration is given to the directivity factor.

Another important factor is the edge noise phenomenon, which is found to exert considerable influence in raising the shielded spectrum level, especially in the low-and mid-frequency region.

Exact theoretical solutions or, alternatively, chart solutions that combine theoretical approximation with field experience on diffraction by simple configurations (such as a point source and a semi-infinite screen), are available in the literature. However, it is still desirable to measure the insertion loss of point sources experimentally in orde to provide some experimental vertifications. Furthermore, the measured point source shielding results can provide a basis for entailing and adaptation of existing theory to deal with non-simple shield shapes. In addition one can assess the effect of extra 'hidden' variables, these are especially important when the source of sound lies at a distance from the screen that is most typical for aeroacoustic applications. Thus experiments have been performed herein to determine the shielding of point sources as function of frequency and position along the jet axis.

6.2 Point Source Experiment

The experimental arrangement consists of the UTIAS point source (Fig. 6.1) (originally developed for refraction studies (Ref. 3)) placed at selected stations along the jet axis. The driver of the point source is enclosed in a cylindrical container designed to suppress stray sound. The only acoustic path is a 0.33 cm inside diameter hypodermic tubing protruding from the unit (Fig. 6-2). The ratio of the tube diameter to wavelengths (highest = 0.15 for 16 kHz) indicates that a nearly omnidirectional pattern is present for all frequencies of interest. The symmetry of the sound field produced by the point source was confirmed by sweeping a microphone in a circular arc in the horizontal plane of the jet axis. In the absence of flow the source radiates an omnidirectional sound field pattern as anticipated. The attenuation due to normal spherical spreading from the source was also measured in the anechoic room. This attenuation shows good agreement with the inverse square law.

Measurements of the insertion loss of a rectangular shield placed at 3 D from the jet axis have been performed. The omnidirectional piont source is driven by a broad band random noise generator. The insertion loss of the shield is determined by measuring the cross spectrum of the input to the point source and the received microphone signal (Fig. 6-3). Interference effects of the sound field radiating from the two edges of the finite shield can be inferred from the 'hills and valleys' of the measured shielding of the point sound source (see Fig. 6-6 or 7-21). The interference phenomenon is also confirmed by performing the measurements via

the technique of signal averaging (Fig. 6-4   ). Here a pulse train is
used as input to the point source.   The signal is phase averaged
(successive repetitions of the received signal are summed) so that these
periodic signals add coherently, whilst or any random backgound noise is
averaged to a small value. This technique enhances the signal-to-noise
ratios roughly proportional to the square root of the number of repeti-
tions N of the signal.   This means a signal-to-noise improvement of
$20 \log \sqrt{N} = 10 \log N$.

The phase averaged output signal indicates multiple transmission paths
exist (Fig. 6-5   ).   The signals going around the two edges of the
shield are identified on the basis of transit time. With the barrier
inserted, the diffracted signal arrives at a later time than the direct
wave, and is greatly reduced in amplitude. The mismatch in wave shape of
the phase averaged signals supports the multiple transmission path idea.
A simple argument based on the path difference between the signal coming
from the two edges appears to account for the observed pattern
(Fig. 6-6). The interference pattern is eliminated when one of the edges
of the shield is extended sufficiently to approximate a single-edged
semi-infinite plane.   Inside an anechoic chamber this experimental
arrangement is seen to be satisfactory for the condition of a semi-
infinite screen in a free field.

In principle, the pulse technique used for identification of an inter-
ference effect can also be used to determine the insertion loss of the
screen. The phase averaged pulse signal and its power spectrum can be
estimated directly by a fast Fourier transform computer. Hence the
transmission loss as a function of frequency can be determined from the

difference in the levels of the shielded and unshielded spectra. This
method can be useful for evaluating the performance of a barrier in noisy
interfering environments such as along roadways, where a relatively
steady random background traffic noise is present. The phase averaging
tends to average out the background noise.

This pulse technique for insertion loss measurement was applied herein
to the measurement of the insertion loss of shields. It was found to
yield poor results. This was in part due to the sensitivity of the
discrete Fourier transform to small perturbations in a 'single time
record' (obtained by phase-averaging). In addition the sound pressure
level of the pulse obtained from the point source was rather low. This
low signal strength is an inherent weakness of the 'point source'
generator. Attempts at obtaining a stronger signal by overdriving tend
to cause failure of the horn driver.

Before attempting to apply the results from cross spectral measurements,
(using broadband noise input) to synthesize the jet source shielding
from the shielding of point sources, the insertion loss was also measured
using other measurement techniques. This is useful for comparison pur-
poses and provides cross checks.

The main alternate technique (cf. Fig. 6-3) was comparison of time average power spectra with and without shield. First, a pure tone input to the point source was used. Within the shadow zone of the barrier the sound field was found to be characterized by a series of peaks and troughs: this indicates the presence of interference effects. This is a considerable departure from the prediction of the theory of diffraction by a half plane where a monotonic function is predicted (Fig. 6-7). In each case the calculated curve is arbitrarily shifted to envelop the measured curve. The irregular pattern is also found at microphone positions close to the shield.

A warbled tone input was used as an alternative. However, the bandwidth of the warbled tone input is still narrow enough for distinct interference fringes to be formed, although the amplitude of the structure is reduced. A comparison with theoretical prediction is shown in (Fig. 6-8).

Finally, 1/3 octave band noise was used as an input, still comparing time-average power spectra. Results from these runs are in good agreement with the data from cross spectral measurements, and also with theory (Fig. 6-9). A detailed discussion of these results in comparison with theoretical predictions is presented in section 7.5.

In summary, several measuring techniques were explored to determine the insertion loss of a semi-infinite half plane shield:

Signal Processing Scheme	Signal
A. Time-average power spectrum (Fig. 6-3)	(1) pure tone
B. Cross-spectrum (Fig. 6-3)	(2) warble tone
C. Phase-averaging + F.F.T. (Fig. 6-4)	(3) 1/3 octave
	(4) broadband
	(5) pulse train

{ random noise

Techniques

A + (1); A + (2); A + (3); B + (4); C + (5).

Insertion loss measurements using signals such as pure tones or warbled tones (A + (1) or A + (2)) appear to suffer from interference effects. The pulsed signal in combination with signal averaging (C + (5)) is useful in identification of the relevant signal paths. 1/3 octave band noise source (A + (3)) and cross spectrum measurements with random noise input (B + (4)) appear to be the most suitable for insertion loss measurements.

The point source measurements discussed above were performed without jet flow. One argument for this simplification is that sound refraction effects within the jet manifest themselves in a small cone (the 'cone of silence'). This cone half angle is about 20 degrees for a cold jet. This also corresponds roughly to the threshold of closest approach. Thus the diffraction should remain relatively unaffected by refraction effects produced by the jet flow. Hopefully, scattering and 'line broading' by turbulence will also be small. The validity of this notion that jet flow has relatively small effect was tested in an experiment described below.

The sound generated by the turbulent flow must travel through turbulence before reaching the microphone, especially at small angles to the jet axis where the sound generated must travel a long path (e.g. several wave-lengths for frequencies > 8 kHz). Thus to assess the effects of turbulence, small angles are preferred.

To determine the overall effect of the acoustic/flow interaction, the point source was placed in the jet flow field and the results were compared with the no flow case (cf. Fig. 6-3 , with the octave filter connected instead of band pass filter). Measurements (Fig. 6-10) show that the turbulent flow does not have a major effect on the insertion loss characteristics determined from the no flow case.

6.3 Synthesis of Jet Noise Shielding from the Shielding of Point Sources

To synthesize the jet noise shielding from the shielding of point sources, the distribution of intensity and frequency of the effective sound sources along the jet axis must be known or estimated. The data used herein was obtained from Grosche's measurements (Ref. 19); he used an acoustic mirror-microphone to deduce the source strength distribution along the jet centerline.

A universal curve of axial source intensity distribution for any given frequency is shown in Fig.(6-11). The peak normalized source distribution is taken to be (Ref. 42).

$$Q\,(St) \;=\; \frac{x}{X_o}\left[e^{-\frac{1}{2}\left(\frac{x}{X}\right)^2} \cdot \sqrt{e}\,\right] \qquad (6.3\text{-}1)$$

with $X_o = X_o\,(St)$
$\qquad\quad = X_o(fD/U)$

and   e = base of natural logarithms

The location X_o of the peak intensity 'Q' as function of Strouhal number (fD/U) is shown in Fig. (6-12) (Ref. 40   ). The values as indicated by the graph are very close to the ones given in Ref. (42) where Eq. (6.3-1) was obtained.

The source strength distribution and the measured insertion loss data are used to estimate the effective overall shielding at each frequency. As is shown in section (7.5), the point source measurement results are in good agreement with those of the exact solution for diffraction by a semi-infinite plane. Hence, for frequencies of interest that lie even outside the measurement range performed, the analytical solution for insertion loss for those particular frequencies can be considered valid.

Since the jet noise is not radiated equally in all directions, the incident sound intensity appropriate to the direction at which it leaves the source before diffraction by the edge must be determined first. From the geometry of shielding configurations tested experimentally, the effective incident angle of the waves diffracted past a shield edge varies from 10° to 35° from the jet axis, depending on the shield length. However, spectral measurement at angles less than 25° cannot be performed, since this region is well within the jet flow field. Thus, the basic jet noise spectrum at 30° (i.e. referred to as the effective emission angle 'θ_e' of the jet sources before diffraction), is used as the baseline data for computing the expected jet noise attenuation. This assumption is also justified by the fact that the far field spectrum levels at $\theta = 30^{\circ}$ are larger than those found at angles away from this peak direction. In addition the peak frequency at 30° is also lower, which contributes more to the diffracted field. The above consideration points out another effect due to the directivity of the jet noise: the shielded spectrum will show an apparent low frequency augmentation in addition to the edge interference noise if the observer is at a position such that $\theta > \theta_e$.

With the assumed source strength distribution (Eq. 6.3 - 1) and the measured insertion loss data, the effective overall shielding of a jet is computed for three observer angles (40°, 60°, and 90°) (Fig. 6 - 13). In all cases, the baseline data is the unshielded jet spectrum corresponding to $\theta = 30^{\circ}$. Two methods were used to implement the engineering approach. The results indicated by dots give the expected attenuation achieved by applying the point source insertion loss to the extended source distribution, Eq. (6.3 - 1). The total attenuation is calculated by summing the source contributions in small steps along the jet axis (c.f. Appendix D). The squares give the results computed by using the same point source data (fitted well by later Eq. (7.3 - 4)) with the extended line source distribution shrunk, at each frequency, to a point; this point is located according to Fig. 6-12. Surprisingly, the much more approximate simplistic approach (squares), appears to agree much better with the measurements than the 'rigorous' approach (dots).

6.4 Extraction of Edge Effect

An attempt is made here to quantify the extent of influence of edge interference noise to the shielded jet noise spectrum. As explained in previous sections, this additional edge-induced noise can be attributed to a distribution of acoustics dipoles along the trailing edge of the shield. For a given flow velocity, the edge noise depends on the distance between the jet axis and the shield. It has shown experimentally that this additional sound weakens as the shield-jet separation is increased.

Due to the dipole characteristic of the edge noise, the angular distribution of the sound field of the edge noise has a pattern with zero intensity in the direction of the jet axis, and maximum at 90°. In this investigation, an evaluation of the interference noise was made at an angle of 90° with respect to the jet axis. At this angle, the edge-induced interference noise should be strongest.

The amount of shielding obtained by placing a barrier between the observer and the source depends on frequency and the respective positions of the source, receiver, and shield. Furthermore, it is pointed out in section 7.5.1 that the exact solution for diffraction by a half plane depends on four parameters, namely the Fresnel number N, distance from source to receiver kR, angle of source ray to edge θ_o, and the diffraction angle $\theta - \theta_o$ (Fig. 7-2). Thus identical shielding can be achieved for certain differing shielding geometries if these four parameters are identical. A possible shielding configuration is

87

illustrated in Fig.(6-14) by which identical attenuation can be realized. Here both the source and receiver position are fixed, therefore kR is held constant. To maintain the Fresnel number, it is required that 'c+d' be kept constant (Fig. 6-14). One can easily see that the plane curve traced out by the tip of the barrier must lie on an ellipse with the nozzle and the microphone at the foci. However, a barrier edge which extends to any point along the ellipse will not result in identical shielding as θ_o and θ will vary. But θ_o and θ are interchangeable according to mirror image reciprocity. Thus a total equivalence of geometry A and B (Fig. 6-14) is possible as far as point source shielding is concerned.

The validity of the above was examined with a point source. This was carried out with the point source placed at 8 D from the edge and a separation of 12 D from the shield (i.e. a=12 D) for both geometry A and B (Fig. 6-14). Results show no difference in the measured attenuation in both cases.

Based on the above reasoning, one can argue that for certain shielding configurations if the jet-shield separation is increased while the four parameters are kept constant with respect to the nozzle and the microphone, one should realize a similar insertion loss with considerable reduction (or complete elimination) of the edge noise. An approximate scheme for extracting the edge noise is to place the barrier near the microphone at a distance identical to the original nozzle-shield separation. The additional edge noise introduced when the shield is placed

88

close to the flow (geometry A) can be quantified in term of Δ dB by subtracting the corresponding measurements made with the shield far away from the flow (geometry B). The difference should be expected to yield a somewhat quantitative description of the jet-shield interaction noise.

There are two main sources of error associated with the 'two shield-position' scheme. First, the jet sources are not all located at the nozzle exit, but are extended along the jet axis (at least out to 15 - 20 D). Thus the lower frequency sources further downstream have larger Fresnel number N (greater attenuation) for geometry B than geometry A. This implies that part of the difference power spectrum Δ dB$_{A-B}$ at low frequency is not edge noise, but is due to lower contribution of low frequency jet noise to the shielded spectrum for geometry B. This effect tends to exaggerate apparent low frequency edge noise. Another source of error is attributable to the pronounced directivity of the jet noise pattern. Thus, the incident wave front that is diffracted by the shield is different for the two geometries considered. The two-shield-position scheme assumes, on the other hand, that the sources are omnidirectional (monopoles). As the jet-shield separation increases, the effective emission angle corresponding to the wavefront being diffracted by the shield also increases, hence the proportion of the high frequency noise contributing to the far field spectra increases. This leads to a spurious high frequency contribution to the resultant 'difference' curve for edge noise.

From the above considerations, one notes that the present two-shield-position scheme yields error at both low and high frequency. The spatial distribution of the noise source yields error at low frequency, and the directivity factor yields error at high frequency. It appears that no part of the 'edge noise' curve so deduced is free of error. However, it is quite clear from our experimental result (see for example, Fig.2-7) that the interference, or edge noise, effect is dominant at the point where the shielded spectrum crosses above the unshielded basic jet spectrum. For any configuration where sufficient edge noise is introduced, such as the case when the shield penetrates the cone of threshold interference, the edge noise augmentation is greater than 15 dB for frequencies below 700 Hz. Thus it is anticipated that the inherent error of the scheme may have small effect in the frequency range of interest (i.e. frequencies that lies below the crossover point) where the edge noise is most significant. For this reason it may be possible to extract the edge noise semi-quantitatively.

Figure 6-15 is a plot of the difference in spectrum level corresponding to the cases when the jet-shield and shield-microphone separations are identical. Positive Δ dB values indicated are attributed to an augmented spectrum level due to edge noise. As the jet-shield separation increases, the augmentation level decreases considerably. At a separation of 9 D (i.e. a = 9 D of Fig. 6-14), the augmented level is reduced to a negligible amount (Fig. 6-15C). The apparent residue excess level existing at the high frequency end is spurious; it is attributable

primarily to the associated directivity of the jet noise pattern. This excess level indicated by the Δ dB curve at the high frequency end increases as the jet-shield separation increases.

It is possible to use the extracted edge noise spectrum (Fig. 8-15) to quantify the extent of influence of the edge interference noise. In other words, to predict the augmentation level. One can first estimate the shielding attainable for a particular frequency component from its most probable source location (Fig. 8-12) and the corresponding Fresnel number. Here, the baseline data is the unshielded jet spectrum at θ = 30°. The difference spectrum (Fig. 8-15), which reflects the amount of augmentation, can then be added to the shielded level as estimated from above to give the resulant level that combines shielding and interference effects. For example, the expected attenuation at about 1 kHz is 11 dB. At this frequency, the expected augmentation level due to interference (Fig. 8-15a) is about 15 dB. Hence the total effect corresponds to an increase of 4 dB above the shielded level. This agrees reasonably well with the shielded spectrum measured at 90 degree (Fig. 8-18).

7. ANALYTICAL AND NUMERICAL STUDY OF DIFFRACTION BY ARBITRARY BARRIERS

7.1 Classical Diffraction Theory

Analytical solutions for the total sound field due to a collection of sound sources opposed by shielding configurations are discussed below.

The diffraction of waves around obstacles is traditionally one of the more challenging analytical problems in classical physics. Even today exact solutions for bodies other than the simple geometric shapes (spheres,cylinders, etc) are yet to be found. Thus many practical problems are treated with approximate methods. The diffraction problem arose in the discipline of optics. Since then applications have extended to areas such as electromagnetic wave propagation and acoustics. The following discussion centers on aspects central to several diffraction theories permitting solutions to some of the body shapes studied experimentally.

Diffraction theory deals mainly with perturbations in the shadow region of an obstacle that has blocked portions of the advancing wavefront. The perturbations can be regarded as an interference between the incident wave field, treated as though the obstacle were absent, and a 'scattered' wave field due to the obstacle. The precise nature of the diffracted field is governed by the reaction of the physical boundaries. A little

thought will show that the reaction at each point on the surface will influence all the other points on the surface. It is this feature which leads to many difficulties, both analytical as well as numerical.

The relatively few known analytical solutions arise from tractable boundary conditions as would be imposed by rigid bodies such as half planes, discs, spheres, circular cylinders, and wedges (Ref. 43). For these geometries the solution of the scalar wave equation is solved via the method of separation of variables. Thus the scattered field is expressed in terms of eigenfunctions. These idealized problems are often used in development and testing of numerical solution describing sound diffraction from complex shapes.

The classical theory of the diffraction of sound builds on the inhomogeneous wave equation

$$\nabla^2 \psi - \frac{1}{c^2} \frac{\partial^2 \psi}{\partial t^2} = -g \qquad (7.1\text{-}1)$$

where $g(\vec{R},t)$ represents a spatial distribution of sound sources. The wave function ψ can be either acoustic pressure 'p' or velocity potential 'ϕ'. The wave equation governs the incident and diffracted sound fields, subject to certain boundary conditions, as well as the radiation condition. The boundary conditions specify normal acoustic impedance z of the barrier (the generally complex ratio of the pressure to the normal acoustic velocity); for the perfect reflectors dealt with herein, z = ∞. The radiation condition ensures the solution consists solely of outgoing waves.

Let V be the volume between arbitrary surfaces S and S_z (Fig. 7-1a). The general solution to the field function ψ at the field point R is given as (Ref. 44).

$$\psi(\vec{R},t) = \frac{1}{4\pi} \iiint \frac{1}{|\vec{R}-\vec{R_o}|} [g] \, dV -$$
$$\frac{1}{4\pi} \iint \left\{ \frac{1}{|\vec{R}-\vec{R_o}|} \left[\frac{\partial \psi}{\partial n} \right] - [\psi] \cdot \frac{\partial}{\partial n} \frac{1}{|\vec{R}-\vec{R_o}|} + \frac{1}{c_o |\vec{R}-\vec{R_o}|} \cdot \frac{\partial}{\partial n} |\vec{R}-\vec{R_o}| \cdot \left[\frac{\partial \psi}{\partial t} \right] \right\} dS$$

$$(7.1\text{-}2)$$

where $\partial/\partial n$ denotes differentiation in the direction of the outward normal to the surface S and [ ] denotes the retarded time $t - |\vec{R}-\vec{R_o}|/c_o$. This result is the well known Kirchhoff integral. The volume integral represents contribution due to sources within the volume V. The surface integral accounts for all disturbances due to sources outside V entering the surfaces S, (e.g., those within V_o).

It is usually desirable to express an arbitrary time function $\psi(\vec{R},t)$ in terms of its Fourier frequency components. By doing this, one can simplify the problem greatly by considering each frequency component separately; the results may then be summed (integrated) to give the complete solution for $\psi(\vec{R},t)$. This amounts to assuming a harmonic time dependence $e^{i\omega t}$, from which the velocity potential ϕ may be written as a product of a space factor and a harmonic time factor

$$\Phi(\vec{R},t) = \phi(\vec{R}) \, e^{i\omega t} \qquad (7.1\text{-}3)$$

On specializing ψ the form ϕ of (7.1-3), the wave equation (7.1-1) for a source free region (g=0) reduces to an equation for ϕ :

$$\nabla^2 \phi + k^2 \phi = 0 \qquad (7.1\text{-}4)$$

where $k^2 = \omega^2/c^2$. This is the well-known Helmholtz equation. Equation (7.1-2), when specialized to harmonic time dependence, is sometimes referred to as the Helmholtz integral (not to be confused with Helmholtz equation (7.1-4)). This integral provides a method for solving harmonic field problems where the source function and a prescribed set of boundary conditions are known. In diffraction problems the Helmholtz integral states that if some physical property of a sound field such as the velocity potential satisfies the Helmholtz equation in a region V, except possibly at the sources, then the potential at a point P can be expressed in terms of an integral evaluated over a closed surface S that either surrounds or excludes the field point P (Fig. 7.1 a, b).

With the specified harmonic time dependence introduced into (7.1-2), it takes the form

$$\phi(P) = \phi_i(P) + \iint_S \left\{ \phi(q) \frac{\partial G(P,q)}{\partial n} - G(P,q) \frac{\partial \phi(q)}{\partial n} \right\} dS$$
$$(7.1\text{-}5)$$

where G(P,q) is the free space Green's function

$$G(P,q) = \frac{e^{-ik|\vec{R}-\vec{R_o}|}}{4\pi|\vec{R}-\vec{R_o}|}$$

and $\partial/\partial n$ denotes differentiation along the outward normal to the surface S at point q (Fig. 7-1a). The above equation is the Helmholtz integral.

Usually the surface S_2 is arbitrary; thus one can treat it as a mathematical surface which is displaced to infinity. The corresponding surface integral represents contributions from inward-travelling waves due to sources at infinity. One imposes the Sommerfeld radiation condition to ensure that the field consists of outgoing wave only at infinity; this takes the form

$$|\phi R| < c$$
$$\text{and } R\left(\frac{\partial \phi}{\partial R} - ik\phi\right) \to 0 \qquad \text{as } R \to \infty \qquad (7.1\text{-}8)$$

It can be shown that when (7.1-8) is satisfied, the contribution to the integral over S_2 will tend to zero as the surface is displaced to infinity. An additional support of the above criterion is that if the surface integral over S_2 is not zero, the field potential at any point within V is not uniquely determined by the boundary value over the surface S alone (Fig. 7-1a).

From a mathematical point of view the first term of Eq.(7.1-5) is the particular integral of the inhomogeneous wave equation due to the direct effect at P of the sources within V. The second term (where $\iint_{S_2} = 0$) represents the effect of the acoustic disturbances - from simple source/or whatever - originating within V_o. If V_o contains an obstacle

- nothing else - these disturbances will be those scattered or diffracted from the obstacle. In the practical application the surface S is made to shrink down until it coincides with the surface of the obstacle.

Equation 7.1-5 is the basis for diffraction calculations. This formula is exact and the acoustic potential at any point in the appropriate region as specified by the formula can be determined if both ϕ and

$\partial\phi/\partial n$ are known at every point on the boundary. These values are not known unless we have already solved the problem. For applications to obstacles only the normal derivative is usually known directly from the boundary condition (for a rigid surface $\partial\phi/\partial n = 0$). Therefore, the value of the potential on the boundary surface S must be determined. In effect, this requires the solution to an integral equation (see later). Usually, ϕ_i is taken to refer to a single point source, not a volume integral. Alternatively, it refers to a plane wave field.

The solution to the integral equation (solved either analytically or numerically) gives the required distribution of normal velocity, $\partial\phi/\partial n$, or, alternatively, ϕ, induced on the surface. Although diffraction of an incoming wave by obstacle is a boundary value problem, the above formulation determines an equivalent monopole and/or dipole layer on the surface of the diffracting object such that the external field is the same

as that of the original boundary value problem. This method of solution is *generally known* as the integral equation method (Refs. 45-48), for obvious reasons.

The usual procedure to obtain the required integral equation is by placing the field point $P(\bar{R})$ on the diffracting surface S. On taking the limit as $P \rightarrow p$, where p is a point on the surface, one finds the resulting integral equation for the unknown surface potential to be: (Appendix E)

$$\frac{1}{2}\,\phi(P) = \phi_i(P) + \iint_{S}\left[\phi(q)\frac{\partial G(P,q)}{\partial n_q} - G(P,q)\frac{\partial\phi(q)}{\partial n_q}\right]dS_q$$

$$(7.1-7)$$

where $\partial/\partial n$ denotes differentiation in the direction of the outward normal to the surface S and p, q denote variable points on the surface.

An alternative integral equation that holds for the normal derivative of the field potential is (Refs. 47,49)

$$\frac{1}{2}\frac{\partial\phi(P)}{\partial n_p} = \frac{\partial\phi_i}{\partial n_p} + \iint_{S}\left[\phi(q)\frac{\partial^2 G(P,q)}{\partial n_p\,\partial n_q} - \frac{\partial\phi(q)}{\partial n_q}\frac{\partial G(P,q)}{\partial n_p}\right]dS_q$$

$$(7.1-9)$$

Eqs.(7.1 - 7) and (7.1 - 8) are integral equations for the limiting value
of the total wave field potential and its normal derivative as the field
point P approaches a point p on the surface along the external normal of
S directed into V (i.e. with respect to the internal normal for the
region V) (Fig. 7 - 1a). Eq.(7.1 - 7) is the Fredholm integral equation
of the second kind for the Dirichlet problem ($\phi(p)$ specified) while
Eq.(7.1 - 8) applies for the Neumann problem ($\partial\phi(p)/\partial n$ specified).
The integral formulations of boundary value problems have the attraction
of reducing the dimensionality by one, and in principle these equations
could be solved numerically by quadrature, given sufficient computer
time and memory. This is just one of the alternate approaches to
diffraction problems.

Some closed form solutions are available for special cases obtained in
different fashions. One of these is diffraction around a semi-infinite
barrier, which approximates situations of practical interest. This
particular case is presented in the section below.

7.2 Exact Solution for the Semi-Infinite Barrier

Analytical solutions for the diffraction of a plane acoustic wave by an
idealized semi-infinite wedge or straight-edge have been obtained by A.
Sommerfeld (1896) (Refs. 13,50)   . They have served as a foundation
for great many diffraction studies. H.S. Carslaw (Ref. 39) obtained an
integral representation of the diffracted field by a thin half plane for
a spherical incidental wave from a point source with no restriction on
source location. This exact solution will be discussed here in order to
determine the validity of some approximate methods employed later herein
for prediction of shielding of jet sources by certain finite barrier
configurations.

Let ϕ be the total velocity potential of the acoustic wave at any point
in the sound field; it must satisfy the Helmholtz equation and the rigid
boundary condition $\partial\phi/\partial n = 0$ on the shield surface. The expression for
the total velocity potential in the sound field due to a point source at
(r_0, θ_0, z_0) (Fig. 7 - 2) is given in terms of contributions from a real
source and a image source as (Refs. 43,51)

$$\phi = U(\theta_s) + U(-\theta_s) \qquad (7.2-1)$$

Potential due   Potential due
to real source   to image source

This combination of source and image fields, when suitably chosen,
serves to cancel $\partial\phi/\partial n$ on the plate, while allowing ϕ and $\partial\phi/\partial n$ to be
continuous beyond the plate edge.

The potential associated with each source in Eq. 7.2-1 is composed of a direct potential ϕ_i (due to an unshielded point source) and a scattered potential[**] ϕ_s (due to the shield), namely,

$$U(\theta_o) = \phi_i(\theta_o) + \phi_s(\theta_o) \qquad (7.2-2a)$$

$$U(-\theta_o) = \phi_i(-\theta_o) + \phi_s(-\theta_o) \qquad (7.2-2b)$$

The rigorous solution for the potential (Ref. 51) is given in terms of cylindrical coordinates (r, θ, z) whose z axis coincides with the plate edge (Fig. 7-2). In what follows a harmonic time factor $e^{-i\omega t}$ is to be understood, but not written out. Hence the unshielded point source potential is $\phi_i = e^{ikR}/R$. An appropriate representation of this incident wave potential is in terms of Hankel functions of the first kind (Refs. 51, 52) as:

$$\phi_i = \frac{ik}{2} \int_{-\infty}^{\infty} H_i^{(1)}(kR\cosh\mu)\, d\mu \qquad (7.2-3)$$

An alternate formulation will later be more convenient: the substitution

$$\cosh\mu = \tau^2/kR + 1$$

leads to

$$\phi_i = ik \int_{-\infty}^{\infty} \frac{H_i^{(1)}(\tau^2 + kR)}{\sqrt{\tau^2 + 2kR}}\, d\tau \qquad (7.2-4)$$

[**] The 'scattered' field includes the 'diffracted' field (as commonly defined) plus 'shadow-forming' fields; see later.

81

The scattered potential ϕ_s is given as (Ref. 51):

$$\phi_s(\theta_o) = \mp ik \int_{im}^{\infty} \frac{H_i^{(1)}(\tau^2 + kR)}{\sqrt{\tau^2 + 2kR}}\, d\tau \qquad (7.2-5)$$

where $m = \pm\sqrt{k(R_1-R)}$, $\mp,\pm$ for $\cos(|\theta - \theta_o|/2) \gtrless 0$. This choice results from the requirement that the combined potential $\phi_i + \phi_s$ for both source and image should satisfy $\partial\phi/\partial n = 0$ on the barrier, with continuity beyond the edge.

Using Eqs. (7.2-4) and (7.2-5), and noting that the argument of $H_1^{(1)}$ is an even function of τ, the two potentials is combined to give:

$$\begin{aligned} U(\theta_o) &= \phi_i(\theta_o) + \phi_s(\theta_o) \\ &= ik \int_{-m}^{\infty} \frac{H_1^{(1)}[\Gamma^2 + kR]}{\sqrt{\Gamma^2 + 2kR}}\, d\Gamma \end{aligned} \qquad (7.2-6)$$

Similarly an expression can be obtained for $U(-\theta_o)$ with R replaced by R'.

Hence the total velocity potential due to diffraction is given by

$$\Phi = ik \int_{-m}^{\infty} \frac{H_1^{(1)}[\Gamma^2 + kR]}{\sqrt{\Gamma^2 + 2kR}}\, d\Gamma + ik \int_{-m'}^{\infty} \frac{H_1^{(1)}[\Gamma^2 + kR']}{\sqrt{\Gamma^2 + 2kR'}}\, d\Gamma \qquad (7.2-7)$$

$$m = \pm\sqrt{k(R_1-R)} \; ; \quad \pm \text{ FOR } \cos(\theta-\theta_o)/2 \gtrless 0 \quad \begin{array}{l}\text{BRIGHT ZONE}\\ \text{SHADOW ZONE}\end{array}$$

$$m' = \pm\sqrt{k(R_1-R')} \; ; \quad \pm \text{ FOR } \cos(\theta+\theta_o)/2 \gtrless 0$$

$$R = \{r^2 + r_o^2 + (z-z_o)^2 - 2rr_o\cos(\theta-\theta_o)\}^{1/2}$$

$$R' = \{r^2 + r_o^2 + (z-z_o)^2 - 2rr_o\cos(\theta+\theta_o)\}^{1/2}$$

$$R_1 = \{(r+r_o)^2 + (z-z_o)^2\}^{1/2} = \{R^2 + 4rr_o\cos^2(\theta-\theta_o)/2\}^{1/2}$$

82

The integration limit $\int_{-m}^{\infty}$ rather than $\int_{-\infty}^{\infty}$ in (7.2-6) represent a partial cancellation between ϕ_i and ϕ_s . This serves to block out the source and image fields in their respective shadow zones[*]. It is common to refer to the remainder after cancellation as the 'diffracted' field. With this reinterpretation the waves in regions I,II,III of figure (7.2b) are as follows: region I: direct (incident), reflected and diffracted waves; region II: direct and diffracted waves; region III: diffracted waves only.

Returning to the resultant potential, Eq.(7.2-7), one can see that the lower limit of integration 'm' is determined by the shortest diffracted path over the edge (this is in the form of $\sqrt{k(R_1-R)} \sim \sqrt{\text{Fresnel number N}}$). The integral may be regarded as consisting of a superposition of diffracted waves over all ray-paths over the edge, starting with this minimum length path.

A conclusion applicable to the general case can be drawn from the limits of integration in Eq.(7.2-7): namely, as the Fresnel number N (see above) increases, the total diffracted potential decreases re the free field value. Hence one would expected higher attenuation as the shadow angle increases.

[*]   See earlier footnote re "shadow forming" fields.

If the argument of $H_1^{(1)}$ is large enough, i.e. $\tau'+kR = kR_1 \gg 1$, the Hankel function

$$H_1^{(1)}(kR_1) = J_1(kR_1) + j\, N_1(kR_1)$$

diminishes in magnitude with increasing kR_1 (i.e. $\sim kR_1^{\frac{1}{2}}$). The asymptotic expansion of the Hankel function $H_1^{(1)}(x)$ for large x is :

$$H_1^{(1)}(x) = e^{-3i\frac{\pi}{4}}\left[\frac{2}{\pi x}\right]^{\frac{1}{2}}\left\{1 + \frac{3i}{8x} + \frac{15}{128\,x^2} - \cdots\right\} e^{ix}$$

Taking only the first term,

$$\lim_{x\to\infty} H_1^{(1)}(x) = \left[\frac{2}{\pi x}\right]^{\frac{1}{2}} e^{ix}\, e^{-3i\frac{\pi}{4}} \qquad (7.2-8)$$

Substitution for the Hankel function in Eq.(7.2-6) by the expression in Eq.(7.2-8) and integrating (see for example Ref. 53) gives an approximate expression for the shield potential. It is decomposed into a geometrical field ϕ_i and a diffracted field ϕ_d as (Ref. 54):

$$\phi = \phi_i + \phi_d \qquad (7.2-9)$$

where

$$\phi_i = \eta(\pi+\theta_o-\theta_o)\frac{e^{ikR}}{R} + \eta(\pi-\theta_o-\theta)\frac{e^{ikR'}}{R'}$$

$$\eta(x) = \begin{matrix}1\\0\end{matrix}\ ,\ \begin{matrix}x>0\\x<0\end{matrix}$$

and

$$\phi_d = -\sqrt{\frac{2}{\pi R_1}}\ e^{i\frac{\pi}{4}}\left\{\ sgn(\pi+\theta_o-\theta)\frac{e^{ikR}}{\sqrt{k(R_1+R)}}\ F\left[\sqrt{k(R_1-R)}\right]\right.$$

$$\left. + sgn(\pi-\theta_o-\theta)\frac{e^{ikR'}}{\sqrt{k(R_1+R')}}\ F\left[\sqrt{k(R_1-R')}\right]\right\}$$

where

$$sgn(x) = \begin{matrix} -1 & x > 0 \\ 1 & < \end{matrix}$$

and $\quad F(a) = Fresnel\ Integral$

$$= \int_a^\infty e^{it^2}\, dt$$

In the later sections, numerical evaluations of both Eqs.(7.2-7) and
(7.2-9) for the semi-infinite shield will be adapted in various ways so
as to approximate the sound attenuation due to finite shielding
configurations.

7.3 Approximate Methods

The above account illustrates that a considerable effort is required, if
an exact solution to a diffraction problem is to be found. It is an accept-
ed rule that closed form solutions (other than pure symbolic ones) are
restricted to certain basic geometries and boundary conditions. For
arbitrary configurations, numerical solutions are a possibility. These,
however, are not always very cost-effective. An alternate approach
would be via an asymptotic theory of diffraction: that is, a theory which
retains much of the underlying physics, but discards certain features so
as to make the solution more tractable. The Kirchhoff theory of dif-
fraction is such a theory. It is an application of Helmholtz's formu-
lation of Huygen's principle for monochromatic scalar waves. The theory
requires a certain representative function of a sound field such as the
velocity potential or pressure to have a harmonic time dependence.

The Kirchhoff theory of diffraction involves making reasonable assumpt-
ions about the unknown quantities ϕ and $\partial\phi/\partial n$ on the surfaces of
integration. These enable the integral to be evaluated directly. The
approximation assumes that the actual field on the side of the surface
that is visible from the source is to be replaced by the incident field,
and by zero on the shadowed side. This neglects the effect of
diffraction over the obstacle and ignores any mutual interaction between
points on the opposite sides, as if the bright side of the diffracting
surface is perfectly absorbent. Thus the assumption is :

$$\phi = \phi_i \quad , \quad \frac{\partial\phi}{\partial n} = \frac{\partial\phi_i}{\partial n} \qquad \text{on bright side}$$

$$\phi = 0 \quad , \quad \frac{\partial\phi}{\partial n} = 0 \qquad \text{on shadow side}$$

(7.3-1)

In this way, the Kirchhoff formula can be written as (c.f. Fig. 7-1a)

$$\phi(P) = \phi_i(P) + \iint_s \left[\frac{e^{-ik|\bar{R}-\bar{R}_o|}}{|\bar{R}-\bar{R}_o|} \frac{\partial \phi_i}{\partial n} - \phi_i \frac{\partial}{\partial n} \frac{e^{-ik|\bar{R}-\bar{R}_o|}}{|\bar{R}-\bar{R}_o|} \right] dS$$

(7.3-2)

where $\partial/\partial n$ denotes differentiation along the inward normal to S. The assumption that the front surface of the diffracting plane is perfectly absorbent is equivalent to neglecting the diffraction effect due to an image source; whereas the exact solution for a semi-infinite straight-edge (Eq. 7.2-7) does account for this effect. Further consideration shows that the boundary conditions given in Eq. (7.3-1) make ϕ and $\partial\phi/\partial n$ discontinuous as one goes around the edge from the bright zone into the shadow zone. Physically these quantities should be continuous, hence this denotes a further shortcoming.

Comparisons with exact theory have shown that this scheme works best if the wavelength is very small in comparison with the typical dimensions of the object, as encountered in optics. In contrast most physical objects encountered in acoustics are not small compared with wavelength, thus Kirchhoff's method must be applied with some caution if it is to provide a useful comparison base for rigorous diffraction analysis. Fig.(7.3) shows a comparison between the exact and Kirchhoff solution. It is evident that considerable discrepancy exists for all observer points within the shadow zone, the error increasing as one goes deeper into the shadow. This is indeed the trend shown by Pierce in Ref.(56), where the Kirchhoff approximation is justified analytically to be valid only if the receiver is located at or near the 'diffraction boundary layer', i.e. region where Fresnel number $N \sim 0$. This approximation is expected to be increasingly less valid the further the observer is from the edge of the shadow zone. Although the Kirchhoff theory does have a rather limited range of validity, it is a

basis for development of approximate theories. For laminar obstacles, it can be cast into a particularly simple formalism due to Rubinowicz. This will be used later herein.

An alternative method for deriving approximate solutions of diffraction problems is based on geometrical acoustics. Although simple ray theory does not explain diffraction phenomena, J.B. Keller has proposed an extension of geometrical optics which accounts for diffraction (Ref. 57). The initial strength of the diffracted ray leaving the edge is determined by multiplying the field of the incident rays by an appropriate diffraction coefficient. The diffraction coefficients are determined by the local geometrical and physical properties in the immediate neighborhood at the point of diffraction, such as the direction of incidence and diffraction, the wavelength, and the geometrical and physical properties of the media. The edge diffracted rays are also found to obey a certain law of edge diffraction, relating a cone of a diffracted rays to the angle the incident ray makes to the edge at the point of diffraction. Keller shows that this approximate solution for diffraction is the asymptotic expansion of the exact solution for Fresnel numbers that are large compared with unity. Keller's geometric optic approach is, however, not very useful in the present context: the usual values of the Fresnel numbers encountered in acoustics are much smaller than the values attained in optics, the discipline from which the theory has acquired most of its experimental confirmation.

For simple shapes, there are numerous engineering prediction schemes based upon asymptotic or approximate solutions. These do not rely on

cumbersome solutions, instead charts and monographs are employed (Refs. 58-61) . The solutions are mostly empirical formulas based on theoretical approximation with field experience. Often explicit correction factors are applied. Such methods are useful for a quick and convenient estimate of barrier performance.

Keller has derived an asymptotic solution for diffraction of spherical waves by semi-infinite barrier as (Ref. 61): (Fig.7 - 4)

$$\Delta \, dB = -20 \, \log \frac{1}{2\pi\sqrt{\delta/\lambda}} - 20 \, \log \frac{d}{A+B} - 20 \, \log \frac{\sqrt{2}}{1+d/(A+B)}$$
$$- 20 \, \log \frac{1}{\sqrt{2}} \left(1 + \frac{\cos \frac{1}{2}(\theta - \alpha)}{\sin \frac{1}{2}(\theta + \alpha)} \right) \qquad (7.3-3)$$

Kurze and Anderson in Ref. (61) pointed out that Eq. (7.3 - 3) does not yield the correct solution for the case when the Fresnel number N is zero: this corresponds to the case when the source, the diffracting edge, and the receiver are collinear. When the field point and the source point is sufficiently far away from the plane of the barrier, the exact value of the insertion loss for N = 0 is 5 dB. The following approximation to Eq. (7.3 - 3), altered by the 5 dB correction, is given by Kurze (Ref. 61) as

$$\Delta \, dB = \left\{ 20 \, \log \frac{2\pi N}{\tanh \sqrt{2\pi N}} + 5 \right\} \, dB \qquad (7.3-4)$$

Eq. (7.3 - 4) is plotted in Fig. (7 - 5) and is in good agreement with Maekawa's measurements for N > 1.

7.4 Rubinowicz's Line Integral Theory of Diffraction

This section outlines a very attractive approach in which the diffraction field component of the Kirchhoff integral is transformed into a line integral along the edge of the diffracting body. Rubinowicz's diffraction formula is (Ref.13):

$$\phi(P) = \alpha \phi_i(P) - \frac{1}{4\pi} \oint \frac{e^{-ik\rho}}{\rho} \, \frac{e^{-ikr}}{r} \, \frac{\vec{r} \cdot (\vec{\rho} \times \vec{dl})}{r\rho + \vec{r} \cdot \vec{\rho}} \qquad (7.4-1)$$

with α = 0 or 1, depending on whether the field point is or is not in the geometrical shadow; $\vec{\rho}$ and $\vec{r}$ denote vectors from the source and field point to the edge element $\vec{dl}$, respectively.

The above formula states that the diffracted field potential can be regarded as being generated by a fictitious line of acoustic sources placed on the rim of the diffracting body. Although this formalism also suffers from the drawbacks arising from the Kirchhoff approximation, the contour integral provides an approximate method for taking the effect of complex geometry in diffraction into account (For example, a hyperbolic cutout section along the edge of a flat shield).

The transformation of the Kirchhoff integral Eq.(7.3-2) from an integral over the area of the surface of the thin barrier to a line integral around the barrier is given in Refs.(13) and (60). The approach of Ref.(60) is outlined here to illustrate the formalism with

the aid of Fig.(7.6 a). The illuminated side S_2 of the abstacle is separated from the 'dark' side S_3 by the simple closed curve Γ . Rays from the source passing through points of Γ and beyond define a kind of cone. Since the surface S_0 that encircles the source is arbitrary, the value of associated surface integral will not be altered if the surface is deformed, provided that the observation point P remains outside. Here, with S_2 kept constant, S_0 is deformed as in Fig.(7-6b) such that the original S_0 is composed of two open surface S_4 and S'_2 with Γ as their rim. Hence one gets

$$ \iint\limits_{S_\circ + S_2} \approx \iint\limits_{S_4 + S_2 + S'_2} $$

Since the normals to S_2 and S'_2 point in opposite directions, the contributions to the surface integral over these portions will cancel. The surface integral over S_0 and S_2 as indicated in Eq.(7.3-2) is thus reduced to an integral over an 'arbitrary' unclosed surface S_4. It also follows that the value of the integral does not depend on the actual shape of the open surface, but only on the form of the rim Γ . In fact, it has been shown in Ref.(50 , p.74-79) that the surface integral over an unclosed surface can be transformed into a line integral along the rim via the Maggi transformation :

$$ \frac{1}{4\pi}\iint\limits_{S_4}\left[\frac{e^{-ik/\bar{R}-\bar{R}_\circ|}}{R-R_\circ}\frac{\partial\phi_i}{\partial n} - \phi_i\frac{\partial}{\partial n}\frac{e^{-ik/\bar{R}-\bar{R}_\circ|}}{|\bar{R}-\bar{R}_\circ|}\right]dS \rightarrow \frac{1}{4\pi}\oint\limits_{\Gamma}\frac{e^{-ik\ell}}{\ell}\frac{e^{-ikr}}{r}\frac{\bar{r}\cdot(\bar{\ell}\times\bar{dl})}{r\ell+\bar{r}\cdot\bar{\ell}} $$

$$ (7.4\text{-}2) $$

where $\partial/\partial n$ denotes differentiation along the inward normal to S.

Hence, for the diffraction geometry of Fig. 7.1-a , the Kirchhoff integral can be expressed as

$$ \Phi(P) = \propto\phi_i(P) - \frac{1}{4\pi}\oint\limits_{\Gamma}\frac{e^{-ik\ell}}{\ell}\frac{e^{-ikr}}{r}\frac{\bar{r}\cdot(\bar{\ell}\times\bar{dl})}{r\ell+\bar{r}\cdot\bar{\ell}} $$

where $\propto = 0$ or 1 according as P is or is not in the geometrical shadow. The effective source at the edge is of monopole type and its strength is determined from the direct path from the source to the particular element of the diffracting edge. The term

$$ \frac{\bar{r}\cdot(\bar{\ell}\times\bar{dl})}{r\ell+\bar{r}\cdot\bar{\ell}} $$

is the inclination factor of the edge wave, and the line integral is sometimes interpreted as generating a 'boundary diffraction wave'. Since this quantity is real, the edge wave has the same phase as the direct wave that travels from the source to the edge before being diffracted by the edge.

7.5 RESULTS AND DISCUSSION

Semi-Infinite Configurations (Straight-Edged Barrier)

7.5.1 Comparison of Theory and Experiment

It was mentioned in section (6.2) that the shield insertion loss in the point source experiments was evaluated by a variety of methods including cross spectral density (for broad band excitation) and signal averaging plus Fourier transform (for pulse train excitation). Comparative power spectra measurements via pure tone excitation, warbled tones and 1/3 octave filtered noise were also used for the insertion loss measurements. In general, these methods show comparable results with the exception of pure and warbled tone excitation. Here an apparent wave interference causes the data to show fluctuations about the smooth results obtained by other measurement techniques.

The measured attenuation obtained by cross spectral density measurements of the input to the point source and the far field microphone signal is shown in Fig.(7.7) together with the theoretical results from the exact solution given by Eq.(7.2 - 7). The results are plotted as functions of the Fresnel number N, defined geometrically as in Fig. 2-3. The theoretical curve was generated by numerical integration of Eq.(7.2 -7) The infinite interval is reduced to a finite interval by ignoring the 'tail' of the integrand. This tail was estimated for various values of the upper limit in the integral for negligible truncation error. A computer program listing for the half plane diffraction using the exact solution is given in Appendix G (Computer listing #1).

Referring to Eq. (7.2 - 7), the theoretical insertion loss in dB is given by $-20 \log |\phi / \phi_i|$. This is a function of the four independent variables[*], R_1, R, θ_0, θ, the first two of which are normalized by wavelength. This takes care of the frequency dependence. The dependence of the solution upon these variables implies that a given degree of attenuation can be achieved with various combinations of source and receiver positions. An example is illustrated in Fig. (7 - 8), where the plane θ_0 is unfolded to the plane θ. The nondimensional shortest distance is therefore a straight line in the unfolded plane. Here the independent variables, hence the attenuation, are kept constant in each case. These independent variables can be expressed in non-dimensional form as kR, kR_1, θ_0 and θ, the first two of which may can be combined to form the Fresnel number

$$N = \{2/\lambda\} (R_1 - R) \qquad (7.5.1)$$
$$= \{k/\pi\} (R_1 - R)$$

Replacing this four-fold dependence (kR, N, θ_0, θ) by a dominant dependence on the Fresnel number N is common, and is supported by experiment. There remains a weak dependence on three of the original four variables. These three then become 'hidden variables' in a plot of insertion loss vs. the single variable N. A more detailed discussion is postponed to a later section.

---

[*] From Eq. 7.2 - 7, it appears that the insertion loss is governed by five non-dimensional variables kR, kR_1, kR', and angles θ and θ_0. kR', however, can be deduced from four other parameters:

$$kR' = \left\{ (kR)^2 + \frac{(kR_1)^2 - (kR)^2}{2 \cos^2[(\theta - \theta_0)/2]} \left[\cos(\theta - \theta_0) - \cos(\theta + \theta_0) \right] \right\}^{1/2}$$

The nine plots of Fig. (7 - 7) refer to three microphone positions at 40, 60, and 90 degrees with respect to the jet axis[*], and three effective source frequencies 4, 6 and 8 kHz. The point source is located along the jet axis and its position is varied from $x/D = 1$ to 15 (cf. Fig. 6 - 2) to alter Fresnel number N. The range of N covered is approximately from 0 to 13. The plane of the microphone traverse direction is perpendicular to the shield and also contains the line traversed by the point source.

With the use of the virtually ideal UTIAS point source and carefully conducted experiments, there is, for the most part, very good agreement (average deviation less than 1 dB) between the data and the theoretical predictions. Some residual bumpiness suggests the existence of interference effects. The maximum deviation from the predicted values is 1.5 dB for data obtained at microphone positions of 40 and (4 kHz only) at 60 degrees. The best agreement appears to be obtained at 90^0 (all frequencies) and for the two higher frequencies at 60^0.

The experimental insertion loss points from Fig. (7-7) for various combinations of source frequencies and shielding geometries are superposed onto a single graph of insertion loss vs Fresnel number (Fig. 7-9a). For a fixed Fresnel number, it can be seen that the scatter range is considerably larger than when each case is observed individually. This was further examined by plotting the corresponding theoretically determined points for all nine cases of Fig. (7-7) on the same graph (Fig. 7-9b). One can see that the calculated points do not fall nearly along a simple curve, but instead they define a scatter band. This

* The jet nozzle is present to be used for   jet shielding measurements; there is no jet flow in the presen. experiments.

represents an apparent indeterminacy due to 'hidden variables', mentioned earlier. It reflects the fact that although N is the dominant variable, there are three other weak variables that have been hidden in the plot. The scatter band arises from the uncontrolled variations in these hidden variables from one to another of the nine cases.

The effect of these 'weak' variables (kR, θ, θ_0) was examined by varying each parameter one at a time. Curves of attenuation vs source/receiver separation kR for a series of Fresnel numbers are plotted in Fig. 7-10; the calculations are based on Eq. 7.2 - 7 with $\theta_0 = 0^0$ and any receiver angle θ (i.e. source or receiver on shield surface). For values of θ_0 other than 0, similar curves have been obtained. It can be seen from Fig. (7-10) that the weak parameters kR, θ_0, $\theta-\theta_0$ have a noticeable effect on attenuation besides that due to the strong parameter N. The variation, however, decreases with increasing kR and approaches a certain value asymptotically. For each set of specified values of θ, θ_0, kR, and N, there are restrictions in allowable source/receiver positions that are compatible with a given set of parameters. For example, for given kR, θ_0, θ there is a maximum value of N that occurs at $z - z_0 = 0$ and $r/r_0 = 1$[*]. This corresponds to the intersection points of the curves

* For given kR, θ, θ_0 one can show that N_{max} occurs when $\partial R_1/\partial(r/r_0)$ and $\partial R/\partial(z-z_0)$ vanish. From this one obtains the required conditions as: $z - z_0 = 0$ and $r/r_0 = 1$. Hence from Eq. (7.5-1) we have

$$N_{max} = \pi^{-1}kR\left(\sqrt{2/(1-\cos(\theta-\theta_0))}-1\right)$$

$$kR_{min} = \pi N/\left(\sqrt{2/(1-\cos(\theta-\theta_0))}-1\right)$$

$$\theta - \theta_{0\,min} = \cos^{-1}\left(1 - 2/\left(1+\frac{\pi N}{kR}\right)^2\right)$$

for constant N and $\theta-\theta_0$ in Fig. (7-10). The abscissa of the intersection point is the minimum allowable kR value to sustain a given Fresnel number. For a fixed N, the minimum allowable kR value generally decreases with increasing angular separation $\theta-\theta_0$ between the source and receiver. This is because as the diffraction angle increases, a given path length difference can be maintained with a smaller source/receiver separation R. These curves also show that the diffraction angle $\theta-\theta_0$ clearly has a more noticeable effect on attenuation than kR for kR > 30 and N < 20. The dimensionless parameter kR of the measurement points is quite large (> 100); it is thus concluded that the scatter band is not much contributed to by variations in kR, but is primarily due to variations in the source angle θ_0 or $\theta-\theta_0$.

The experimental attenuation points for all nine cases of Fig.(7-7) are superposed on the theoretical band vs. Fresnel number (Fig. 7-9b) in Fig. (7-11). The data collapse is very good, only occasionally departing from the theoretical band by as little as 1.5 dB.

The asymptotic solution via the Fresnel integral Eq. (7.2-9) has also been computed with an asymptotic series representation for the real and imaginary part of the integrand. As expected, the approximate solution is in good agreement with the exact solution since the Fresnel number is quite large and the dimensionless parameter kR_1 (Eq. 7.2-7) has a value well above 100 for the geometry considered experimentally (Table 1).

7.5.2. Exact vs Approximate Solution

To examine the feasibility of the engineering scheme, the prediction from Eq.(7.3-4)

$$\Delta\, dB = \left\{ 20\, \log \frac{2\pi N}{\tanh \sqrt{2\pi N}} + 5 \right\}\, dB \qquad 7.3\text{-}4$$

is plotted in Fig.(7-12) together with the exact solution (Eq. 7.2-7) for several source-receiver geometries. The approximate formula is at most 1.5 dB from the exact solution. This agreement is quite good if we consider that only one parameter, N, is involved in the formula whereas the exact solution requires four: it depend on features of the geometry as well as on N. As seen from Fig.(7-12), the approximate scheme consistently overpredicts the exact solution for the geometry of the present experiments by 1.5 dB for these geometries.

The discrepancy in the approximate solution (Eq. 7.3-4) is in fact due to the dependence of the solution upon some of the 'weak' parameters contained in the exact solution. For the particular geometries considered (Fig. 7-12), it can be shown that the disagreement is explained by variations in the angular dependence, θ_0 and $\theta-\theta_0$.

This is illustrated in Fig.(7-13) by plots of exact solutions showing the effect of the angular dependence of the solution on the

source angle θ_0 and the observer angle θ in reference to the barrier plane. For each N, the dashed line shows the attenuation calculated by the approximate solution (Eq. 7.3-4), which is clearly a constant function of $(\theta-\theta_0)$. Over the range of Fresnel numbers for those geometries considered in Fig.(7-12), the approximate solution over-predicts the exact solution for $N > 1$ and underpredicts for $N < 1$. A case is considered below where the expected discrepancy, which can be deduced from Fig. (7-13), is shown to be compatible with the trend indicated in Fig. (7-12C). For this shielding configuration simple geometrical calculations show that the measurements for $N > 1$ correspond to a change in value of θ_0 from 11^0 to 37^0 and $\theta-\theta_0$ from 270^0 to 244^0 as N approaches 1 from the higher values. More precisely,

$$N = 1 \quad \longrightarrow \quad \theta-\theta_0 = 240^0, \; \theta_0 = 37^0$$
$$N = 5 \quad \longrightarrow \quad \theta-\theta_0 = 264^0, \; \theta_0 = 17^0$$

The computations are based on kR = 200; a value typical for most cases examined experimentally. For the above values of the parameters, one can see that the expected discrepancy, as estimated from Fig.(7-13) (indicated by arrows), corresponds very closely to the error indicated in Fig. (7-12C) for the corresponding N. For $N \to 0$, $\theta-\theta_0 \to 180^0$, it is quite clear from Fig. (7-13) that the approximate solution predicts a lower attenuation than the exact solution, this also confirms the trend in Fig. (7 - 12). It should be noted that the boundary of the shaded zone in Fig. (7-12) marks the minimum allowable diffraction angle $\theta-\theta_0$ for designated values of Fresnel numbers. Effectively, the attenuation occurring at $(\theta-\theta_0)_{min}$ is the maximum attainable for given N, kR and θ_0.

7.5.3. Modified Semi-Infinite Configurations (Hyperbolic Cutouts)

Other than the integral equation approach, there is no known analytical solution for predicting the difffraction of sound for complicated geometries. Although the solutions for the classical problem of diffraction by semi-infinite thin screen are adequate for many practical situations, it is sometimes necessary to consider the effect of a perturbation to the shape of basically similar barriers. When dealing with a geometry such as a hyperbolic cutout along an edge of a thin barrier, the straightedged solution is clearly not applicable.

As discussed in section (7-4), the approach due to Maggi and Rubinowicz shows that the value of the surface integral in the Kirchhoff formula depends only on the shape of the rim of the unclosed surface; in fact, the surface integral is replaced by a line integral. Thus, one would expect that the line integral could accommodate a change in shape of the contour along the edge.

In recent publications Embleton (Ref.82,83) has applied the line integral to calculate the barrier attenuation in the presence of the ground. Embleton has gone further and transformed Eq.(7.4-1) from a line integral to an ordinary single variable integral. His modified version of Eq.(7.4-1) which gives the diffracted field in the shadow zone is (Ref. 82) (Fig. 7-14) :

$$\phi = -\frac{A}{2\pi} e^{-i\omega t} r_s \sin\theta \; \frac{e^{ik\sec\beta[r_r + (r_s^2\cos^2\beta + r_r^2\sin^2\beta)^{1/2}]}}{E} \cos^2\beta \; d\beta$$

where

$$E = (r_s^2\cos^2\beta + r_r^2\sin^2\beta)^{1/2}\left[r_r\sin^2\beta + (r_s^2\cos^2\beta + r_r^2\sin^2\beta)^{1/2} - r_s\cos\theta\cos^2\beta\right]$$

$$(7.5-2)$$

However, the above transformed integral is only applicable for a straightedged barrier. For the present purpose, the original form as in Eq.(7.4-1) is more appropriate when the diffracting object is arbitrarily shaped.

For a semi-infinite barrier, the line integral is evaluated along the edge which extends to infinity and joins by a semi-circular arc to both ends. In the present configuration, the point source is located much closer to the edge than is the observer. The dominant contribution to the line integral for the diffracted field, which can be thought of as representing fictitious acoustic sources along the edge of the barrier, will come from a relatively short section of the edge located nearest to the source. Hence the line integral need not necessarily be performed over the entire length of the barrier.

To test the above assumption, Eq.(7.4-1) is evaluated for a straight-edged barrier with the line integral performed over various distances on one side of the axis of symmetry (and doubled). The value of the

101

integral exhibits a damped oscillatory characteristic about an asymptotic value (Fig. 7-15). For a frequency of 8 kHz, the calculations indicate that a half-span about 6 wave-lengths from the point of closest distance to the source is sufficient for a source located at about 15 D (6.7 wave-lengths) from the edge (Fig. 7-15b). If the source is moved closer to the edge, the half-span integrating distance required by the line integral decreases. For a source-to-edge separation of less than 8 D (3.6 wave-lengths), it is only necessary to perform the line integration for 4 wave-lengths along the edge to yield an error of less than 0.5 dB (Fig. 7-15e). In each case, the half-span line segment of integration is approximately equal to the source/edge separation. This is also found to be true for other frequencies.

The strength of the sources at the edge is inversely proportional to the distance of the point source from an edge element. The length of the effective line source (see above) equals about twice the source/edge separation. Thus the diffracted field effectively originates from a finite distribution of simple sources with a sound source intensity varying from a maximum value, determined by shortest distance from the edge to the source, up to a point where the effective strength is decreased by a factor of .707 (i.e. 3 dB).

For comparison, Embleton's formula (Eq. 7.5-2) is also evaluated for various value of β for a straight-edge. β is the angle specifying the location of the line element along the edge relative to the receiver (Fig. 7-14). Taking symmetry into account, the edge wave is generated as β varies from 0 to $\pi/2$ for an edge that extends to infinity. The

102

calculations indicate that an upper limit of $\beta = 10^0$ gives an error of less than 0.5 dB. From the geometry, this corresponds to a distance of about 6.5 wave-lengths from the axis of symmetry, in good agreement with the previous result.

In view of these findings, the sound field as predicted by the line integral theory is calculated herein with the lowest appropriate upper limit in the numerical integration. This is done to save CPU time on computer. Calculations comparing the exact solution with the line integral approximation are shown in Fig.(7-12). Since the line integral formulation is a development of the Kirchhoff theory of diffr-action, it also contains all the shortcomings of the original Kirchhoff approximation. The results show a discrepancy similar to that in Fig.(7-3b), namely an over-prediction. Generally speaking, the accuracy improves in the region close to the shadow boundary where the Fresnel number N approaches zero.

As discussed earlier, Rubinowicz's diffraction integral suggests that the structure of the edge wave generated at the rim of a barrier depends only on the separation and orientation of the edge element, with respect to the source, at the point of diffraction: this determines the strength of the simple sources on the edge and the inclination factor. It is also noted that in this theory each point on the contour does not influence the other points on the contour. This assumption of no mutual inter-ference seems unrealistic in the case of the field diffracted by narrow slits or cutouts whose opening is less than a few wave-length across.

103

To evaluate the diffracted field due to a cutout by means of the line integral (Eq. 7.4.1), suppose (x,y,z) denotes an arbitrary point lying on the edge (Fig. 7-16). One can write:

$$\bar{\rho} = (x - x_s)\,\hat{\imath} + y_s\,\hat{\jmath} + z\,\hat{k} \qquad (a)$$

$$\bar{r} = x\,\hat{\imath} - y_r\,\hat{\jmath} + z\,\hat{k} \qquad (b)$$

$$\bar{\rho} \times \vec{dl} = [y_s\,dz]\,\hat{\imath} + [z\,dx - (x - x_s)\,dz]\,\hat{\jmath} - [y_s\,dx]\,\hat{k} \qquad (c)$$

$$\vec{r} \cdot (\bar{\rho} \times \vec{dl}) = [-z(y_r + y_s)]\,dx + [x\,y_s + y_r\,(x - x_s)]\,dz \qquad (d)$$

$$\bar{r} \cdot \bar{\rho} = x(x - x_s) - y_s\,y_r + z^2 \qquad (e)$$

$$(7.5-3)$$

where source point $= (x_s,\ -y_s,\ 0)$, and field point $= (0,\ y_r,\ 0)$.

Along the straight portion of the edge

$$dx = dl$$

whereas along the cutout portion

$$dx = \frac{dl}{\sqrt{1 + (dz/dx)^2}}$$

applies for constant step of dl. The diffracted field is calculated by substituting Eq. (7.5-3) into Eq. (7.4-1). As for the straight-edged configuration, the line integral need only be performed numerically along the shield edge for some distance where the sources along the rim contribute significantly to the diffracted wave.

Prior to applying this prediction scheme to the hyperbolic cutout, the present method was examined on a cutout following a cosine shape. This form allows the cutout contour to blend in smoothly with the straight portion. A feature which is appropriate for examining the effect of varying the cutout width. The form of contour chosen was

$$Z/D = 12 - 4 \cos (\Pi Z/Z_m) \qquad 7.5-4$$

where z_m denotes the cutout halfwidth. The straight-edged portion $(z \geq z_m)$ has a shield length of 16 D. The vertex point of the contour is at 8 D. The source and field points are located as in Fig. (7-16). This particular geometry and the basic shield lengths are typical of configurations tested experimentally.

The change in attenuation of a cosine cutout is plotted in Fig. (7-17) with respect to a semi-infinite straight-edged barrier without a cutout. The source frequency is 8 kHz, and the attenuation is plotted against normalized cutout half-width z_m/λ. There is no change in attenuation at $z_m/\lambda = 2.4$. Surprisingly, if the cutout width is narrower than this value, there is an apparent improved shielding performance over that of the datum rectangular shield. This may be due to interference due to

close proximity of the edges. For cutout widths of the order of 3 or 4 wave-lengths, the performance of the barrier deteriorates at a rate of about 1 dB per wave-length increase in width. Beyond a cutout width of 6 wave-lengths, the attenuation is relatively insensitive to further increase in the cutout width. This is consistent with the previous results for a straight-edge calculation where, for that shielding geometry, only a limited extent of sources along the edge make significant contribution to the diffracted sound field.

This cosine shape calculation leads us to computation of the diffracted field due to a semi-infinite planar straight-edged shield with a hyperbolic cutout section via the line integral approach. If one takes the center point of the nozzle exit as the origin of coordinates, the cutout is represented by the equation of a hyperbola in the form (Fig. 7-18).

$$\chi = \frac{\sqrt{z^2 + h^2} - D/2}{\tan \alpha} \qquad (7.5-5)$$

where

    h = distance of jet axis from shield

    D = jet diameter

    α = half angle of cone

        (later identified with threshold cone of interference of a jet).

The diffracted sound field due to this cutout can be calculated by using Eq. (7.5 - 3) and Eq. (7.5 - 5). The result for this configuration shows higher attenuation than the corresponding cosine cutout with identical cutout width at the edge. This shows that the shielding effect is very much influenced by the geometry of the contour (i.e. the inclination factor).

It is quite clear that the discrepancies in the Rubinowicz line integral results are quite substantial in the shielding calculation for a straight-edged barrier. Depending on the source and receiver positions, the error can be as large as 8 dB over a wide range of Fresnel numbers (Fig.7-12). Similarly, there should be comparable errors in the same direction between the measurements and the results from the line integral theory evaluated for a cutout. This expected trend is consistent with the fact that the inclination factor of the edge wave depends solely upon the geometry of the boundary. Each line element dl can be interpreted as a portion of a hypothetical straight-edged barrier (Fig. 7 - 19). In general, therefore, one can anticipate that the error associated with a cutout configuration should be comparable to that of a straight-edged barrier. Thus, for similar source-shield positions, the numerical results calculated for a cutout configuration can be adjusted via an appropriate approximate correction factor that can be determined from the straight-edge calculations. It can be seen from Fig. (7-19) that the hypothetical straight-edged barrier height 'h' corresponding to a line element dl varies as the slope of dl varies. In general 'h' is a function of distance along the contour. For a hyperbolic cutout, 'h' is largest for a line element at the vertex point and decreases to its

smallest value at the end point of the contour. It is quite clear from Fig. (7-12) that as the Fresnel number decreases, i.e. as barrier height decreases, the accuracy of the line integral improves. To this end, the decision was made to derive a correction factor that was based on the largest 'h', i.e. a point on the contour corresponding to the path of the shortest diffracted ray, for the particular source/receiver geometry. For example, comparison between the exact solution (Eq. 7.2 -7) and the line integral solution for frequencies between 4 k to 8 kHz shows an error ranging from about 6 dB at a source to edge distance 's' of s/D = 6 to 3.5 dB at s/D = 2 for a semi-infinite straight-edged barrier. With these values applied with reversed sign as a correction to a cutout configuration with similar source-shield positions, one can see that the calculated results agree with experimental measurements within acceptable limits (Table 2-A). Here the shielding geometry is identical to Fig.(7-16), with the hyperbolic cutout replacing the cosine cutout.

Furthermore, ignoring any mutual interference effects that might exist between the boundary diffraction waves that are generated along the cutout contour, it is expected that the shielding performance of a hyperbolic cutout which occupies a certain portion of a straight-edged barrier should be between the attenuation provided by the corresponding straight-edged barrier without a cutout and one that extends up to the vertex point. This behaviour is indeed observed for sources located at less than 2 D from the vertex point of the cutout along the axis of symmetry. Thus correction factors based on the average performance of such a configuration can be derived. The analytical predictions so deduced are seen to track the point source measurements with an improved accuracy (Table 2-B).

Finite Configurations

7.5.4 Planar Rectangular Shields

The semi-infinite configurations were studied in order to provide a baseline comparison with other shielding configurations. As opposed to empirical correlations, it has the attraction of being amenable to rigorous theoretical prediction of the shielding attenuation. As discussed below, the analysis also serves as a basis for approximate solutions for finite planar configurations.

In practical applications we must consider finite shielding configurations. The boundary value problem formulated for a planar configuration usually involves Wiener-Hopf techniques. These give a system of integral equations that are often very difficult to solve exactly. Among the few cases where solutions exist, the one that has the closest resemblance to a planar rectangular shape is that of a semi-infinite strip. The solution is expressed in terms of Mathieu functions and is not directly applicable for finite size (Ref. 4 3). Because of the short-comings, it may be preferable to obtain approximate closed form solution for finite barrier in terms of semi-infinite barrier solutions.

One method for approximating the shielding by a finite rectangular shield is suggested by Broadbent and others (Refs. 55,52,54,61): one apply the semi-infinite half plane solution for the potential to each edge of the shield. The magnitude of the sum of the complex valued pressures is considered to approximate the total field. This method is

justified by the principle of stationary phase when the incident wavelength is sufficiently small compared to other distances. From Eq.(7.4-1) or Eq. (7.3-2), one sees that the integrand consists of the product of a complex exponential with a phase dependance of $k_i \ell + r$ and an obliquity factor in the form of $f(e,r)/\rho r$. When the wave number k is large, the dominant contribution to the integral comes from points at which the phase is stationary (Refs. 52,55) . For a straight edge, this corresponds to the points at which the path length from the source to the observer is minimum. This then implies that in the high frequency limit one can take a given edge of a finite shield, and calculate the shielding due to that edge as if it were extending to plus and minus infinity, by means of the semi-infinite half plane solution.

This method of approximating shielding of a finite barrier by summing the diffracted field calculated for each edge separately using the corresponding semi-infinite solution also amounts to assuming there is no mutual interference between the incident wave at the diffracting edges. This can be justified if the separation 'd' of the edges is a few wavelengths across. For the present configuration, the ratio of the width to wavelength $d/\lambda = 3.6$, 5.4, and 7.2 for frequencies of 4, 6, 8 kHz respectively.

The accuracy of the above scheme was tested with a source/shield arrangement as shown in (Fig 7-20). The location of the point source is varied between the two long edges. At any source position, the two long

edges will contribute more significantly than the short edges which are relatively far away from the point source. This geometry has practical relevance to typical jet-source/wing-shield configuration, and hence it is desirable to determine the accuracy of the method for wing shielding of jet sources.

The effect of the corners of a rectangular shield is discussed in Ref. 52. The contribution of a corner is shown to be substantially less than that of an edge in the regime where the method of stationary phase is applicable. Hence, for a rectangular shield where the corners are sufficiently far away from the point of minimum path length, the main contribution will be due to edge diffraction alone.

The predicted and measured shielding are plotted as a function of distance from one edge in Fig.(7-21). The top and bottom edges were neglected in the calculation due to their large distances from the point source as compared to the other two edges. Also, in the experimental setup, the bottom edge was secured at several points to a base in close contact with the edge for maintaining proper orientation. In contrast to the semi-infinite configuration, the diffraction pattern for a finite shield consists of a series of peaks and troughs of considerable amplitudes.

The quantitative agreement is very good except for several of the highest peaks. Any discrepancies in the form of overprediction or underprediction of the amplitude are limited to the range of 1 to 4 dB. This could be due to inaccuracy in positioning of the point source. This source of experimentally induced error is more apparent in the finite configuration than in the semi-infinite case. Another contributing factor to the error is the presence of the settling chamber for the model air jet in the close proximity of the shield (Fig. 7-20) in the experimental setup. Even though this chamber is covered with fibreglass there may be some reflections. These will alter the incident sound field at one edge to some degree.

At source locations near the downstream edge and at $\theta = 40^0$, there is more significant contribution from this edge than other edges by virtue of the large difference in Fresnel number. It can be seen that the prediction scheme shows fairly good agreement with these measurements, where the error caused by reflection is less significant.

7.5.5   Half Round Shields

The half round cylindrical scoop shield is a more complex shape than the planar shield. Exact or approximate closed form solution are not available in the literature. The alternative is the generalized integral equation approach which can be formulated specifically for any particular problem. Diffraction by thin sheets have been solved by the integral equation methods (Refs. 46,49). In particular, the formulation and method of solution due to Terai (Ref. 49) will be developed and adapted herein to solve the diffracted sound field around a rigid half circular cylindrical shell.

As discussed in section 7.1 , Eqs.(7.1-7) and (7.1-8) are central to the calculation of acoustic scattering from arbitrary shapes. These are integral equations of the second kind characterizing the diffraction phenomenon in the form of :

$$f(x) = g(x) + \int K(x,y) f(y) \, dy \qquad (7.5-6)$$

with g , and k given and f is the unknown function. In general for arbitrary body shapes, numerical procedures must be employed to obtain solutions.

As stated before, the field potential ϕ in E..(7.1-7) and (7.1-8) is that of the total wave and is composed of the incident field potential and the diffracted potential ϕ_d. For an acoustically hard surface, the appropriate boundary condition is $\partial\phi/\partial n = 0$ on S. In order to take adventage of the homogenity of the boundary condition for a hard surface, it is usually more convenient to use Eq.(7.1-8).

Now, a thin rigid plate can be considered as the limit at which the thickness of a finite body decreases to zero. In this case, Eqs.(7.1-7) and (7.1-8), which are appropriate for finite bodies, require modifications. The following integral equations replacing Eqs. (7.1-7) and (7.1 - 8) respectively are appropriate for thin plates as presented by Terai (Ref. 49):

$$\frac{1}{2}\left[\phi_{(p_1)} + \phi_{(p_2)}\right] = \phi_i + \iint_S \left\{\left[\phi_{(q_1)} - \phi_{(q_2)}\right]\frac{\partial\, G_{(p,q)}}{\partial n_q} - \left[\frac{\partial\phi_{(q_1)}}{\partial n_q} - \frac{\partial\phi_{(q_2)}}{\partial n_q}\right] G_{(p,q)}\right\} dS_q$$
$$(7.5-7)$$

$$\frac{1}{2}\left[\frac{\partial\phi_{(p_1)}}{\partial n_p} + \frac{\partial\phi_{(p_2)}}{\partial n_p}\right] = \frac{\partial\phi_i}{\partial n_p} + \iint_S \left\{\left[\phi_{(q_1)} - \phi_{(q_2)}\right]\frac{\partial^2 G_{(p,q)}}{\partial n_p \partial n_q} - \left[\frac{\partial\phi_{(q_1)}}{\partial n_q} - \frac{\partial\phi_{(q_2)}}{\partial n_q}\right]\frac{\partial G_{(p,q)}}{\partial n_p}\right\} dS_q$$
$$(7.5-8)$$

where $\partial/\partial n$ denotes differentiation in the direction of the normal to the plate taken outward from one of the surfaces of the plate and the subscripts (1), (2) denote points on opposite sides of the plate at a.

Using Eq.(7.5-8), with $\partial \phi / \partial n = 0$ applied on both surfaces of S, the integral equation reduces to

$$- \frac{\partial \phi_i}{\partial n_p} = \iint_S \left[\phi(q_1) - \phi(q_2) \right] \frac{\partial^2 G(p,q)}{\partial n_p \partial n_q} \, dS_q \qquad (7.5-9)$$

Eq.(7.5-9) is an integral equation of the first kind written in the form

$$g(x) = \int f(y) \, K(x,y) \, dy \qquad (7.5-10)$$

with $g(x)$ and $K(x,y)$ given. The problem is to solve for the unknown function $f(y)$. The function K is call the kernel of the integral equation. With the free space Green's function defined as (see Fig. 7.22a):

$$G(P,Q) = \text{GREEN'S FUNCTION}$$
$$= \frac{e^{-ik|\vec{R}-\vec{R}_o|}}{4\pi |\vec{R}-\vec{R}_o|}$$

and $\vec{r} = \vec{R}-\vec{R}_o$, $r = |\vec{R}-\vec{R}_o|$, the kernel K is expressed as :

$$K(p,q) = \frac{\partial^2}{\partial n_p \partial n_q} \left[\frac{e^{-ikr}}{r} \right] \qquad (7.5-11)$$

$$= \frac{e^{-ikr}}{r^3} \left\{ \left[k^2 r^2 - 3ikr - 3 \right] [\hat{r} \cdot \hat{n}_p][\hat{r} \cdot \hat{n}_q] + [1 + ikr][\hat{n}_p \cdot \hat{n}_q] \right\}$$

115

The kernel can be interpreted as the gradient in the $\hat{n}_q$ direction of the field at point q due to a unit dipole with axis $\hat{n}_p$ at point p.

A numerical representation of the integral equation can be obtained with the elementary discretization method : that is, the surface is divided into a finite number of elemental areas. The area of each element must be taken sufficiently small, i.e. dimensions $\ll \lambda$. From this, we can assume that the surface potential within the element is constant and represented by the value at the center.

Under these considerations, the unknown potential function in Eq.(7.5-9) can be taken outside the integral sign and the resulting integral equation is discretized and converted into a system of simultaneous algebraic equations :

$$F_i = K_{ij} \, \phi_j \qquad (7.5-12a)$$

which may also be written as

$$[F] = [K][\phi] \qquad (7.5-12b)$$

Here [ϕ] is a column matrix for the unknown surface potential jump.

[K] is a square matrix defined by the kernel function.

[F] is a known column matrix denoting the negative of the incident normal velocity component $\partial \phi_i / \partial n$, on the surface.

116

The body surface is subdivided into m elemental areas (finite elements) (Fig. 7-22b). F_i refers to the center of the i-th element, ϕ_j to the center of the j-th element, K_{ij} is the mutual influence kernel (Eq. 7.5-11) referring to both elements.

Numerical solution of Eq.(7.5-12) involves

(1) Evaluation of the kernel function K_{ij} = [K] over all combinations of i = 1 ... m, and j = 1 ... m.

(2) Evaluation of $[\phi]$ via $[K]^{-1}[F]$; the matrix inversion and subsequent multiplication is performed on a digital computer.

The input data includes the coordinates of the control points where the surface potential jump is to be calculated, the outward normal at each point, and the normal component of the acoustic velocity $\partial \phi_i/\partial n$ at the control points.

Recall that the matrix coefficient are defined by integrals of the form:

$$\iint \frac{\partial^2}{\partial n_p \partial n_q} \left[\frac{e^{ikr}}{r} \right] dS = \iint \frac{e^{-ikr}}{r^3} \{ [k^2 r^2 - 3ikr - 3][\hat{r} \cdot \hat{n}_p][\hat{r} \cdot n_q] + [1 + ikr][\hat{n}_p \cdot \hat{n}_q] \} dS$$

(7.5-13)

Thus when p=q, r vanishes (Fig. 7-22a), and the integrand (kernel) becomes singular due to the factor e^{-ikr}/r^3 ; the form in Eq.(7.5-13) is then inapplicable. To examine the behaviour of the singular kernel, one may consider the use of planar elements that are sufficiently small in size to fit quite reasonably well into a surface to approximate an arbitrary body. In any event, even when planar elements can not be used readily, regardless of the type chosen, the curvature of the element is usually small. Thus, the behaviour of the kernel as the point p approaches the point q can be investigated by considering a planar element in the neighborhood of such a point.

To treat the singularity, the first step is to transform the surface integral to a line integral around the boundary of the element (Ref. 49). Assuming a point P is at a distance z above the plane that contains the element (Fig. 7-23b), one can write

$$r_{pq}^2 = r^2$$
$$= \rho^2 + z^2$$
$$r\, dr = \rho\, d\rho$$

and
$$\iint_{element} dS = \int_{\theta_1}^{\theta_2} \int_{r_1}^{r_2} r\, dr\, d\theta$$

If the element contains the point p, then the kernel becomes singular at the point where p=q, as a point P off the surface approaches the point p along a normal $\hat{n}_p$ (Fig. 7-23b). For this particular case, one excludes

the point where $\rho = 0$ and surrounds it with a small circle of radius σ. It follows that

$$(\hat{r} \cdot \hat{n}_p)(\hat{r} \cdot \hat{n}_q) = (z/r)^2$$

Therefore, Eq.(7.5-13) can be written as

$$K = -\int_o^{2\pi} d\theta \int_\sigma^{R(\theta)} \frac{e^{-ikr}}{r^3} \left\{ \left[3(1+ikr)+(ikr)^2 \right] \left(\frac{z}{r}\right)^2 - (1+ikr) \right\} r\, dr\, d\theta \qquad (7.5\text{-}14)$$

The integration with respect to the variable r is evaluated by means of integration by parts, applied successively to terms of the form :

$$\int \frac{e^{-ikr}}{r^4}\, dr = -\frac{e^{-ikr}}{3r^3} - \int \frac{ik}{3r^3}\, e^{-ikr}\, dr$$

$$\int \frac{e^{-ikr}}{r^3}\, dr = -\frac{e^{-ikr}}{2r^2} - \int \frac{ik}{2}\frac{e^{-ikr}}{r}\, dr$$

and $\quad \int \frac{e^{-ikr}}{r^2}\, dr = -\frac{e^{-ikr}}{r} - \int ik \frac{e^{-ikr}}{r}\, dr$

The integration yields :

$$K = -\int_o^{2\pi} d\theta \cdot \frac{e^{-ikr}}{r} \left[(1+ikr)\left(\frac{z}{r}\right)^2 - 1 \right]_\sigma^{r(\theta)} \qquad (7.5\text{-}15)$$

In the limit as $P \to p$, z tends to zero. The value of the integral evaluated along the outer boundary $\rho(\theta)$ is

$$\frac{e^{-ik\rho(\theta)}}{\rho(\theta)}$$

For the inner boundary as σ tends to zero,

$$(\hat{r} \cdot \hat{n}_p)\ ,\ (\hat{r} \cdot \hat{n}_q) \to -1$$

hence

$$(\hat{r} \cdot \hat{n}_p)(\hat{r} \cdot \hat{n}_q) = \left(\frac{z}{r}\right)^2 \to 1$$

this yields a factor independent of θ :

$$\left. \frac{e^{-ik\sigma}}{\sigma} \left[1+ik\sigma -1 \right] \right|_{\sigma \to o} = ik$$

Thus for an element which contains the point 'p' where the kernel becomes singular, the matrix coefficient has the value

$$K = -\oint \frac{e^{-ik\rho(\theta)}}{\rho(\theta)}\, d\theta - 2\pi ik \qquad (7.5\text{-}16)$$

If the diffracting surface is planar, the matrix coefficient for an element lying in the same plane as, but not containing, the point 'p' is given by the first term of Eq.(7.5-16). For any element,

$$\hat{r} \cdot \hat{n}_p \ , \quad \hat{r} \cdot \hat{n}_q \ = 0$$

and $\qquad \hat{n}_p \cdot \hat{n}_q = 1$

Eq.(7.5-13) is reduced to

$$K = \iint \frac{e^{-ikr}}{r^3} [1 + ikr] \, dS \qquad\qquad (7.5\text{-}17)$$

$$= \int d\theta \int [\frac{e^{-ikr}}{r^2} + ik \ \frac{e^{-ikr}}{r}] \, dr$$

$$= \int d\theta \int [-\frac{e^{-ikr}}{r} - ik \ \frac{e^{-ikr}}{r} + ik \ \frac{e^{-ikr}}{r}] \, dr$$

$$= -\oint \frac{e^{-ik\rho(\theta)}}{\rho(\theta)} \, d\theta \qquad\qquad (7.5\text{-}18)$$

where $\rho_1(\theta)$ and $\rho_2(\theta)$ are the intersection of the radius vector with the boundary and its near and far side respectively (Fig.7.23a). Eqs.(7.5-9), (7.5-11),(7.5-16) and (7.5-18) can be used to determine the distribution of the acoustic potential jump '$\phi(q_1) - \phi(q_2)$' on the surface of any thin plate by solving the system of equations (Eq. 7.5-12)

with complex coefficients. Once the surface potential is found on the surafce Eq.(7.1-5) with $\partial\phi/\partial n = 0$ can be used to calculate the total acoustic potential at any point in the field off the diffracting body.

The accuracy of the method was tested for a rectangular plate so as to compare with published experiemental results (Ref.49). This also allows one to investigate the limitation of the formalism before applying it to more complicated shapes. The diffracted field was computed for a rectangular rigid panel of dimension .2m x .3m with source - panel distance of 5 m and panel-receiver distance of .31 m. A point source emitting a 1000 Hz tone is situated on the central axis of the panel. The panel has been approximated by 96 square elements with dimension L = .025 m for each side. The control points are taken as the centroid of each element. Here the boundary condition is imposed; it requires tnat the normal velocity component be

$$\frac{\partial r_i}{\partial n_p} = \frac{\partial}{\partial n_p}\left[\frac{e^{-ik|\vec{R}-\vec{R}_o|}}{4\pi |\vec{R}-\vec{R}_o|}\right]$$

$$= -\frac{e^{-ik|\vec{R}-\vec{R}_o|}}{4\pi |\vec{R}-\vec{R}_o|} \left[ik + \frac{1}{|\vec{R}-\vec{R}_o|}\right] \hat{n}_p \cdot (\vec{R} - \hat{\vec{R}}_o)$$

$$\qquad\qquad\qquad (7.5\text{-}19)$$

where $\overline{R}-\overline{R}_o$ denotes a vector directed from the point source to a control point 'p' on the body.

The ratio of the acoustic wavelength to the linear dimension L of the element chosen is quite large, of the order $\lambda/L \approx 13$. Thus it is clear that kr does not vary greatly over the element. In addition if L/r is also small (i.e. the control point is far away from the element), a first approximation to the value of the integral of Eq. (7.6-17) can be obtained by setting $r = r_o$, where r_o is the distance between each control point. Under those circumstances the integrand can be treated as a constant. Thus the matrix coefficients are determined as follows:

(a) if $p \neq q$, Eq.(7.5-17) is approximated as

e^{-ikr_o} / r_o^3 $(1 + ikr_c)$ · area of element

(b) If $p = q$, Eq. (7.5-16) is approximatd by replacing the element by a disk of equal area and peforming the line integral over the circumference (Ref. 46).

The results from this first approximation are plotted in Fig. (7-24). The experimental measurements of Reference 49 are also shown. It can be seen that the calculated results show only qualitative agreement and fail to predict the locations and magnitudes of the peaks and valleys. A further decrease in size of the element (half-divided) does not show

noticeable improvement. The above approximation requires that L/r_o be small. This is valid only if the element is far away from a control point 'p', whereas L/r_o is not small for elements in the immediate vicinity of point 'p'. Since the boundary condition can be applied accurately, it is felt that the error is largely due to inability of the approximations (a) and (b) to evaluate the kernel accurately.

An obvious alternative for a more accurate evaluation of the integral of the kernel is to further divide the element into a number of smaller area subelements. If necessary each subelement can be further subdivided until an accurate representation of the integral is obtained. However, the subdividing scheme is time consuming on a computer; furthermore, it is anticipated that the accuracy increases rather slowly and a more elegant second approximation should be devised.

To this end Eqs. (7.5-16) and (7.5-18), due to Terai (Ref. 49), are the starting points of the present development; they give the potential in terms of a line integral along the boundary of an element. In this approach, it is convenient to evaluate the line integral in terms of a local coordinate system attached to an element in which the origin of the coordinate system is taken to coincide with the control point (x_1,y_1) of that element.

Fig. (7-25) illustrates the geometry used to calculate the potential at a general control point p due to an element lying in the same plane.

With reference to the local coordinate system, the angle α changes from 0 to 2π for a complete integration around the perimeter.

On making the change of variable

$$d\theta = \frac{\partial \theta}{\partial \alpha}\, d\alpha \qquad (7.5\text{-}20)$$

Eq. $(7.5\text{-}18)$ reduces to

$$- \oint \frac{e^{-ik\rho(\theta)}}{\rho(\theta)}\, \frac{\partial \theta}{\partial \alpha}\, d\alpha \qquad (7.5\text{-}21)$$

The quantities that are varied during the integration of Eq. $(7.5\text{-}21)$ are 'ρ' and the Jacobian of the transformation $\partial \theta / \partial \alpha$. From the cosine law, is expressed as (Fig. 7-25)

$$\rho = \sqrt{l^2 + \rho_o^2 - 2\rho_o l \cos\beta} \qquad (7.5\text{-}22)$$

The Jacobian $\partial \theta / \partial \alpha$ can be expressed as follows (Appendix F)

For sides 1 and 3 (Fig. 7-25)

$$\frac{\partial \theta}{\partial \alpha} = -\frac{\partial \ell}{\partial \alpha}\, \frac{\tan\theta}{\rho}$$

where

$$\rho(\alpha) = \left[d^2 \csc^2\alpha + \rho_o^2 \pm 2\rho_o d\, (\cos\theta_o \cot\alpha + \sin\theta_o) \right]^{1/2}$$

$$\tan\theta = [y_o \pm d]\,/\,[x_o \pm d\cot\alpha]$$

$$\frac{\partial \ell}{\partial \alpha} = -\frac{1}{\rho}\left[d^2 \cos\alpha \csc^3\alpha \pm \right.$$
$$\left. \rho_o d\,(\cos\theta_o \cot^2\alpha + \sin\theta_o \cot\alpha - \cot\alpha \sin\theta + \cos\theta_o) \right]$$

$$\cdot \pm \;\; \text{for side } {}^{1}_{3} \qquad (7.5\text{-}23)$$

For sides 2 and 4

$$\frac{\partial \theta}{\partial \alpha} = \frac{\partial \ell}{\partial \alpha}\, \frac{1}{\rho \tan\theta}$$

Where

$$\rho(\alpha) = \left[d^2 \sec^2\alpha + \rho_o^2 \mp 2\rho_o d\,(\sin\theta_o \tan\alpha + \cos\theta_o) \right]^{1/2}$$

$$\tan\theta = [y_o \mp d\tan\alpha]\,/\,[x_o \mp d] \;\; ;$$

$$\frac{\partial \ell}{\partial \alpha} = \frac{1}{\rho}\left[d^2 \sin\alpha \sec^3\alpha \mp \right.$$
$$\left. \rho_o d\,(\sin\theta_o \tan^2\alpha + \cos\theta_o \tan\alpha - \tan\alpha \cos\theta_o + \sin\theta_o) \right]$$

$$\cdot \mp \;\; \text{for side } {}^{2}_{4} \qquad (7.5\text{-}24)$$

The evaluation of the singular element (Eq. 7.5-18) requires but a single integration along one line segment.

The numerical evaluation of the matrix coefficients may be performed by many existing numerical integration schemes such as Simpson's rule, the trapezoidal rule, and some general quadrature formulas. However, for most bounded integrals the Gaussian method is known to yield remarkable accuracy with only a few ordinates. In the present calculation, a four point Gaussian quadrature formula is used to evaluate the line integral. The Gaussian integration formula that approximates the integration of f(x)dx between the limits 'a' and 'b' is expressed as

$$\int_a^b f(x) \, dx = \frac{b-a}{2} \sum_{i=1}^{N} w_i \, f\left[\frac{(b-a) t_i + (b+a)}{2} \right]$$

(7.5-25)

where w_i are weighting coefficients and

t_i are roots of the Legendre polynomial $P_N(t) = 0$

In the present context,

$$f(x) = \frac{e^{-ik \rho(\theta)}}{\rho(\theta)} \frac{\partial \theta}{\partial \alpha}$$

(7.5-26)

For each segment of the boundary, the ordinates are given by

$X_i = (0.25 \, t_i + .5)$	side 1
$X_i = (0.25 \, t_i + 1)$	side 2
$X_i = (0.25 \, t_i + 1.5)$	side 3
$X_i = (0.25 \, t_i)$	side 4

The weighting coefficients w_i and associated points t_i are

t_i	w_i
$\pm$ 0.339 981 044	0.652 145 155
$\pm$ 0.861 136 312	0.347 854 845

The matrix equations as indicated in Eq.(7.5-12) are conventional linear matrix equations except that the matrix elements are generally complex valued. For the present work, the IMSL library subroutine LEQT1C was used for solving these equations to obtain the surface potential. An integral equation computer program listing for point source diffraction by a rectangular flat plate is given in Appendix G (Computer Listing #2).

The calculated results from the line integral approach are compared with the experimental ones at field points off the plate in the field at a radius of 0.31 meter. For these results the panel was again divided into 96 elements. With this method, excellent agreement between the measured and predicated value of the acoustic potential due to diffraction is obtained (Fig. 7-26   ) except at small angles. Positive dB values indicate attenuation while negative values indicate amplification. Such is the case for the 'bright spot' on the axis of the shadow ($\theta=180^\circ$).

127

128

To check the number of elements needed for accurate solution, the acoustic potential was calculated as before except for double element size. For the cases tested a four-fold reduction in the number of elements does not appreciably alter the results except in the region near the peak behind the plate. This is the region where approximations (a) and (b) (see p.123) also show the largest discrepancy (c.f. Fig.7-24). Table 3 lists the magnitude of the surface potential jump '$\phi(q_1) - \phi(q_2)$' obtained with $N = 96$ and $N = 24$, where N = number of elememts. Because of symmetry, only one half of the distribution from one edge is shown. Despite the difference in the values of the calculated surface potential jump, the final solution that expresses the diffracted sound in a logarithmic reprsentation (dB levels) appears to be accurate enough. On a whole, it appears that the total field potential is adequately predicted by element size less than $\lambda/6$ for a flat plate.

The accuracy of the integral equation scheme has been demonstrated by the thin flat plate diffraction problem. In the next section the same approach is adapted to the more complicated half round configuration with slight modification due to the curvature of the surface.

7.5.6 Numerical Solution for Half Round Shields by Development of Integral Equation Method of Terai

For a general body surface, it is possible to approximate it by a large number of small plane elements. In the present analysis, however, there is no real adventage to implementing this procedure for solving the diffraction problem of a half round shield. There are two reasons. First, the element equations can be readily formulated in terms of the natural coordinates. From experience, this leads to considerable simplification in the analysis. Second, although the surface can approximated accurately by plane elements if the gridwork is sufficiently fine. However, the number of elements that can be used is limited by the computer storage requirement. It is sometimes impractical to increase the accuracy by increasing the number of elements; an increase in the number of element by a factor N is accompanied by a N^2 fold increase in the size of the coefficient matrix. In some cases, the increase is in excess of the storage space available. Aside, for comparable size of the coefficient matrix, one can expect a higher accuracy of the solution from the cylindrical coordinate formalism. This is due to a more accurate evaluation of the kernel function which depends solely on the geometry of the surface.

In view of the above considerations the element equations are derived in terms of cylindrical coordinates. Referring to Fig. (7-27), the half round configuration is represented by the equation of a cylinder

$$F(x,y) = x^2 + y^2 - R^2$$

where R is the radius of the half cylinder.

The inward normal at any point p(x,y) on the surface is

$$\hat{n}_p = \frac{-\nabla F}{|\nabla F|}$$

$$= \frac{-x_p \hat{\imath} - y_p \hat{\jmath}}{[x_p^2 + y_p^2]^{1/2}} \qquad (7.5\text{-}27)$$

In clindrical coordinates, $\hat{n}_p$ can be expressed as $n_p(r_{np}, \theta_{np})$

where $\qquad r_{np} = 1, \qquad \theta_{np} = \tan^{-1}(y_p/x_p) + \pi$

Define $\qquad \vec{r} \qquad$ a vector directed from the point p to point q

where $\qquad \vec{r} = \vec{r}_q - \vec{r}_p$

and where $\qquad \vec{r}_q = x_q \hat{\imath} + y_q \hat{\jmath} + z_q \hat{k}$

$$\vec{r}_p = x_p \hat{\imath} + y_p \hat{\jmath} + z_p \hat{k}$$

The unit vector $\hat{r}$ may be written as

$$\hat{r} = (\vec{r}_q - \vec{r}_p)/|\vec{r}_q - \vec{r}_p| \qquad (7.5\text{-}28)$$

In cylindrical coordinates, the two components of $\hat{r}$ are:

$$\ell_{rq} = \frac{1}{|\vec{r}_q - \vec{r}_p|}[x_q^2 + y_q^2]^{1/2}$$

$$\theta_{rq} = \tan^{-1}(y_q/x_q) \qquad (7.5\text{-}29a)$$

$$z_{rq} = z_q/|\vec{r}_q - \vec{r}_p|$$

and

$$\ell_{rp} = \frac{1}{\vec{r}_q - \vec{r}_p}[x_p^2 + y_p^2]^{1/2}$$

$$\theta_{rp} = \tan^{-1}[y_p/x_p] \qquad (7.5\text{-}29b)$$

$$z_{rp} = z_p/|\vec{r}_q - \vec{r}_p|$$

Thus, the dot products required by the kernel function can be expressed as:

$$\hat{n}_p \cdot \hat{r} = \hat{n}_p \cdot \frac{\vec{r}_q - \vec{r}_p}{|\vec{r}_q - \vec{r}_p|}$$

$$= \frac{[x_q^2 + y_q^2]^{1/2}}{|\vec{r}_q - \vec{r}_p|}\cos(\theta_{np} - \theta_{rq}) - \frac{[x_p^2 + y_p^2]^{1/2}}{|\vec{r}_q - \vec{r}_p|}\cos(\theta_{np} - \theta_{rp})$$

$$= \frac{R}{r}\left[\cos(\theta_{np} - \theta_{rq}) - \cos(\theta_{np} - \theta_{rp})\right]$$

$$(7.5\text{-}30a)$$

and similarly

$$\hat{n}_q \cdot \hat{r} = \frac{R}{r} \left[\cos(\theta_{nq} - \theta_{rq}) - \cos(\theta_{nq} - \theta_{rp}) \right] \qquad (7.5\text{-}30b)$$

$$\hat{n}_p \cdot \hat{n}_q = \cos(\theta_{np} - \theta_{rq}) \qquad (7.5\text{-}30c)$$

Since $(\hat{n}_p, \hat{r}_p)$ and $(\hat{n}_q, \hat{r}_q)$ points in opposite direction (Fig. 7-28),

therefore

$$\theta_{np} - \theta_{rp} \quad ; \quad \theta_{nq} - \theta_{rq} = \pi$$

This implies

$$\cos(\theta_{np} - \theta_{rp}) \; , \; \cos(\theta_{nq} - \theta_{rq}) = -1$$

Upon using Eq. 7.5-30, we get

$$(\hat{n}_p \cdot \hat{r})(\hat{n}_q \cdot \hat{r}) = -\frac{R^2}{r^2} \left[1 + \cos(\theta_{rp} + \pi - \theta_{rq}) \right] \left[1 + \cos(\theta_{rq} + \pi - \theta_{rp}) \right]$$

$$= -\frac{R^2}{r^2} \left[1 - 2\cos(\theta_{rp} - \theta_{rq}) + \cos^2(\theta_{rp} - \theta_{rq}) \right]$$

$$(7.5\text{-}30d)$$

Using Eqs. (7.5 - 30), the integrals in Eq. (7.5 - 13) can be written as:

$$K = \iint \frac{e^{-ikr}}{r^3} \left\{ \left[k^2 r^2 - 3ikr - 3 \right][\hat{r} \cdot \hat{n}_p][\hat{r} \cdot \hat{n}_q] + [1 + ikr][\hat{n}_p \cdot \hat{n}_q] \right\} dS_q$$

$$= \iint \frac{e^{-ik\{2R^2[1 - \cos(\theta_q - \theta_p)] + (z_q - z_p)^2\}^{1/2}}}{\{2R^2[1 - \cos(\theta_q - \theta_p)] + (z_q - z_p)^2\}^{1/2}} \cdot$$

$$\left\{ \left[3\left(1 + ik\{2R^2[1 - \cos(\theta_q - \theta_p)] + (z_q - z_p)^2\}^{1/2}\right) - \right. \right.$$

$$2k^2 R^2 \left[1 - \cos(\theta_q - \theta_p) \right] + (z_q - z_p)^2 \right] \cdot$$

$$\left[\frac{R^3 \{(1 - 2\cos(\theta_q - \theta_p) + \cos^2(\theta_q - \theta_p)\}}{2R^2[1 - \cos(\theta_q - \theta_p) + (z_q - z_p)^2]} \right] +$$

$$R \cos(\theta_{rp} - \theta_{rq}) \left[1 + ik\{2R^2[1 - \cos(\theta_q - \theta_p)] + (z_q - z_p)^2\}^{1/2} \right] \right\} d\theta_q dz_q$$

$$(7.5 - 31)$$

The multiple integral of Eq. (7.5-31) can be evaluated by applying successively the formula for one-dimensional integration. Thus the double integral is expressed as

$$K = \int_{z_1}^{z_2}\int_{\theta_1}^{\theta_2} f(\theta, z)\, d\theta\, dz$$

$$= \frac{\Delta z}{2}\frac{\Delta \theta}{2} \sum_i \sum_j w_i\, w_j\, f(\theta_i, z_j)$$

where

$$\theta_i = \frac{\Delta \theta}{2} t_i + \theta_{rq}$$

$$z_j = \frac{\Delta z}{2} t_j + z_q$$

and where t_j , w_j are abscissas and weight factors for Legendre -Gauss integration.

The accuracy of this quadrature formula for two dimensional integration was also tested for the planar configuration considered earlier. The calculated results are extremely close to the results from the line integral scheme (Eq. 7.5-18).

When the points 'p' and 'q' coincide, the kernel is singular, as is the case for the planar shield. It is shown in Refs (47) and (48) that the singular integral (Eq. 7.5-13)

$$\iint \varphi(q) \frac{\partial^2}{\partial n_p \partial n_q}\left(\frac{e^{-ikr}}{r}\right) dS_q$$

is equivalent to the sum of three regular integrals. The integral is, therefore, finite in spite of the singular kernel. In the calculations performed in this study, the surface of the half round scoop shield is divided into equal cylindrical elements. If the mesh used to approximate the surface is sufficiently fine, the surface can in fact be fitted quite well by planar surface element in the neighborhood of each control point. Aside from this, the error introduced in the evaluation of the self-induced influence coefficient is also small for planar element approximation. For example, if the control points are separated at 12^0 intervals in the circumferential direction of the scoop shield, this would correspond to a 15 x 15 gridwork subdividing the surface into 225 equal curved elements. The problem then requires solution of a 225 x 225 system of complex equations. A coefficient matrix of this size is still within the limitations imposed by computer storage available. In the computation aspect, the difference in direction of the normal near the boundary to that of the centroid of the element where a control point is denoted will be at most 6^0. Thus if the surface element is assumed to be flat, the maximum error induced in the dot products in the integrand of Eq. (7.5-13), namely $\hat{r}\cdot\hat{n}_p$, $\hat{r}\cdot\hat{n}_q$ and $\hat{n}_p\cdot\hat{n}_q$ is not greater than 0.1% and 0.5% respectively. In addition, the error in the magnitude of $\vec{r}$ is also not greater than 0.5%. This suggests that the local effect term can be estimated with sufficient accuracy by means of Equation 7.5-16, namely:

$$K = -\oint \frac{e^{-ik\rho(\theta)}}{\rho(\theta)}\, d\theta - 2\pi i k$$

An alternative approach to evaluate the singular kernel is outlined in Reference (45) page 26, 27. Therein an approximate expression for the

local effect term is given for $ko \ll 1$ where $\pi b^2 = S$, and S is the area of an element. Numerical solutions to various cases investigated (see Figure 7-28) using this approximation for the self-induced coefficient show that, on the average, the magnitude of the surface potential is different by about 6 % and the diffracted sound field is different by less than 1 dB compared with the former approach (i.e. self induced coefficient evaluated by Eq. 7.5-16).

Using the formulation described above in terms of integral equations, a suitable numerical procedure has been applied to predict the total sound field due to diffraction for a 10D diameter scoop shield of length 16D. The point source is located at a certain point on the axis of the scoop shield. The surface of the shield is assumed to be perfectly reflecting. For all cases considered, the predicted results are compared with laboratory measurements.

Numerical approximation of the integral equation is obtained by sub-dividing the half round shield into equal curved elements. A point is then chosen in the center of each element where the potential will be determined. The total number of control points examined are 96 and 225 which corresponds to a 12x8 and 15x15 grid on the shield surface respectively. The ratio of the element area is about two to one. Solutions to the diffraction problem thus require 96x96 or 225x225 systems of complex equations. For the second approximation (225 elements), computation of the surface potential and the resulting diffracted field required under 3.5 minutes of computing time on the U.of T. IBM 370 computer. The storage requirement is about 850 kilobytes, which is below

the full capacity of 1000 kilobytes. These basic requirements are indicative of all cases considered. In all cases the integral equation methods are found to be adequate within the frequency range tested. For the present configuration, the ratio of wavelength/scatter dimension is about 0.5 to 1.5. In this mid frequency region, neither low nor high frequency approximate solutions are applicable. A computer program listing for the half round diffraction problem is given in Appendix 3 (Computer listing #3).

Figure 7-28 shows the computed and the experimental results. The general agreement between the predicted and measured sound fields is seen to be good in all cases; in general, the finer the mesh the better the agreement. In Fig. 7-28 a,b the total sound field is plotted against source positions along the axis of the half cylinder. The receiving point is at 90° to the shield axis, and the problem has symmetry with respect to the line connecting the mid point of the shield to the receiver. For the two frequencies considered, good degree of symmetry is observed in the measured results. Maximum attenuation is found at source positions close to the edge, gradually decreasing to a minimum at the center. In Fig.7-28 c,d the curves also show attenuation versus source position but the receiving point is at 40° with respect to the axis of the scoop shield. For this geometry, maximum shielding occurs for sources located further away from the edges. The measured shielding for 700 Hz at this maximum can not be determined accurately from the recorded spectrum as the level is too close to the noise floor. Nevertheless, the agreement is satisfactory.

The cases considered next were the diffraction of spherical waves into the region surrounding the scoop shield. The sound source is located at the mid point of the shield axis. The angular variation of the sound field about the source point is surveyed both in the shadow and bright region. In the experimental set-up, the source and microphone are fixed; the measurement was carried out by turning the scoop shield about the point source every 10^0. It can be seen that agreement is again satisfactory, but the accuracy deteriorates as the frequency increases. It should be noted that the surface potential distribution is obtained by solving the matrix equation with certain input vectors which depend on the source position. Hence the accuracy of the subsequent calculation of the directivity pattern is largely dictated by the accuracy of the calculated surface potential. The general shape of the curve for the 1000 Hz case is similar to that of a flat shield. The first peak at 20^0 is compatible with the corresponding peak calculated for flat plate geometry. This points out possible error in Terai's measurement in this range (Fig. 7-26). Maximum attenuation occurs at the same direction (θ $=40^0$) into the shadow region for both flat and curved configurations. In the region between $\theta=30^0$ and 90^0 and directly behind the shield at $\theta=180^0$, the results for the curved shield are somewhat different from those of the planar shield because of diversified shielding geometry and hence diffraction effects. In the planar configuration, the source is closer to the shield than the receiver, hence the diffraction pattern is expected to be different to some degree. The curved shield shows less local maxima or minima and the sound field in the region directly behind the shield is not higher than it would be if there were no shield. The so-called Arago's spot appears to be a phenomenon characteristic of flat surfaced obstacles with no curvatures such as thin plate, disk, and parallelpiped (Ref. 49).

8. CONCLUDING REMARKS

The present study is aimed at the exploration of shielding concepts in jet noise reduction. A variety of shielding configurations have been examined experimentally and analytically.

The extensive collection of measurements suggests that two factors limit the effectiveness of the shields: namely, the finite size of the shield and the source distribution in a jet flow. The former in conjunction with the non-compactness of the source region allows some direct radiation to be received at most observer positions. Furthermore, the source distribution along the jet axis, as well as the very nature of diffractive barriers, favours noise reduction only at moderate and high Strouhal numbers. In order to be effective barriers must be large and close to either the source or the observer. When a barrier is moved sufficiently close to the jet flow intensive 'edge noise' is generated. This severely limits the shield length, and hence the effective shielding that can be obtained. A hyperbolic cutout allows the barrier length to be increased without unduly enhancing the edge noise. Such configurations offer significant improvement over a straightedged barrier generating comparable edge noise. A localized wing extension of the cutout configuration attains similar noise suppression with a smaller shield area.

Composite shields that extend the effective length of a shield by means of a hot refractive layer have also been examined. For example an array of flames emanating from the trailing edge of a shield constitute a

refractive extension of the shield. As a sound barrier it has only a limited effective downstream length. This is due to the entrainment of colder air that progressively weakens the refractive capability. This shielding configuration results in a marginal increase in shielding at high frequencies, suggesting a potential for significant increase in shielding capability if a large flame mass flow can be generated. Spectral measurements show that this scheme, where the burning occurs near the turbulent jet, suffers at low frequencies from spurious or extra noise due to jet/flame interaction.

On the whole, the measured insertion loss or overall decrease in the sound pressure level has not been spectacular. It is of the order of 3 to 4 dB in the direction of peak noise, depending on the particular configuration. Scoop shields offer comparable reduction at a significant savings of material. The 10 D and 15 D shields provide peak broadband reduction of 4 dB. Maximum reduction of 5 dB is obtainable at a shield length of 20 D. Nevertheless, owing to the frequency sensitivity of the ear, the subjective impact on perceived noise level, measured in PNdB is more impressive. On the average a 5 to 6 drop in PN dB level has been measured. More importantly, up to 66% decrease in the area of certain equal PNdB contours ('noise footprints') for simulated flyover situations has been demonstrated.

There are several factors that influence the relatively poor performance of the shields. The edge-noise phenomenon appears to be a principal agent. The shield effectively acts as a sounding board for the nearfield

pressures. The largest portion of these are otherwise nonradiating and therefore would not normally contribute to the far field sound.

Secondly, the extended nature of the jet flow gives rise to a spatial distribution of noise sources. This results in an unfavourable diffraction effect which is dominated by the lowest Fresnel number; the high frequency noise source generated close to the nozzle will suffer substantial shielding, whereas the low frequency noise generated in the downstream region, possibly close to the shield edge, is affected by diffraction only. Furthermore, due to the non-uniform directivity of the jet noise pattern, the low frequency sound, which has a directional maximum at small angles to the jet axis, is the principal source of incident waves diffracted by the shield edge.

The low frequency augmentation of jet noise (edge noise) is found in almost all shielded jet noise spectra. The peak noise level of this effect has a fifth power velocity dependence, a trend characteristic of dipole sources for two dimensional configurations. The nearfield measurements of the low frequency augmentation level at the shield trailing edge show a one-to-one correspondence with the far field measurements. The experimental validation of the noise scaling law shows quantitative agreement with the predictions.

The experimental work is complemented by a programme directed at the prediction of the acoustic performance of shields. This is broadly divided into an engineering approach for jet noise shielding and a more rigorous analysis for point source shielding. The former approach starts with measurements (or prediction) of the shielding of 'point sources' as function of frequencies and positions along the jet axis. For the specified source pattern of jet noise the results are summed in such a way as to give the overall attenuation of the jet noise at each frequency. A scheme for extraction of edge noise could also be incorporated. On the whole, the predicted augmentation and shielding effects are found to be in reasonable agreement with measured spectra if the principal features of flow noise generation and diffraction are accounted for.

For point source shielding theoretical calculations based on the exact solution for a half-plane are successful for simple planar shield configurations. The line integral approach involving the Kirchhoff approximation results in large error. However, reasonable predictions for rectangular configurations including cutouts, are possible if certain corrections are applied. Integral equation methods (solved numerically) are considered for more demanding geometries such as half round sugar scoop shields. A computer code has been developed to deal with problems of diffraction by thin obstacles. Generally speaking, the method is found to give satisfactory agreement with measurements within the frequency range examined.

REFERENCES

1. Maglieri, D.J. Shielding Flap Type Jet Engine Noise Suppressor. Jour. of the Acoustical Society of America, Vol. 31, no. 4, 1959.

2. Grosche, F.R. On the Generation of Sound Resulting from the Passage of a Turbulent Air Jet Over a Flat Plate of Finite Dimensions. Royal Aircraft Establishment Translation 1460, 1970.

3. Tiggelaar, J.J. Estimation of the Shielding Effect on the Wing on Aircraft Engine Noise, Using the Kirchhoff Approximation. National Aerospace Lab., Netherlands, Report NLR TR73033U, 1973.

4. von Glahn, U.
   Groesbeck, D.
   Reshotko, M. Geometry Considerations for Jet Noise Shielding with CTOL Engine-Over-The-Wing Concept. NASA TMX-17562, 1974.

5. Conticelli, V.M.
   DiBlasi, A.
   O'Keefe, J.V. Noise Shielding Effects for Engine - Over-Wing Installation. AIAA Paper 75-474, 1975.

6. Bloomer, H.E. Investigation of Wing Shielding Effects on CTOL Engine Noise. AIAA paper No. 79-0669, 1979.

7. Groesbeck, D.
   von Glahn, U. Assessment at Full Scale of Nozzle/Wing Geometry Effect on OTW Aeroacoustic Characteristics. Jour. of the Acoustical Society of America, Vol. 65 (S1), 1979.

8. Atvars, J. Refraction of Sound by a Jet Velocity Field. M.A.Sc Thesis (unpublished), Univ. of Toronto, Institute for Aerospace Studies, 1964.

9. Richarz, W.G. Direct Correlation of Noise and Flow of a Jet Using Laser Doppler. UTIAS Report 230, 1978.

10. Ffowcs-Williams, J.E.
    Hall, L.H. Aerodynamic Sound Generation by Turbulent Flow in the Vicinity of scattering half Plane. Jour. of Fluid Mechanics, 40 (4), 1970.

11. Crighton, D.G. Basic Principles of Aerodynamic Noise Generation. Prog. Aerospace Sci. Vol. 16, No. 1, 1975.

12. Lamb, H. Hydrodynamics. Dover Publications, New York, 1945.

13. Skudrzyk, E. The Foundations of Acoustics. Springer-Verlag, New York, 1971.

14. Ribner, H.S. The Generation of Sound by Turbulent Jets. Advances in Applied Mechanics, Vol. 8, 1964.

15. Hayden, R.E. Noise from Interaction of Flow with Rigid Surfaces: A Review of Current Status of Prediction Techniques. NASA CR-2126, 1972.

16. Howe, M.S. A Review of the Theory of Trailing Edge Noise. Jour. of Sound and Vibration, Vol. 61, No. 3, 1978.

17. Kuchemann, D. Aerodynamics of Propulsion. McGraw Hill, 1953.

18. Head, R. W.
    Fisher, M.J. Jet/Surface Interaction Noise: Analysis of Farfield Low Frequency Augmentation of Jet Noise due to the Presence of a Solid Shield. AIAA Paper 76-502, 1976.

19. Grosche, F.R. Distribution of Sound Source Intensities in Subsonic and Supersonic Jets. AGARD CP-131, 1974.

20. Beranek, L.L. Noise and Vibration Control. McGraw-Hill, New York, 1971.

21. Kerrebrock, J.L. Aircraft Engines and Gas Turbines. MIT Press, 1977

22. Brekhovskikh, L.M. Waves in Layered Media. Academic Press, 1960.

23. Rudnick, I. Acoustic Transmission Through a Fluid Lamina. Jour. of the Acoustical Society of America. Vol. 17, Nc. 3, 1946.

24. Keller, J.B. Reflection and Transmission of Sound by a Moving Medium. Jour. of the Acoustical Society of America, Vol 27, No. 6, 1955.

25. Franken, P.
    Ingard, U. Sound Propagation into a Moving Medium. Jour. of the Acoustical Society of America, Vol. 28, No. 1, 1956.

26. Ribner, H.S.

Reflection, Transmission and Amplification of Sound by a Moving Medium. Jour. of the Acoustical Society of America, Vol. 29, No. 4, 1957.

27. Miles, J.W.

On the Reflection of Sound at an Interface of Relative Motion. Jour. of the Acoustical Society of America, Vol. 29, No. 2, 1957.

28. Jones, I.S.F.

Jet Noise Suppression by an Impedance Shroud. Boeing Scientific Research Laboratory Document D1-82-0984 (1970).

29. Norum, T.D.

Measured and Calculated Transmission Losses of Sound Waves Through a Helium Layer. NASA TND-7230, 1973.

30. Cowan, S.J.
    Crouch, R.W.

Transmission of Sound Through a Two-Dimensional Shielding Jet. AIAA Paper No. 73-1002.

31. Yeh, C.

A Further Note on the Reflection and Transmission of Sound Waves by a Moving Fluid Layer. Jour. of the Acoustical Society of America, Vol. 43, No. 5, 1968.

32. Jost, W.

Explosion and Combustion Process in Gases. McGraw Hill, 1946.

33. Yamamoto, K.
    Arndt, R.E.A.

Peak Strouhal Frequency of Subsonic Jet Noise as a Function of Reynolds Number. AIAA Journal Technical Notes Vo. 17, No. 5, p. 529-531, 1979.

34. Richards, E.J.

Noise and Acoustic Fatigue in Aeronautics. John Wiley, 1968

35. Pinker, R.A.

Mathematical Formulation of the Noy Tables. Jour. of Sound and Vibration, Vol. 8, No. 3, 1968.

36. Sutherland, L.C.
    Piercy, J.E.
    Bass, H.E.
    Evans, L.G.

A Method For Calculating the Absorption of Sound by the Atmosphere. Invited Paper Before 88th Meeting of the Acoustical Society of America, 1974.

37. Michalke, A.
    Michel, U.

Prediction of Jet Noise in Flight from Static Test. Jour. of Sound and Vibration, Vol. 67, No. 3, 1979.

38. Reddy, N.N.
    Tanna, H.K.

Installation Effects on Jet Noise in Flight. AIAA Paper No. 80-1044, 1980.

39. Carslaw, H.S.

Some Multiform Solutions of the Partial Differential Equations of Physical Mathematics and their Applications. Proc. London Math. Soc. 30 (1899).

40. Fisher, M.J.
    Harper-Bourne, M.
    Glegg, S.A.L.

Jet Engine Noise Source Location: The Polar Correlation Technique. Jour. of Sound and Vibration, Vol. 51, No. 1. 1977.

41. Johnston, G. W.

Diffraction of Arbitrarily Oriented Directional Sources by Rigid Planar Screens. Jour. of the Acoustical Society of America. Vol. 64, No. 2, Aug. 1978.

42. Michel, U.
    Fuchs, H.V.

The Far Field Condition in Jet noise Experiments. AIAA Paper 79-0572, 1979

43. Bowman, J.J.
    Senior, T.B.A.
    Uslenghi, P.L.E.

Electromagnetic and Acoustic Scattering by Simple Shapes. John Wiley, New York, 1969.

44. Stratton, J.A.

Electromagnetic Theory. McGraw Hill, 1941.

45. Chertock, G.

Integral Equation Methods in Sound Radiation and Scattering from Arbitrary Shapes. Naval Ship Research and Development Center Report 3538, June, 1971.

46. Filippi, P.J.T.

Layer Potentials and Acoustic Diffraction. Jour. of the Acoustical Society of America, Vol. 54, No. 4, 1977.

47. Burton, A.J.

Numerical Solution of Scalar Diffraction Problems. National Physical Lab. Report.

48. Meyer, W.L.
    Bell, W.A.
    Zinn, B.T.

Boundary Integral Solutions of Three Dimensional Acoustic Radiation Problems. Jour. of the Acoustical Society of America, Vol. 52 No. 2, 1978.

49. Terai, T.

On Calculation of Sound Field Around Three Dimensional Objects by Integral Equation Methods. Jour. of Sound and Vibration, Vol. 69, No. 1, 1989.

50. Baker, B.B.
    Copson, E.T.

The Mathematical Theory of Huygens' Principle. Oxford University Press, 1950.

51. Kawai, T.
    Fujimoto, J.
    Itow, T.

Noise Propagation Around a Thin Half-Plane. Acustica, Vol. 38, 1977.

52. Jones, D.S.

The Mathematical Theory of Noise Shielding.
Prog. Aerospace Sci. Vol. 17, 1977.

53. Cooke, J.C.

Notes on the Diffraction of Sound.
Aeronautical Research Council, C.P. No.
1192, 1972.

54. Ahtye, W.F.
    McCulley, G.

Evaluation of Approximate Methods for the
Prediction of Noise Shielding by Airframe
Components.
NASA Technical Paper 1004, 1980.

55. Broadbent, E.G.

Noise Shielding for Aircraft.
Prog. Aerospace Sci. Vol. 17, 1977.

56. Pierce, A.D.

Diffraction of Sound Around Corners and
Over Wide Barriers.
Jour. of the Acoustical Society of America,
Vol. 55, No. 5, 1974.

57. Keller, J.B.

Geomerical Theory of Diffraction.
Journal of the Optical Society of America.
Vol. 52, No. 2, 1962.

58. Maekawa, Z.

Noise Reduction by Screens.
Applied. Acoustics (1), 1968.

59. Jonasson, A.G.

Sound Reduction by Barriers on the Ground.
Jour. of Sound and Vibration, Vol. 22,
No. 1, 1972.

60. Kurze, U.J.

Noise Reduction by Barriers.
Jour. of Sound and Vibration, Vol. 55,
No. 3, 1974.

61. Kurze, U.J.
    Anderson, G.S.

Sound Attenuation by Barriers.
Applied Acoustics (4), 1971.

62. Embleton, T.F.W.

Line Integral Theory of Barrier Attenuation
in the Presence of the Ground.
Jour. of the Acoustical Society of America,
Vol. 67, No. 1, 1980.

63. Isei, T.
    Embleton, T.F.W.
    Piercy, J.E.

Noise Reduction by Barrier on Finite
Impedance. Jour. of the Acoustical Society
of America, Vol. 67, No. 1, 1980.

64. Officer, C.B.

Introduction to the Theory of Sound
Transmission.
McGraw-Hill, New York 1958.

65. Kinsler, L.E.
    Frey, A.R.

Fundamentals of Acoustics
Johy Wiley, 1962.

TABLE 1

Comparison between exact (A_e) and asymptotic (A_a) solution computed for thin barrier

θ = 40°, f = 4 kHz | θ = 40°, f = 8 kHz

N	kR_1	$A_{(e)}$(dB)	$A_{(a)}$	N	kR_1	$A_{(e)}$(dB)	$A_{(a)}$(dB)
1.14	121.6	12.67	12.64	2.27	243.2	15.50	15.43
1.03	118.9	12.37	12.35	2.06	240.5	15.20	15.18
0.92	117.5	12.04	12.02	1.85	237.8	14.83	14.86
0.82	116.2	11.69	11.66	1.63	235.1	14.44	14.42
0.71	114.8	11.29	11.27	1.42	232.4	14.01	13.91
0.60	113.5	10.85	10.83	1.20	229.7	13.52	13.40
0.49	112.2	10.36	10.33	0.99	227.0	12.97	12.89
0.39	110.9	9.79	9.76	0.78	224.4	12.29	12.28
0.29	109.6	9.13	9.11	0.57	221.8	11.48	11.47
0.19	108.4	8.37	8.35	0.38	219.3	10.50	10.49
0.11	107.2	7.46	7.44	0.21	216.8	9.26	9.29
0.04	106.2	6.36	6.35	0.08	214.5	7.70	7.70
0.00	105.3	5.04	5.03	0.01	212.4	5.72	5.72

θ = 90°, f = 4 kHz | θ = 90°, f = 8 kHz

N	kR_1	$A_{(e)}$(dB)	$A_{(a)}$(dB)	N	kR_1	$A_{(e)}$(dB)	$A_{(a)}$(dB)
6.14	138.4	19.52	19.38	12.29	276.8	22.53	22.50
5.70	137.0	19.17	19.08	11.40	274.1	22.16	22.14
5.25	135.7	18.81	18.71	10.51	271.3	21.85	21.75
4.80	134.3	18.41	18.23	9.61	268.6	21.38	21.32
4.35	133.0	17.99	17.92	8.70	265.9	20.99	20.86
3.90	131.6	17.92	17.54	7.79	263.2	20.50	20.36
3.44	130.3	17.00	16.92	6.88	260.6	20.00	19.84
2.98	129.0	16.45	16.38	5.96	257.9	19.42	19.27
2.52	127.7	15.82	15.76	5.05	255.3	18.79	18.65
2.07	126.4	15.09	14.98	4.14	252.8	18.05	18.06
1.63	125.2	14.25	14.24	3.26	250.4	17.18	17.15
1.20	124.0	13.25	13.25	2.40	248.0	16.14	16.07
0.80	123.0	12.04	12.01	1.60	245.9	14.79	14.71
0.45	122.1	10.50	10.47	0.89	244.2	13.05	13.00
0.18	121.5	8.54	8.52	0.35	242.9	10.60	10.57

TABLE 2-A

Numerical Results for Cutout Configuration via Line Integral

X/D	Frequency (Hz)	Uncorrected results (dB)	Correction based on shortest diffracting path (dB)	Corrected results (dB)	Measurements (dB)
3	8K	37.6	-6.2	31.4	27.5
	6K	31.8	-6.2	25.6	25.0
	4K	27.3	-6.3	21.0	21.0
5	8K	33.3	-5.3	28.0	23.0
	6K	29.1	-5.3	23.8	21.4
	4K	24.7	-5.3	19.4	16.5
7	8K	25.1	-3.3	21.8	19.5
	6K	24.1	-3.7	20.4	18.0
	4K	20.6	-3.8	16.8	13.0

Numerical Results for Cutout Configuration via Line Integral

X/D	Frequency (Hz)	Unconnected results (dB)	Correction based on average performance (dB)	Corrected results (dB)	Measurements (dB)
3	8K	37.6	-7.1	30.5	27.5
	6K	31.8	-7.2	24.6	25.0
	4K	27.3	-7.2	20.1	21.0
5	8K	33.3	-6.5	26.8	23.0
	6K	29.1	-6.5	22.6	21.4
	4K	24.7	-6.6	18.1	16.5
7	8K	25.1	-5.4	19.8	19.5
	6K	24.11	-5.6	18.5	18.0
	4K	20.6	-5.6	15.0	13.0

TABLE 3

Magnitude of the Surface Potential

$(\emptyset(q_1)-\emptyset(q_2))$ On Plate

	.343	.333	.313	.282	.238	.169
	.524	.507	.473	.422	.348	.238
	.640	.618	.575	.508	.415	.279
96 elements	.698	.674	.625	.551	.447	.298
(12 x 8)	.698	.674	.625	.551	.447	.298
	.640	.618	.575	.508	.415	.279
	.524	.507	.473	.422	.348	.238
	.343	.333	.313	.282	.238	.169

	.459	.406	.292
	.660	.575	.396
24 elements	.660	.575	.396
(6 x 4)	.459	.406	.292

NOISE REDUCTION BY BARRIER
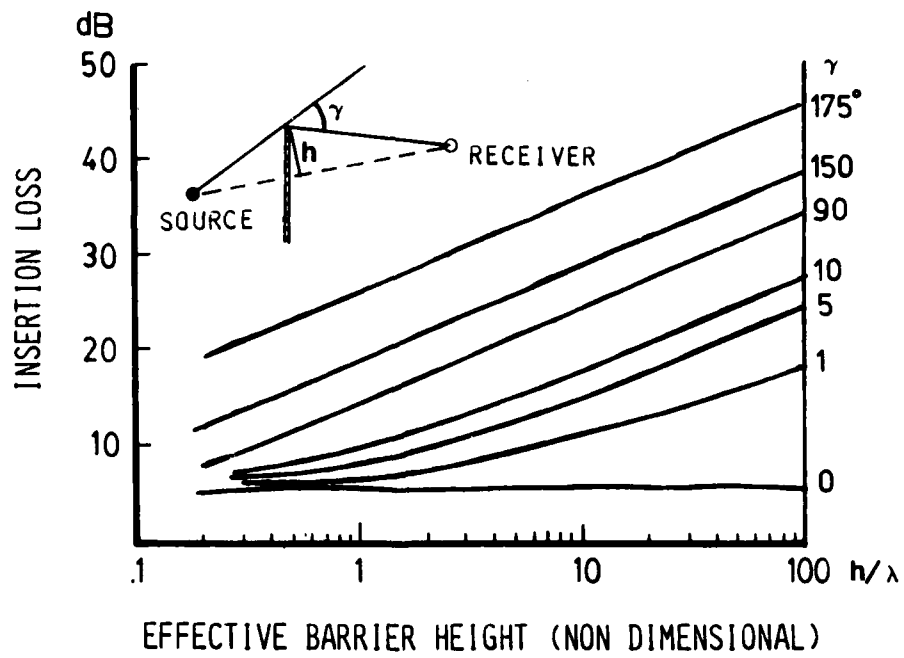
FIG. 2.1 NOISE REDUCTION BY BARRIER PLACED BETWEEN NOISE
SOURCE AND RECEIVER (Ref. 54)
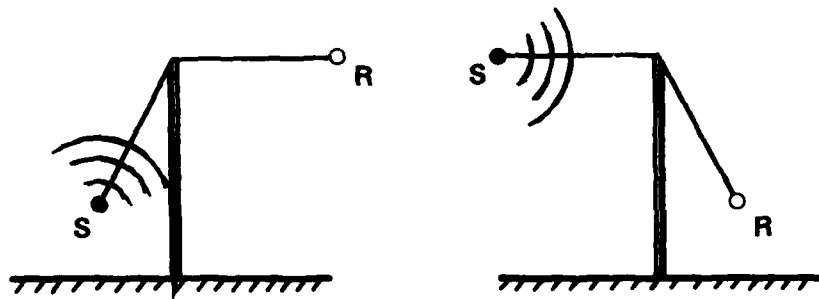
FIG. 2.2 GEOMETRIES OF SOUND SOURCE AND RECEIVER FOR
IDENTICAL DIFFRACTIVE ATTENUATION

Fresnel number
$N = 2(a+b-c)/\lambda$

Source

Receiver
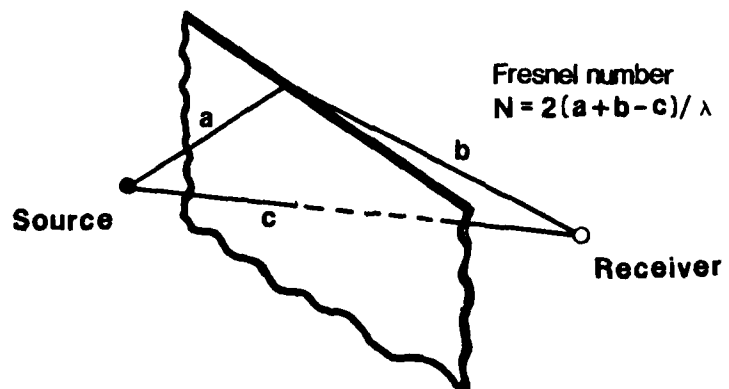
FIG. 2.3 GEOMETRY OF SOUND PROPAGATION PATH OVER A BARRIER
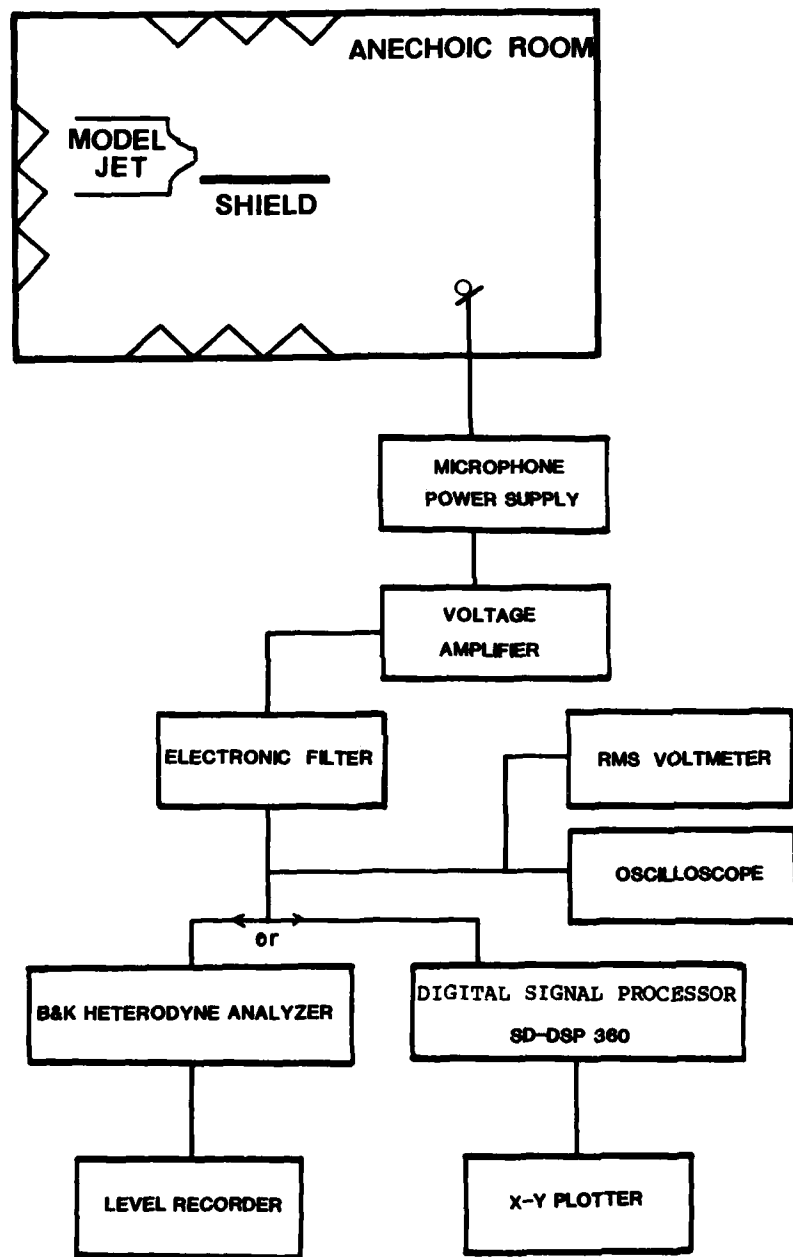
FIG. 2-4   BLOCK DIAGRAM OF INSTRUMENTATION FOR
SHIELDING MEASUREMENTS
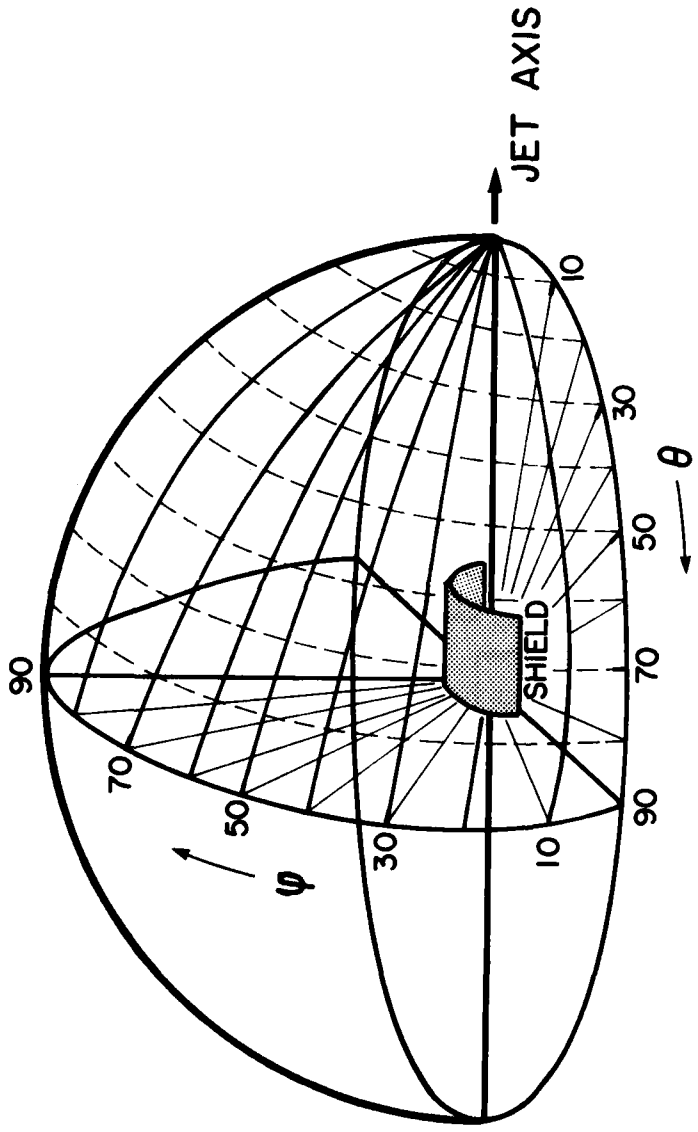
FIG. 2-5   MICROPHONE POSITION IN TERMS OF r,θ,φ OVER A HEMISPHERICAL
SURFACE CENTERED AT THE JET NOZZLE.

SIDELINE PLANE   φ = 0°
FLYOVER PLANE   φ = 90°
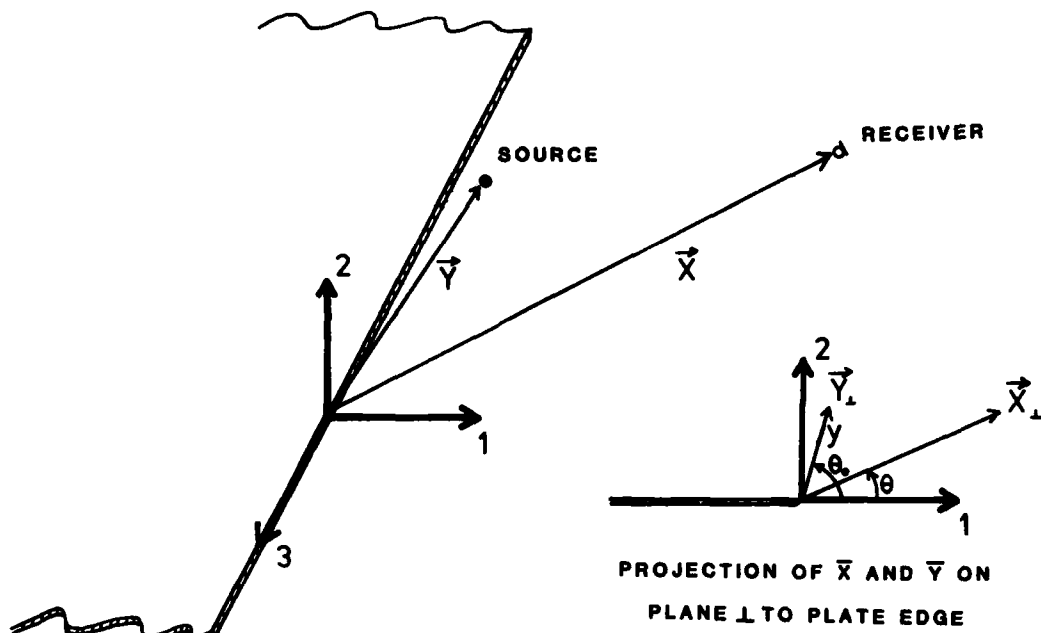
FIG. 2-6   GEOMETRY FOR SCATTERING BY A HALF PLANE

PROJECTION OF $\overline{X}$ AND $\overline{Y}$ ON
PLANE ⊥ TO PLATE EDGE
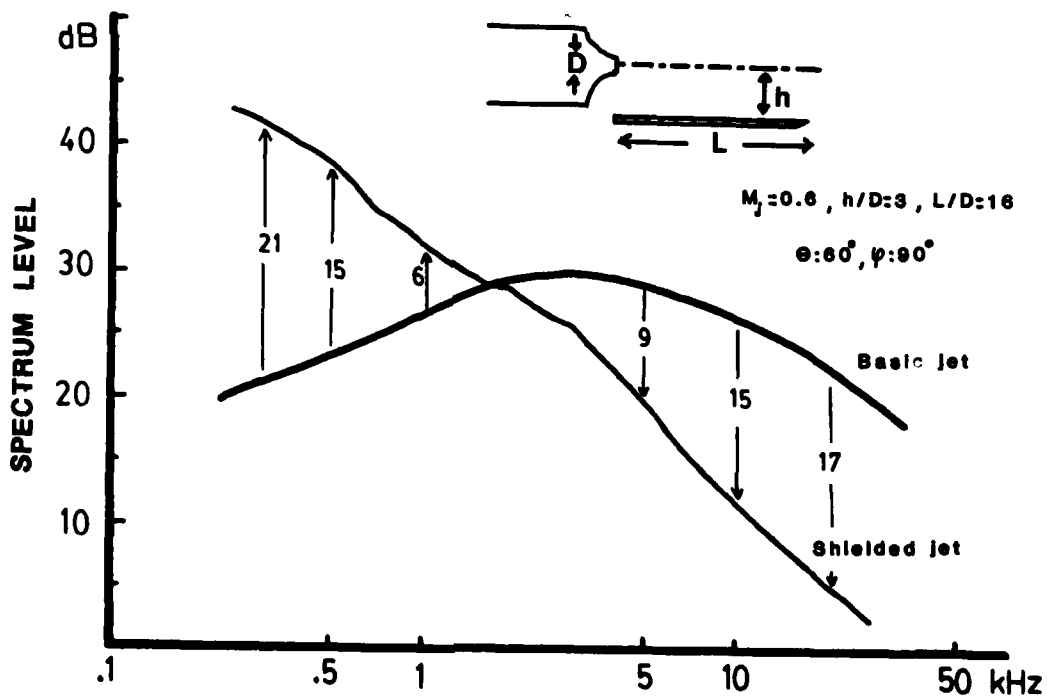
FIG. 2-7   LOW FREQUENCY EDGE NOISE GENERATED BY PROXIMITY
OF FLOW AND SOLID BARRIER
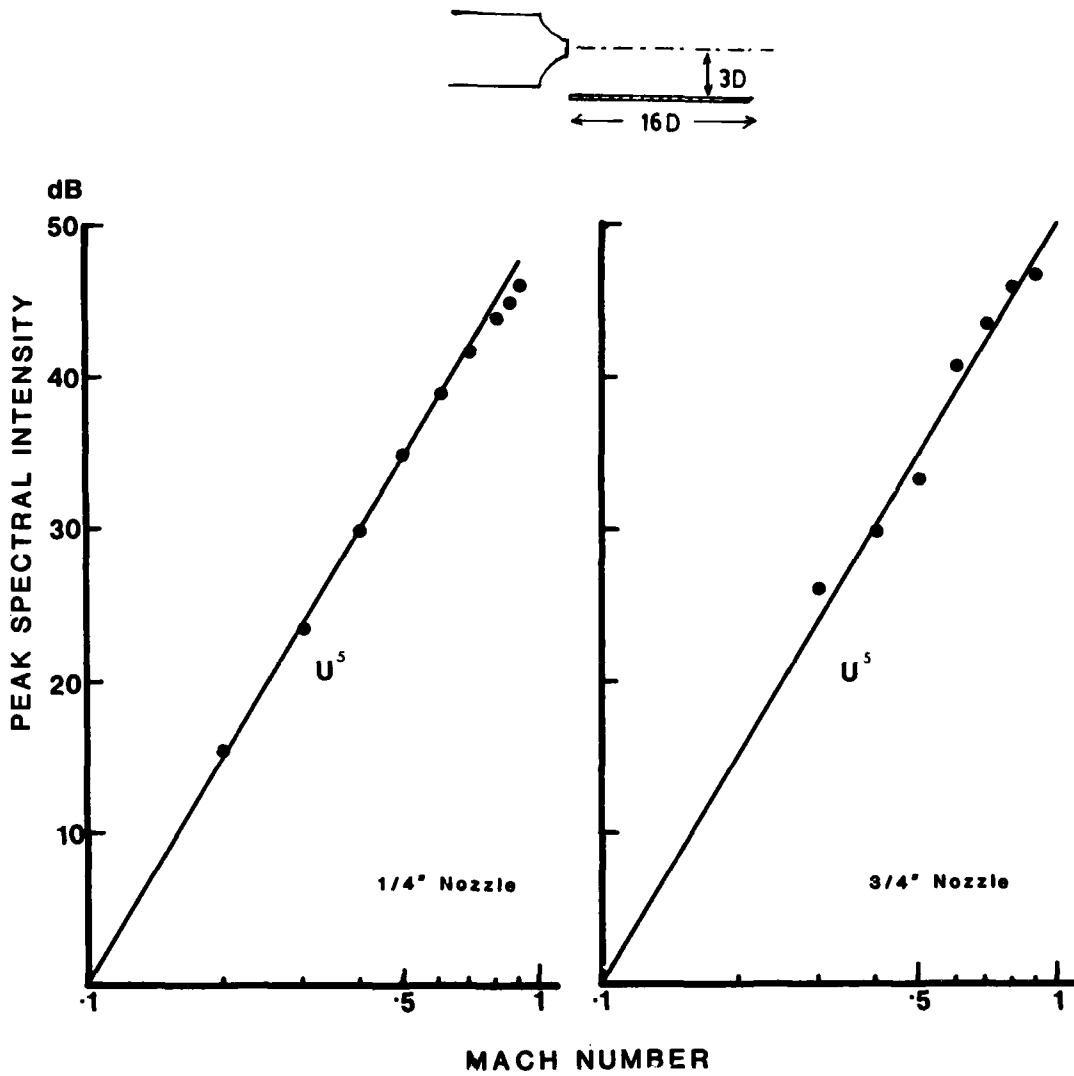
FIG. 2-8 PEAK SPECTRAL INTENSITY OF EDGE NOISE (Θ:60)
(φ:90°)
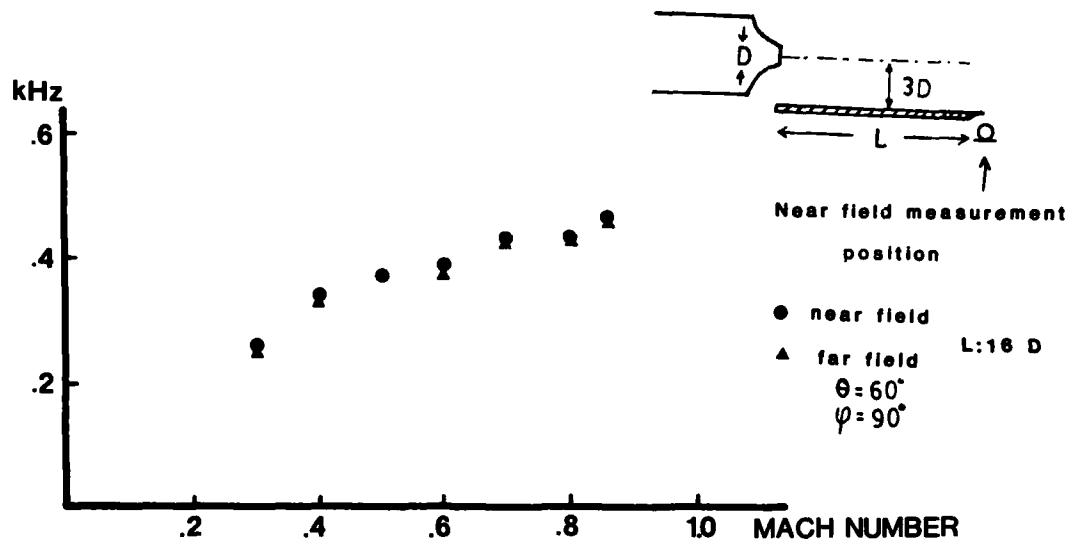
FIG. 2-9a FAR FIELD PEAK FREQUENCY AND NEAR FIELD PEAK
FREQUENCY OF EDGE NOISE
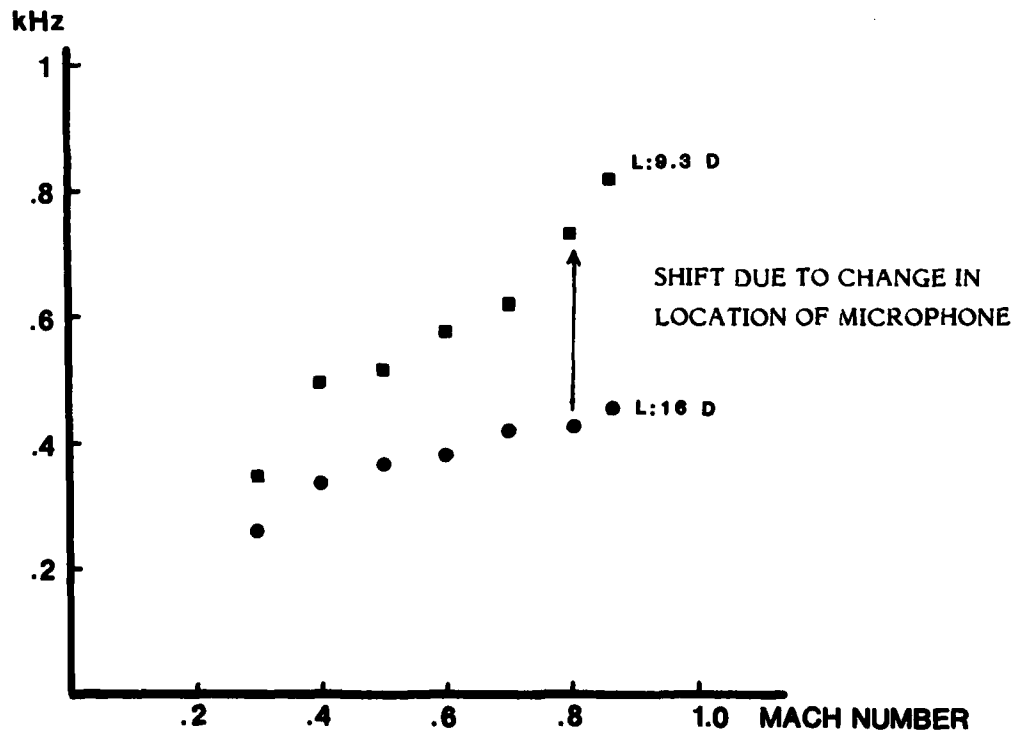
FIG. 2-9b SHIFT IN NEAR FIELD PEAK FREQUENCY OF EDGE NOISE
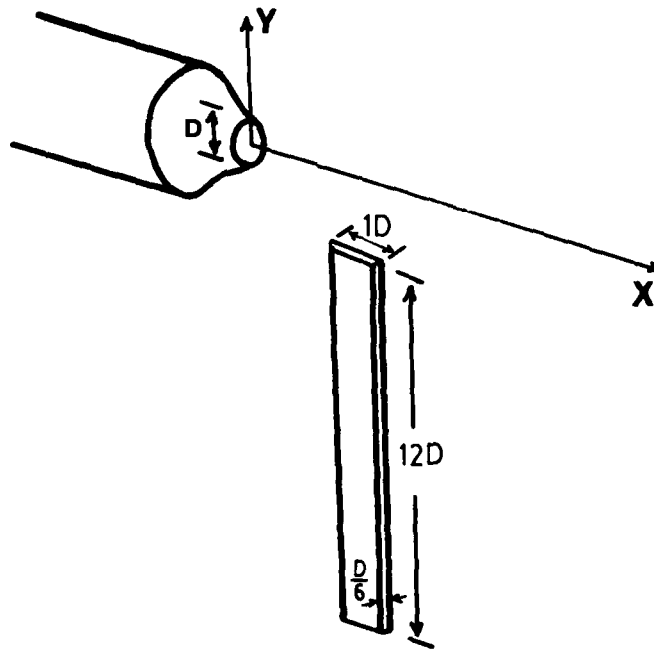
FIG. 2-10a ARRANGEMENT OF INTERFERENCE PROBE

● measurement

α ▬ angle between horizontal and line which passes through nozzle lip
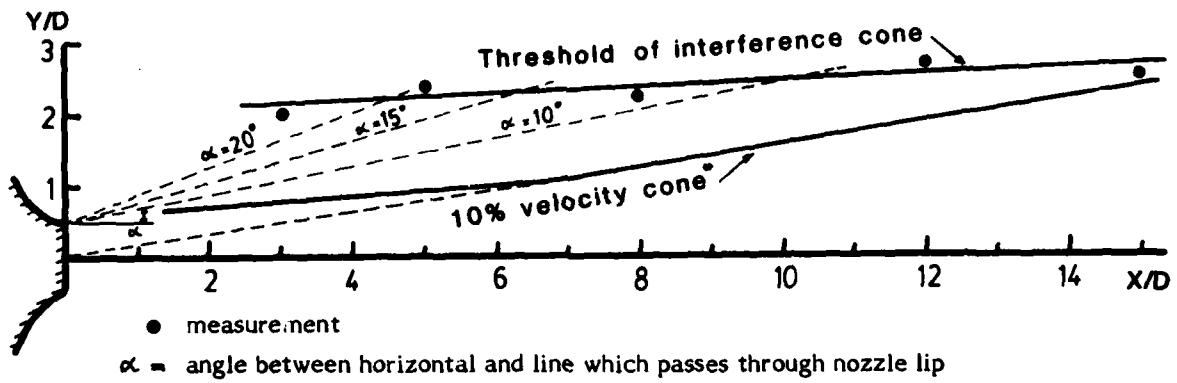
FIG. 2.10b BOUNDARY OF CONE LIMIT FOR ≤ 1 dB INTERFERENCE , M_j = 0.6

* (Ref. 17)
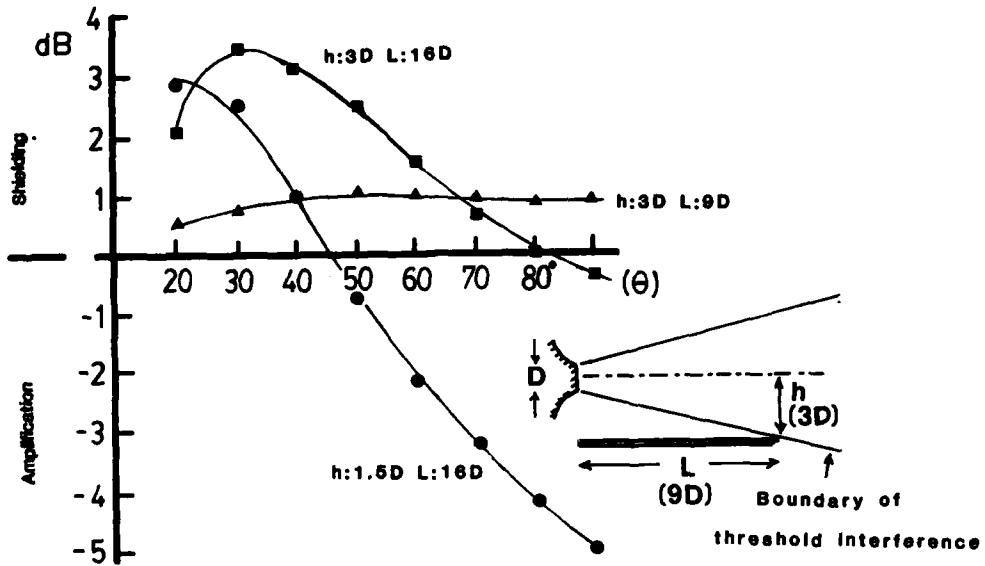
FIG. 2-11a   EFFECT OF EDGE NOISE ON SHIELDING PERFORMANCE OF
PLANAR CONFIGURATION ; $M_j = 0.6$, $\varphi = 90^\circ$

h:3D L:9D M_j:0.6
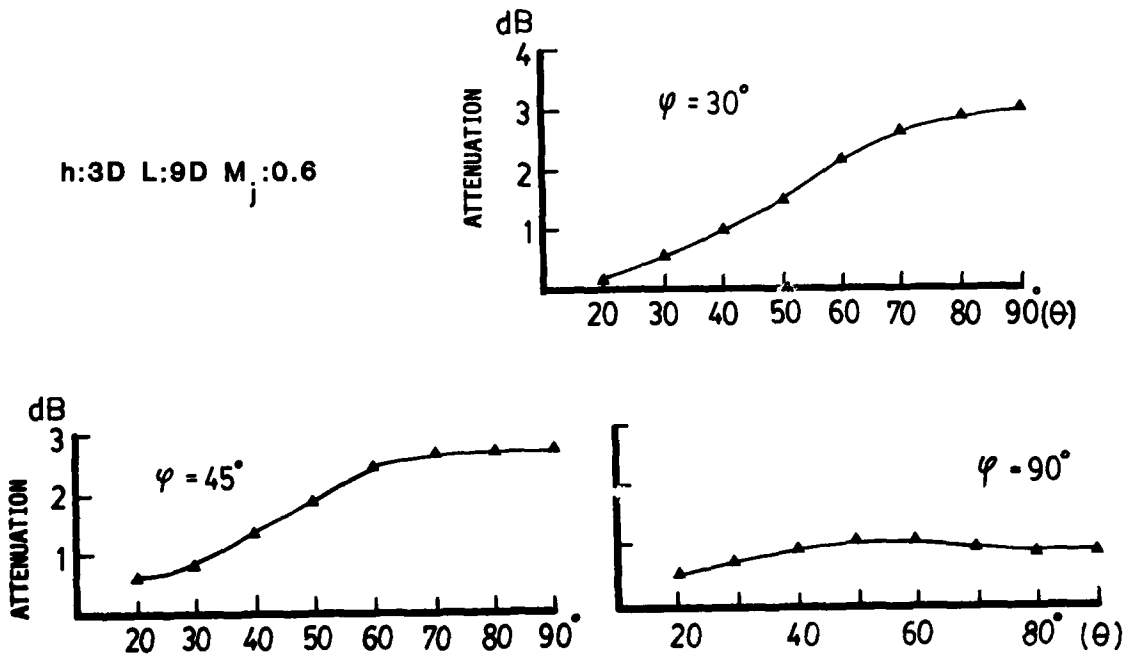
FIG. 2-11b   SOUND ATTENUATION MEASURED BY SEMI-INFINITE
RECTANGULAR SHIELD

$M_j = 0.6$
$h = 1.5 D, 3D$
$L = 16 D$

α = angle between horizontal and ray
to apex of cutout, in vertical plane,
measured from lower nozzle lip.

SPECTRUM LEVEL dB

—·— $\alpha = 0°$
—o—o— $\alpha = 5°$
—x—x—x— $\alpha = 10°$
—•—•—•— $\alpha = 15°$

UNSHIELDED

$\Theta = 30°$
$\varphi = 90°$

.1   .2   .5   1   2   5   10   20   50 KHz

(a)

FIG.2-12   SHIELDED SPECTRAL TRENDS OF RECTANGULAR SHIELDS
WITH HYPERBOLIC CUTOUTS (h/D = 1.5)

FIG.2-12 SHIELDED SPECTRAL TRENDS OF RECTANGULAR SHIELDS
WITH HYPERBOLIC CUTOUTS (h/D = 1.5)

FIG. 2-13   SHIELDED SPECTRAL TRENDS OF RECTANGULAR SHIELDS
WITH HYPERBOLIC CUTOUTS (h/D = 3)

FIG. 2-13   SHIELDED SPECTRAL TRENDS OF RECTANGULAR SHIELDS
WITH HYPERBOLIC CUTOUTS (h/D = 3)

MICROCOPY RESOLUTION TEST CHART

NATIONAL BUREAU OF STANDARDS-1963-A

$M_j = 0.6$

$h = 3D$

$\varphi = 90°$

$\varphi = 45°$

FIG. 2-14   SHIELDING CHARACTERISTICS FOR PLANAR SHIELDS WITH AND
WITHOUT HYPERBOLIC CUTOUTS

$\varphi = 45°$

dB

ATTENUATION

4

3

2

1

20 30 40 50 60 70 80 90° (θ)

16D

h/D = 3, $M_j = 0.6$

$\varphi = 90°$

dB

ATTENUATION

4

3

2

1

20 30 40 50 60 70 80 90° (θ)

9D

FIG. 2-15   SHIELDING CHARACTERISTICS FOR CUTOUT CONFIGURATION,
'TRIMMED' EXTENSION PROVIDES COMPARABLE PERFORMANCE

110

dB

EPNL

102

100

93

90

sideline and approach

takeoff

10   100   1000

Takeoff gross weight, 10^3 lbs

FIG. 2-16   NOISE LIMIT IMPOSED BY FAR-36   (Ref. 21)

FIG. 2-17   TYPICAL SUGAR SCOOP SHIELDS
(5, 10, 15D DIAMETER)

$\varphi = 90°$ $M_j = .6$

	L(D)
△	4
▼	7
▲	11
□	16

FIG. 2-18   SHIELDING PERFORMANCE OF 5 D SCOOP SHIELD

FIG. 2-19a JET NOISE ATTENUATION PROVIDED BY 10 D SCOOP SHIELD
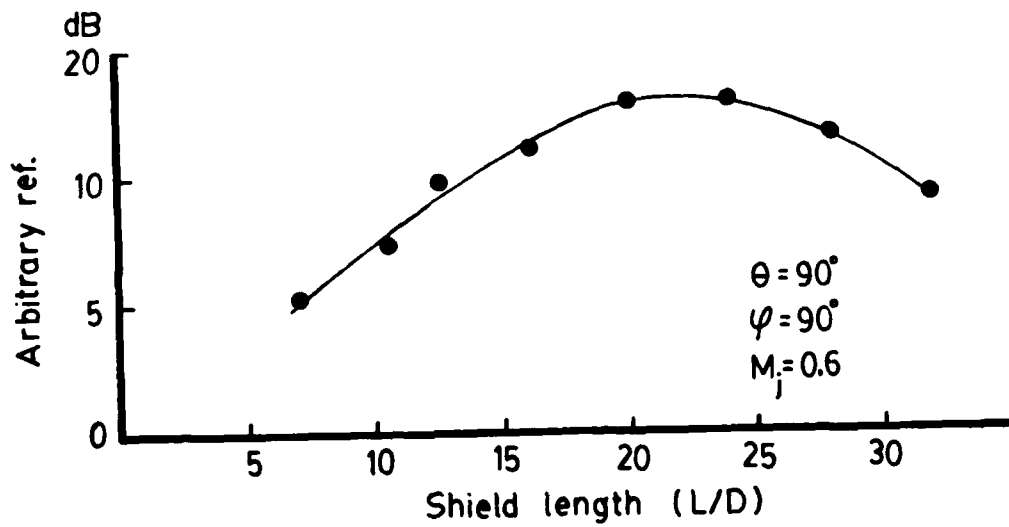
FIG. 2-19b LOW FREQUENCY AUGMENTATION PEAK LEVEL vs. SHIELD LENGTH

(10 D DIAMETER SCOOP SHIELD)

OASPL

M$_j$ = .6
φ = 0°

2 dB

PLANAR SHIELD
(trimmed extension, h/D=3,
cf. Fig.2.15)

INSERTION LOSS

BASIC JET

10D SCOOP SHIELD

20°   40°   60°   80° (θ)
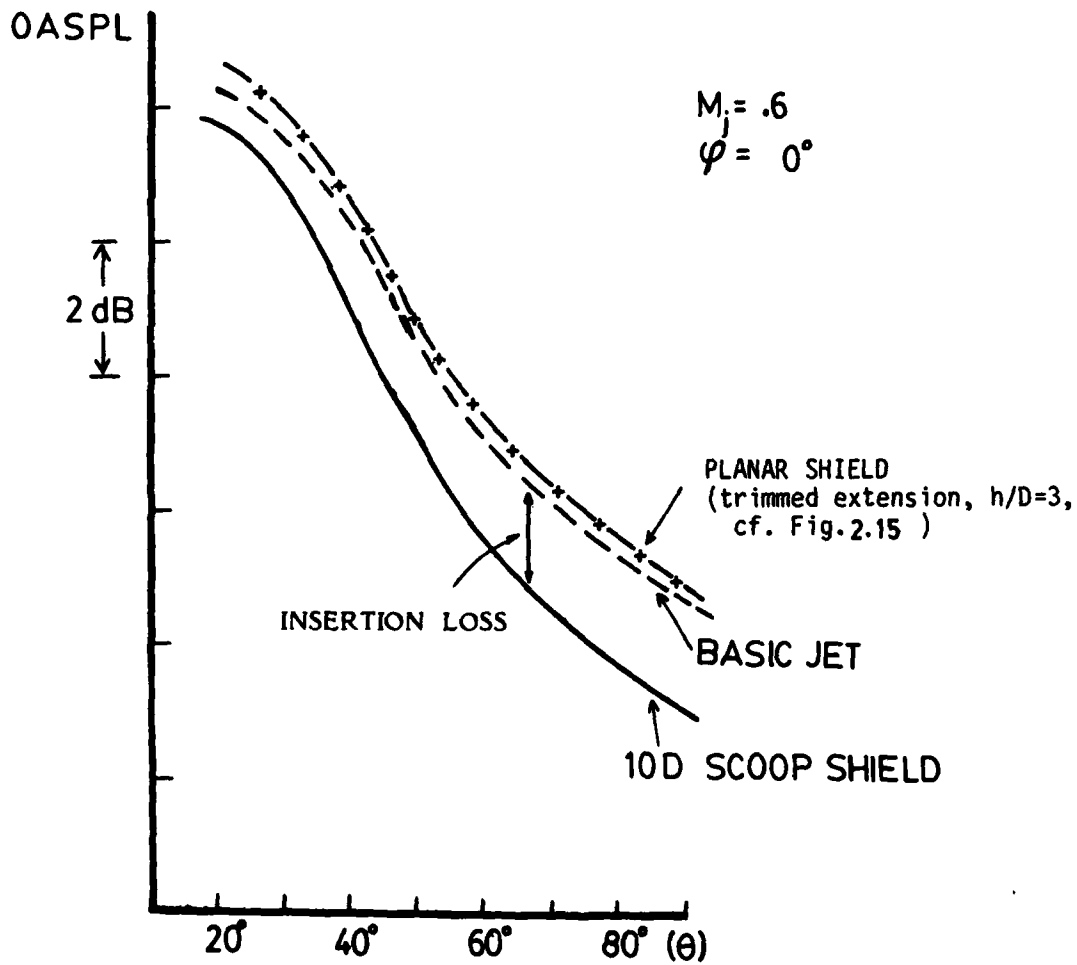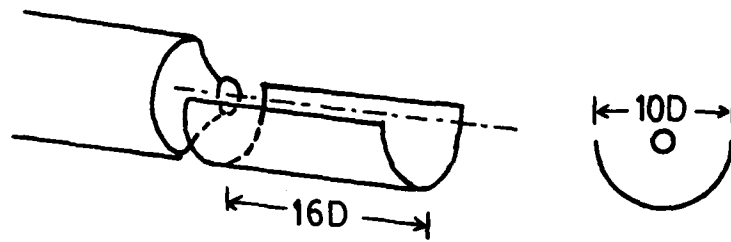
FIG.2-19c   OVERALL INSERTION LOSS PROVIDED BY 10D SCOOP
SHIELD   IN THE SIDELINE DIRECTION (φ = 0°)
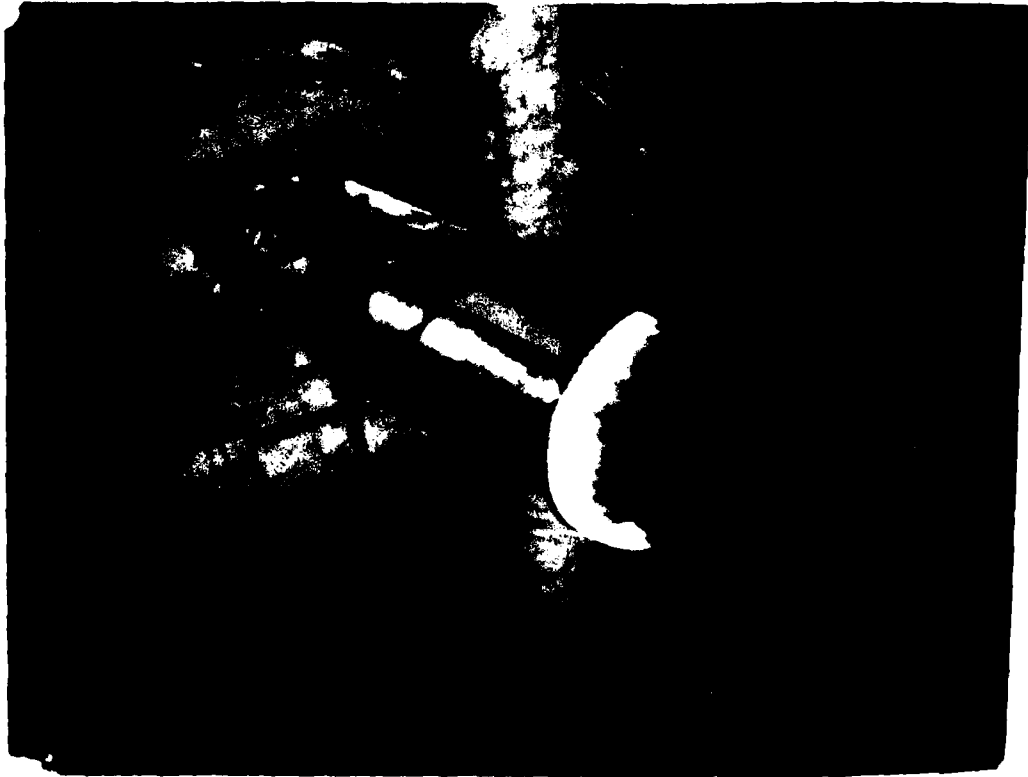
FIG 2-20a VIEW OF SOLID (SCOOP) SHIELD PLUS HOT GAS LAYER
IN OPERATING MODE
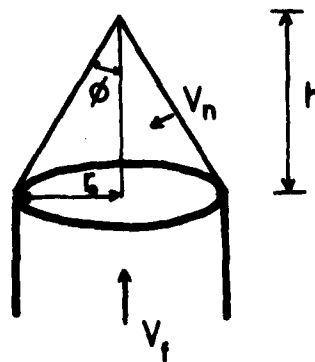
FIG. 2-20b GEOMETRY OF THE BURNING CONE FOR ESTIMATION OF FLAME SPEED
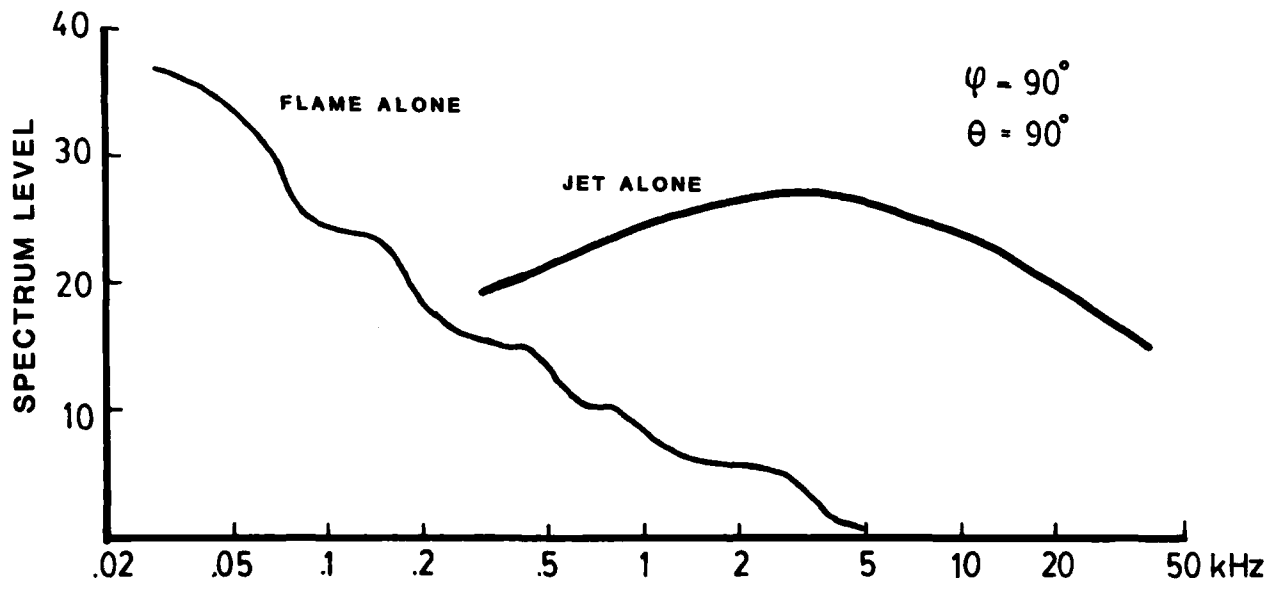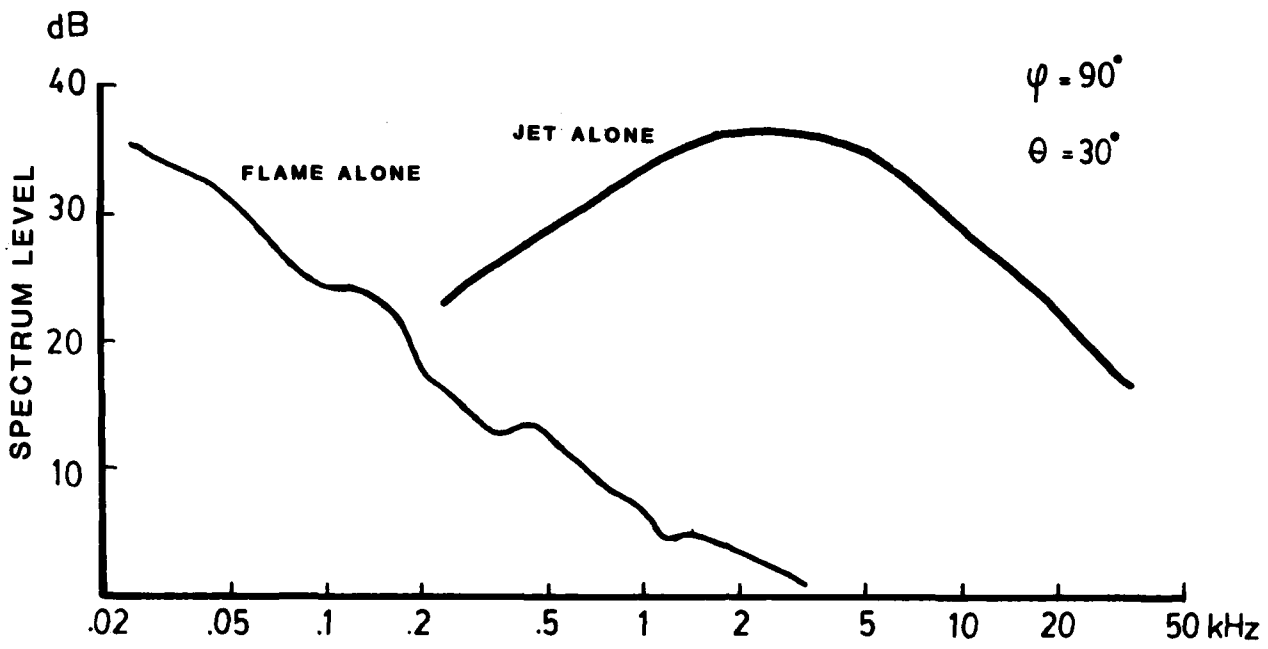
FIG. 2-21   COMPARISON OF SPECTRUM LEVELS FOR FLAME SHROUD
AND JET NOISE ($M_j = 0.6$)
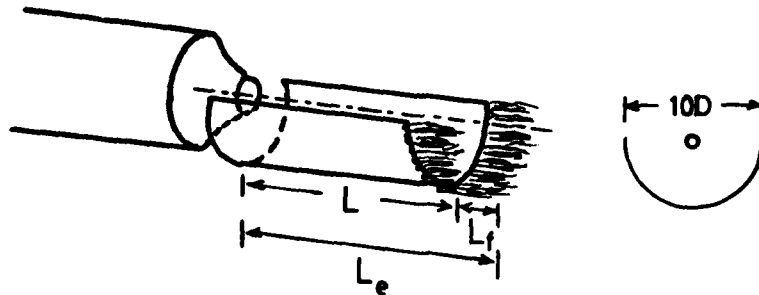
$$L/D = 14, \; L_f = 3.8 \text{ CM}, \; L_e = 16 \text{ D}, \; M_j = 0.6$$
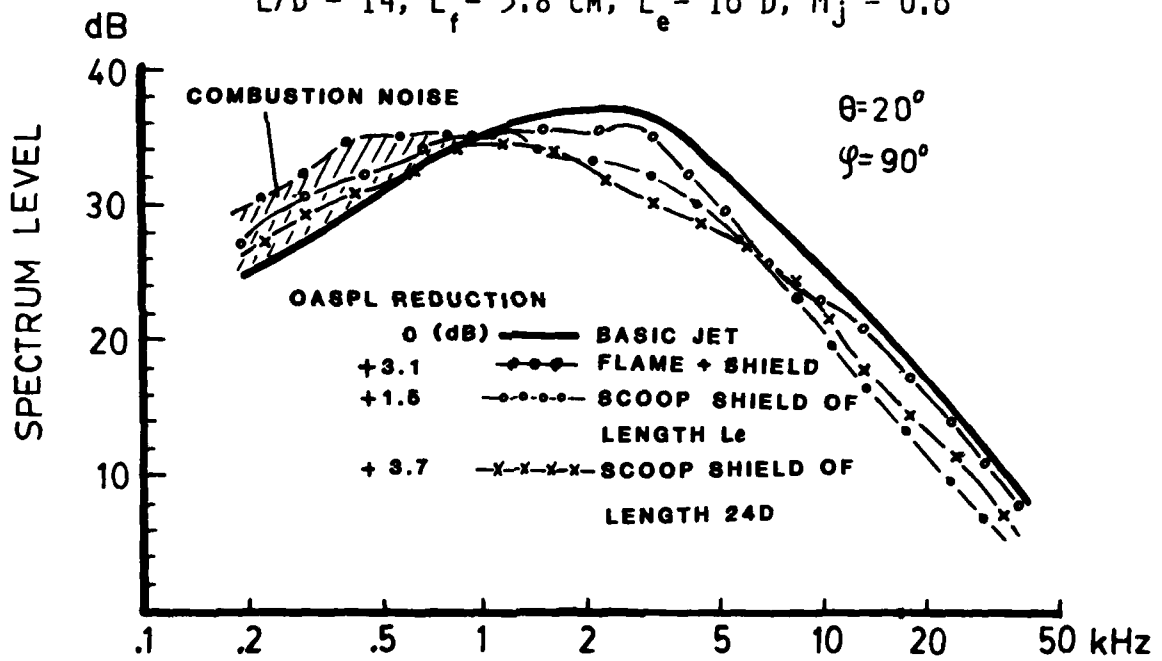
FIG. 2-22   JET NOISE SHIELDING WITH 10D DIAMETER
SOLID (SCOOP) SHIELD PLUS HOT GAS LAYER
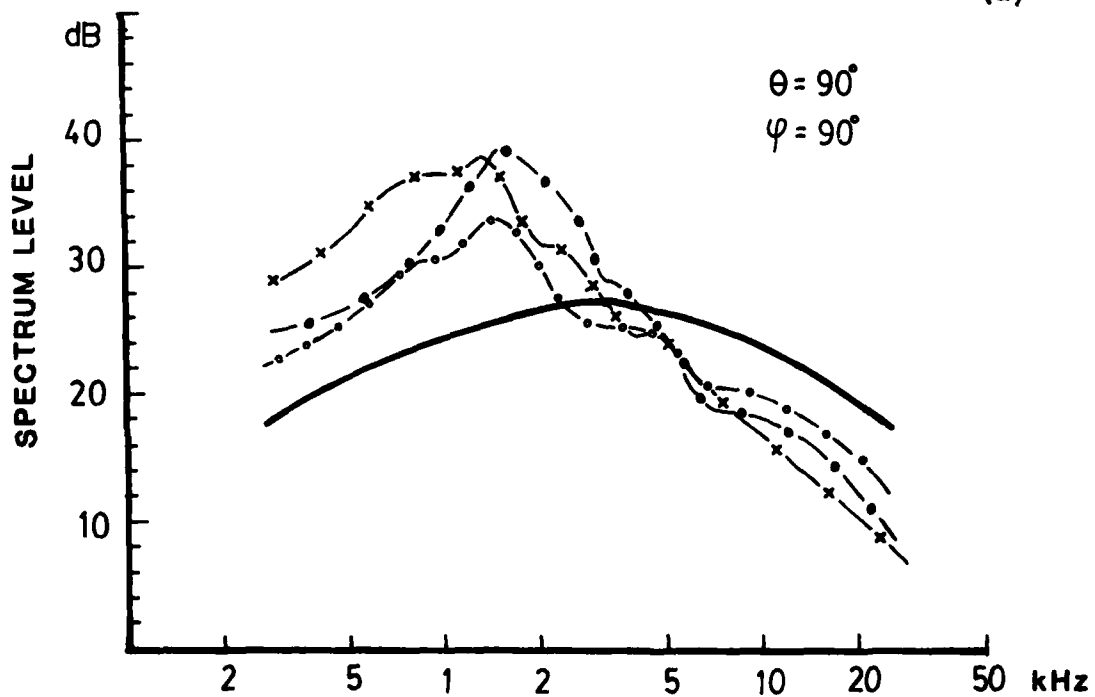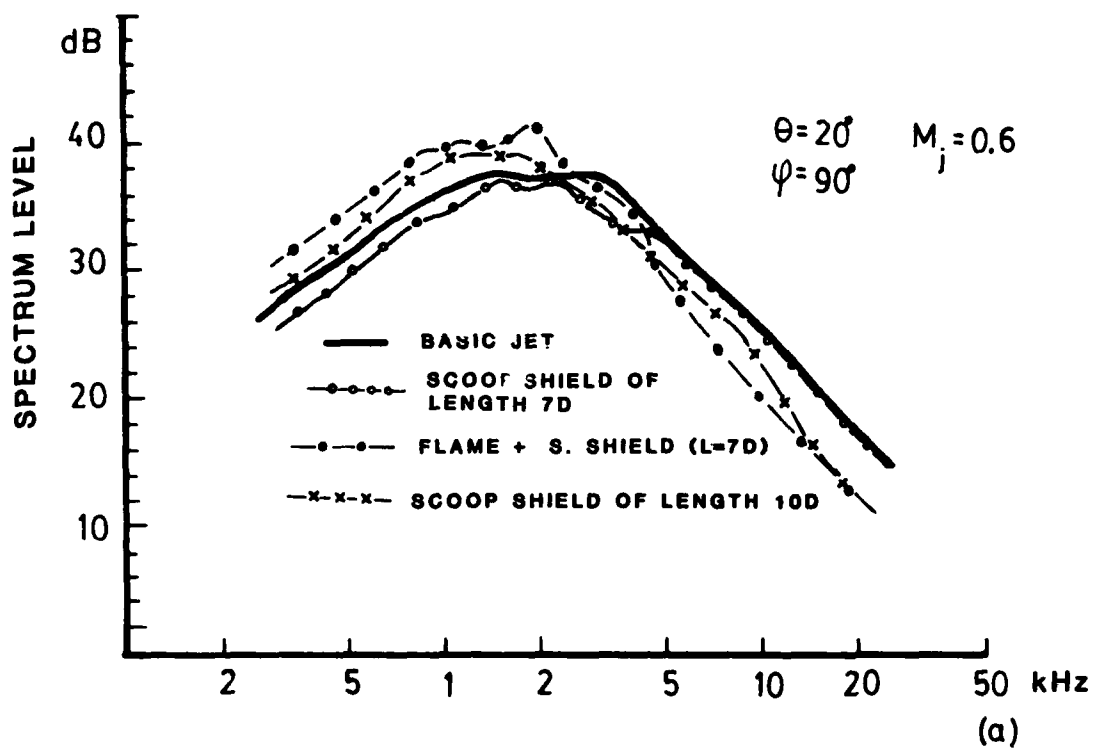
FIG. 2-23   JET NOISE SHIELDING WITH 5D DIAMETER
SOLID (SCOOP) SHIELD PLUS HOT GAS LAYER
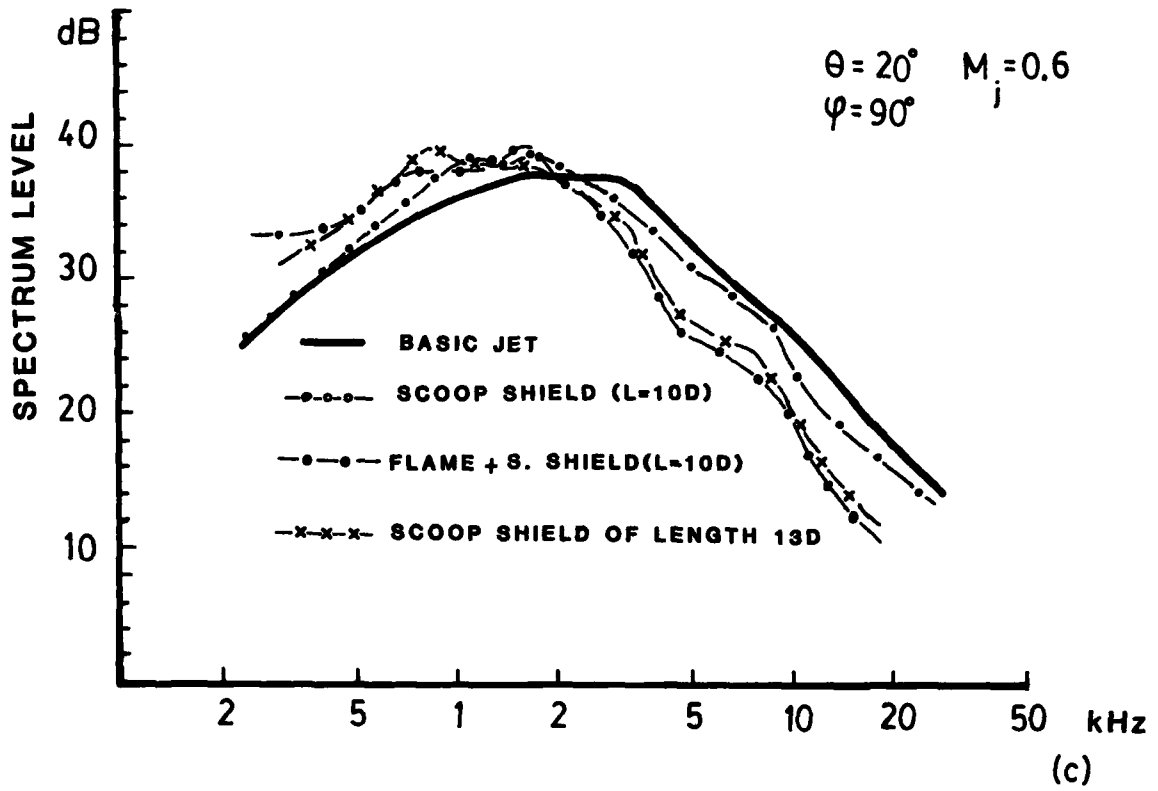
FIG.2-23   JET NOISE SHIELDING WITH 5D DIAMETER
SOLID (SCOOP) SHIELD PLUS HOT GAS LAYER
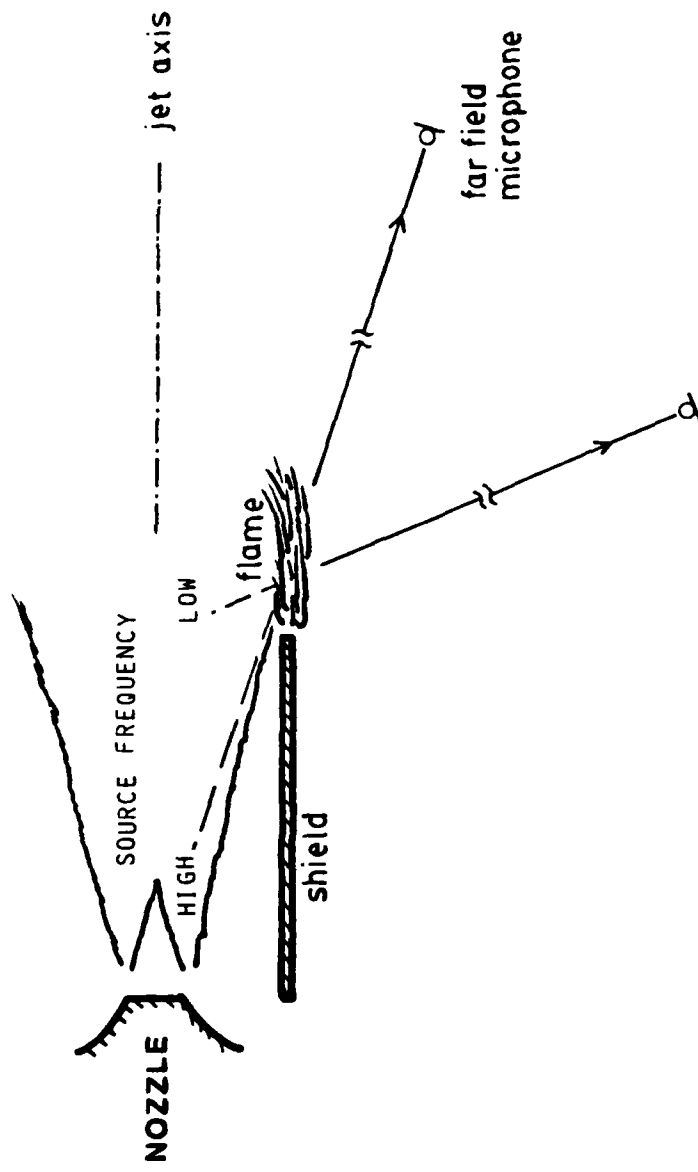
FIG. 2-24   NOISE TRANSMISSION PATHS THROUGH A FLUID LAYER ACOUSTIC
SHIELD: THE FLAME LAYER IS MORE EFFECTIVE AT SMALL
ANGLE WITH RESPECT TO THE JET AXIS BECAUSE THE SOUND
TRAVELLING THROUGH THE IMPEDANCE LAYER IS OF HIGHER
FREQUENCY.
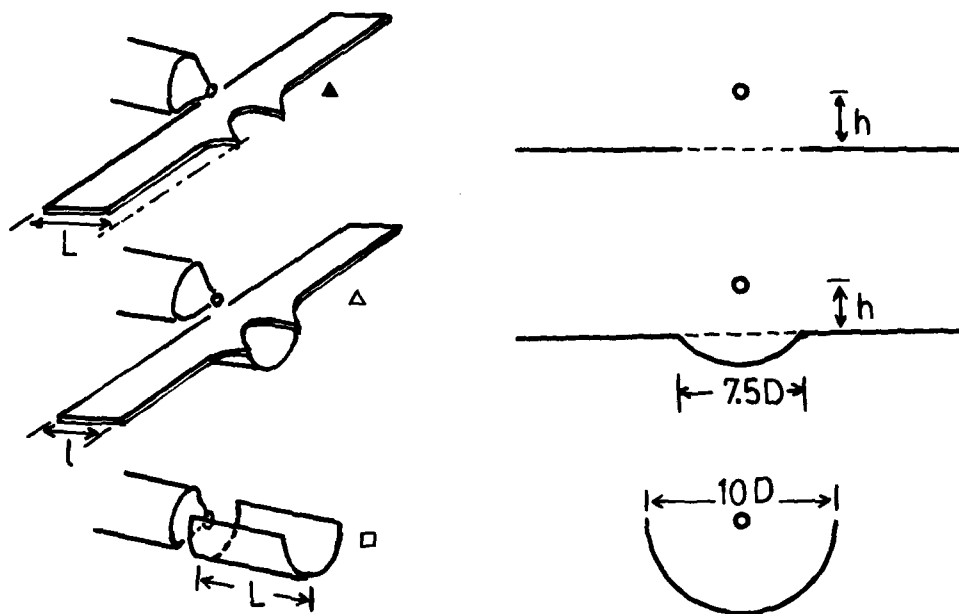
h/D = 3

L/D = 16 $M_j = 0.6$

l/D = 7
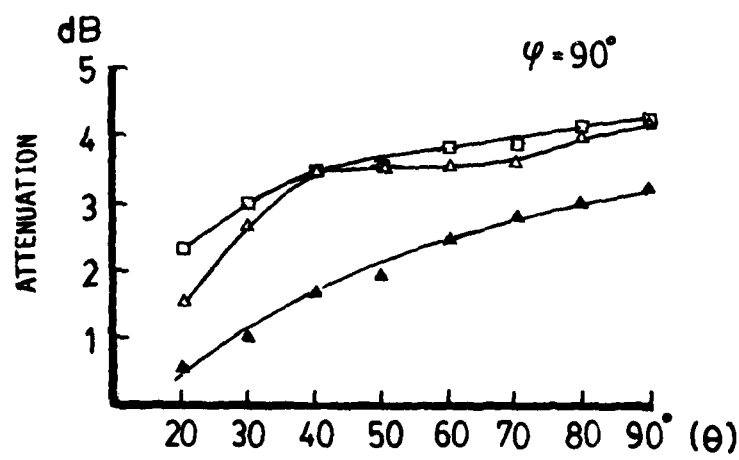
FIG. 2-25   COMPARISON OF SHIELDING CHARACTERISTICS FOR VARIOUS CONFIGURATIONS
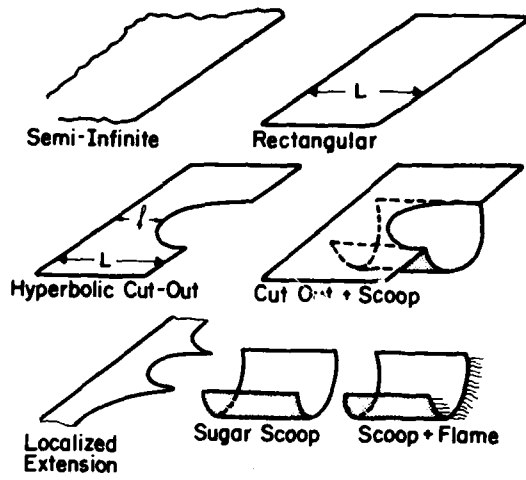
FIG. 3-1   SHIELDING CONFIGURATIONS STUDIED

$$nD_j = x\lambda_j \qquad\qquad nD_m = x\lambda_m$$

$$\frac{D_j}{\lambda_j} = \frac{x}{n} \qquad\qquad \frac{D_m}{\lambda_m} = \frac{x}{n}$$

$$\frac{D_j}{\lambda_j} = \frac{D_m}{\lambda_m}$$
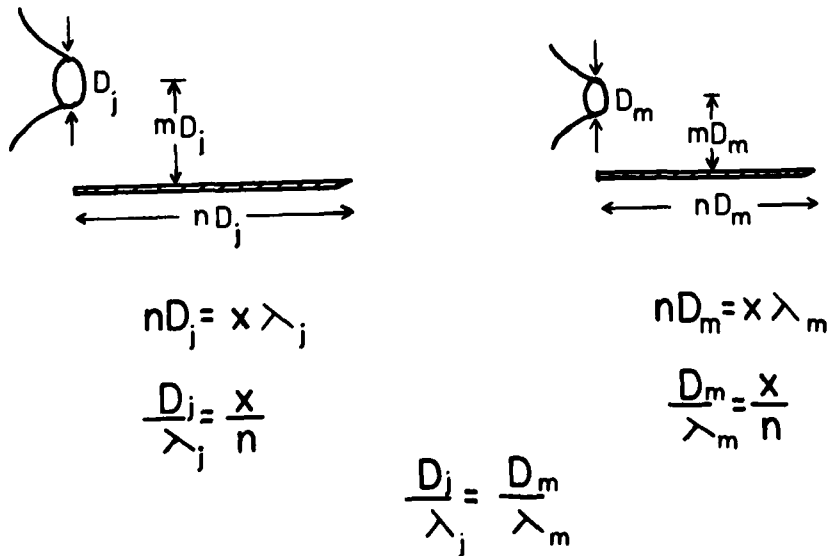
FIG.4-1   JET NOISE SCALING SCHEME
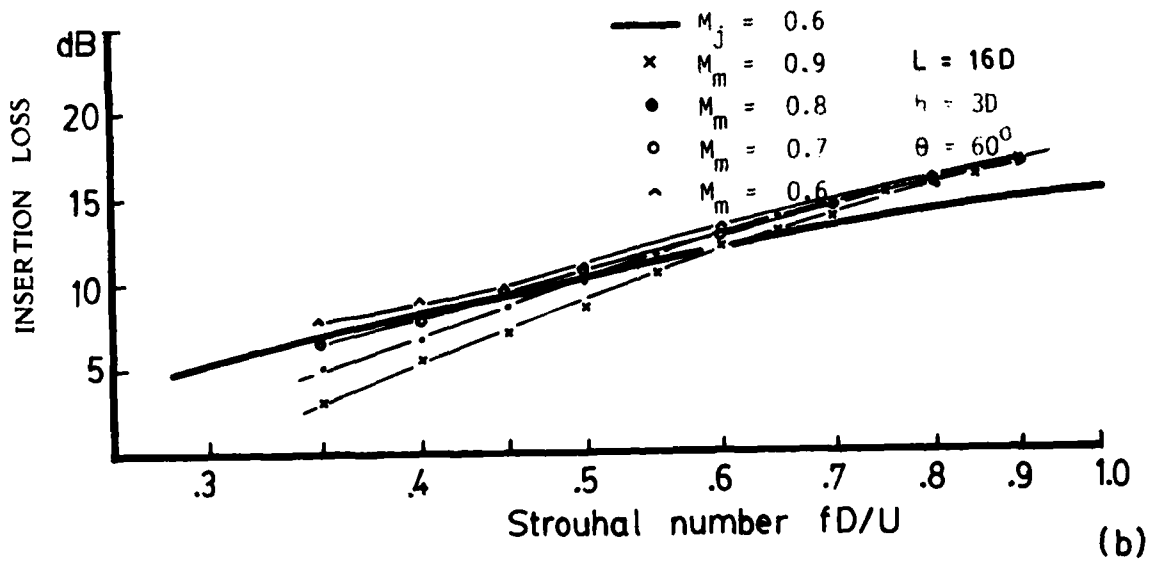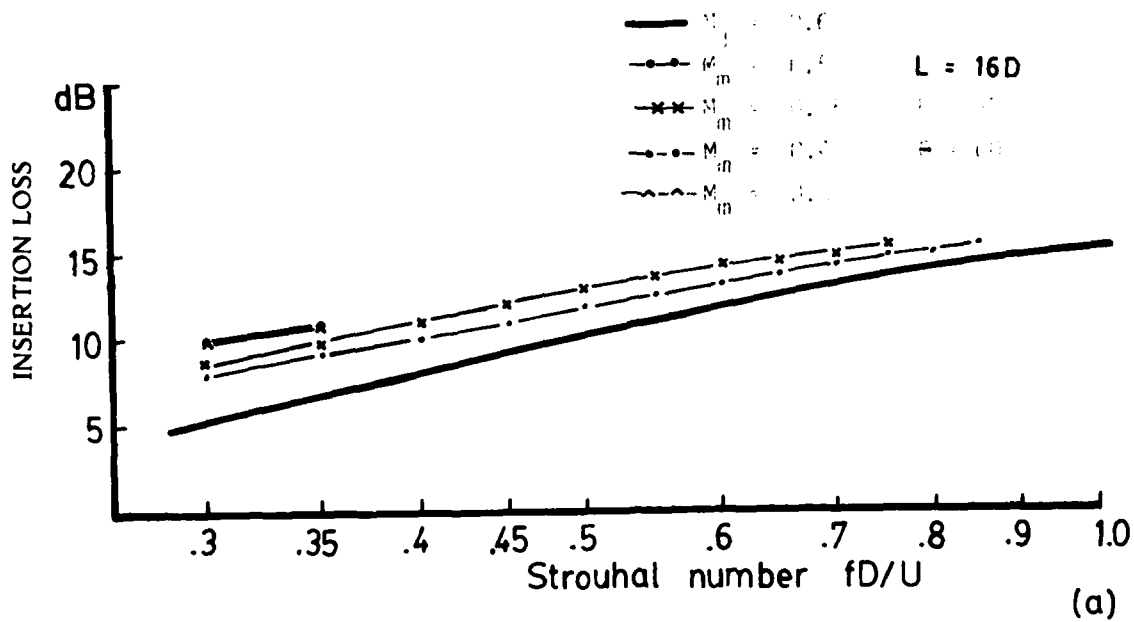
FIG. 4-2   COMPARISON OF LARGE (D_j = 3/4") AND SMALL (D_m = 1/4")
MODEL SHIELDING MEASUREMENTS BASED ON MODIFIED
STROUHAL NUMBER   (φ = 90°, θ = 60°)
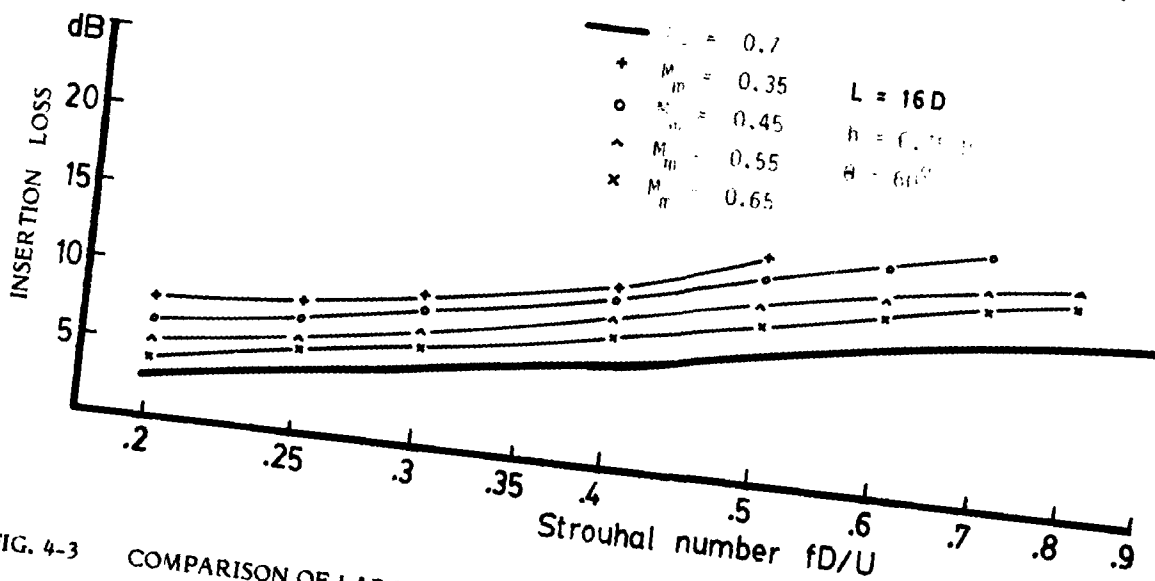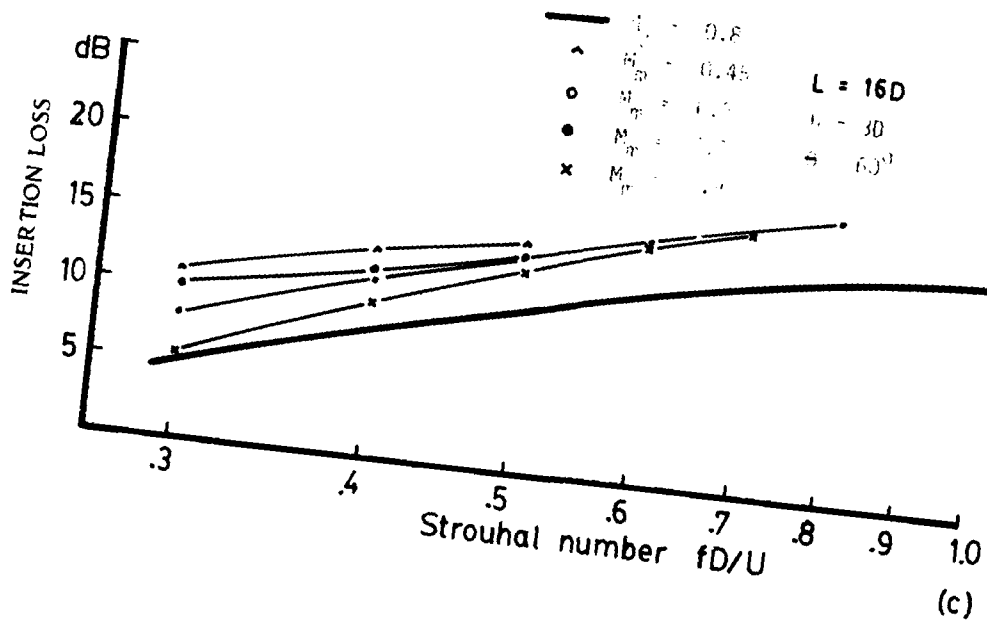
FIG. 4-3   COMPARISON OF LARGE (D_j = 3/4")-AND SMALL (D_m = 1/4")-MODEL SHIELDING
MEASUREMENTS BASED ON MODIFIED STROUHAL NUMBER

φ = 90°, θ = 60°
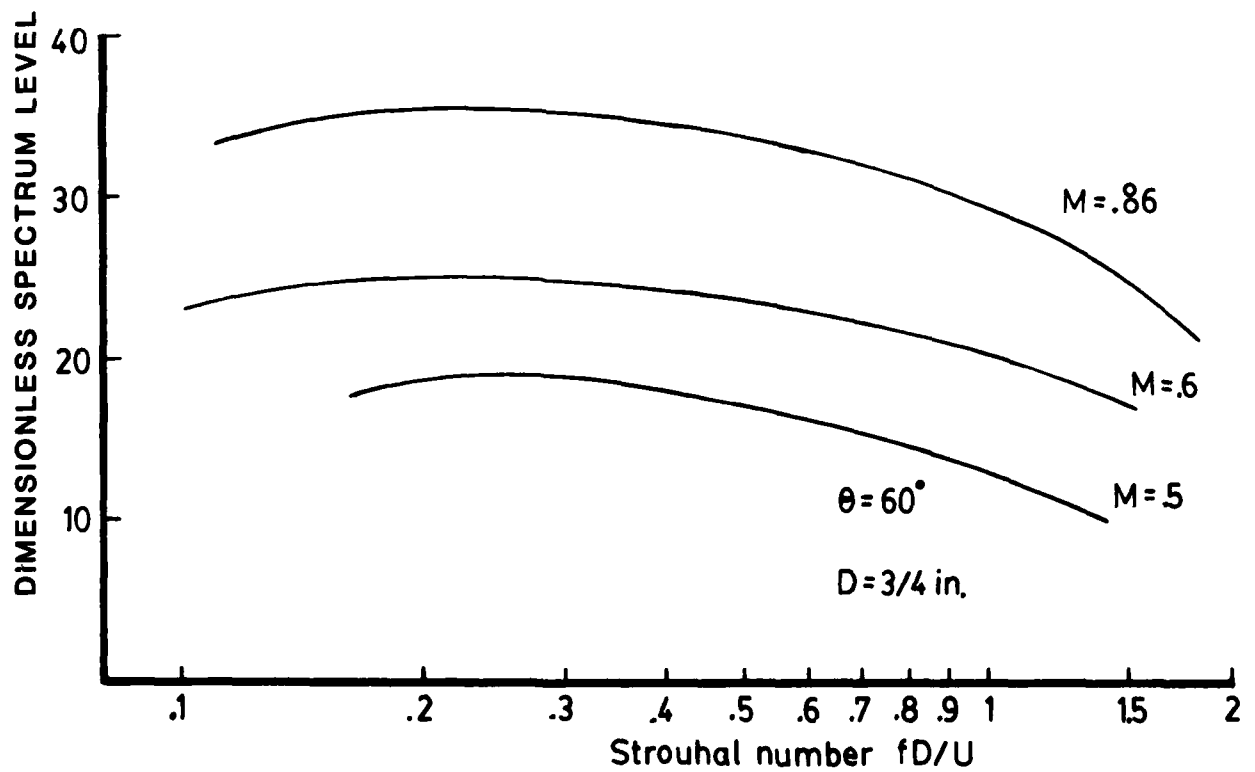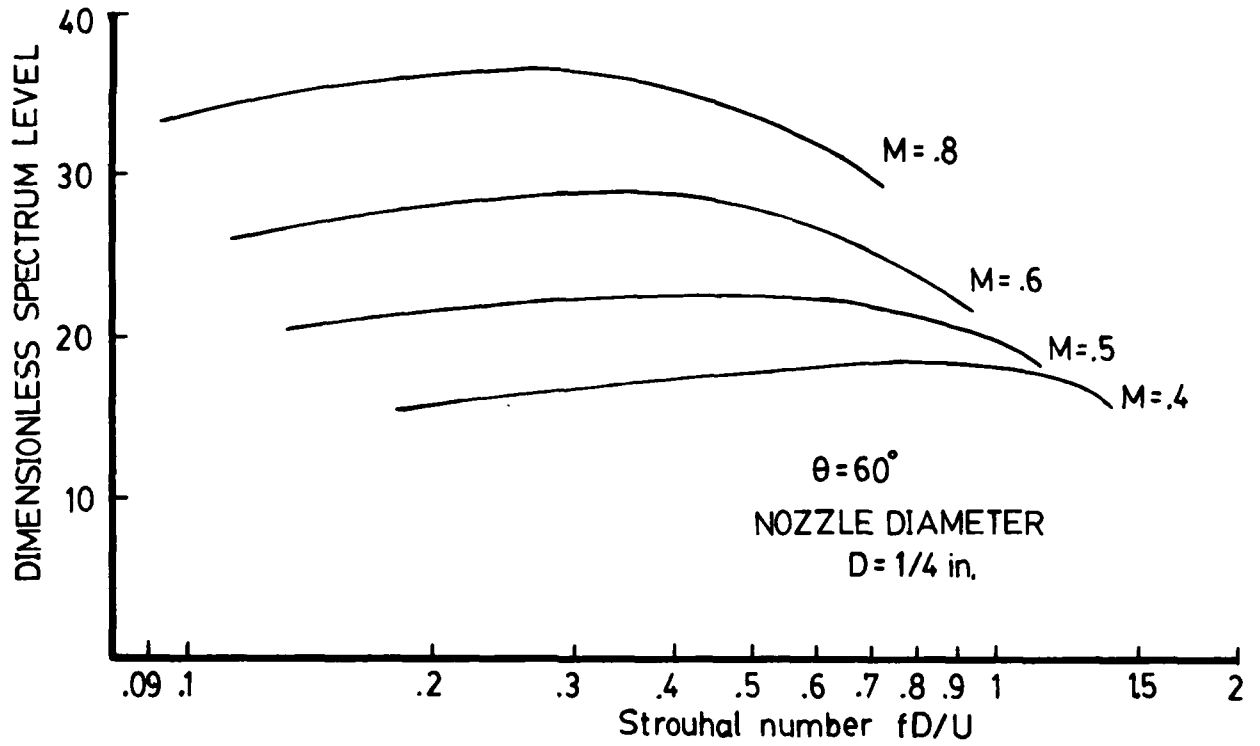
FIG. 4-4   DIMENSIONLESS POWER SPECTRUM FOR SUBSONIC JET
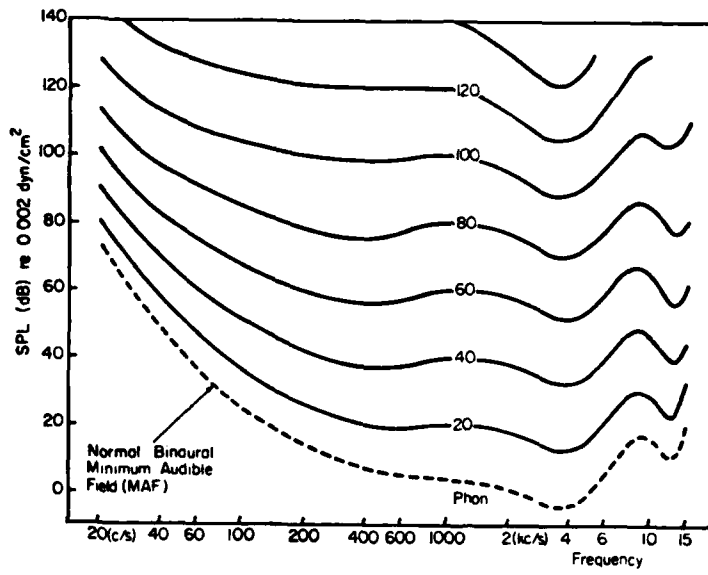
FIG. 5-1 CONTOURS OF EQUAL LOUDNESS (Ref. 34)
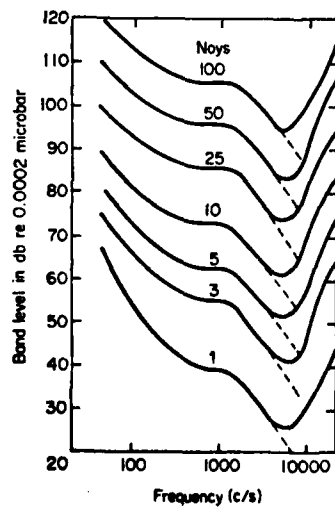
FIG. 5-2 EQUAL NOISINESS CONTOUR (Ref. 34)

Typical grid point on
ground plane
(R, θ, φ) in O'
$(x, y, 0)$ in O
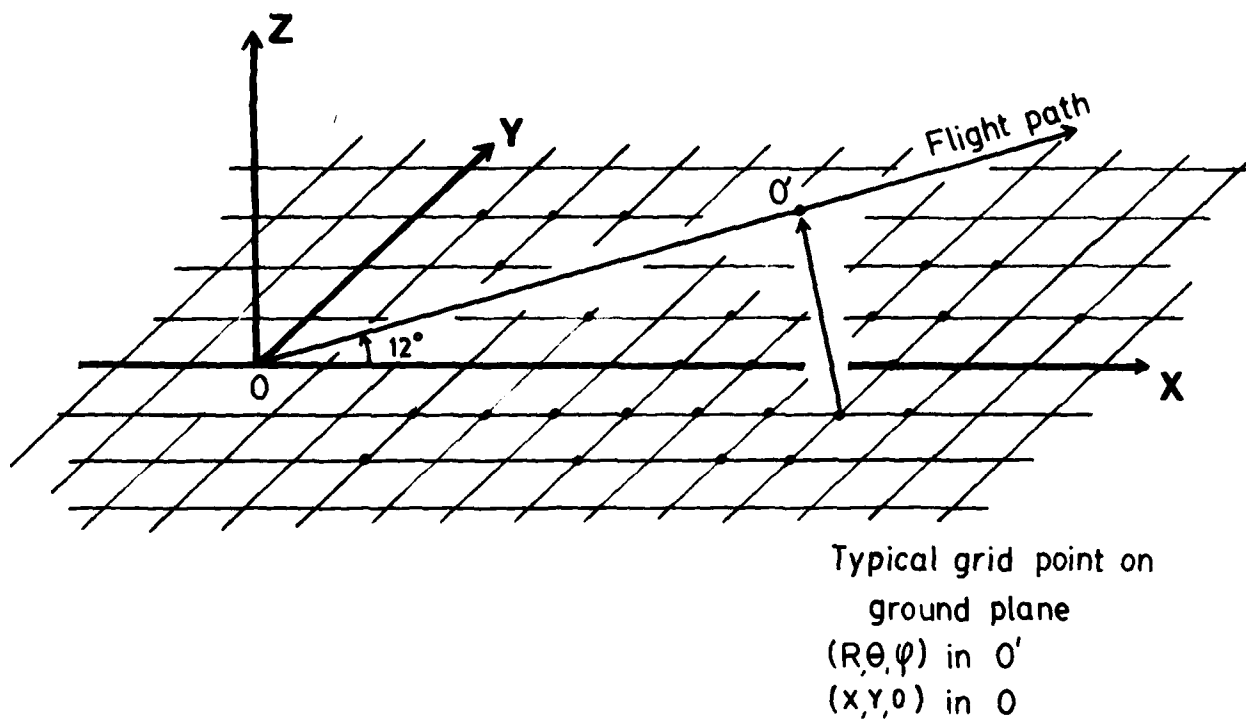
FIG. 5-3   GEOMETRY FOR TAKE-OFF PROCEDURE AND GRID POINTS
ON GROUND PLANE FOR FOOTPRINT CALCULATIONS. THE
GROUND RUN IS NEGLECTED, AND THE JET AXIS IS TAKEN
TO BE ALIGNED WITH THE FLIGHT PATH

Flow Chart for Ground Contour Calculations

```
┌─────────────────────┐          ┌──────────────────────────┐
│  Set up grid points │          │ Maximum level of PN dB   │
│  on ground plane    │          │ level at each grid point │
│                     │          │ is selected from time    │
└─────────┬───────────┘          │ history of the SPL       │
          │                      └────────────┬─────────────┘
          ▼                                   │
┌─────────────────────┐                       ▼
│  Obtain equation of │          ┌──────────────────────────┐
│  flight path   ①    │          │ Interpolate the contour  │
└─────────┬───────────┘          │ of constant PN dB from   │
          │                      │ maxima calculated at     │
          ▼                      │ each grid point          │
┌─────────────────────┐          └──────────────────────────┘
│ Obtain coordinates  │
│ of grid points      │
│ (X₁Y₁Z₁) reference  │
│ to A/C frame        │
│ (X₂Y₂Z₂)      ②     │
└─────────┬───────────┘
          │
          ▼
┌─────────────────────┐          ┌──────────────────────────┐
│ Transform (X₂Y₂Z₂)  │          │ Scale level to simulate  │
│ to spherical        │          │ a full size engine       │
│ coordinate          │          └────────────┬─────────────┘
│ (R,θ,φ)        ③    │                       │
└─────────┬───────────┘                       │
          │                                   │
          ▼                                   │
┌─────────────────────┐                       │
│ Determine the sound │                       │
│ pressure level at   │───────────────────────┘
│ (R,θ,φ) from        │
│ experimentally      │
│ measured value at   │
│ (R₀,θᵢ,φᵢ)     ④    │
└─────────────────────┘
```

The circled number in the boxes refer to sets of equations in Appendix C

FIG. 5-4

PN dB GROUND CONTOURS

100 ft/div.

FIG. 5-5   PN dB GROUND CONTOURS

"POINT" SOURCE
HYPODERMIC TUBE
WOOD'S METAL
O-RING SEAL
SUPPORT SPRING

STEEL
SAND
LEAD
FIBERGLAS
STEEL
FOAM RUBBER

DRIVER UNIT

CORK PADS

14¾"

12½"
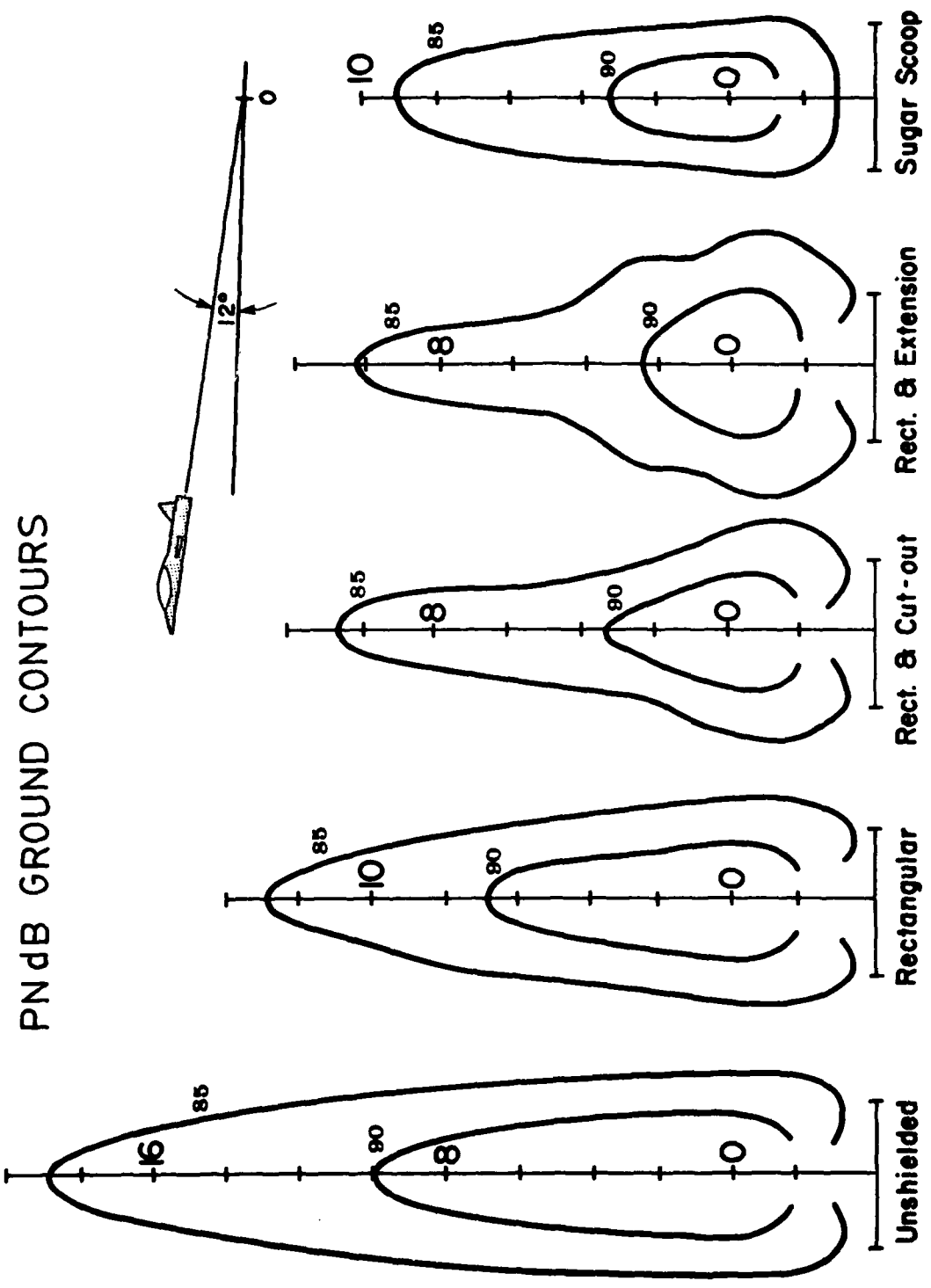
FIG. 6-2   CROSS-SECTIONAL VIEW
OF POINT SOURCE

FIG. 6-1   EXPERIMENTAL ARRANGEMENT OF POINT
SOURCE INSIDE ANECHOIC CHAMBER
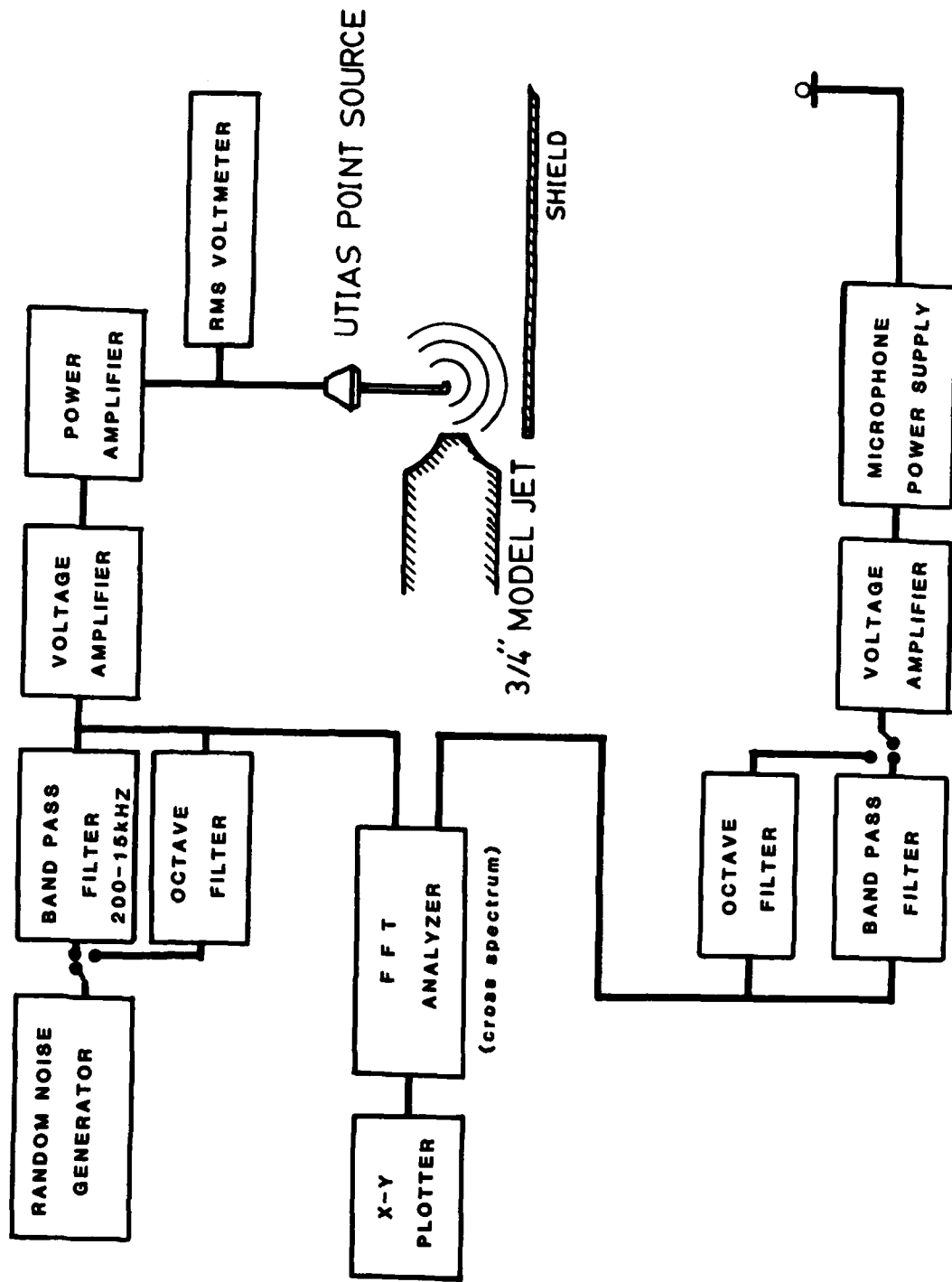
FIG. 6-3   SCHEMATIC FOR POINT SOURCE EXPERIMENT
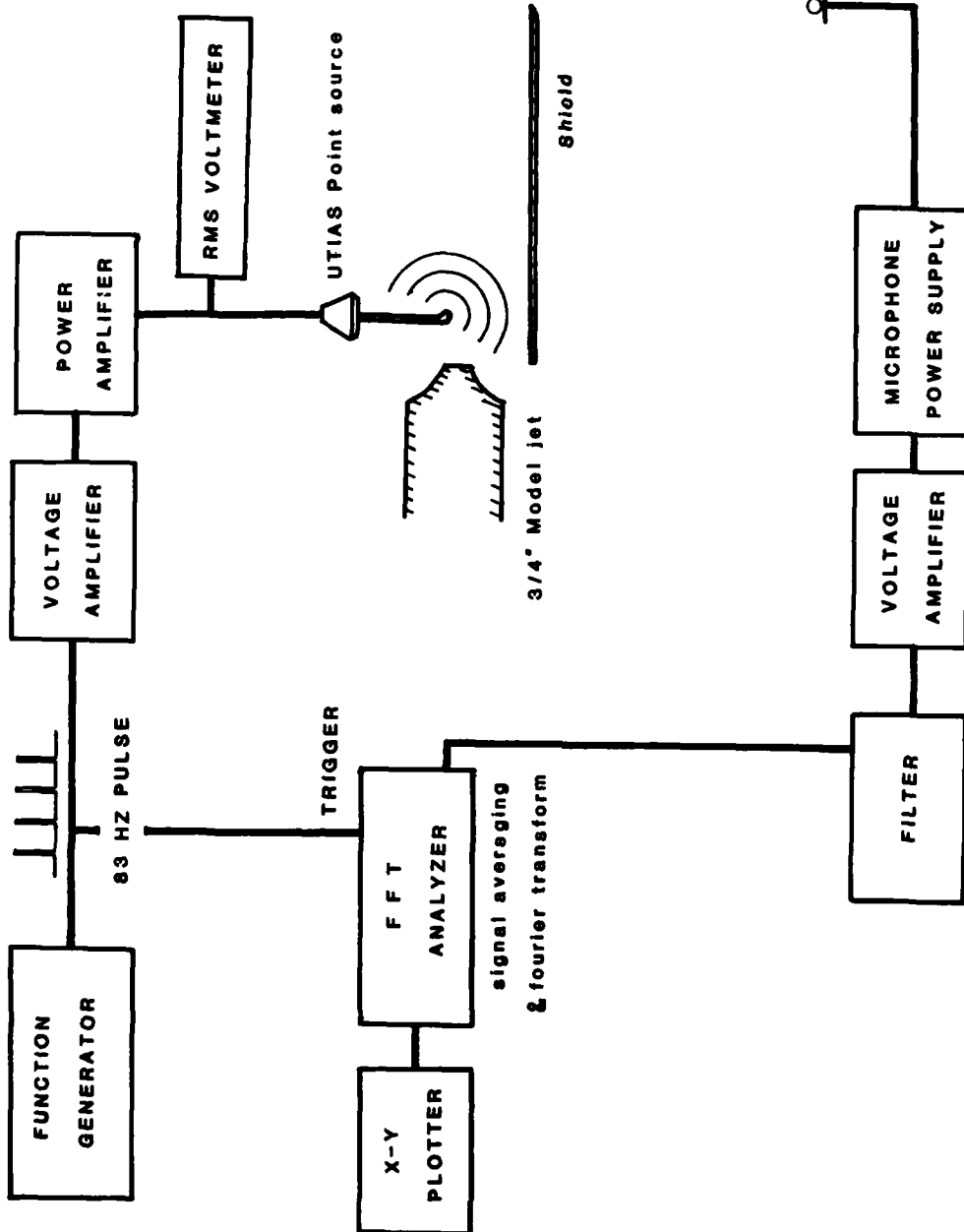
FIG. 6-4   SCHEMATIC FOR PULSE TECHNIQUE FOR ASSERTION OF
MULTIPLE TRANSMISSION PATH AROUND THE EDGES OF
FINITE BARRIER
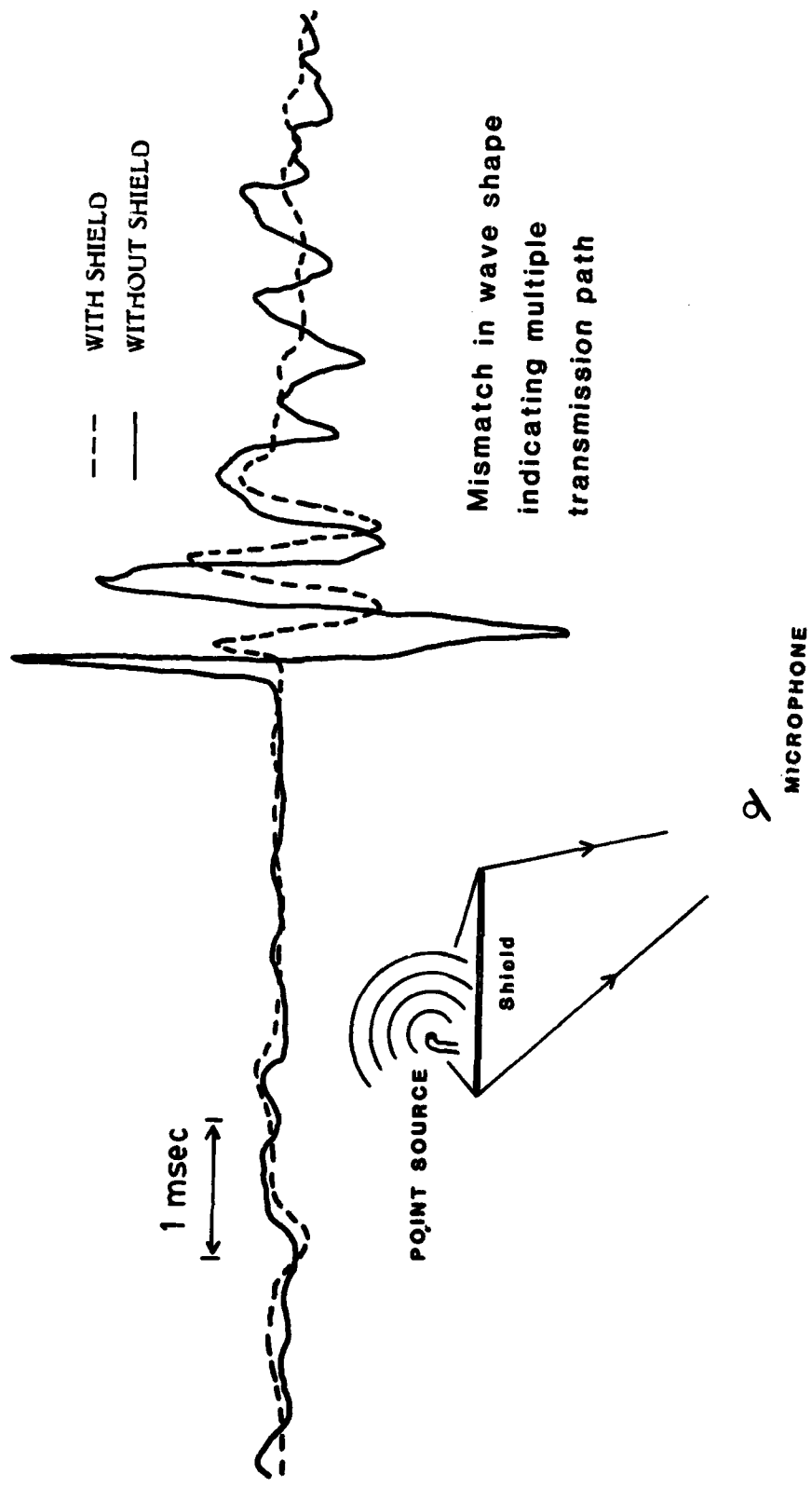
FIG. 6-5 PHASE AVERAGED OUTPUT FROM PULSED SIGNAL INPUT
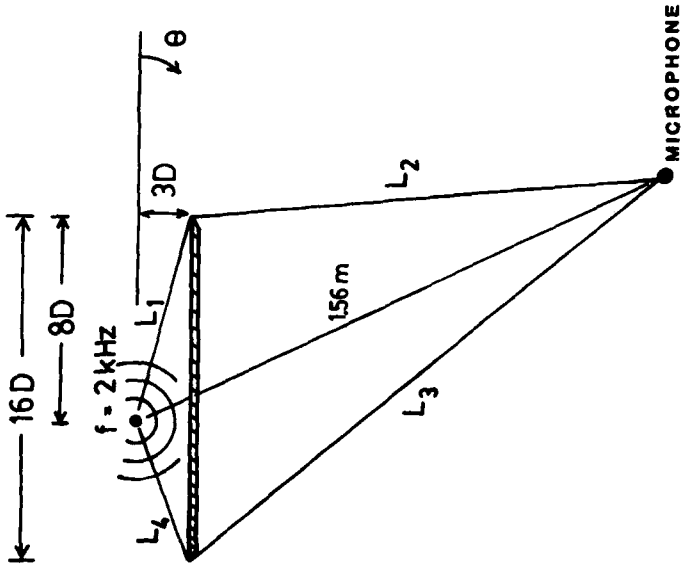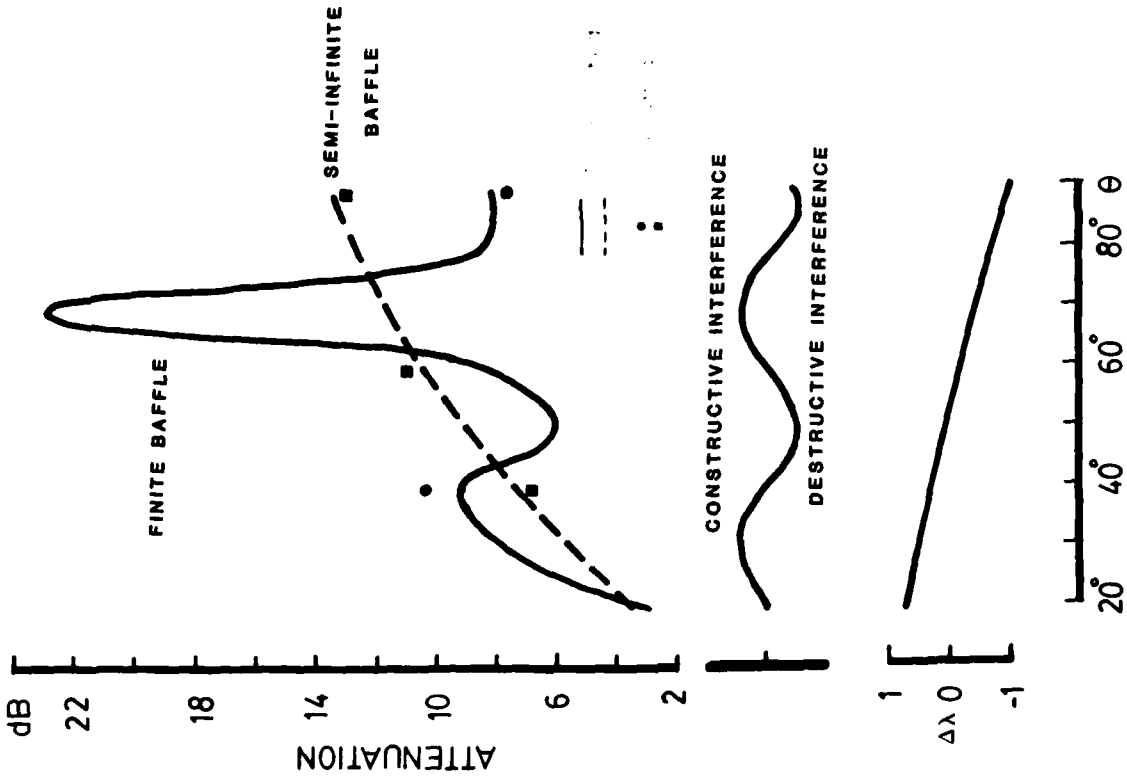
FIG. 6-6 INTERFERENCE PATTERN FROM DIFFRACTION PAST MORE THAN ONE EDGE

$$\Delta\lambda = ([L_3+L_4]-[L_1+L_2])/\lambda/2$$
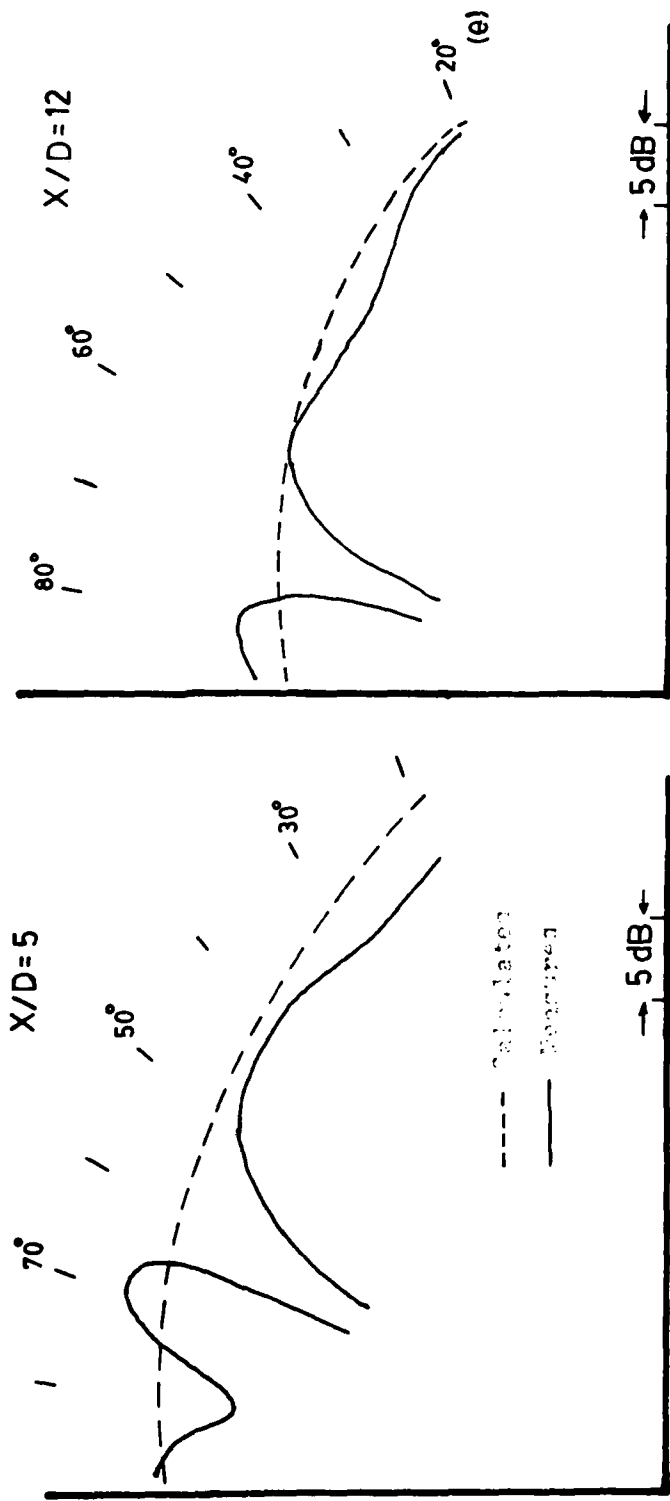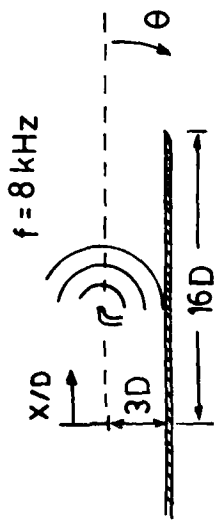
FIG. 6-7   POLAR PLOT OF LOOP PATTERNS FROM PURE TONE INPUT
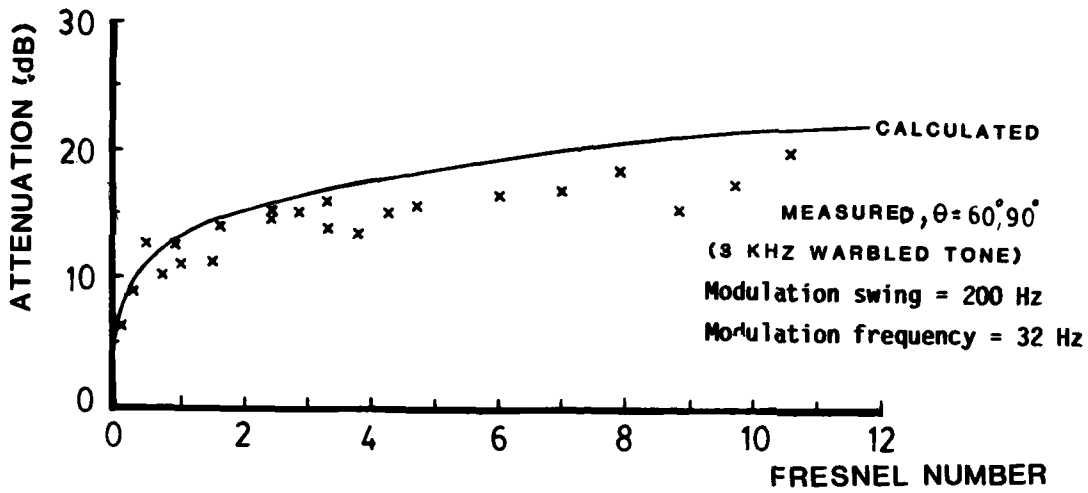
FIG. 6-8   SOUND ATTENUATION OF A SEMI-INFINITE BARRIER
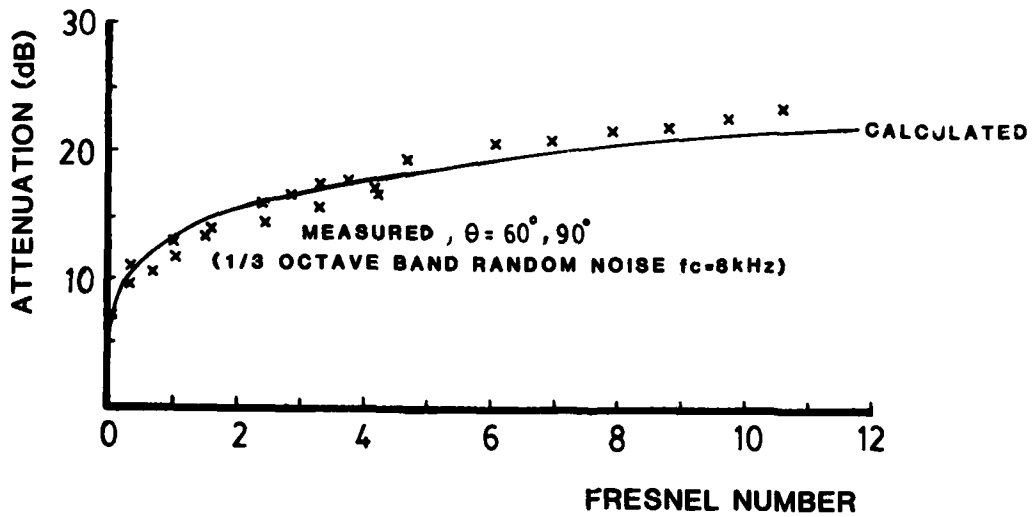
FIG. 6-9   SOUND ATTENUATION OF A SEMI-INFINITE BARRIER
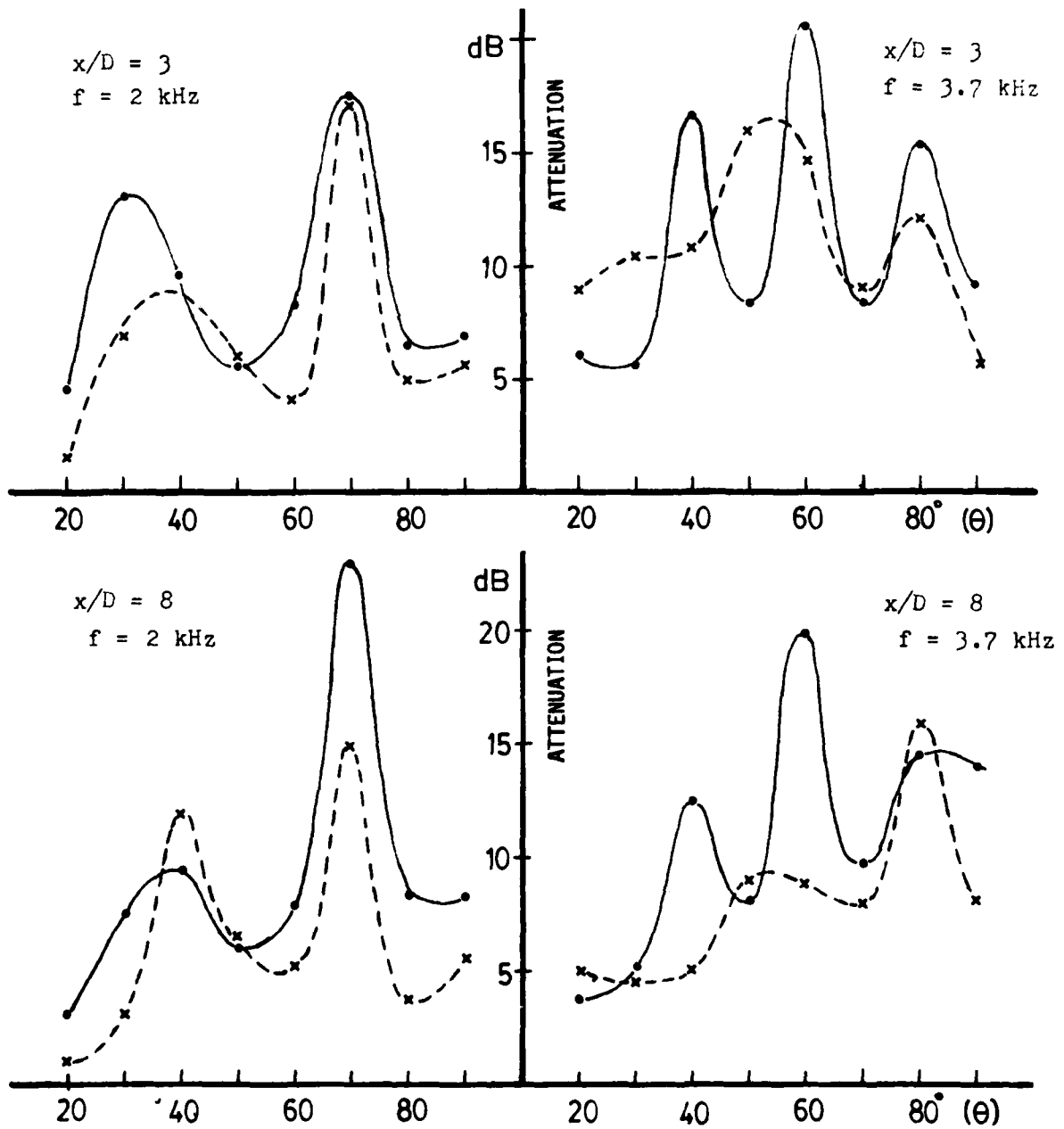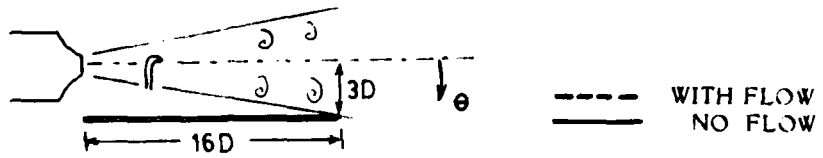
FIG. 6-10   EFFECT OF ACOUSTIC/FLOW INTERACTION
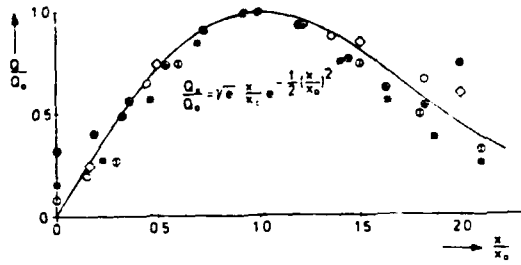
FIG. 6-11   AXIAL SOURCE INTENSITY DISTRIBUTION (Ref. 42)
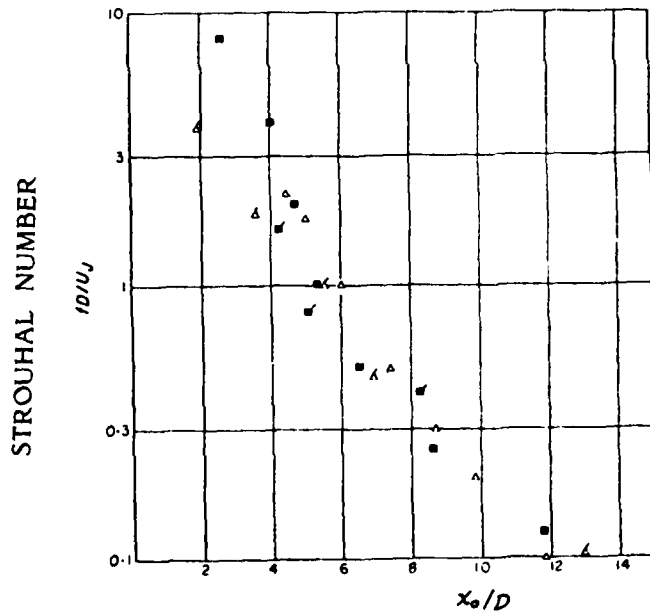
FIG. 6-12   PEAK SOURCE STRENGTH POSITION (Ref. 40)
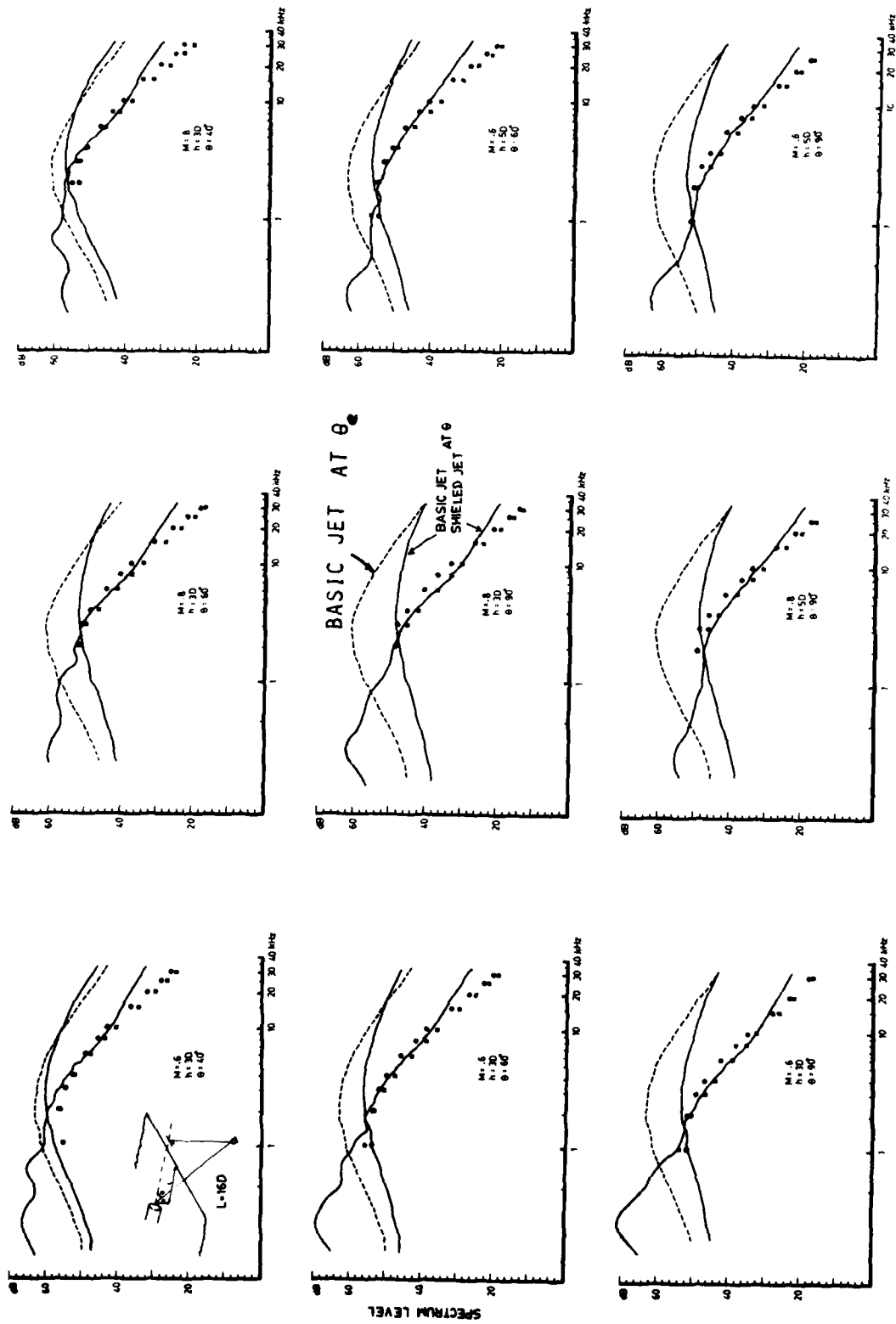
FIG. 6-13 PREDICTED JET NOISE SHIELDING FROM A POINT SOURCE MODEL. THE DASHED CURVE IS THE BASIC JET NOISE SPECTRUM MEASURED AT A DIRECTION CORRESPONDING TO THE EFFECTIVE EMISSION ANGLE OF THE JET SOURCES BEFORE DIFFRACTION. (FOR MOST CONFIGURATIONS THIS ANGLE IS OF THE ORDER OF 30°)

MEASUREMENT
PREDICTION

LOCUS OF CONSTANT
FRESNEL NUMBER

MICROPHONE
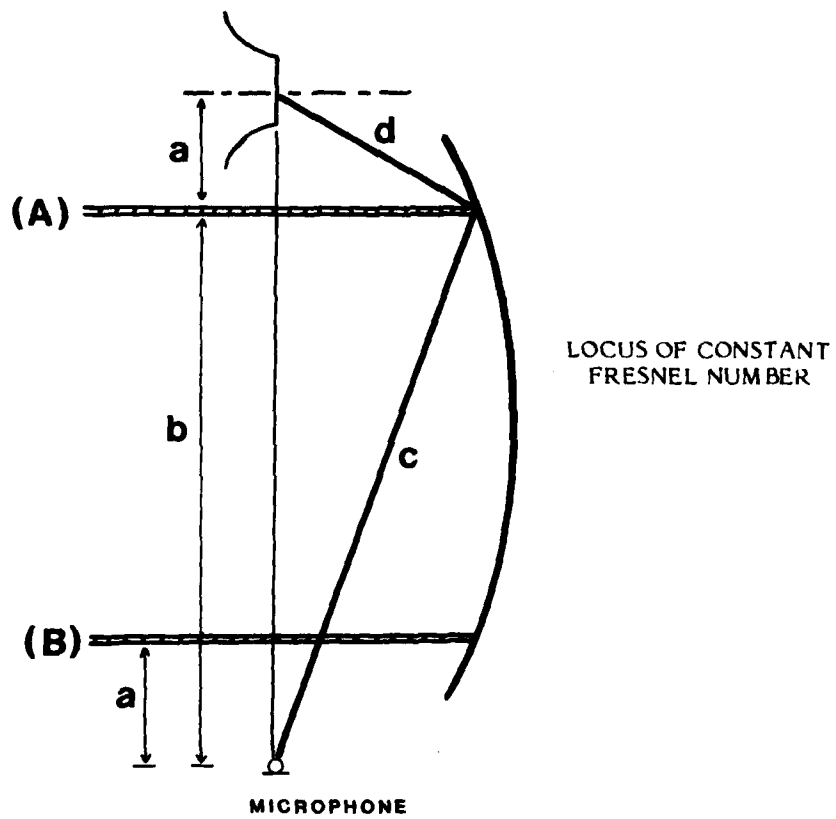
FIG. 6-14   GEOMETRIES A AND B PROVIDE SIMILAR INSERTION LOSS FOR
            POINT SOURCE. THIS IS USED AS A FIRST-CUT APPROXIMATE
            SCHEME FOR THE EXTRACTION OF INTERFERENCE EFFECT FOR
            JET NOISE SHIELDING
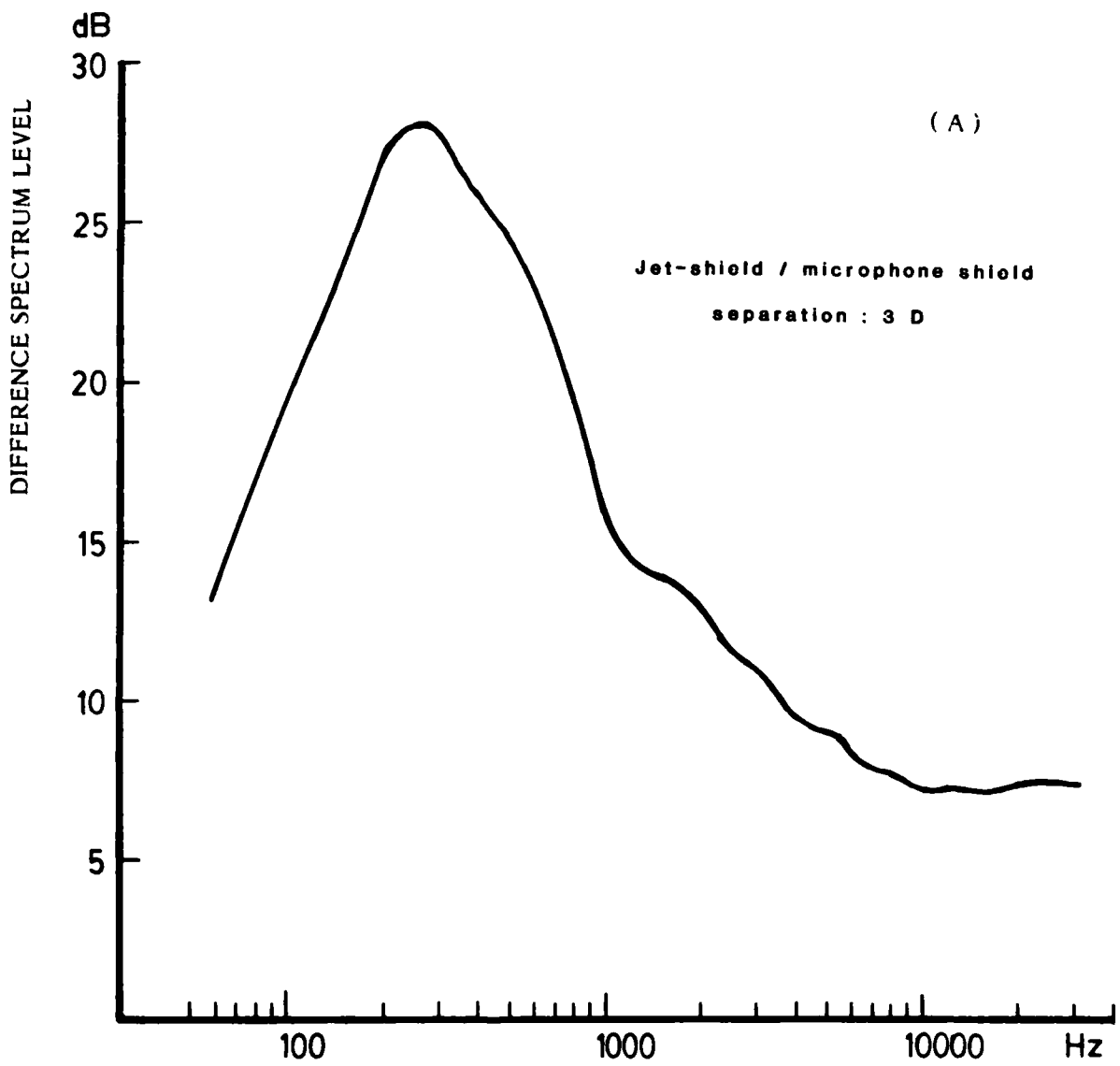
FIG. 6-15   EXTRACTION OF EDGE NOISE: DIFFERENCE IN SPECTRUM
LEVELS BETWEEN GEOMETRIES A AND B IN FIG. 6-14 IS THE
EDGE NOISE
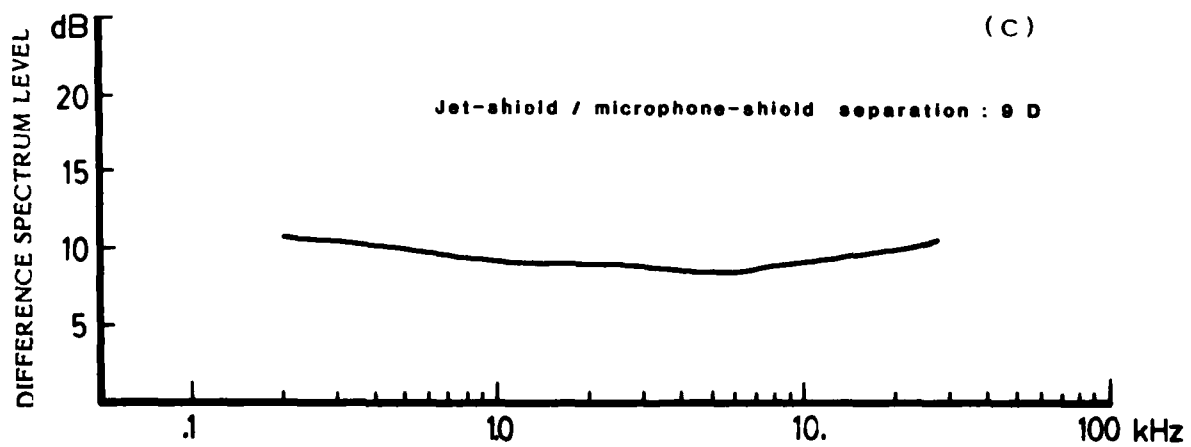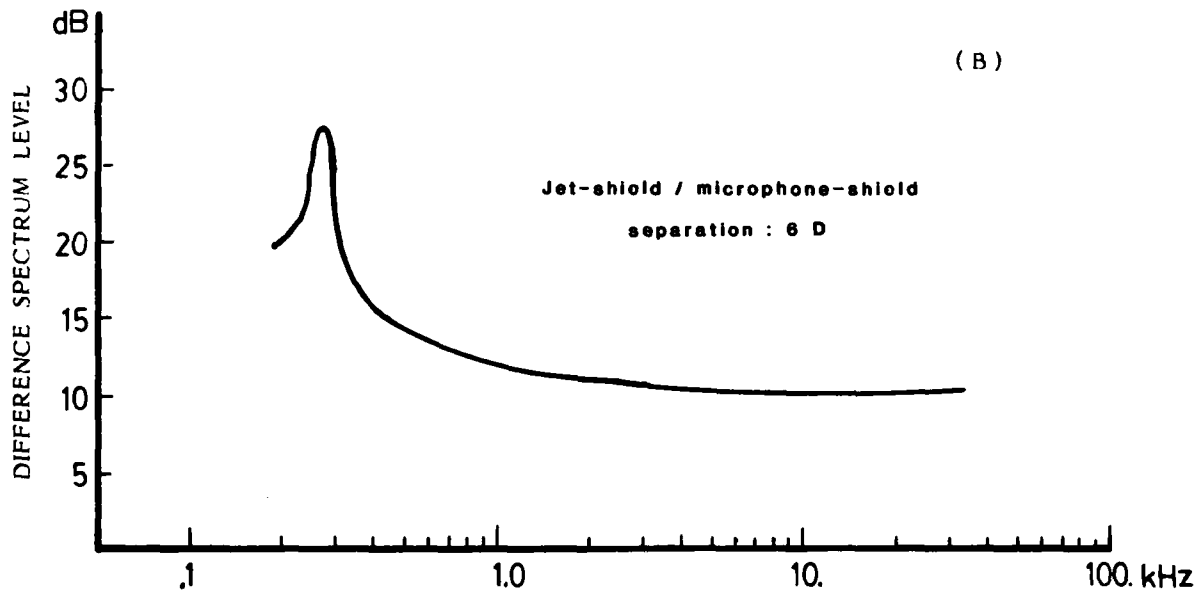
FIG. 6-15   EXTRACTION OF EDGE NOISE: DIFFERENCE IN SPECTRUM
LEVELS BETWEEN GEOMETRIES A AND B IN FIG. 6-14 IS THE
EDGE NOISE
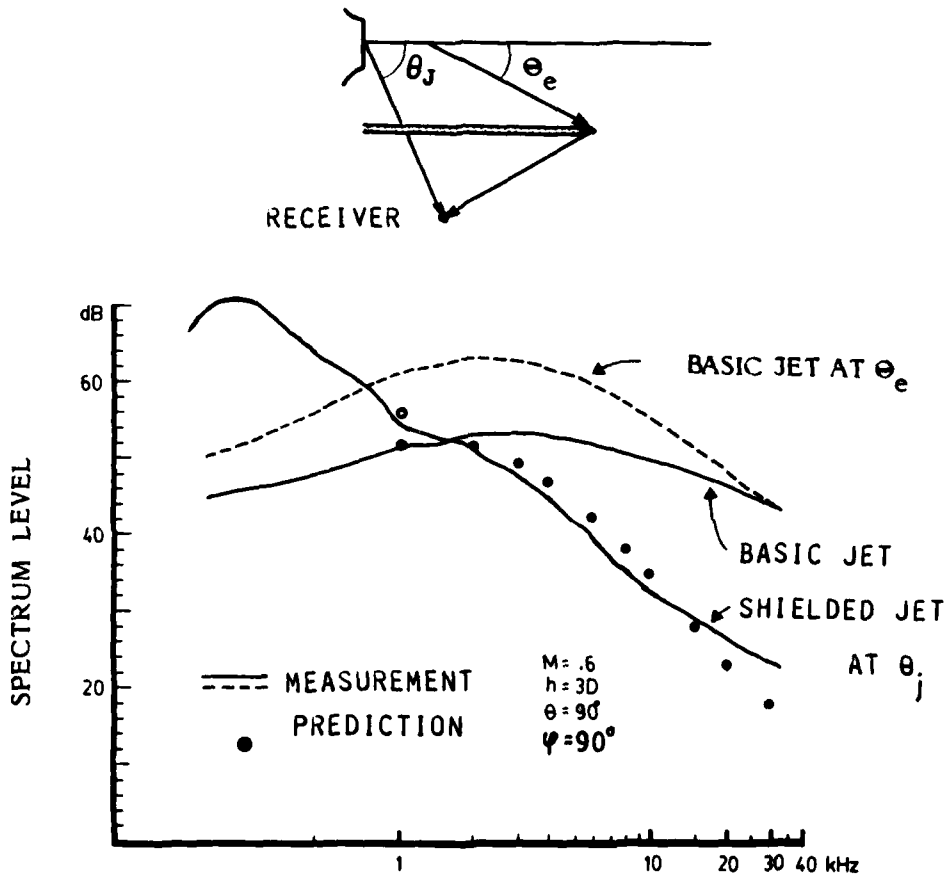
FIG. 6-16   PREDICTED JET NOISE SHIELDING FROM A POINT SOURCE
MODEL (●) (cf. FIG 6-13), OPEN CIRCLE (o) INDICATES
SHIELDED LEVEL WITH EDGE NOISE INTERFERENCE TAKEN
INTO ACCOUNT
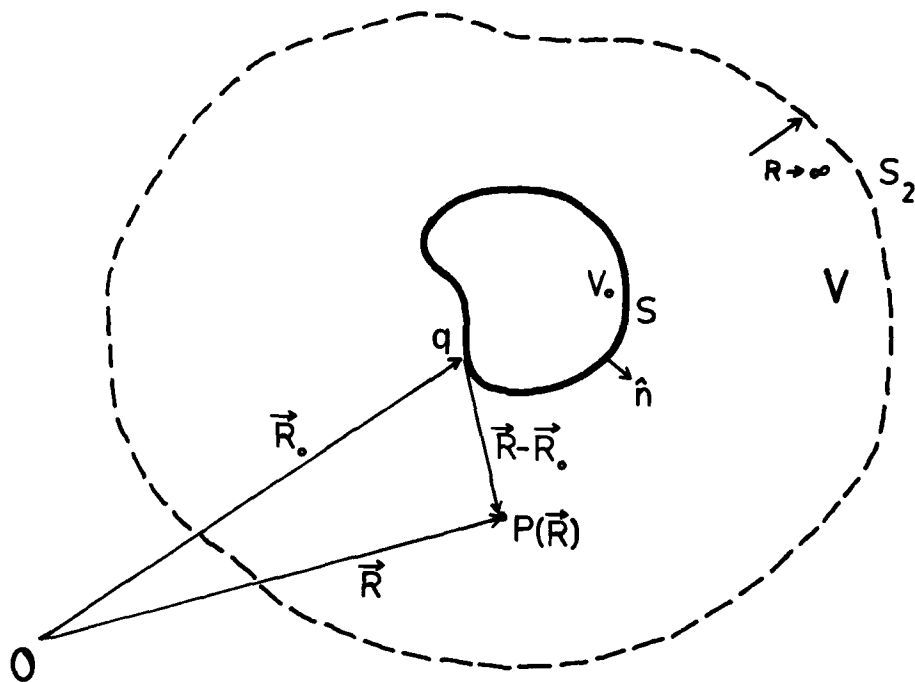
(a) Field point outside surface of integration
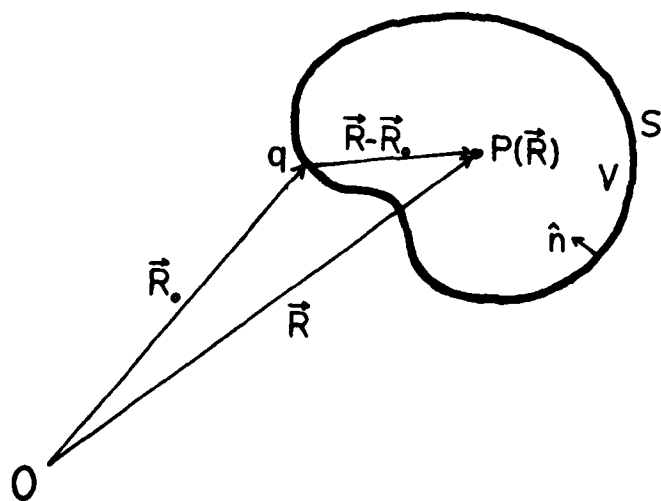
(b) Field point inside surface of integration

FIG. 7-1   POSSIBLE DIFFRACTION GEOMETRIES

Z

Receiver
(r,Θ,z)

Image
(r₀,-Θ₀,z₀)

X

Source
(r₀,Θ₀,z₀)

Y

Semi-infinite barrier

[a]

I

Y

X

r₀

Θ₀

θ

II

-Θ₀

III

r

[b]
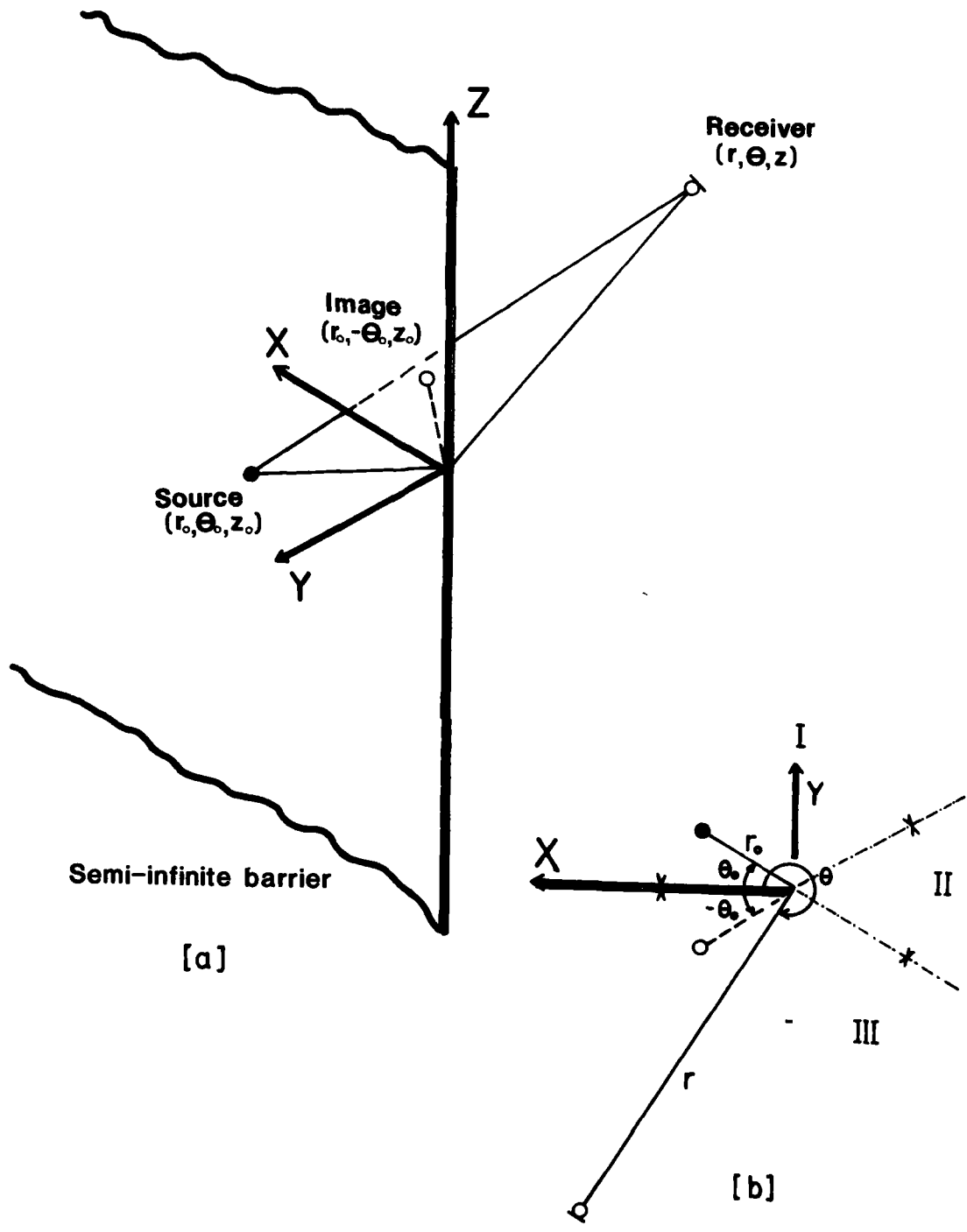
FIG. 7-2   GEOMETRY OF SEMI-INFINITE BARRIER SHIELDING
OF POINT SOURCE IN CYLINDRICAL COORDINATES

[a]

[b]

$\theta_o = 20°$, $kr_o = 190$

Exact hard

Kirchhoff soft

Kirchhoff hard

Exact soft
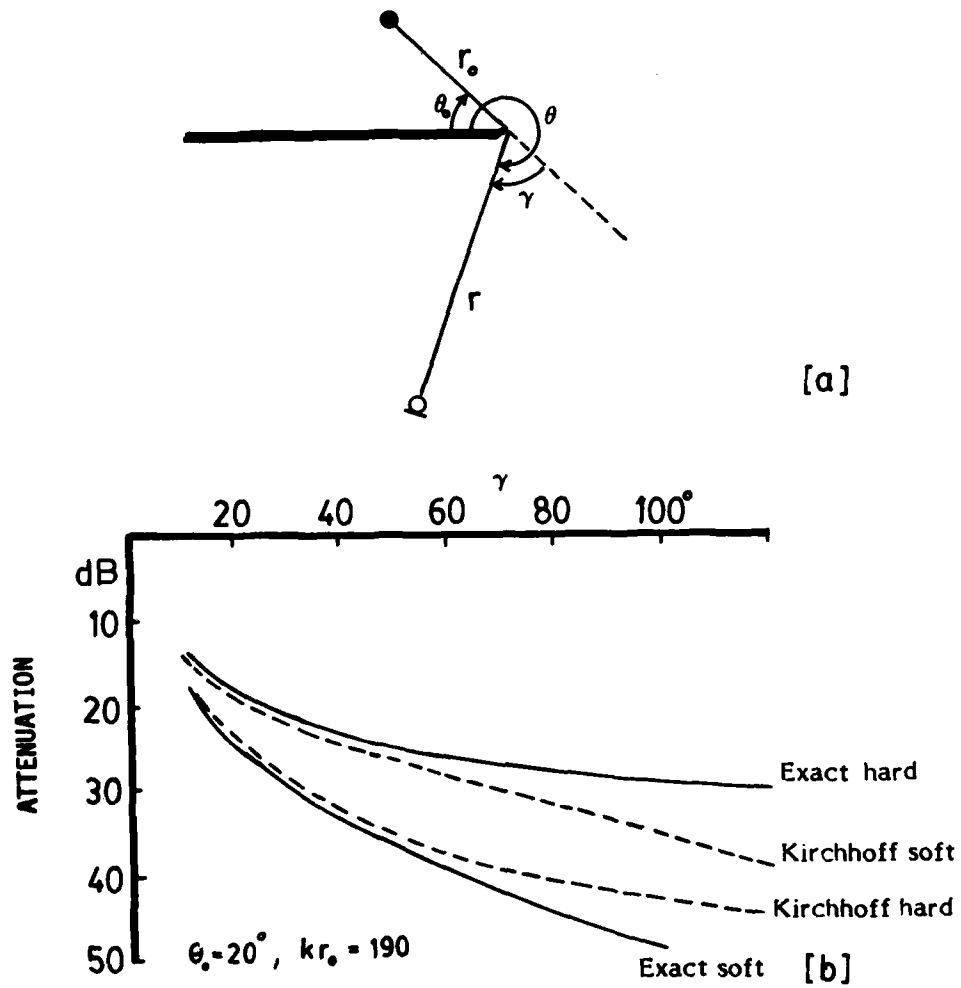
FIG. 7-3 DIFFRACTION BY A HALF-PLANE.
EXACT AND KIRCHHOFF SOLUTIONS (Ref. 55)

(A)

(B)
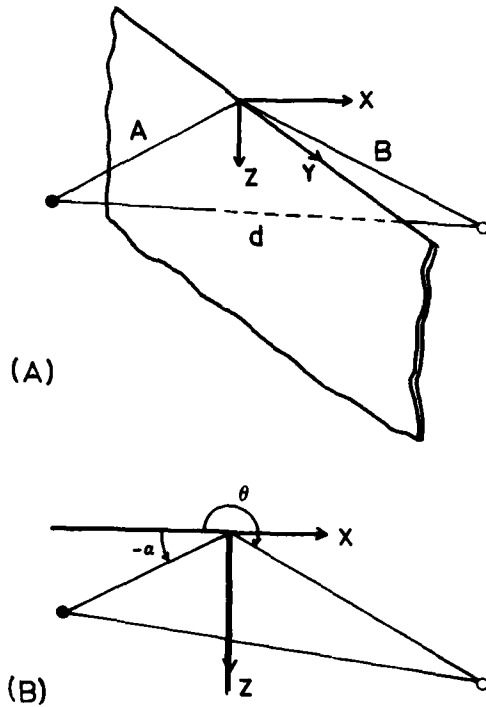
FIG. 7-4   (A) PERSPECTIVE VIEW OF A BARRIER

(B) PROJECTION ON THE X-Z PLANE   (Ref. 61)
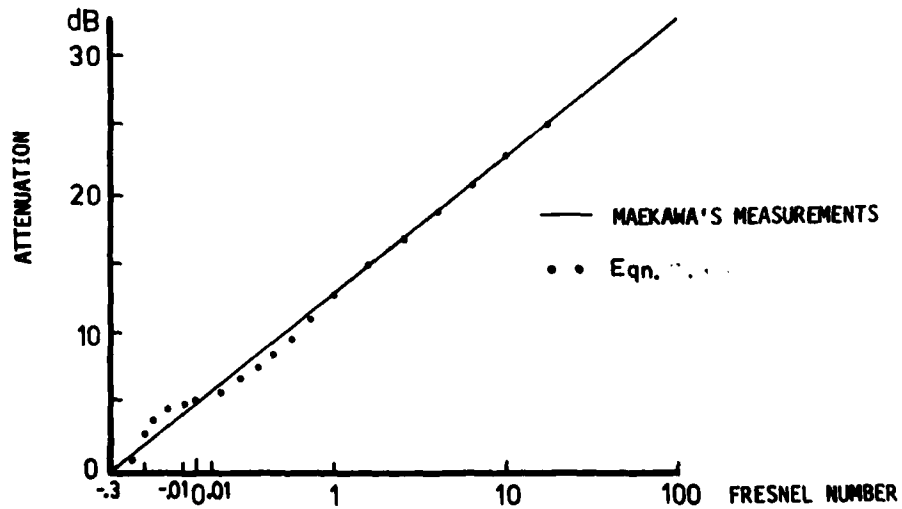
FIG. 7-5   ATTENUATION OF SOUND FROM A POINT SOURCE BY RIGID
BARRIER AS A FUNCTION OF FRESNEL NUMBER (Ref. 60)
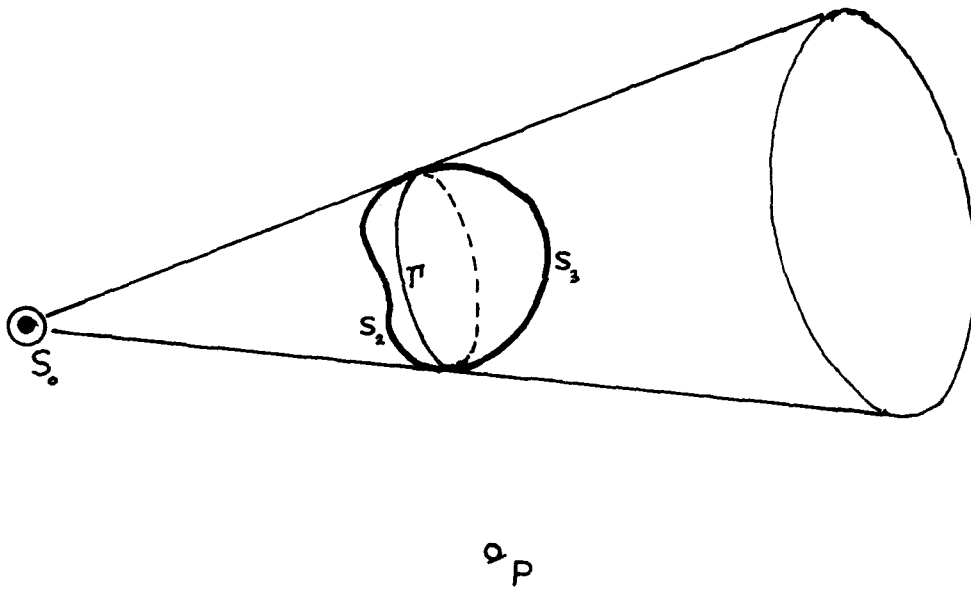
FIG. 7-6a   GEOMETRY OF THE DIFFRACTION CONTOUR IN
RUBINOWICZ'S LINE INTEGRAL
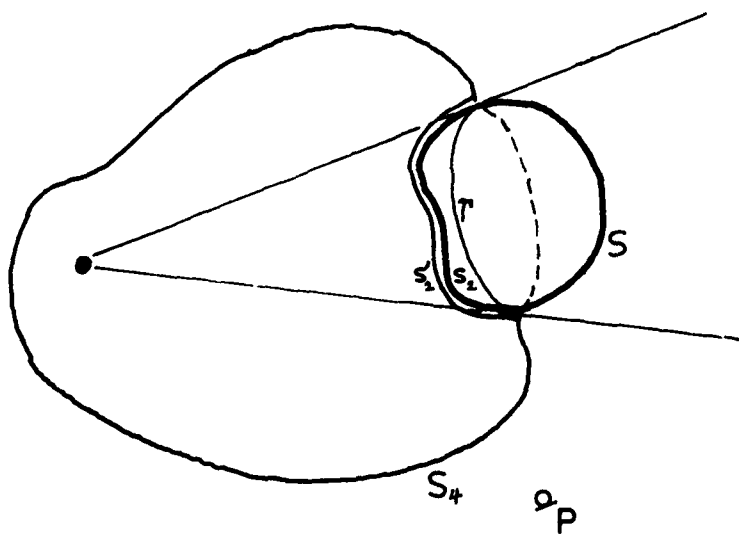
FIG. 7-6b   DEFORMATION OF THE SURFACE S_0 AS IN FIG. 7-6a
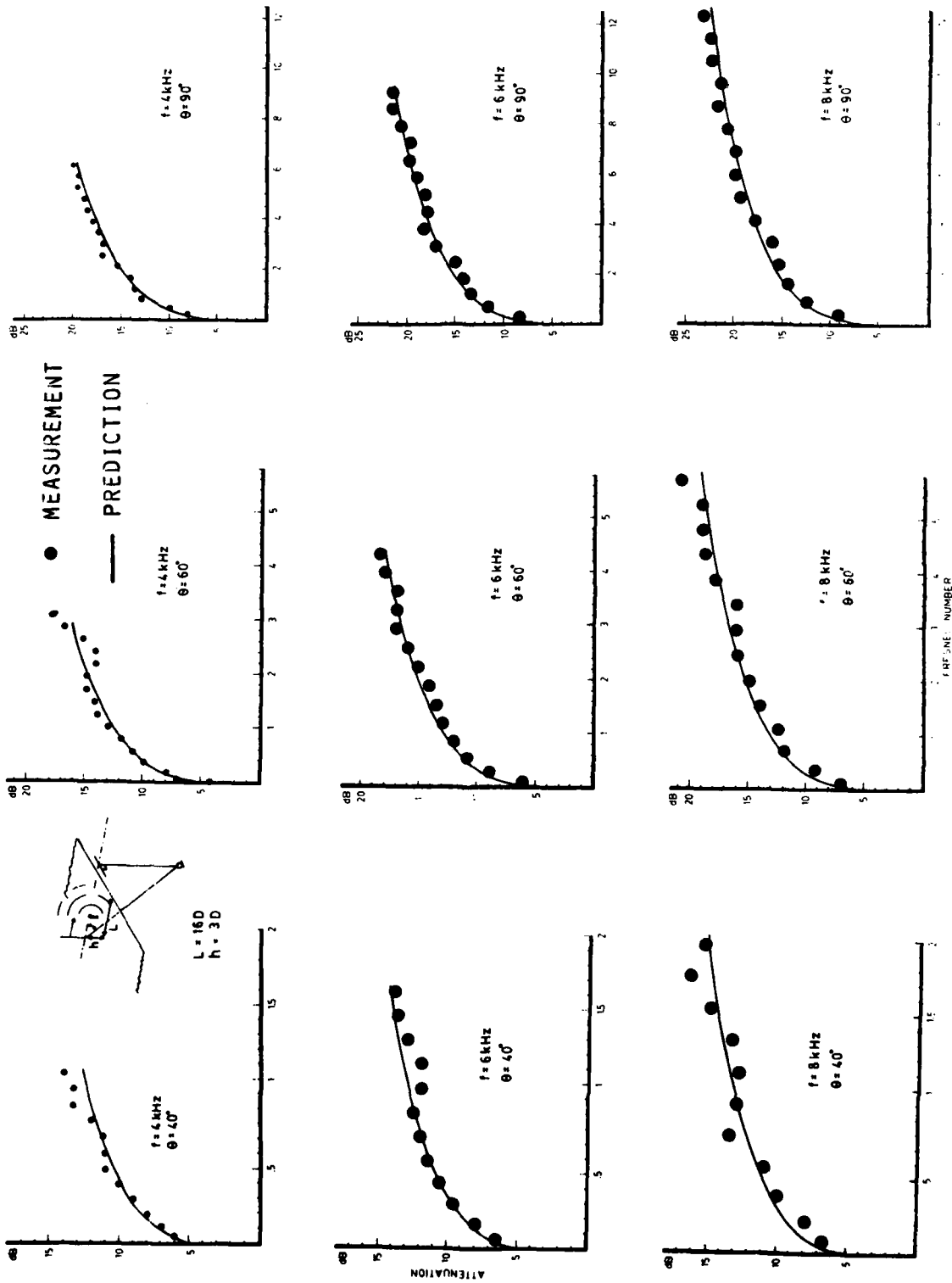
FIG. 7-7 DIFFRACTION BY A HALF PLANE.
COMPARISON BETWEEN MEASUREMENT AND THEORY (EQ. 7.2-7)

$N=0.3$ $\theta_{\circ}=11.3°$ $\theta-\theta_{\circ}=216.9°$ $kR=29.3$ $kR_1=30.2$

$kr_{\circ}=24.9$ 244   22.7   19.5   16.1   11.4

kR_1 z

$z_{\circ}$

$kr=5.7$ 5.4   5.8   6.7   8.1   11.4

$z-z_{\circ}=0$
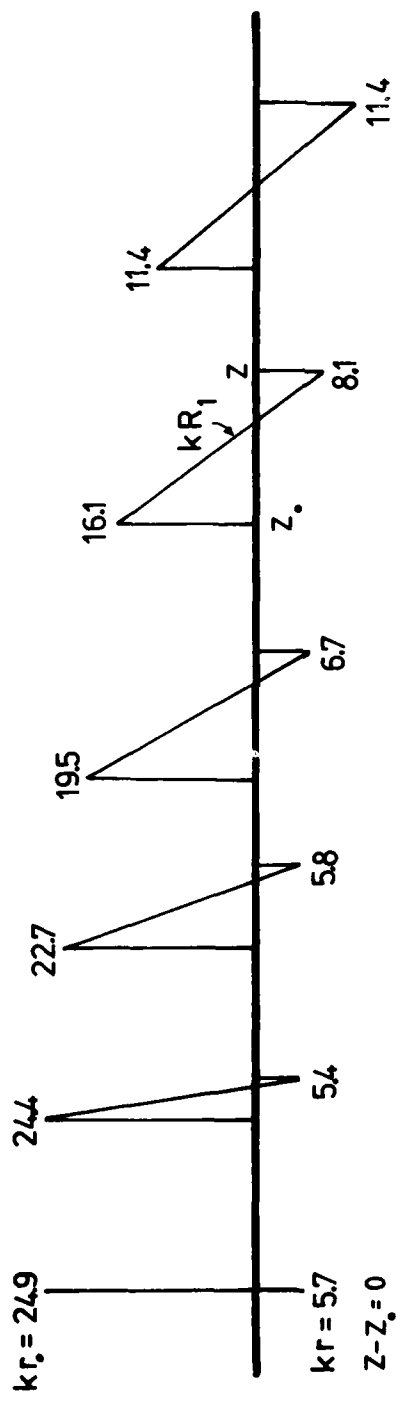
FIG. 7-8

COMBINATIONS OF SOURCE-RECEIVER POSITIONS FOR IDENTICAL ATTENUATION PROVIDED BY SEMI-INFINITE BARRIER (i.e. ALL INDEPENDENT PARAMETERS OF EQ. (7.2-7) ARE KEPT CONSTANT IN EACH CASE)
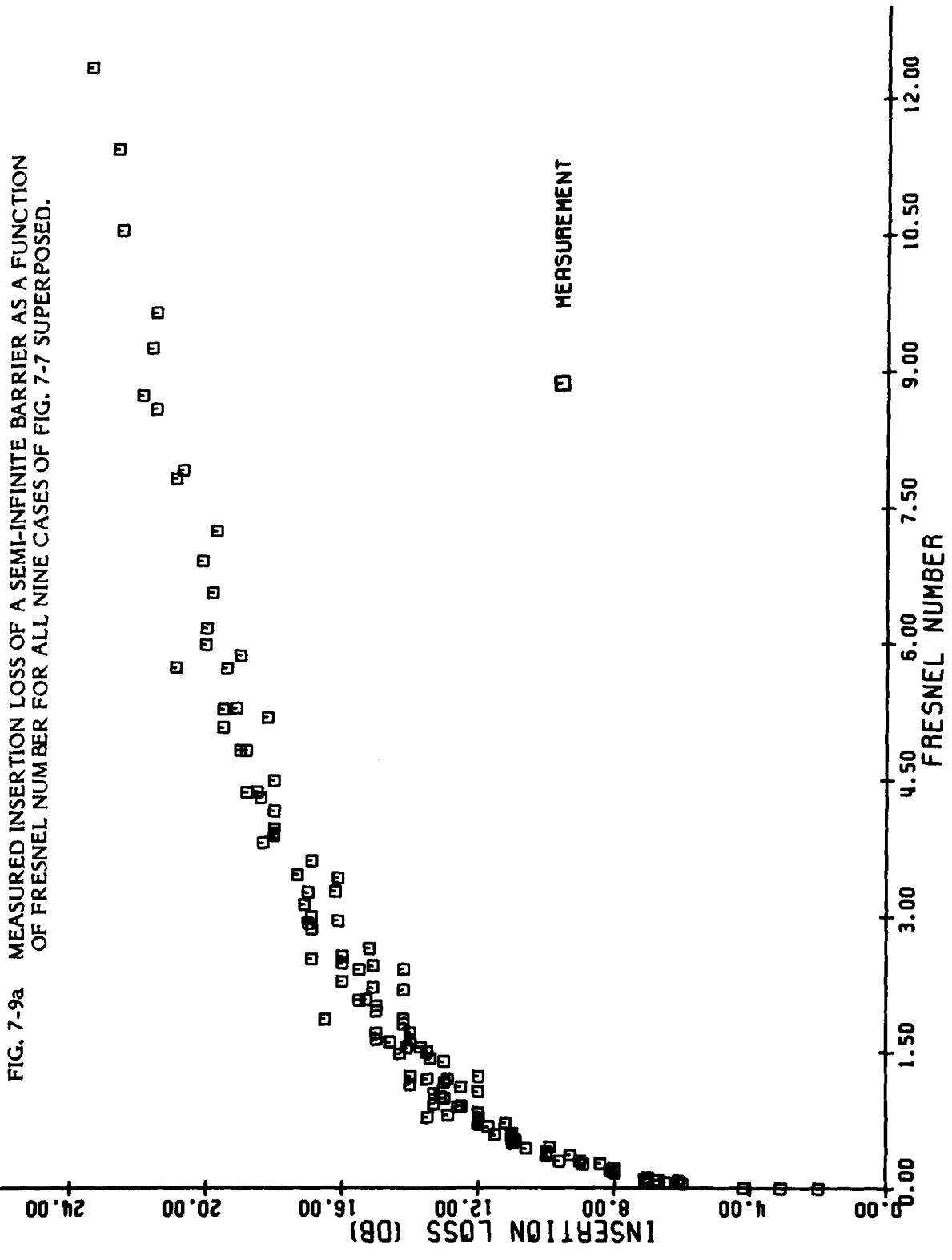
FIG. 7-9a   MEASURED INSERTION LOSS OF A SEMI-INFINITE BARRIER AS A FUNCTION
OF FRESNEL NUMBER FOR ALL NINE CASES OF FIG. 7-7 SUPERPOSED.

FIG. 7-9b   CALCULATED THEORETICAL ATTENUATION (EQ. 7.2-7) vs FRESNEL
NUMBER FOR ALL NINE CASES OF FIG. 7-7 SUPERPOSED. SCATTER
BAND ARISES FROM UNCONTROLLED VARIATION OF THE WEAK PARAMETERS.
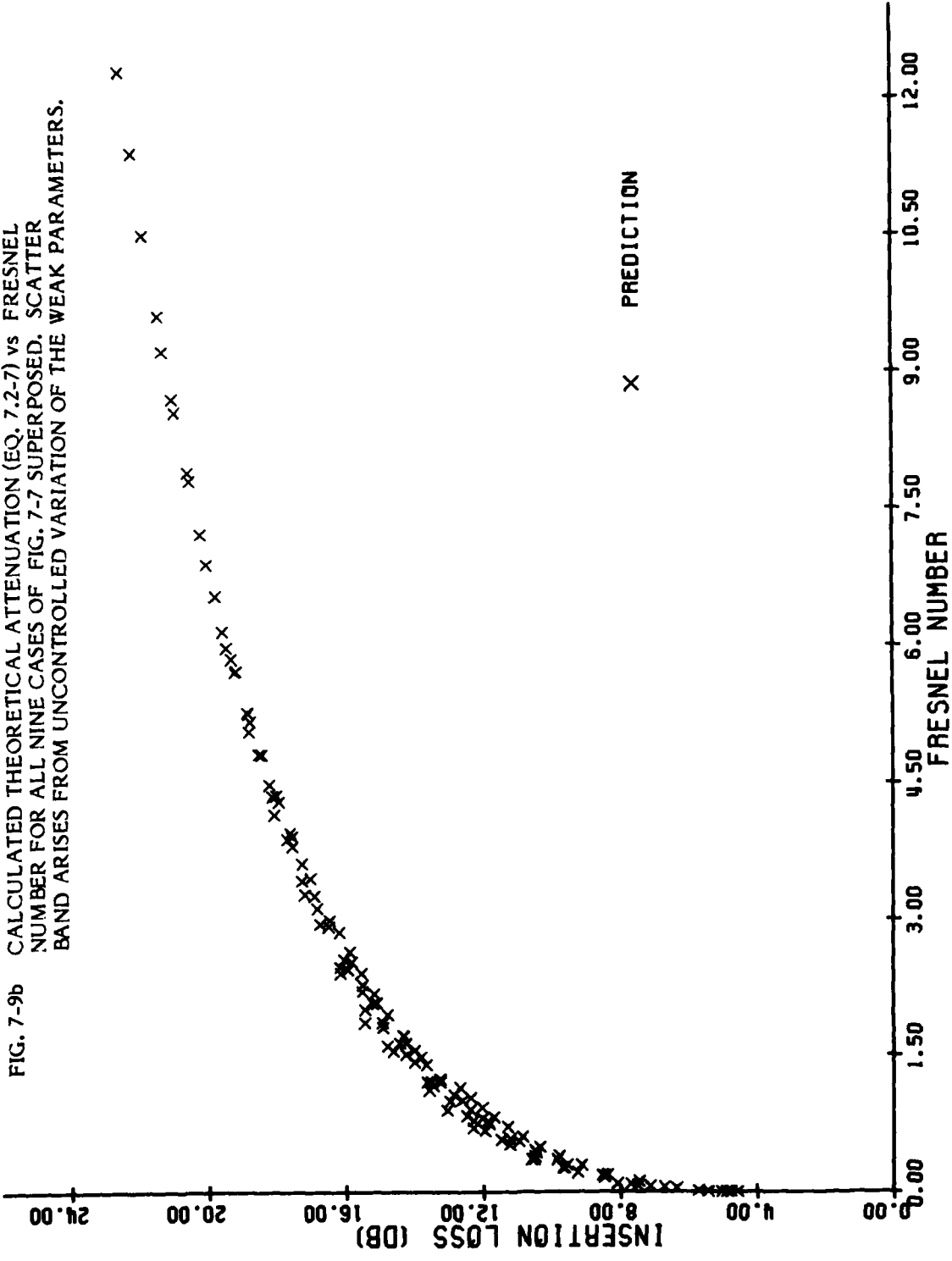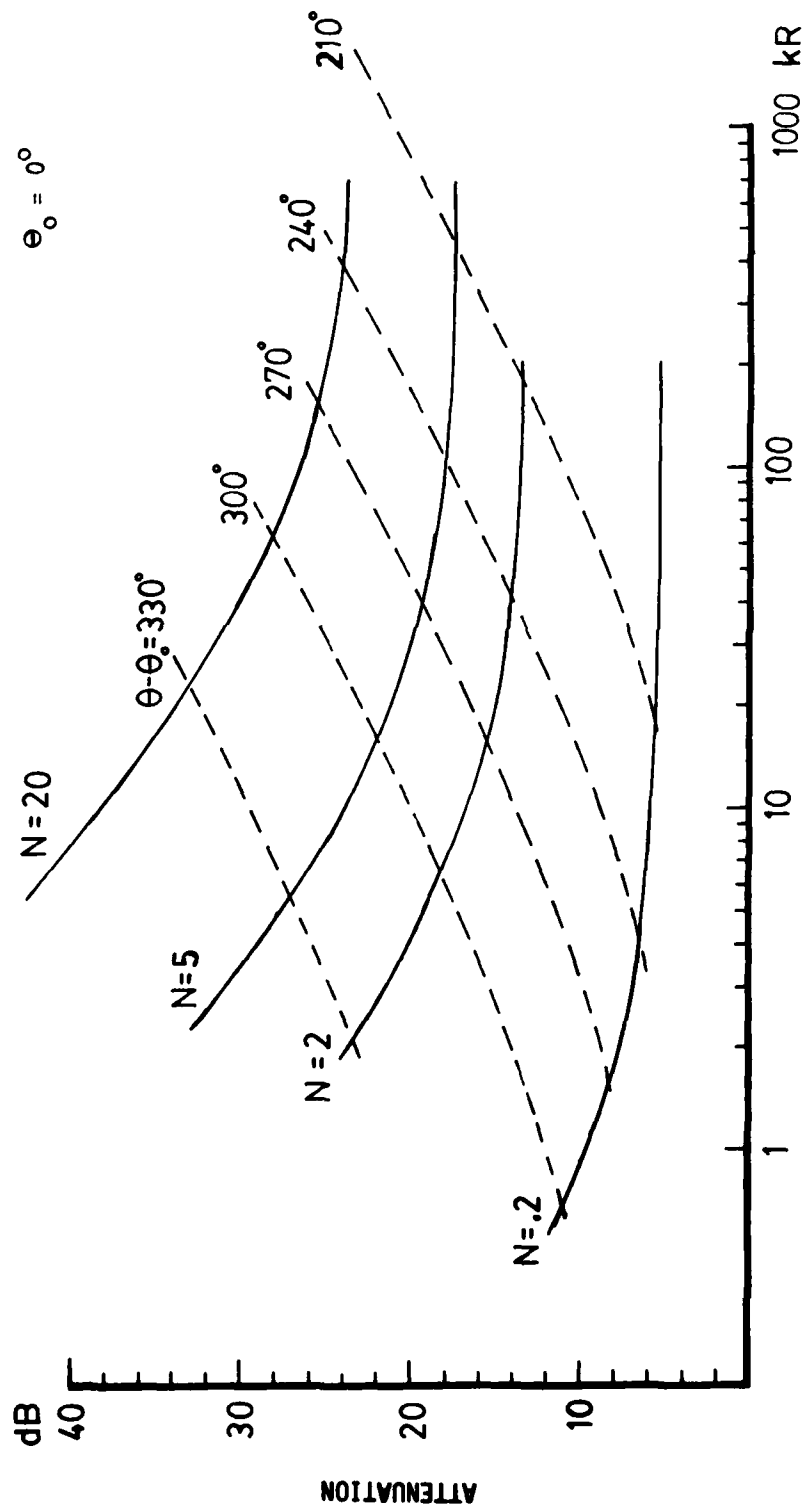
FIG. 7-10   PLOTS OF ATTENUATION vs. kR AS FUNCTION OF FRESNEL NUMBER FOR SEMI-INFINITE HALF PLANE

FIG. 7-11   COMPARISON OF EXPERIMENTAL SHIELDING OF POINT SOURCE WITH
THEORETICAL SHIELDING (EQ. 7.2-7) FOR SEMI-INFINITE BARRIER
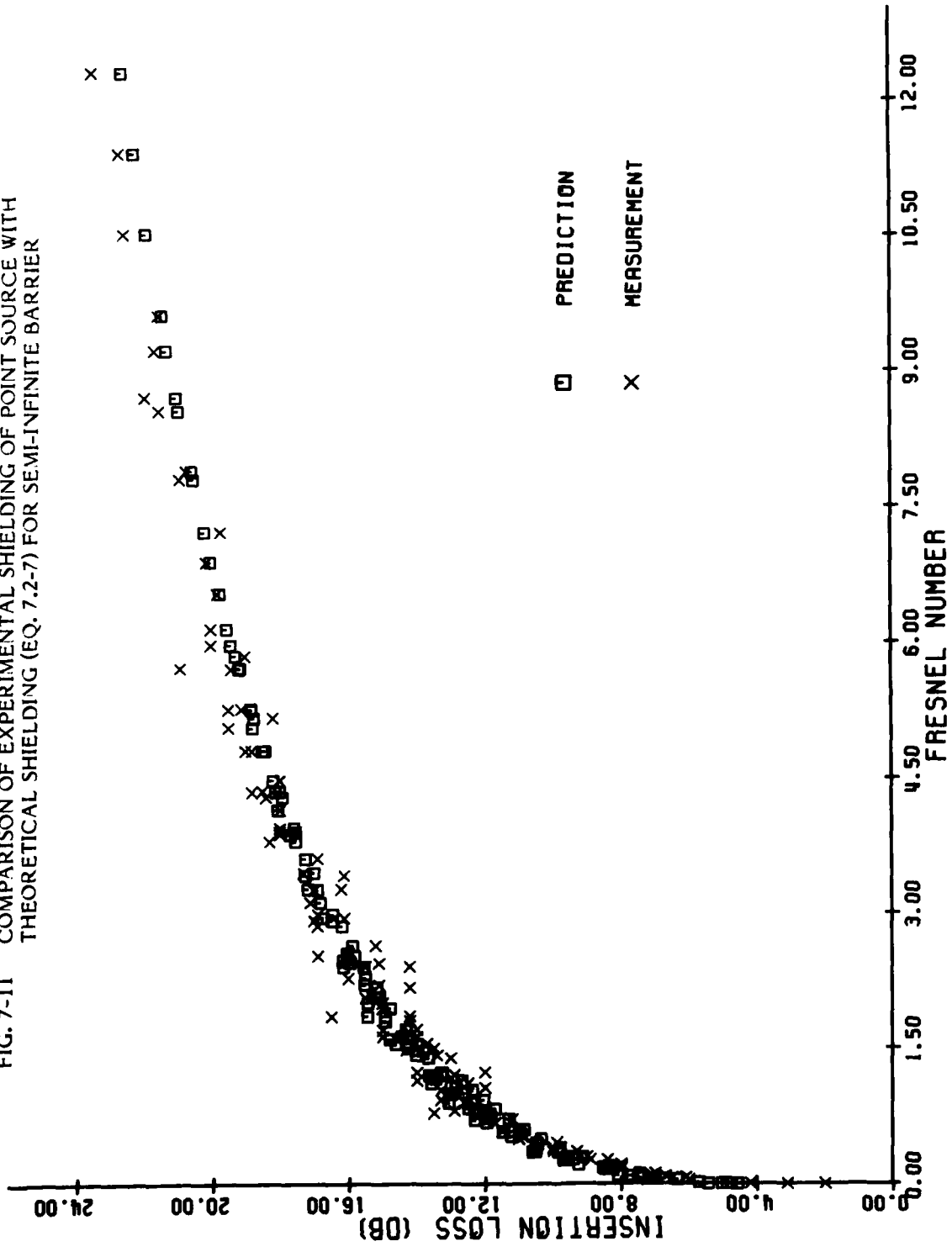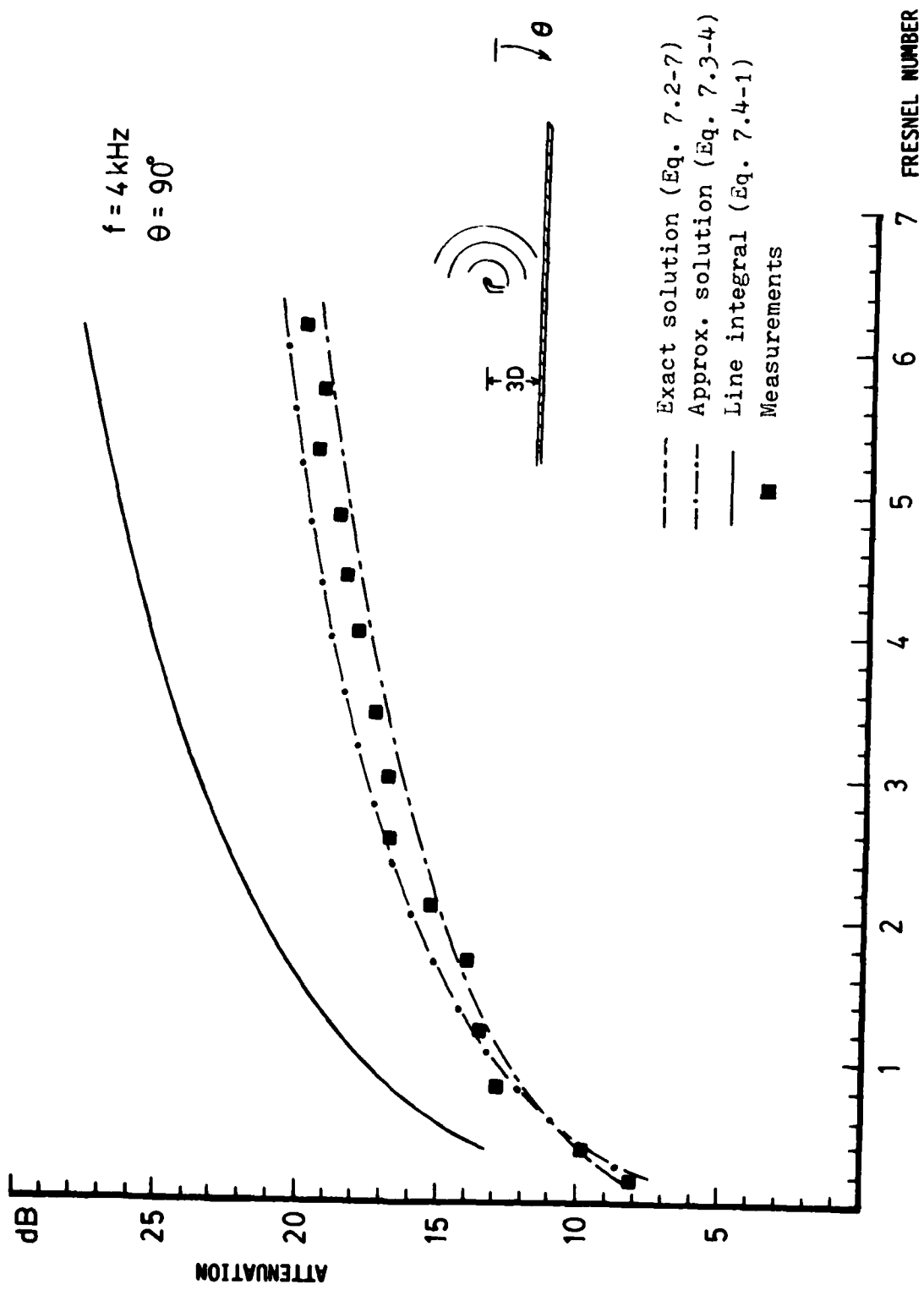
FIG. 7-12a COMPARISON OF POINT SOURCE SHIELDING MEASUREMENTS WITH VARIOUS PREDICTIONS
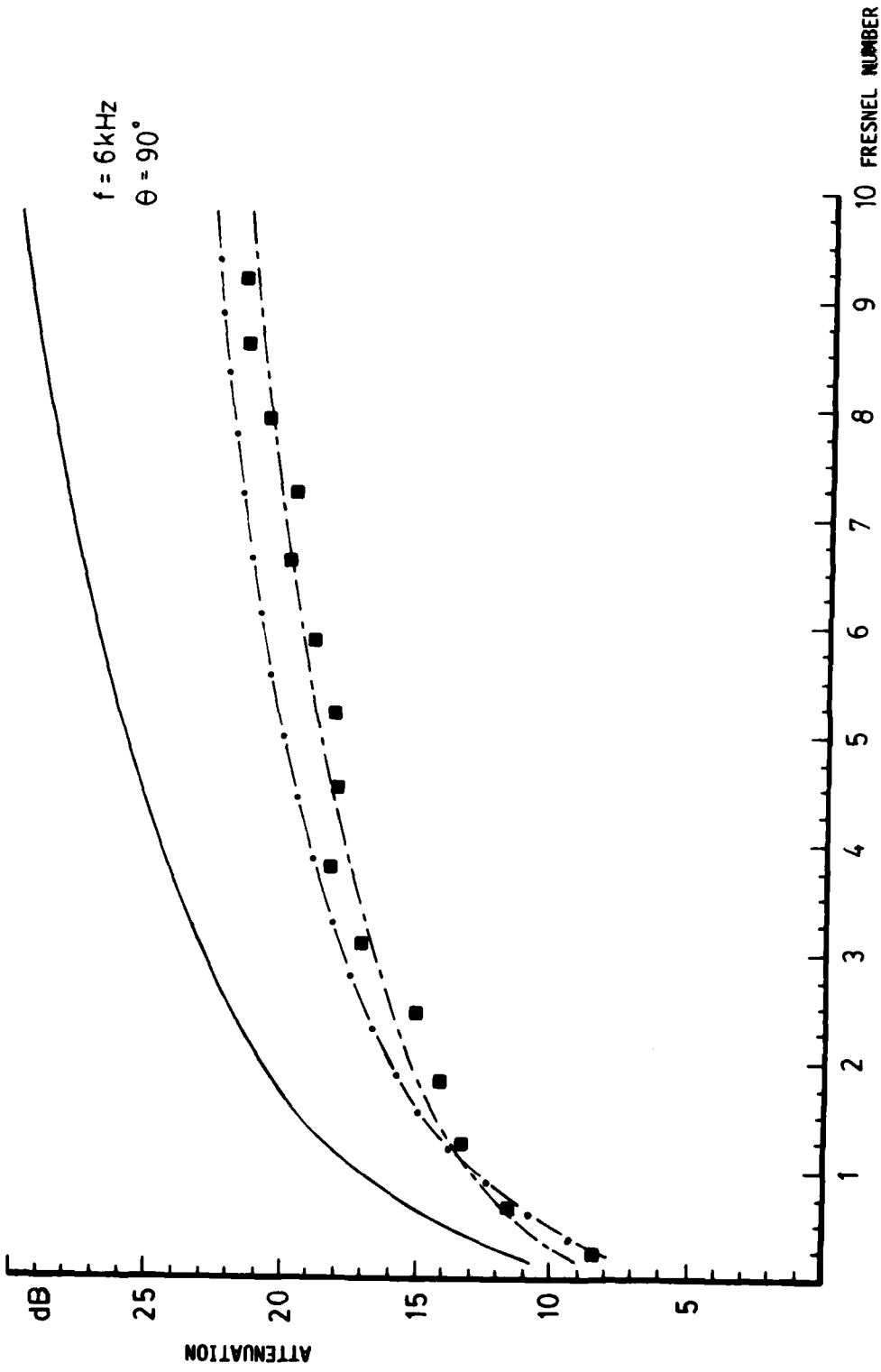
FIG. 7-12b COMPARISON OF POINT SOURCE SHIELDING MEASUREMENTS WITH VARIOUS PREDICTIONS
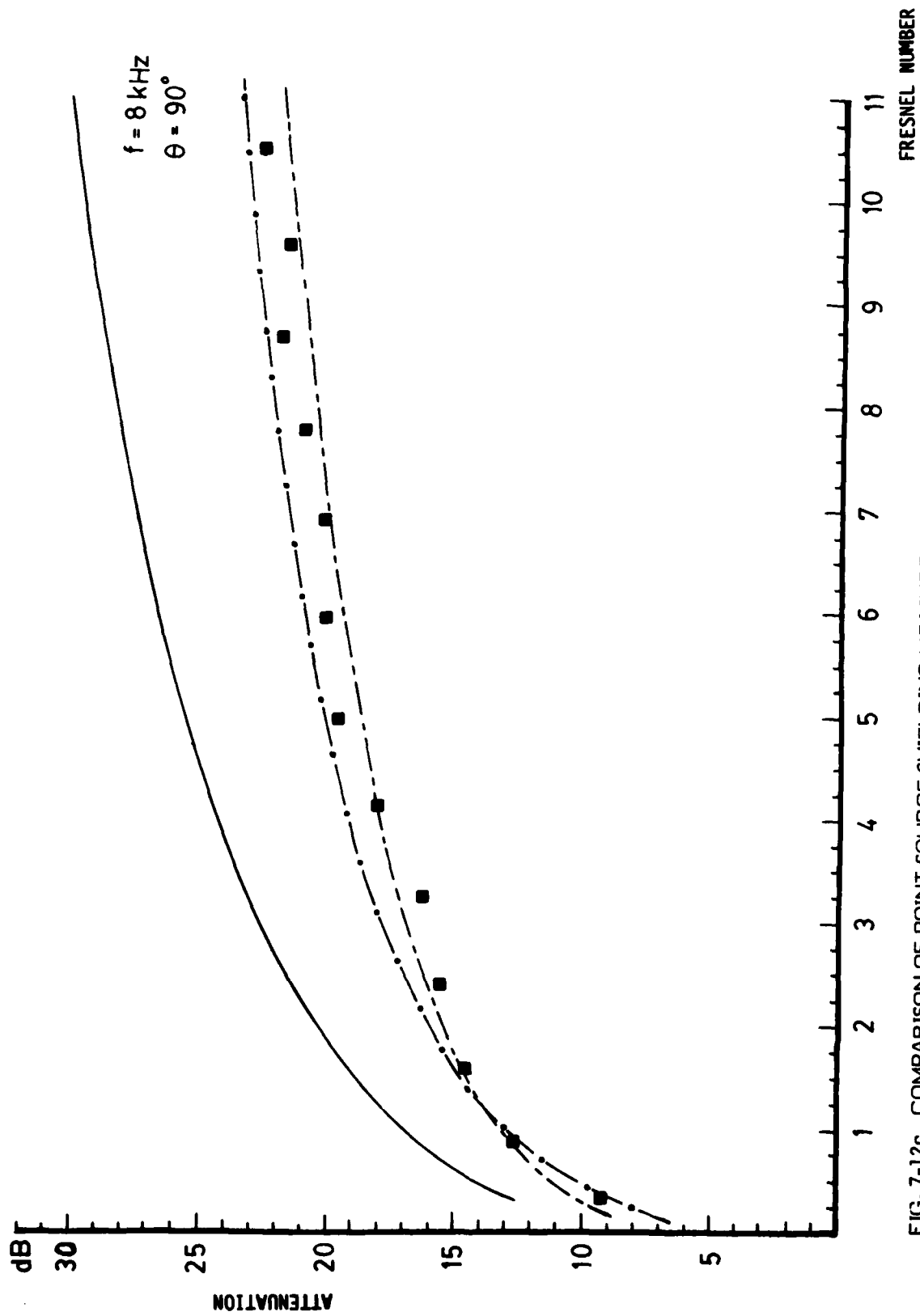
FIG. 7-12c COMPARISON OF POINT SOURCE SHIELDING MEASUREMENTS WITH VARIOUS PREDICTIONS
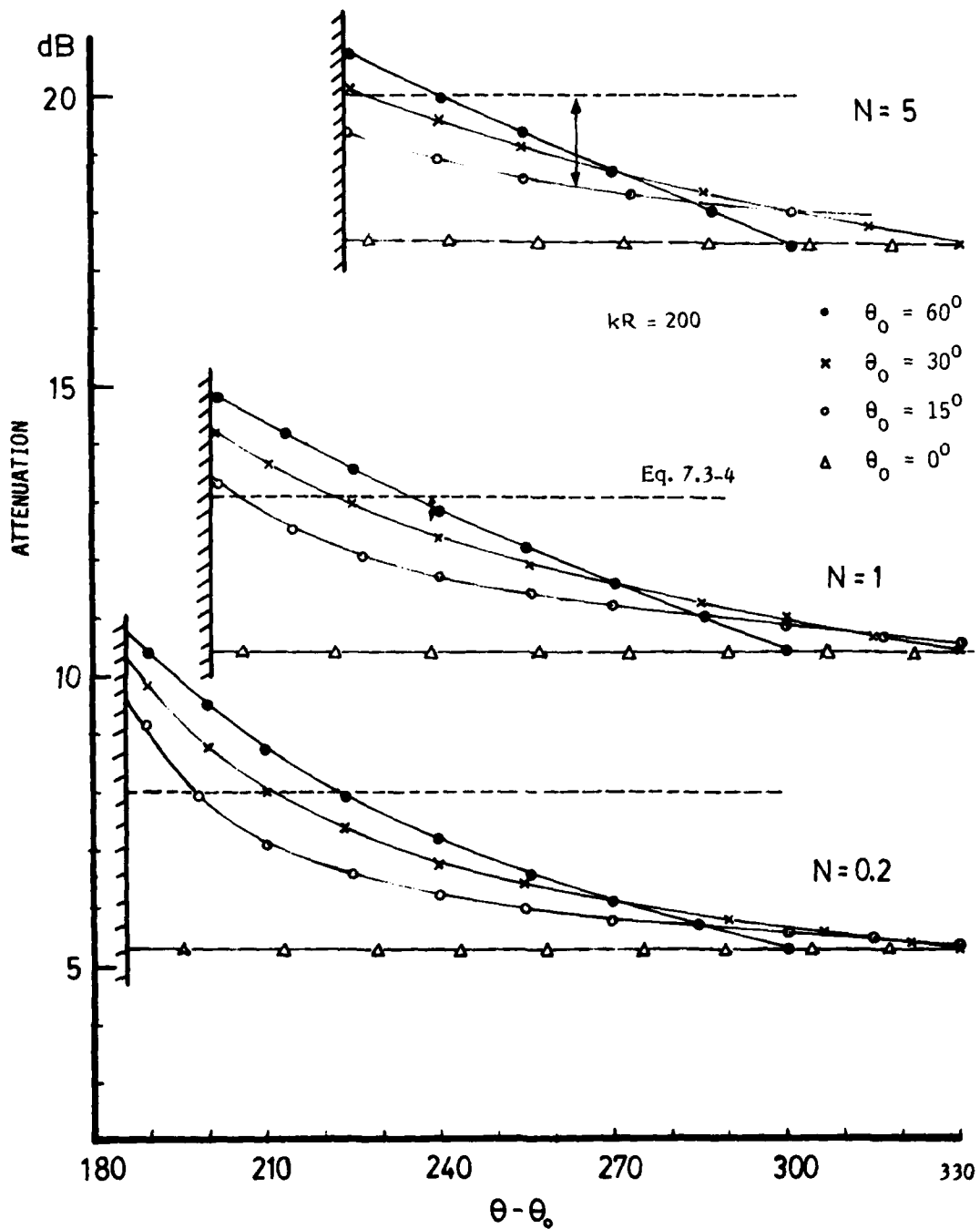
FIG. 7-13   PLOTS OF ATTENUATION (CALCULATED BY EXACT SOLUTION, EQ. 7.2-7) vs. DIFFRACTION ANGLE FOR DIFFERENT VALUES OF FRESNEL NUMBER N AND SOURCE ANGLE θ_0 IN REFERENCE TO THE BARRIER PLANE. DASHED LINES SHOW APPROXIMATE SOLUTION BY EQ. (7.3-4).
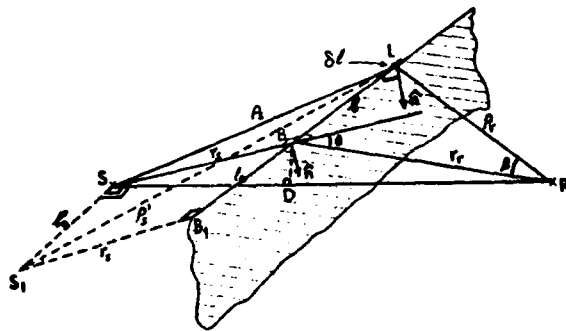
FIG. 7-14   SCHEMATIC DIAGRAM SHOWING COORDINATE SYSTEM
AND PARAMETERS USED IN EQ. 7.5-2   (Ref. 62)
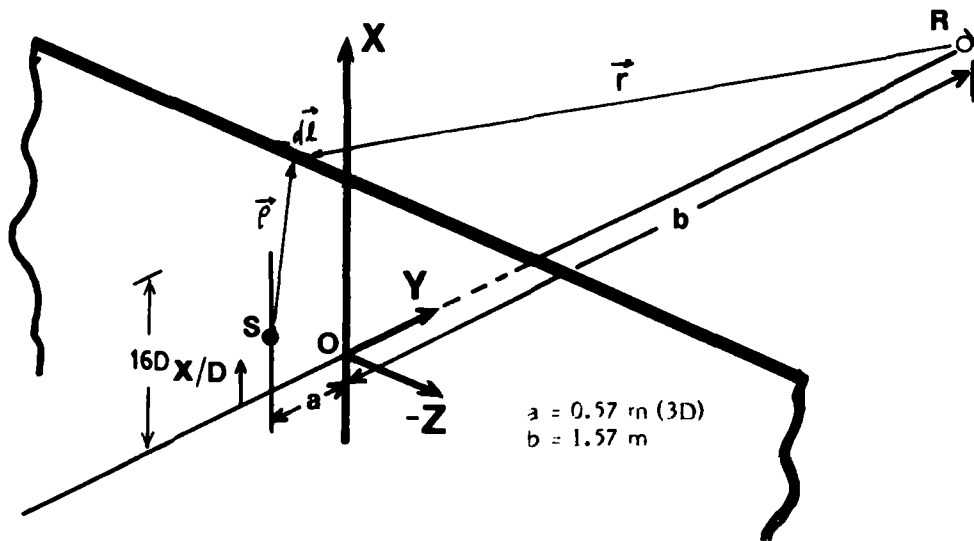
FIG. 7-15a GEOMETRY FOR COMPUTATION OF THE DIFFRACTED WAVE
BY LINE INTEGRAL ALONG BARRIER EDGE
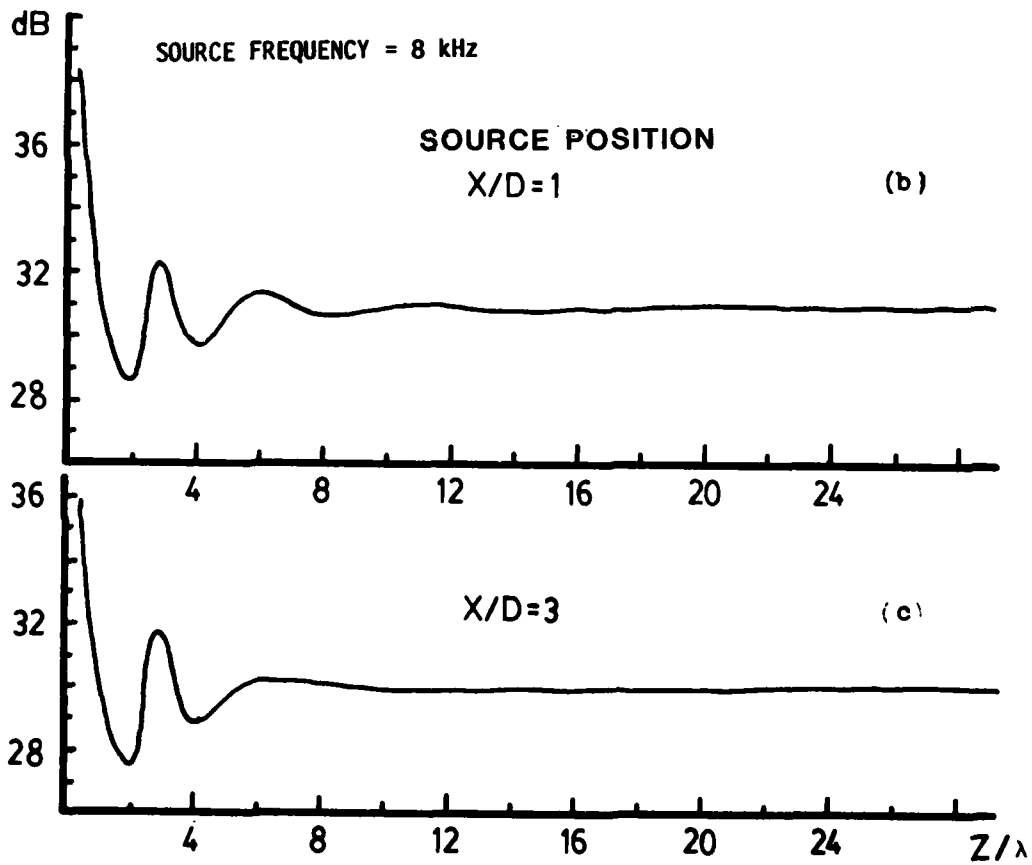
FIG. 7-15 b, c   VALUE OF DIFFRACTED POTENTIAL RE FREE FIELD AS FUNCTION
OF INTEGRATING DISTANCE ALONG THE BARRIER EDGE
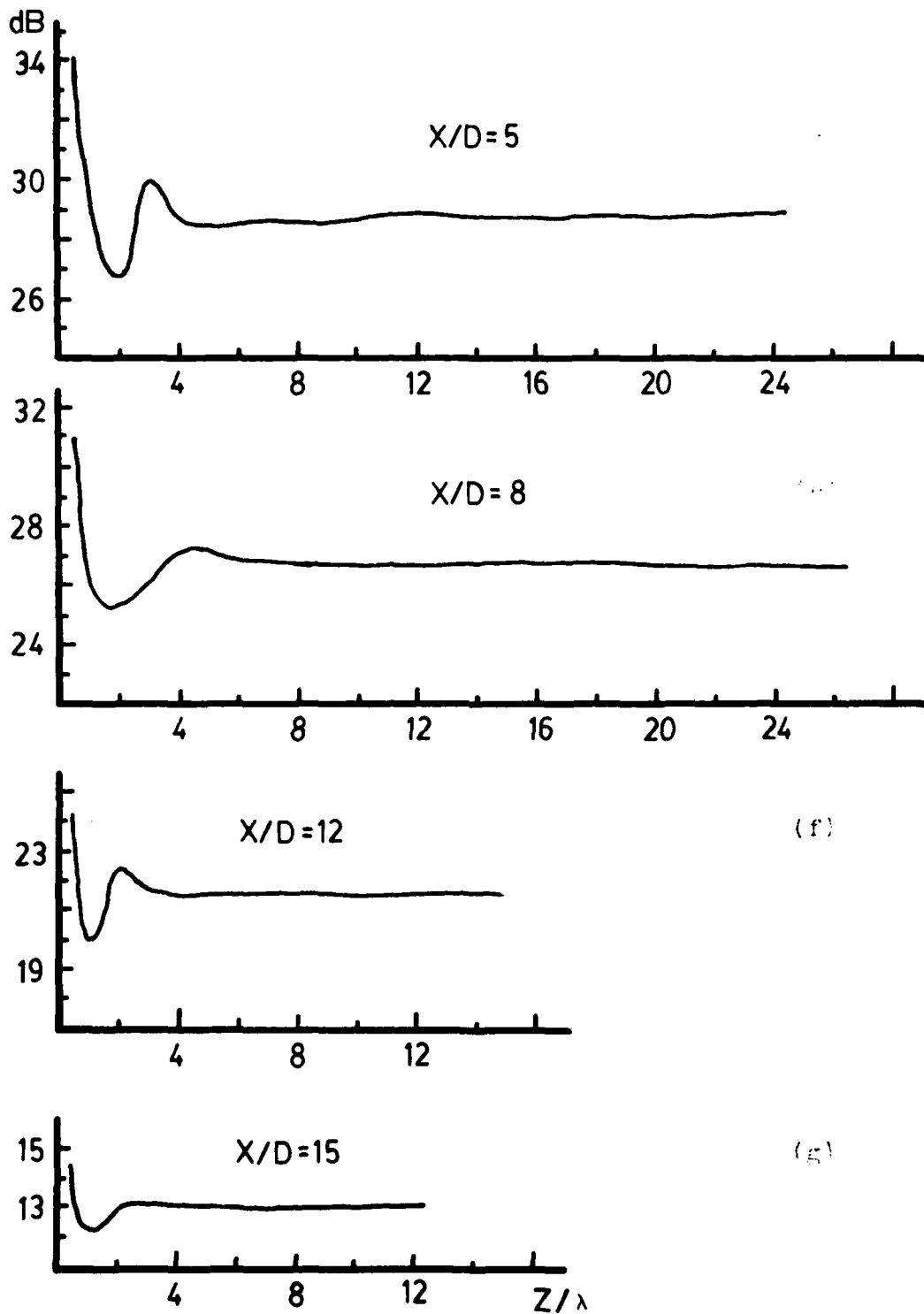
FIG. 7-15 d, e, f, g   VALUE OF DIFFRACTED POTENTIAL RE FREE FIELD AS FUNCTION
OF INTEGRATING DISTANCE ALONG THE BARRIER EDGE

a = 0.57 m (3D)
b = 1.57 m

COSINE CUTOUT $\frac{X}{D} = [12 - 4 \cos \pi z / z_m]$
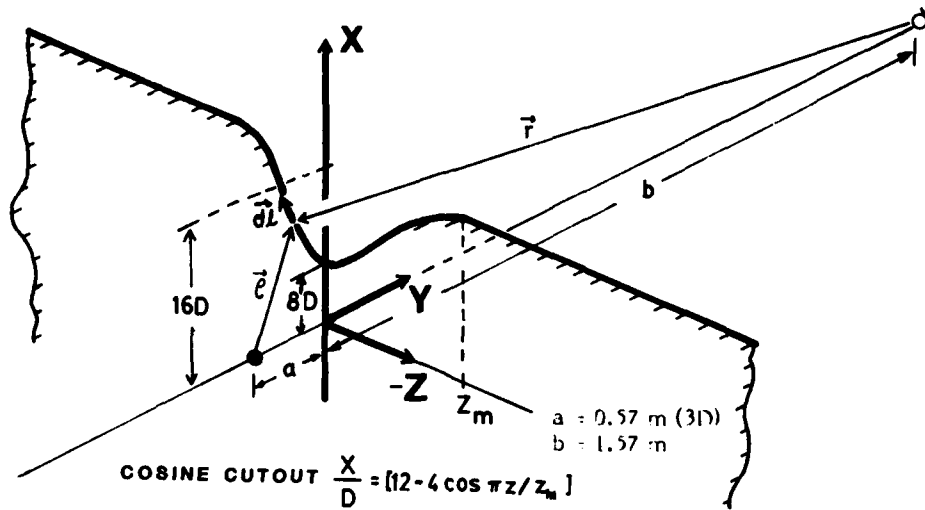
FIG. 7-16   GEOMETRY FOR DIFFRACTION BY CUTOUT CONFIGURATION

SOURCE FREQUENCY = 8 kHz

8 D HIGH BARRIER
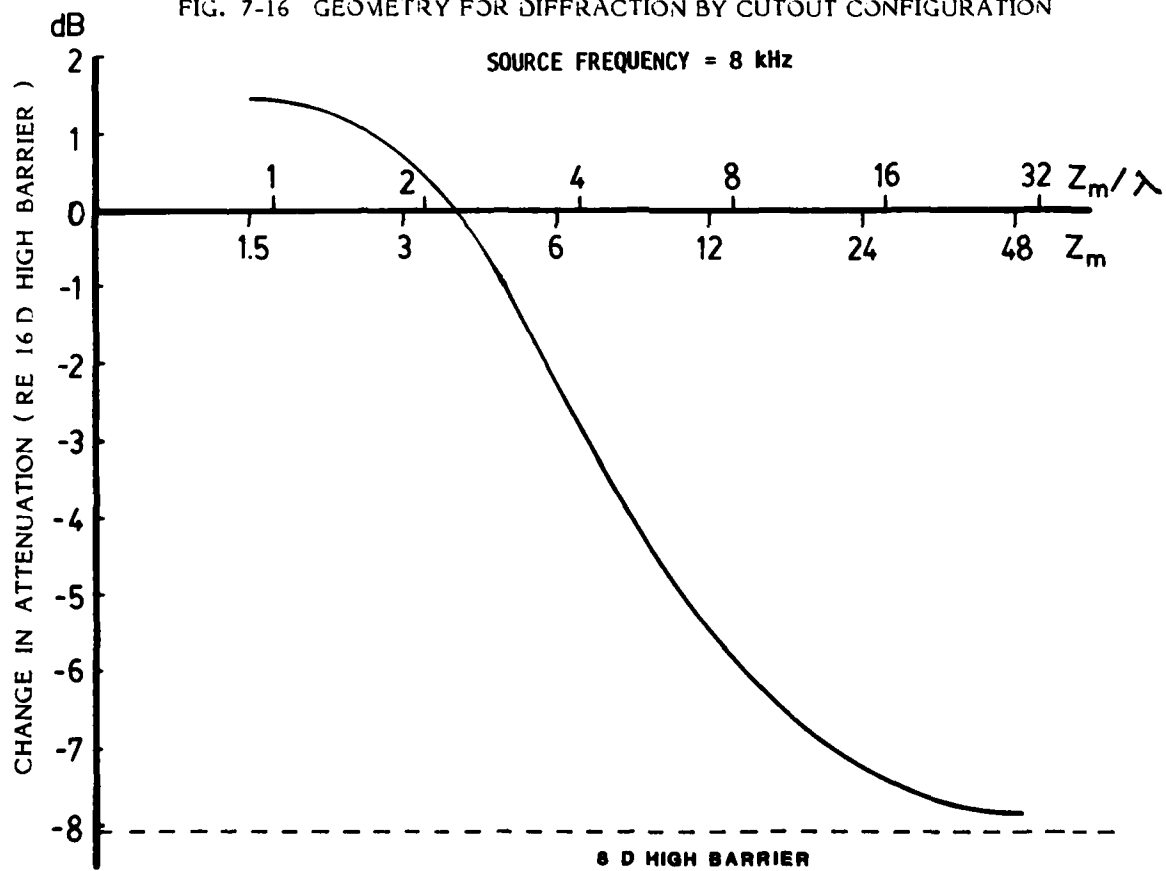
FIG. 7-17   CHANGE IN ATTENUATION OF COSINE CUTOUT RE SEMI-INFINITE
STRAIGHTEDGED BARRIER

X1 : SHIELD/CONE INTERSECTION : $h/\tan\alpha$

X2: DISTANCE OF CONE ORIGIN BEHIND JET EXIT : $(D/2)/\tan\alpha$

L : SHIELD LENGTH FROM JET EXIT : 16 D

h : SHIELD DISTANCE BELOW JET CENTERLINE (3 D)

α : HALF ANGLE OF CONE OF THRESHOLD INTERFERENCE

    (ASSUMED 15 DEGREES)

Z_m: CUTOUT WIDTH : $((L\tan\alpha + D/2)^2 - h^2)^{\frac{1}{2}}$

EQUATION OF HYPERBOLIC CUTOUT

$$X = [(Z^2 + h^2)^{1/2} - D/2]/\tan\alpha$$

FIG. 7-18   GEOMETRY OF HYPERBOLIC CUTOUT DEFINED BY INTERSECTION OF SHIELD AND

CONE OF THRESHOLD INTERFERENCE
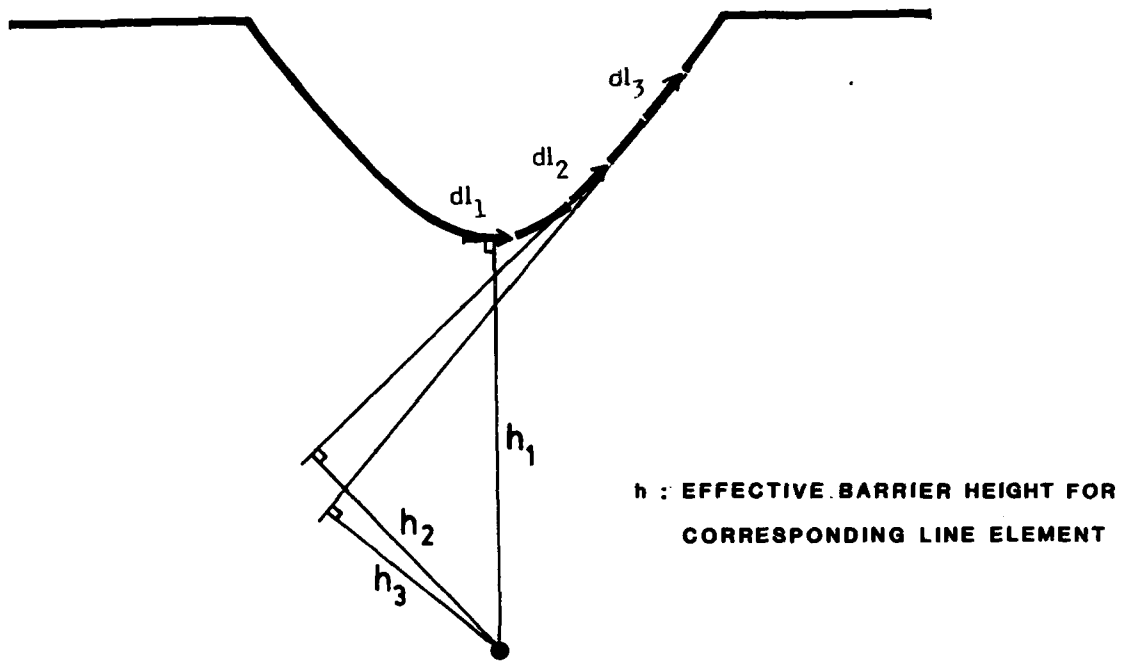
FIG. 7-19   DIAGRAM OF A HYPERBOLIC CUTOUT CONFIGURATION:
EACH LINE ELEMENT dl CAN BE INTERPRETED AS PORTION
OF A STRAIGHTEDGED BARRIER OF CERTAIN EFFECTIVE
HEIGHT 'h'
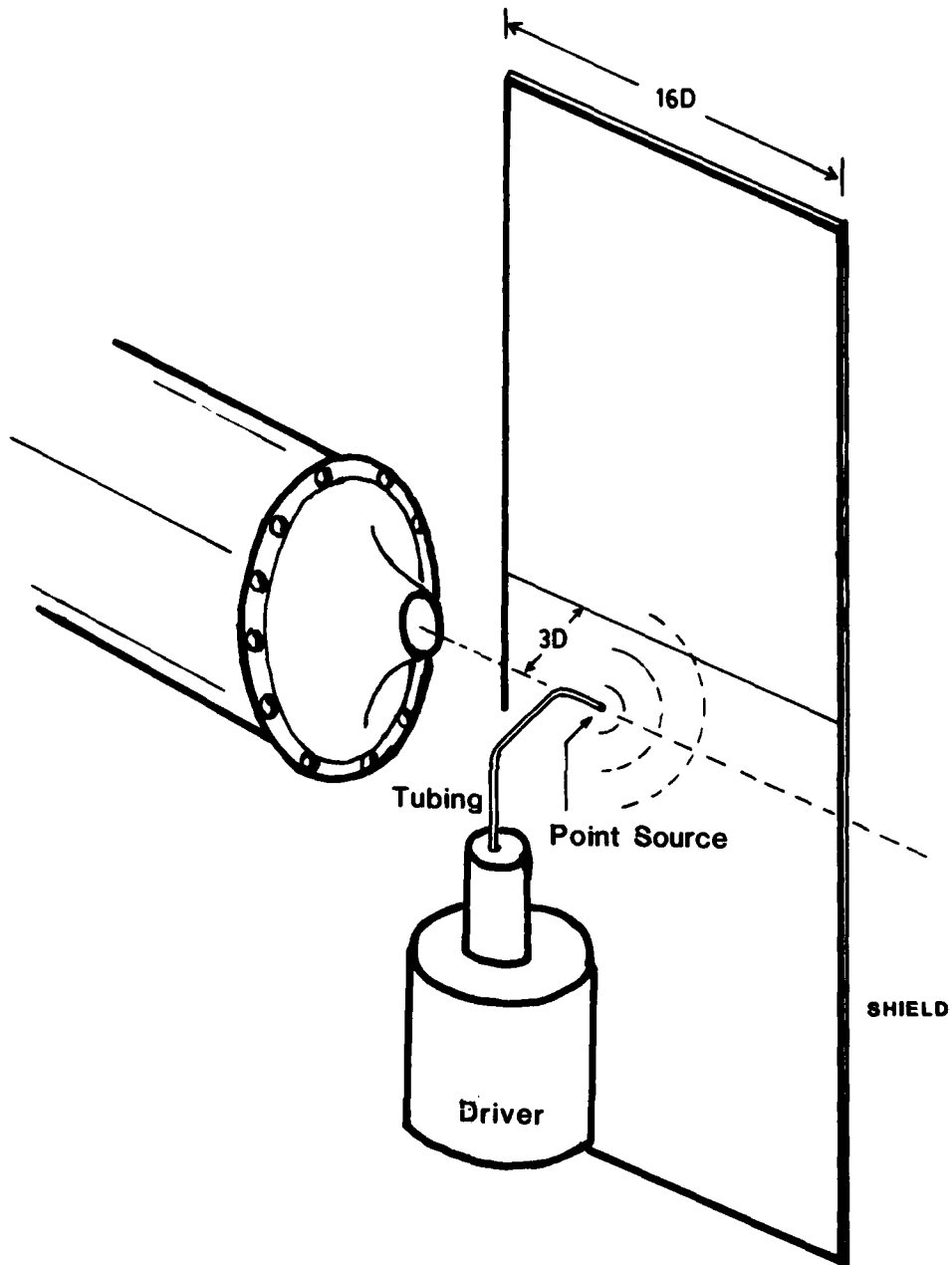
FIG. 7-20 EXPERIMENTAL ARRANGEMENT FOR MEASUREMENT OF SOUND
ATTENUATION BY A FINITE BARRIER
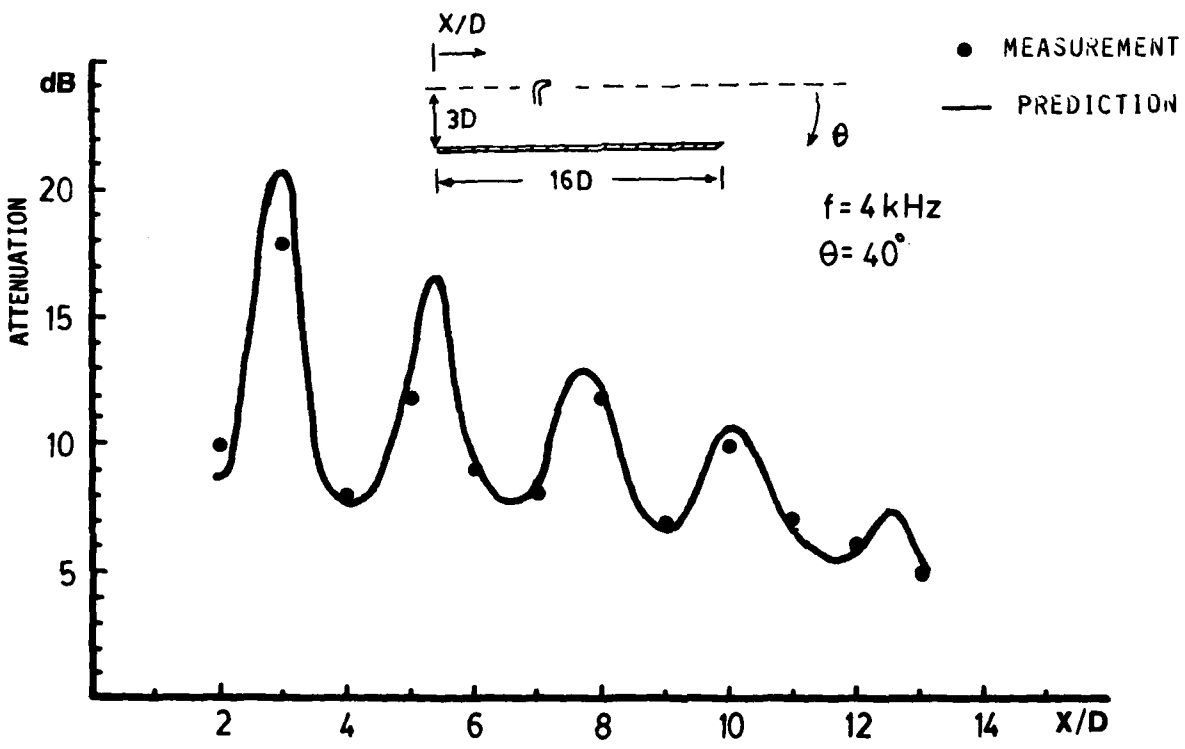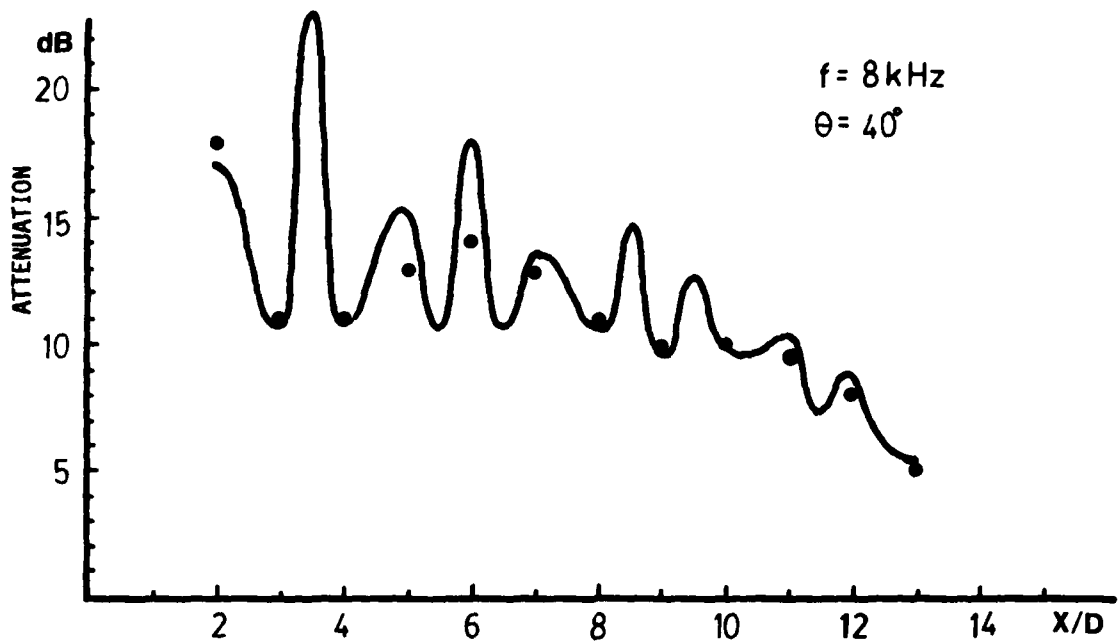
FIG.7-21   EXPERIMENTAL AND THEORETICAL SHIELDING FOR FINITE RECTANGULAR SHIELD
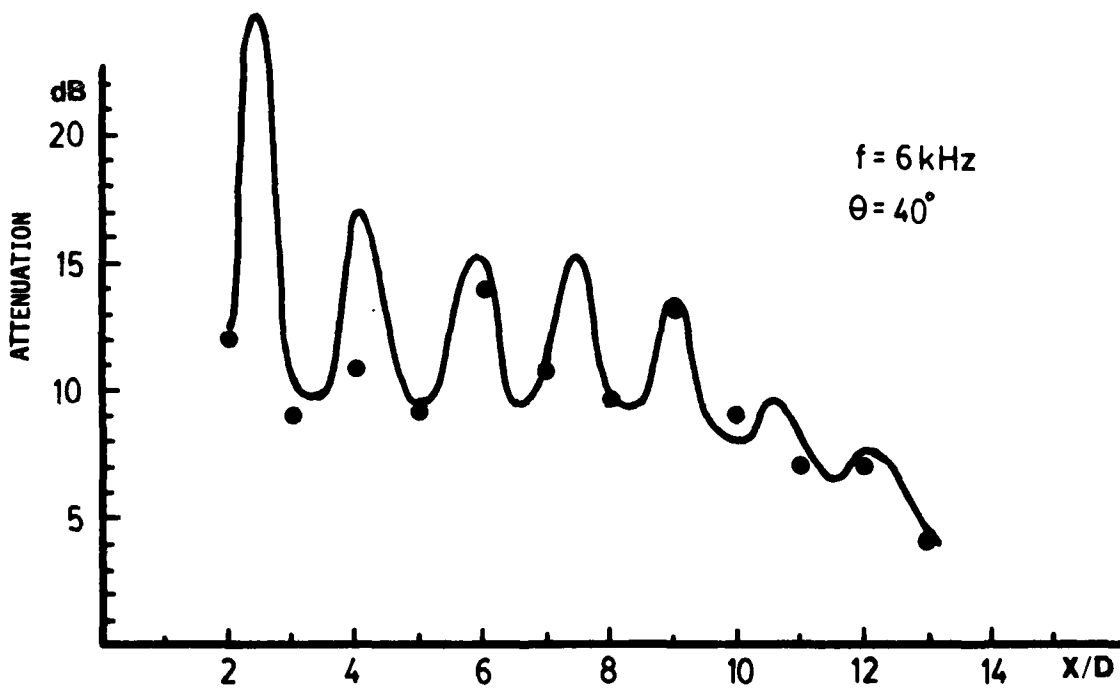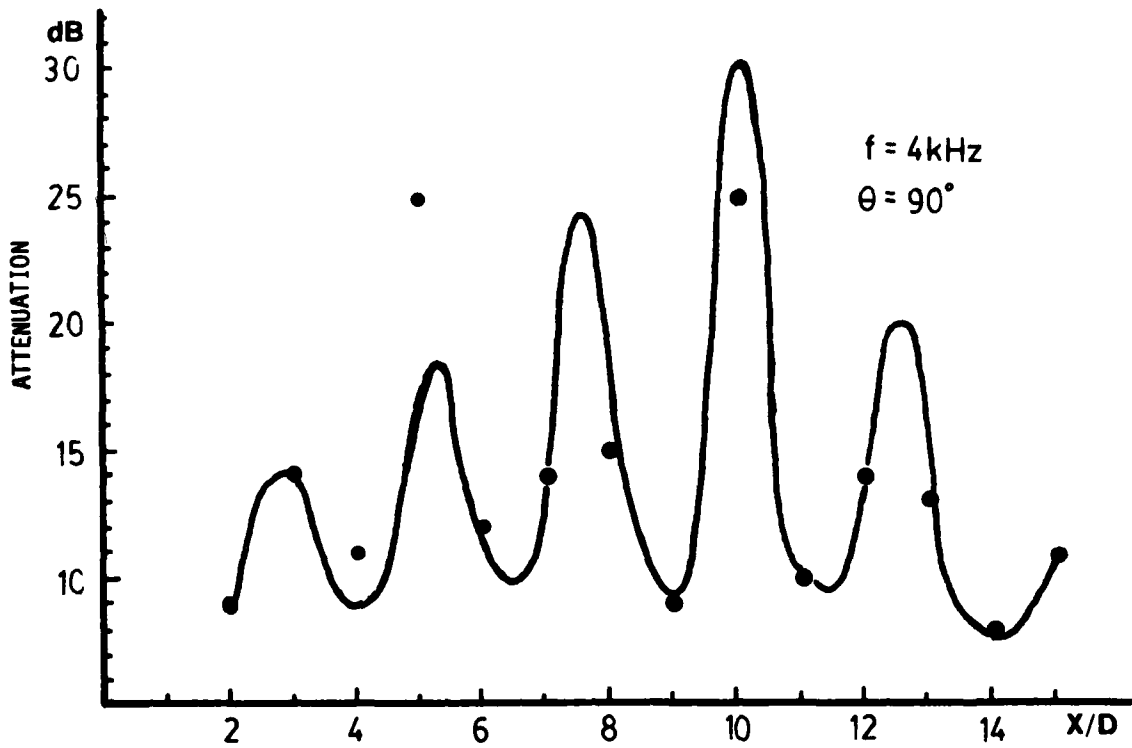
FIG. 7-21 EXPERIMENTAL AND THEORETICAL SHIELDING FOR FINITE
RECTANGULAR SHIELD
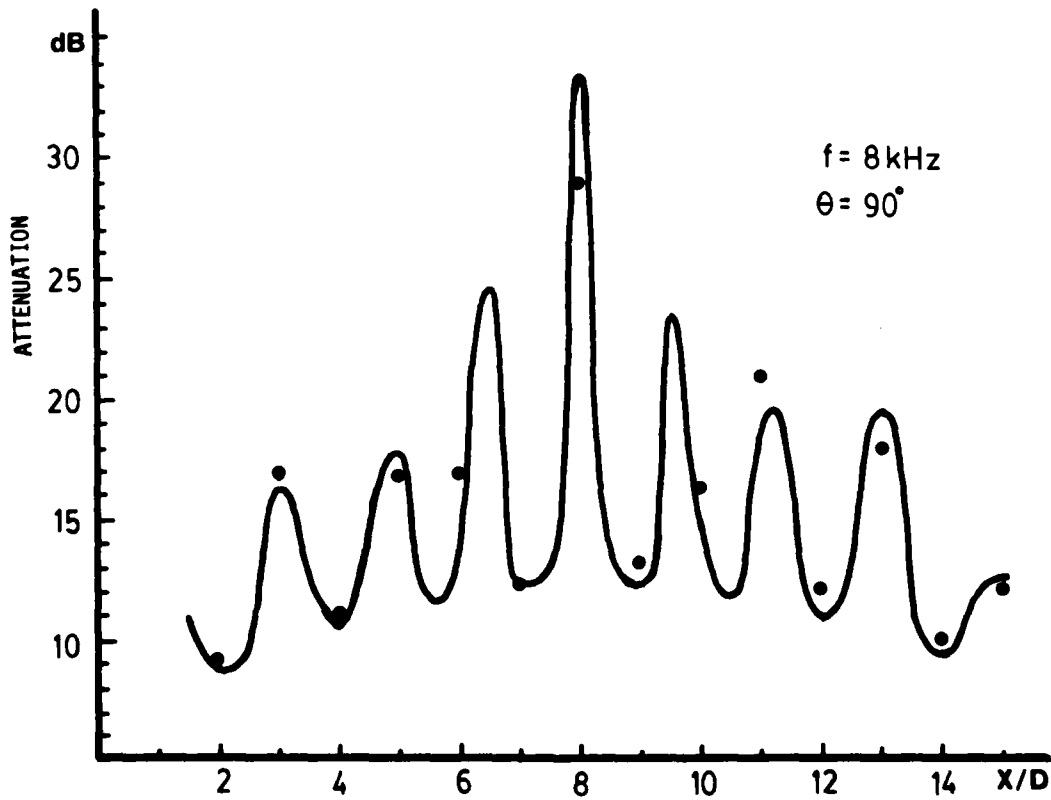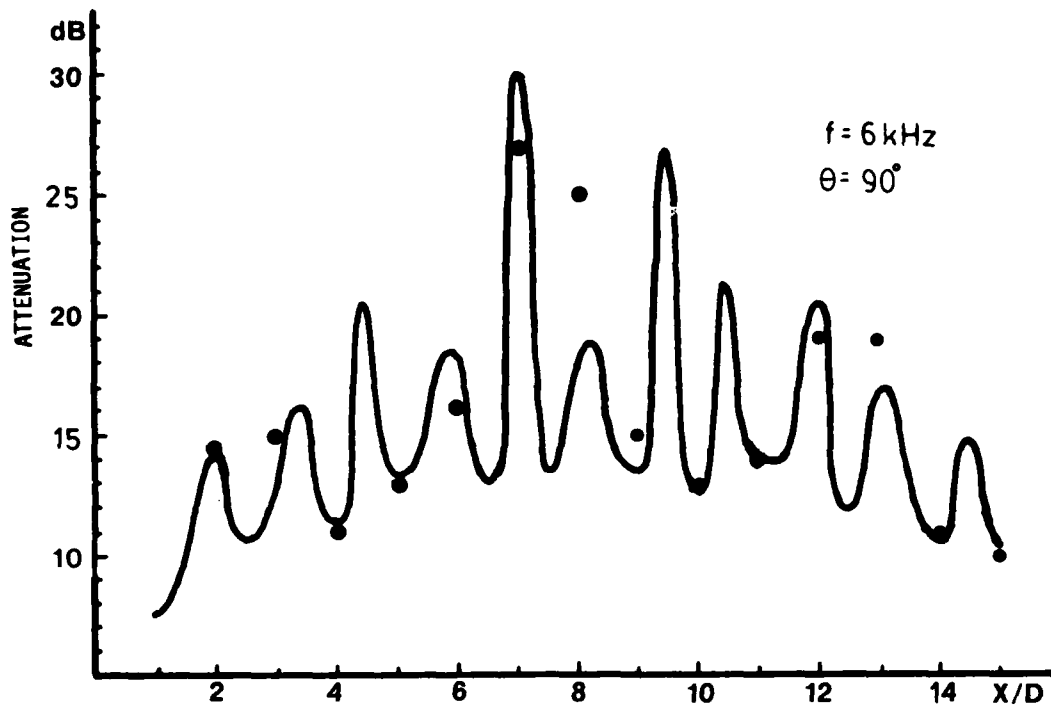
EXPERIMENTAL AND THEORETICAL SHIELDING FOR FINITE RECTANGULAR SHIELD
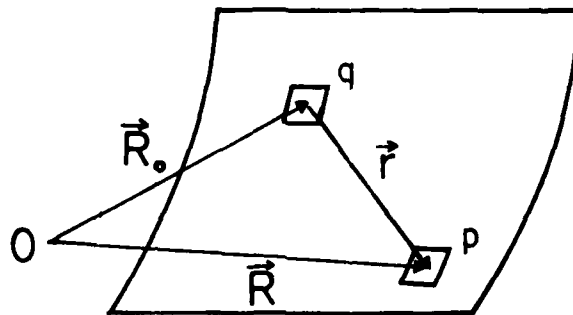
Fig. 7-22a   GEOMETRICAL QUANTITIES FOR CALCULATION
OF POTENTIAL AT p DUE TO SOURCE
LAYER ON ELEMENT q.
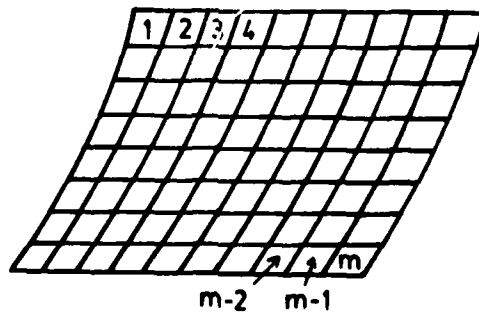
FIG. 7-22b   DISCRETIZATIONS FOR ACOUSTIC
DIFFRACTION PROBLEM
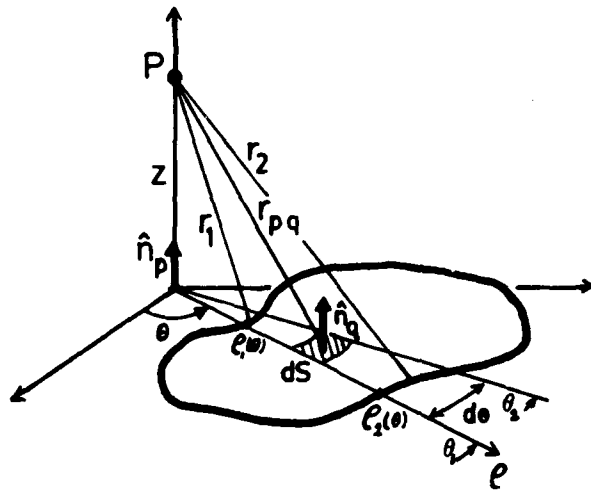
FIG. 7-23a GEOMETRY FOR AN ARBITRARY SURFACE ELEMENT
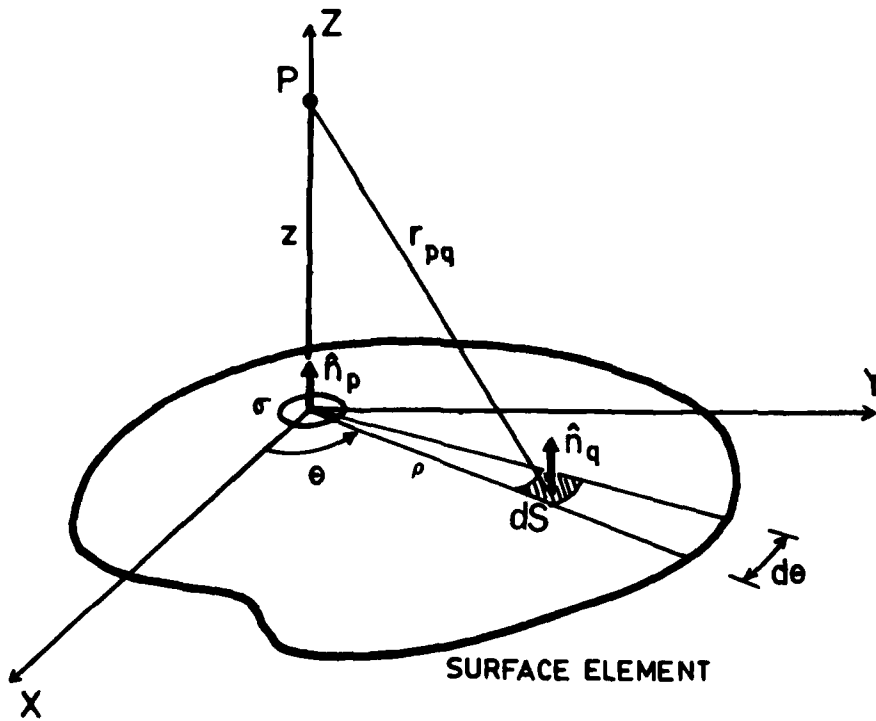
SURFACE ELEMENT

FIG. 7-23b GEOMETRY FOR SURFACE ELEMENT CONTAINING
CONTROL POINT 'P'

SOURCE-PANEL DISTANCE :   .5 M
PANEL-RECEIVER DISTANCE :   .31 M
SOURCE FREQUENCY :   1000 Hz

MEASURED (Ref. 49)

dB

180°

160

120

100

[θ]

80

60

40

20

o   96   elements
△ 168
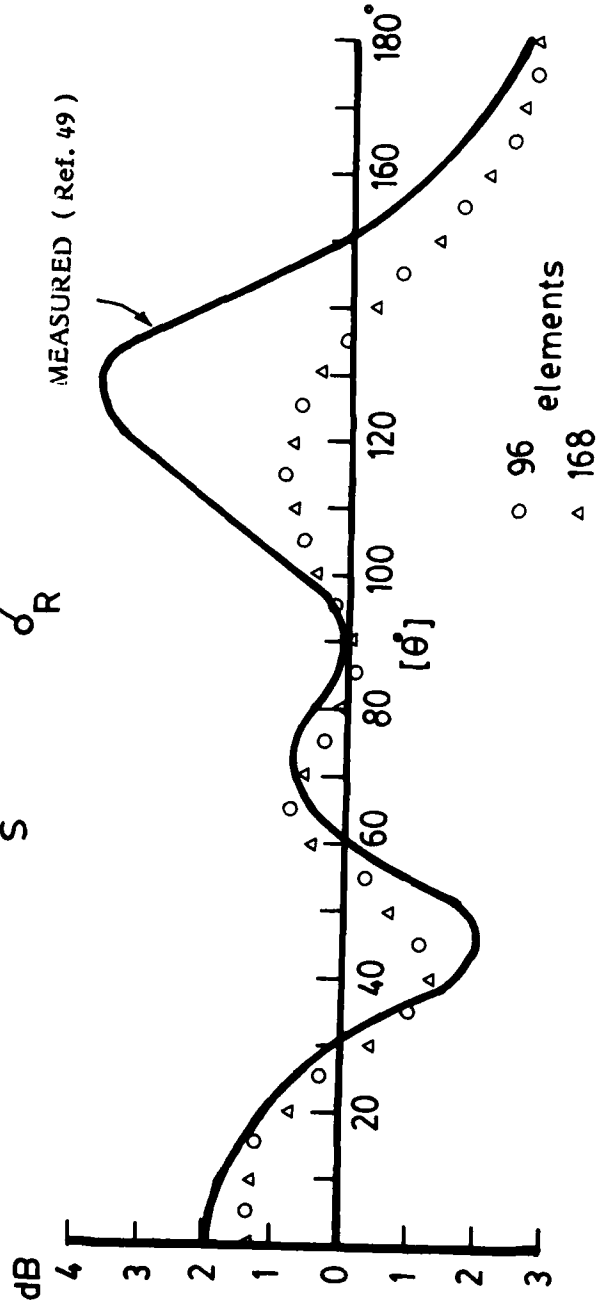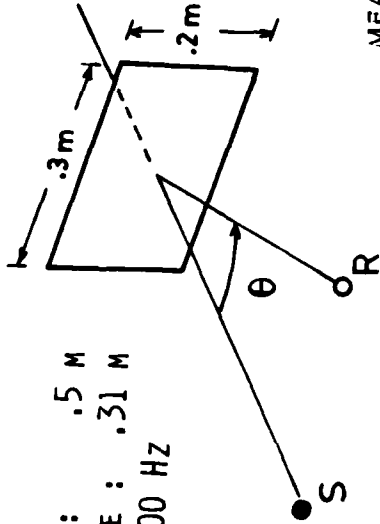
FIG. 7-24   COMPARISON OF PREDICTED AND MEASURED CHANGES IN
SPL RE FREE FIELD FOR A RIGID PANEL
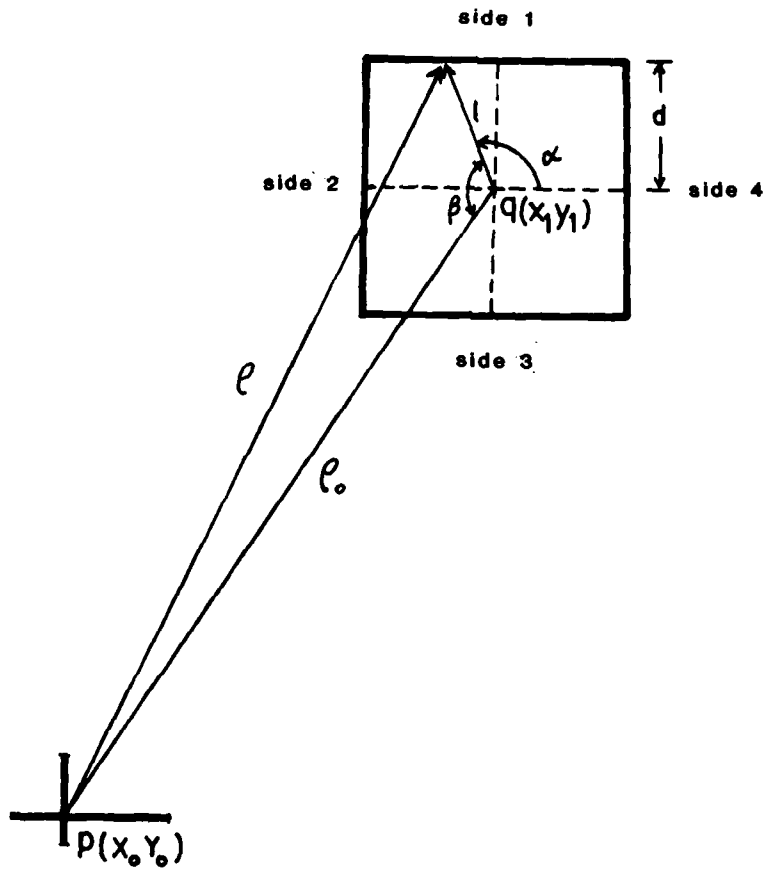
FIG. 7-25   GEOMETRICAL QUANTITIES USED IN THE LINE
             INTEGRATION OVER A SIDE OF AN ELEMENT

FIG. 7-26   COMPARISON OF PREDICTED AND MEASURED CHANGE IN SPL
RE FREE FIELD FOR A RIGID PANEL

SOURCE-PANEL DISTANCE :   .5 M
PANEL-RECEIVER DISTANCE :   .31 M
SOURCE FREQUENCY :   1000 Hz

MEASURED (TERAI)   ————

CALCULATED   △ 24   ELEMENTS
              ○ 96
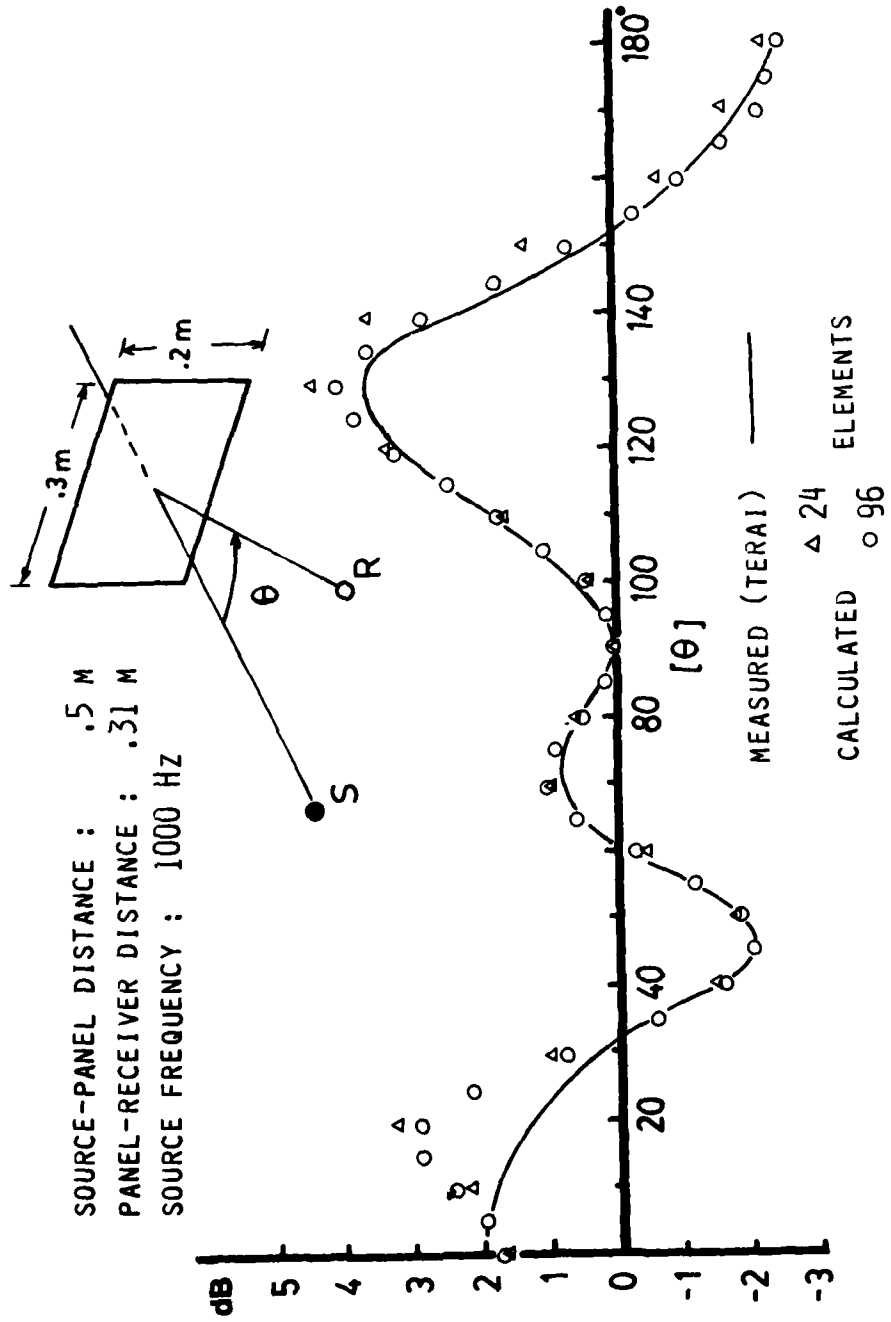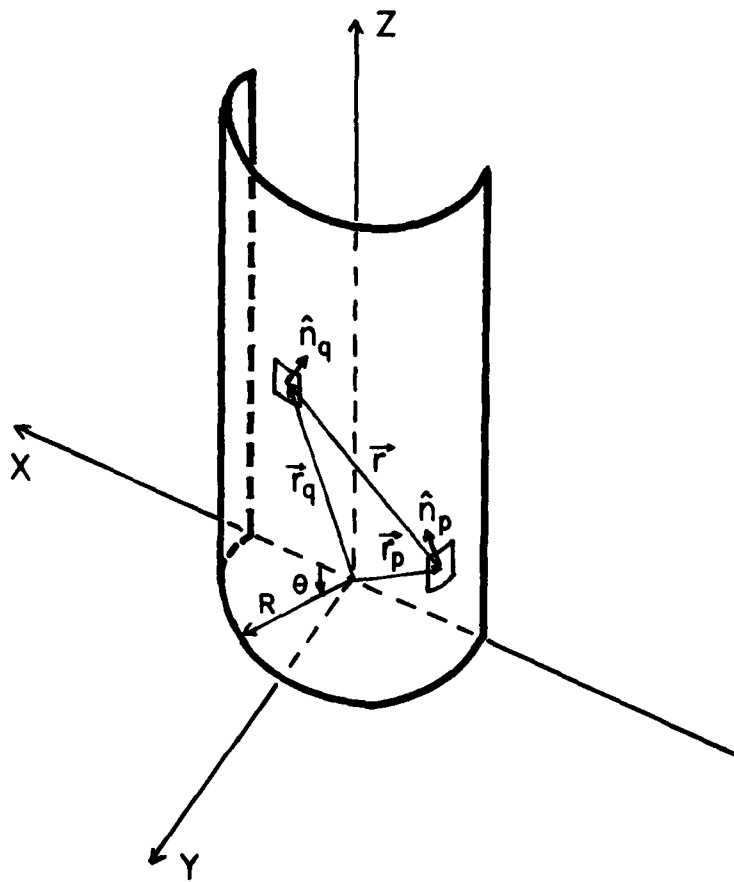
FIG. 7-27   GEOMETRY AND PARAMETERS FOR DIFFRACTION BY A HALF
ROUND SHIELD
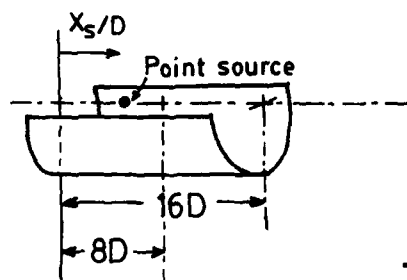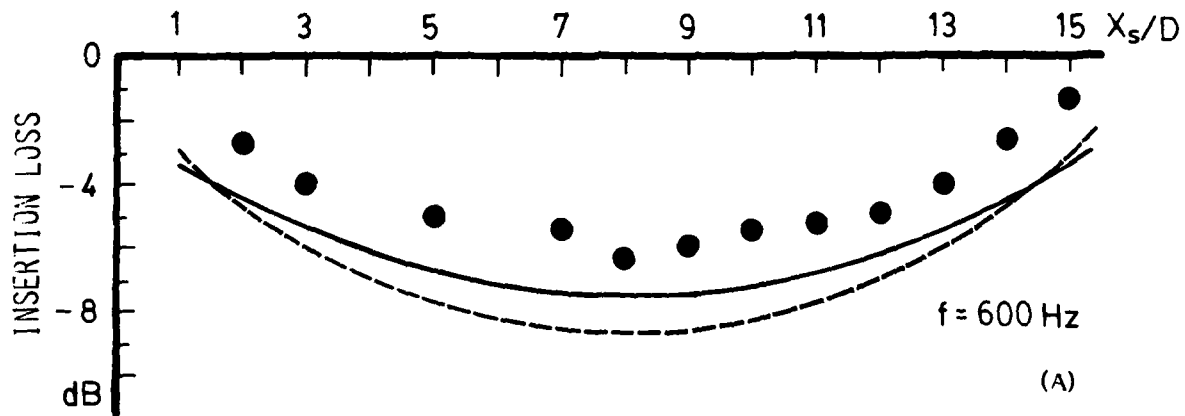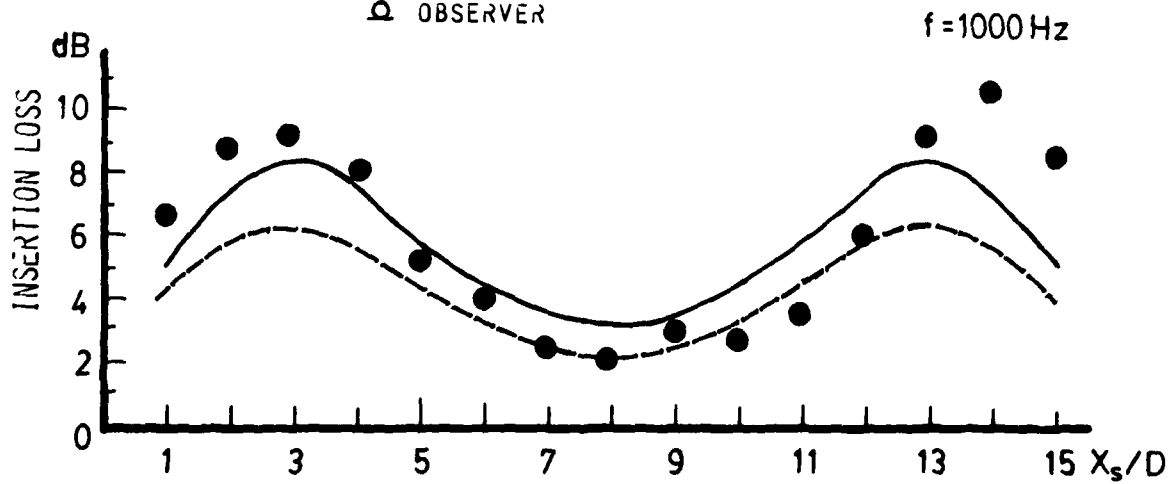
FIG. 7-28, A, B   COMPARISON BETWEEN CALCULATED AND MEASURED POINT
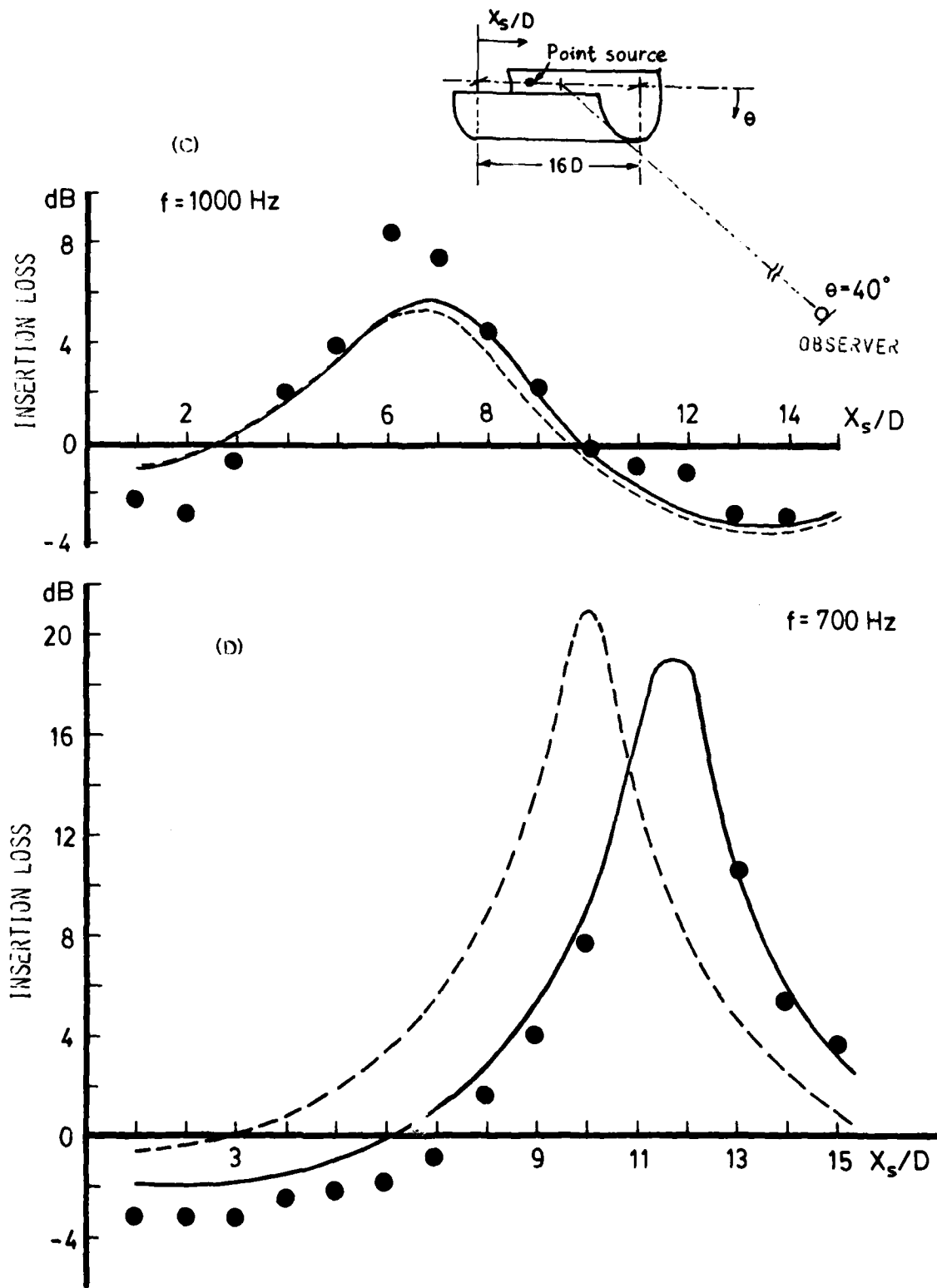SOURCE INSERTION LOSS FOR 10D DIAMETER SCOOP SHIELD

FIG. 7 - 28 C, D   COMPARISON BETWEEN CALCULATED AND MEASURED POINT
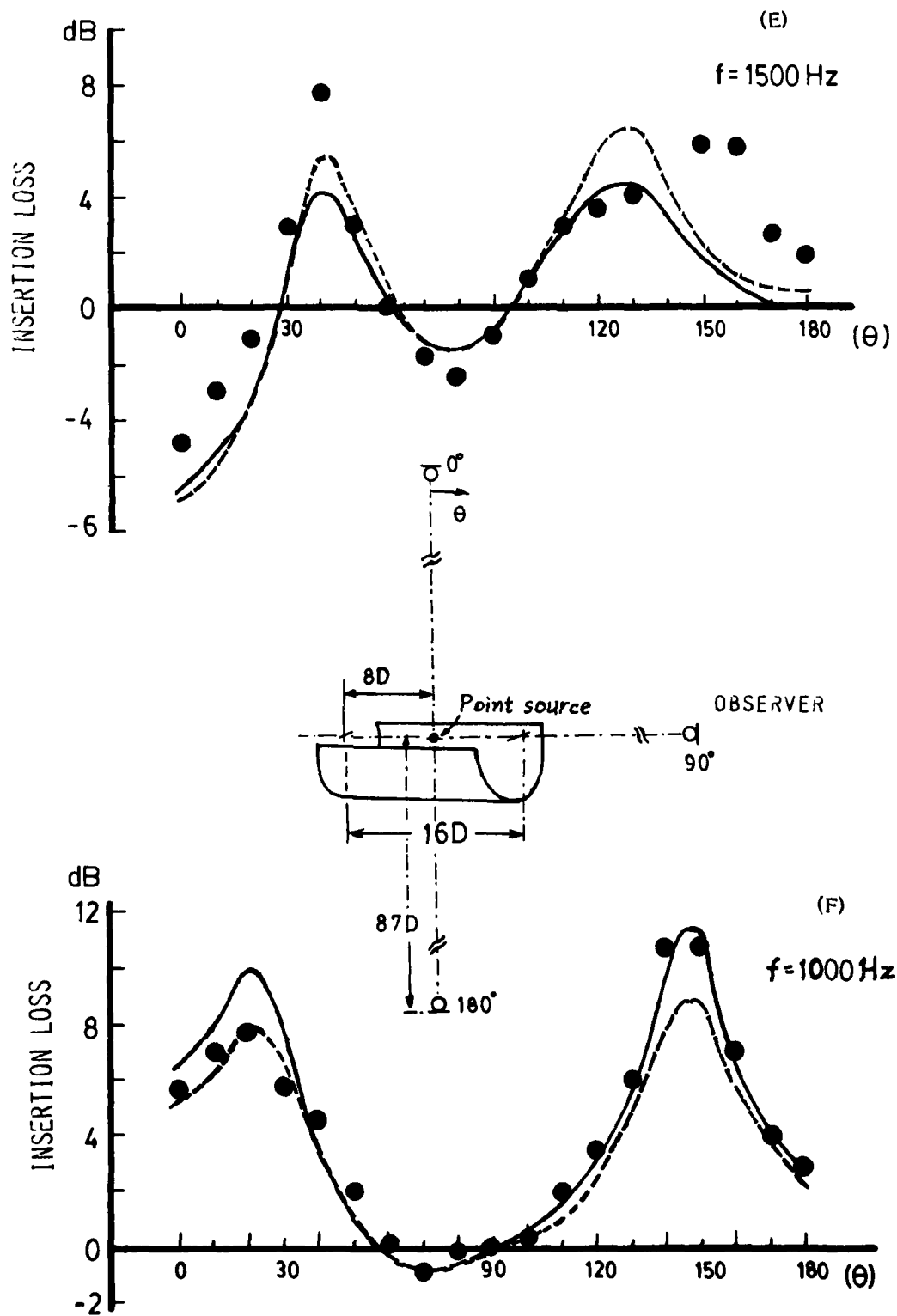SOURCE INSERTION LOSS FOR 10D DIAMETER SCOOP SHIELD

FIG. 7 - 28 E, F   COMPARISON BETWEEN CALCULATED AND MEASURED POINT
SOURCE INSERTION LOSS FOR 10D DIAMETER SCOOP SHIELD

APPENDIX A

(A) REFLECTION AND REFRACTION OF SOUND WAVES AT AN INTERFACE.

Consider a plane harmonic sound wave of frequency ω incident at an angle θ_1 (Fig.A-1) to the vertical upon an interface separating two half spaces of characteristic impedance $\rho_1 c_1$ and $\rho_2 c_2$ respectively. The boundary conditions at the interface are

(I) continuity of pressure

(II) equality of normal component of particle velocity

There will be a reflected wave at angle θ_1 to the vertical in medium I and a transmitted (refracted) wave at angle θ_2 to the vertical in medium ii. Straight forward analysis using (I) and (II), yields

(i) $\qquad \omega_{inc.} = \omega_{refl.} = \omega_{transmitted}$ $\qquad$ (A-1)

(ii) $\qquad k_1 \sin \theta_1 = k_2 \sin \theta_2 \qquad$ (Snell's law) $\qquad$ (A-2)

along the boundary. ((i) and (ii) implies common angular frequency and the continuity of the component of wave number along the interface). Further applications of (i) and (ii) result in expressions for the reflected amplitude R and transmitted amplitude T. After some work, one finds:

$$R = \frac{m \cos \theta_1 - \sqrt{n^2 - \sin^2 \theta_1}}{m \cos \theta_1 + \sqrt{n^2 - \sin^2 \theta_1}} \qquad (A-3)$$

and $\qquad T = (1 + R) / m$, where $m = \rho_2 / \rho_1$. $\qquad$ (A-4)
$$n = c_1/c_2 = \sin \theta_1 / \sin \theta_2$$

Define $Z_1 = \rho_1 c_1 / \cos \theta_1$, $Z_2 = \rho_2 c_2 / \cos \theta_2$. The reflected amplitude R can be written as

$$R = (Z_2 - Z_1)/(Z_1 + Z_2) \qquad (A-5)$$

Eq. (A-3) indicates the possibility of complete reflection if $c_2 > c_1$, hence $n < 1$ ($n = \sin \theta_1 / \sin \theta_2 = c_1/c_2$ = index of refraction). If the angle of incidence satisfies the condition $\sin \theta_1 > n$, R becomes complex and $|R| = 1$, which indicates complete reflection of incident wave.

This simple analysis serves to illustrate the major concept of a reflective gas layer shield. A layer of gas with higher sound speed than the medium of the jet will partially shield an area below it. The situation will become more complex when the reflective layer is of finite thickness and the medium is in motion. For layered media, it can be shown that the reflection and transmission coefficients are frequency dependent (Ref. 64), and in general, both coefficients will show a series of maxima and minima as a function of frequency at a particular angle of incidence. The frequencies and amplitudes of the maxima and minima will also be functions of the angle of incidence.

(B) REFLECTION AND TRANSMISSION OF SOUND WAVES IN LAYERED MEDIUM IN RELATIVE MOTION

In case there is relative motion between the two media, Ribner Ref.(26) and Miles (Ref. 27) have generalized the second boundary condition as given in (A) to

(II a) continuity of the normal component of particle displacement across the interface.

Equality of trace velocity on the interface yields

$$c_1 \csc \theta_1 - U = c_2 \csc \theta_2 = v$$

Here U is the relative velocity of the upper medium to lower in the direction of the incident sound rays. The boundary conditions II and IIa are equivalent when U = 0, but differ when U ≠ 0. Earlier workers on the problem erred in using boundary condition (II). The equality of wave number component along the boundary implies

$$k_1 \sin \theta_1 = k_2 \sin \theta_2 = m$$

Thus, common angular frequency ($\omega = mv$) requires

$$k_1(c_1 + v_1 \sin \theta_1) = k_2(c_2 + v_2 \sin \theta_2)$$

The above expressions are the equations of constraint. Together with the appropriate boundary conditions, Yeh (Ref. 31) has generalized the above equations to sound incident on a two dimensional moving gas layer (jet) (Fig. A-2a) that can be used to model a fluid-layer acoustic shield. He originally used the incorrect B.C.(II), but later corrected on advice from Ribner. The resulting complex reflection and transmission coefficients are:

$$R = e^{2ik_0 d \cos\theta_0} \frac{[(1 - T_1 T_2) \cos(k_1 d \cos\theta_1) - i(T_1 - T_2)\sin(k_1 d \cos\theta_1)]}{[(1 + T_1 T_2)\cos(k_1 d \cos\theta_1) + i(T_1 + T_2)\sin(k_1 d \cos\theta_1)]}$$

$$T = \frac{2 e^{ik_0 d \cos\theta_0}}{[(1 + T_1 T_2)\cos(k_1 d \cos\theta_1) + i(T_1 + T_2)\sin(k_1 d \cos\theta_1)]}$$

$$\text{where} \quad T_1 = \frac{\rho_0 c_0^2 \sin 2\theta_1}{\rho_1 c_1^2 \sin 2\theta_0} \ , \quad T_2 = \frac{\rho_1 c_1^2 \sin 2\theta_2}{\rho_2 c_2^2 \sin 2\theta_1}$$

A-3

Fig.(A-2) shows the transmission loss as a function of the different parameters of the medium. The values of ρ and c of the media, the thickness d and the velocities all affect the transmitted amplitude T. Also, increasing v_1, c_1, d, and decreasing the incident angle towards the glancing direction all results in predicted increased shielding.
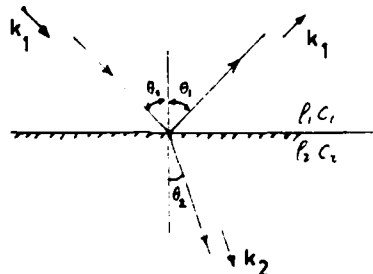
A-4

FIG. A-1 THE REFLECTION AND TRANSMISSION OF A SOUND
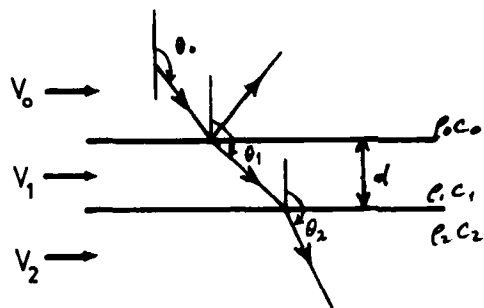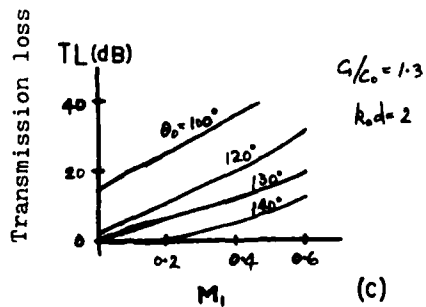WAVE AT A BOUNDARY

FIG. A-2a THREE-LAYERED ACOUSTIC SHIELD

(a)

(b)

(c)
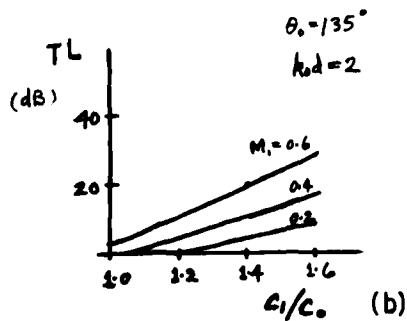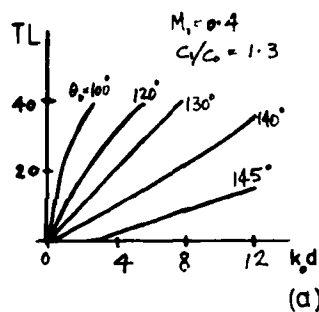
FIG. A-2 b PREDICTED SHIELD CHARACTERISTICS (Ref. 30)
(M_0 , M_2 = 0 , and C_2/C_0 = 1)

A - 5

MATHEMATICAL FORMULATION OF THE NOY TABLES FOR PN dB CALCULATIONS BY COMPUTERS (REF. 35)

The subjective sensation of loudness of a complex noise signal is evaluated from the octave band sound pressure levels of the noise at centre frequencies of 63, 125, 250, 500, 1000, 2000, 4000, and 8000 Hz. According to Fig. (5-2), each octave band has a loudness index (NOY value) depending on the sound pressure level and frequency. To implement this into a computer code for calculating PN dB levels, a table of NOY values (Fig B-1) can be stored in the computer. This is inefficient in terms of both computer storage and time. An alternative is a mathematical formulation of the NOY tables.

The feasibility is apparent if the NOY tables are plotted as sound pressure level $\log_{10}$ (NOY): a series of straight lines are obtained (Fig. B-2). For frequency bands with centre frequency f_c such that $50 < f_c < 315$ Hz, and $6300 < f_c < 1000$ Hz, the plots appear to consist of two intersecting straight lines. Whereas for $400 < f_c < 500$ Hz, a single straight line is adequate. Hence, by specifying the slope and the intercept of the straight lines for different bands (Fig. B-3), a mathematical formulation of the NOY tables is possible.

The following procedure illustrates the evaluation of PN dB from octave band SPL by means of the constants shown in Fig. B-3.

(1) Input data consists of 8 octave band SPL values at corresponding centre frequencies from 6' to 8000 Hz.

(2) Each octave band SPL value is then converted into NOY values according to

$$NOY = 10^{M(SPL-S)}$$

where values of M and S depend on band centre frequency as well as SPL magnitude as indicated in Fig. B-3. For band centre frequencies such as $f_c \leq 250$ or ≥ 8000 Hz

If   SPL $\leq$ L

$$NOY = 10^{M_1(SPL-S_1)}$$

If   SPL $>$ L

$$NOY = 10^{M_2(SPL-S_2)}$$

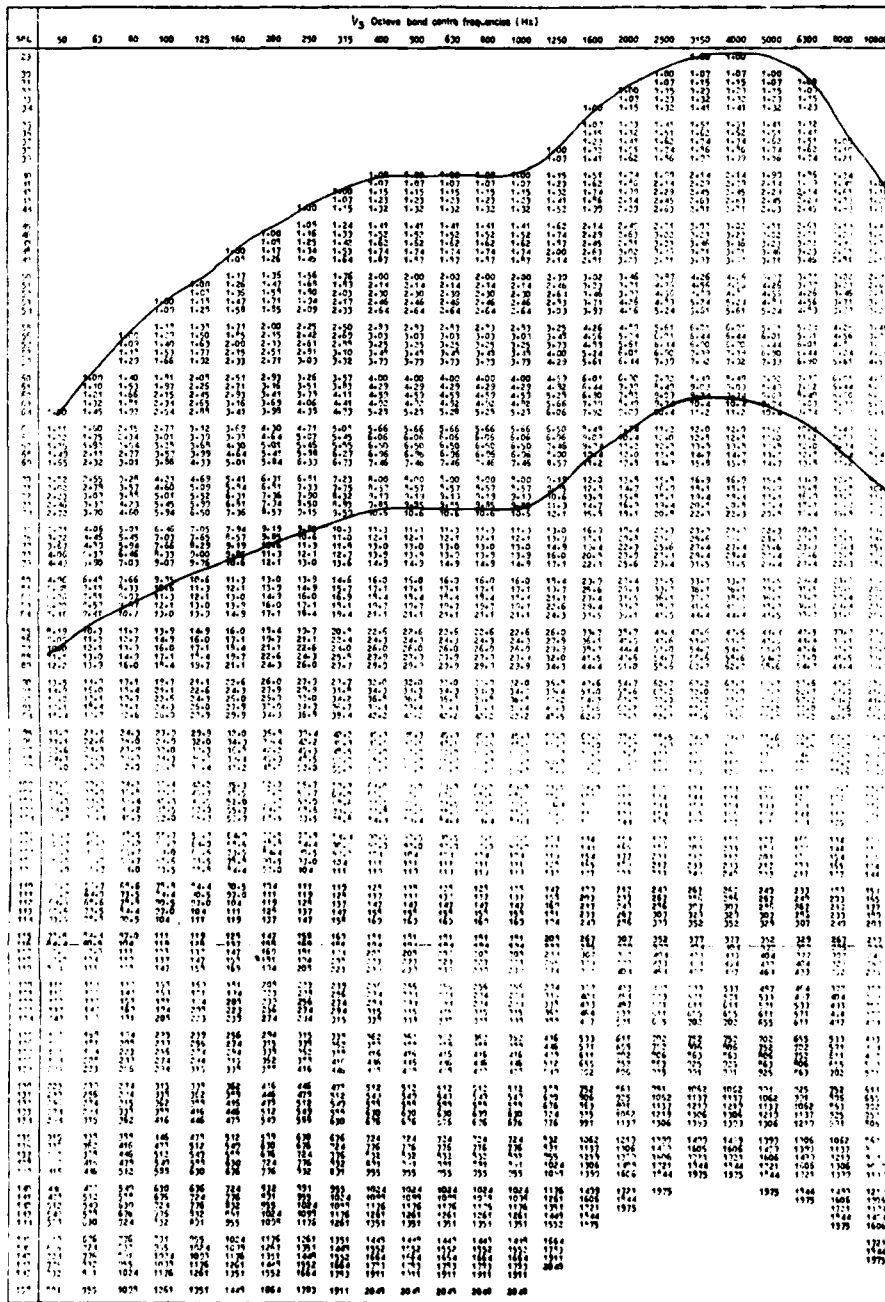For $500 \leq f_c \leq 4000$ Hz

$$NOY = 10^{M_2(SPL-S_2)}$$

(3) The NOY values for all 8 octave bands are then converted into perceived noise level (PNL) according to

$$PNL = 40 + \frac{\log_{10}(N_m + 0.3(\sum_{i=1}^{8} N_i - N_m))}{0.03} \quad PN \ dB$$

Where ΣN = summation of all NOY values for all 8 octave bands

N_m = maximum NOY value in the octave bands.

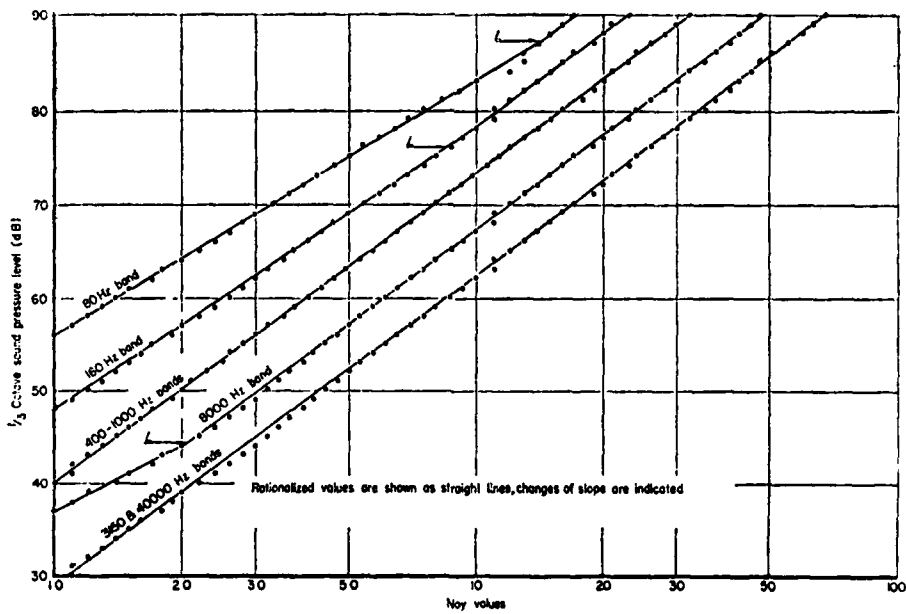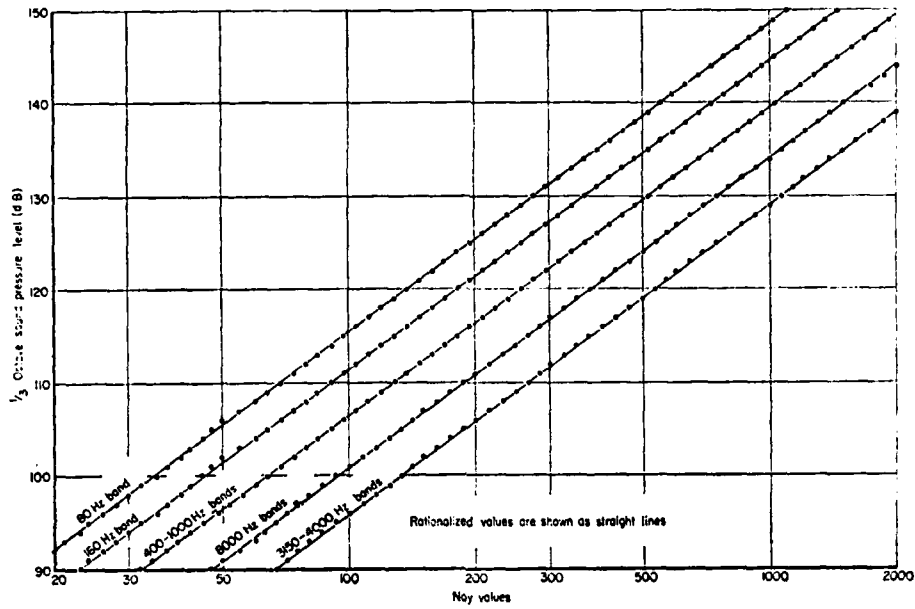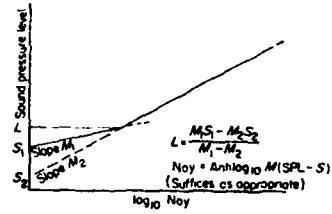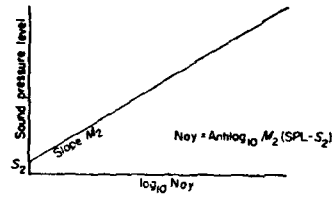FIG B-1   *Noys as a function of sound pressure level (1967)*

FIG. B-2 PLOTS OF SPL vs NOY VALUES FOR VARIOUS FREQUENCIES
(Ref. 35)

B-5

$$L = \frac{M_1 S_1 - M_2 S_2}{M_1 - M_2}$$

Noy = Antilog$_{10}$ M(SPL $-$ S)
(Suffices as appropriate)

Applicable to bands 315 Hz and below 8000 Hz and above

Noy = Antilog$_{10}$ M_2(SPL-S_2)

Applicable to bands 400 to 6300 Hz inclusive

where M_1 = slope of first line to intersection at L,
M_2 = slope of second line from intersection at L,
S_1 = intersection of first line on the SPL axis,
S_2 = intersection of second line on the SPL axis,
L = SPL ordinate of intersection,
Noy = Antilog$_{10}$ M(SPL $-$ S) with suffices as appropriate.

$$L = \frac{M_1 S_1 - M_2 S_2}{M_1 - M_2}.$$

Band Centre freq.(Hz)	M_1	S_1	L	M_2	S_2
63	.040570	60	85.9	.030103	51
125	.035336	51	79.8	.030103	46
250	.032051	44	74.9	.030103	42
500				.030103	40
1000				.030103	40
2000				.029960	32
4000				.029960	29
8000	.042285	37	44.3	.029960	34

FIG. B-3   TABLE OF CONSTANTS FOR PN dB CALCULATIONS (Ref. 35)

B-6

APPENDIX C

EQUATIONS AND PROCEDURES FOR GROUND CONTOUR CALCULATIONS
(RE : FLOW CHART , FIG. 5.4)

(1) Equation of flight path

$X = Vt \cos \gamma$

$Y = Y$

$Z = Vt \sin \gamma$

where V = aircraft speed

(2) Coordinates of grid point on ground plane reference to aircraft frame O'.

$X_1 = X - X_G$

$Y_1 = Y$

$Z_1 = Z$
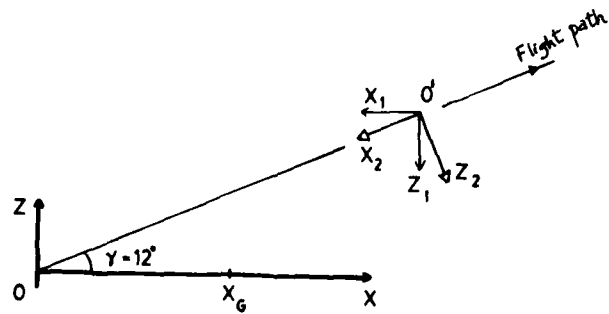
C - 1

Rotate about the Y_1 axis to obtain coordinate relative to coordinate system with X_2 aligned with the jet axis

$X_2 = X_1 \cos \gamma + Z_1 \sin \gamma$

$Y_2 = Y_1$

$Z_2 = Z_1 \cos \gamma - X_1 \sin \gamma$

(3) Coordinate transformation $(X_2 \ Y_2 \ Z_2) \rightarrow (R, \theta, \varphi)$
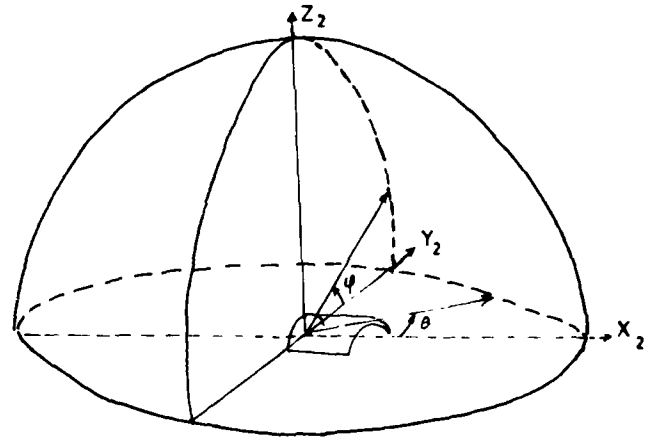
$R = \sqrt{X_2^2 + Y_2^2 + Z_2^2}$

$\theta = \tan^{-1} (Y_2/X_2)$

$\varphi = \tan^{-1} (Z_2/Y_2)$
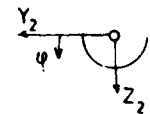
C - 2

④ The levels at points intermediate to data points[*] are estimated by means of a two dimensional cubic spline interpolation scheme.

[*] (Actually measured values are $\overrightarrow{p^2}(R_o, \theta_i, \psi_j)$

where θ_i = 20°, 30°, 40°, 50°, 60°, 70°, 80°, 90°
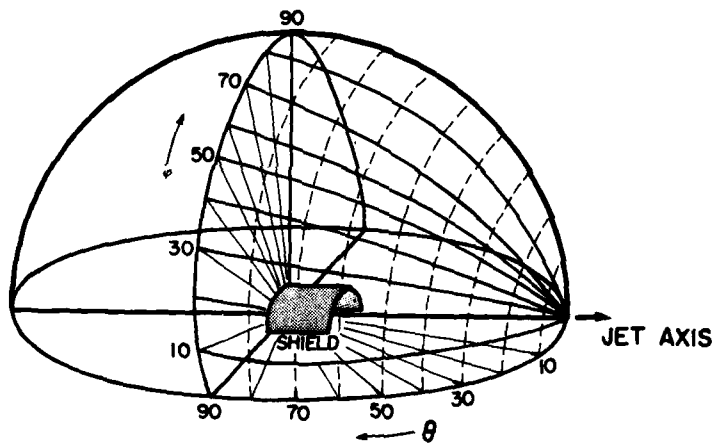
ψ_j = 0°, 15°, 30°, 45°, 60°, 75°, 90°

MICROPHONE POSITION IN TERMS OF r,θ,ψ OVER A HEMISPHERICAL SURFACE CENTERED AT THE JET NOZZLE.
SIDELINE PLANE ψ = 0°
FLYOVER PLANE ψ = 90°

C-3

APPENDIX D

<u>SYNTHESIS OF THE JET NOISE SHIELDING FROM POINT SOURCE SHIELDING</u>

Let $\overline{p^2}(\theta)$ be the unshielded jet noise level corresponding to a particular observation angle θ and frequency f_1.

$$\therefore \quad \overline{p^2}(\theta) = \iint \Phi(f_1,\theta,x) \, df_1 \, dx$$

where $\Phi(f_1,\theta,x)$ is the source intensity distribution as function of frequency and distance 'x' along the jet axis (Fig. D-1)

Similarly, the corresponding shielded level can also be expressed as

$$\overline{p^2}_{sh}(\theta) = \quad \Psi(f_1,\theta,x) \, df_1 \, dx$$

where $\Psi(f_1,\theta,x)$ is the equivalent shielded intensity distribution (Fig. D-1)

For a particular source position x_i and frequency f_1, one can express the observed attenuation $\Delta \, dB_i$ as

$$\text{Atten. } dB(f_1,\theta,x_i) = \Delta \, dB_i = 10 \log \Phi_i / \Psi_i$$

$$\text{or} \quad \Psi_i \Big|_{f_1} = \left(10^{-\Delta dB_i / 10}\right) \Phi_i \Big|_{f_1}$$

Let $$\sum_i \Phi(f_1,x_i,\theta) = \Phi(f_1,\theta)$$

and $$\sum_i \Psi(f_1,x_i,\theta) = \Psi(f_1,\theta)$$

The total contribution from all sources located along the jet axis then equals

$$\sum_i \Psi(f_1,x_i,\theta) = \sum_i \left[10^{-\Delta dB_i / 10}\right] \Phi_i(f_1,x_i,\theta)$$

The overall attenuation of frequency f_1 at angle θ is obtained from the ratio

$$\sum_i \Phi \Big/ \sum_i \Psi$$

as

$$\text{Atten } dB(f_1,\theta) = 10 \log \left[\frac{\sum_i \Phi_i(f_1,x_i,\theta)}{\sum_i \Psi_i(f_1,x_i,\theta)}\right]$$

$$= 10 \log \left[\frac{\Phi(f_1,\theta)}{\Psi(f_1,\theta)}\right]$$

A shielded spectrum can be built up to synthesize the jet noise shielding if $\Phi(f_1,x_i,\theta)$ is known. This can be modelled by using Eq. (6.3-1), which is

$$\Phi(x,\theta) = \Phi_0(\theta) \, x/x_0 \left[e^{-\frac{1}{2}(x/x_0)^2} \sqrt{e}\right]$$

where $x_0 = x_0$ (Strouhal number)

Hence, the overall attenuation for a particular frequency can be estimated from

$$\text{Atten. } dB(f_1, \theta) = 10 \log\left[\frac{\Phi(f_1, \theta)}{\Psi(f_1, \theta)}\right]$$

$$= 10 \log\left[\frac{\sum \Phi(x_i, \theta, f_1)}{\sum 10^{-\Delta dB_i/10} \Phi(x_i, \theta, f_1)}\right]$$

Where ΔdB_i is the attenuation of a point source determined (either experimentally or analytically) as function of position and frequency along the jet axis.
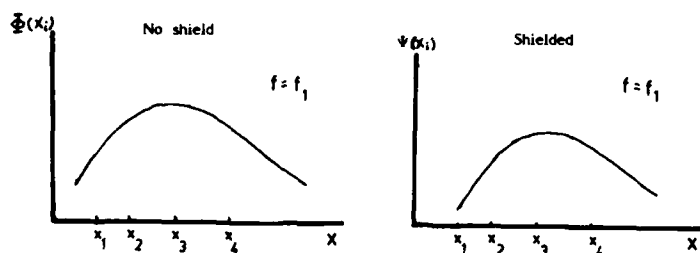

FIG. D-1 ASSUMED PROFILE OF SOURCE INTENSITY DISTRIBUTION AS FUNCTION OF POSITION ALONG THE JET AXIS

D-3

EVALUATION OF VOLUME INTEGRAL IN KIRCHHOFF EQUATION (EQ. 7.1-5) FOR FIELD POINT ON SURFACE OF INTEGRATION

In diffraction problems, an exact representation of the induced surface potential is possible via Kirchhoff's integral. An integral equation could be derived by placing the field point $P(\vec{R})$ on the surface of the obstacle (Fig. E-1). On taking the limit as $P \to p$, where p is a point on the surface, one finds the resulting integral equation to be (c.f. Eq.7.1-7)

$$\frac{\phi(p)}{2} = \phi_i(p) + \iint \left[\phi(q) \frac{\partial G(p,q)}{\partial n} - G(p,q) \frac{\partial \phi(q)}{\partial n} \right] dS$$

where $\partial/\partial n$ denotes differentiation along the outward normal to S and p,q denote variable points on the surface. The derivation of the integral equation requires the following mathematical relation: The Green's theorem for a region V in three dimensions bounded by a closed surface S is:

$$\iiint \left[\varphi_1 \nabla^2 \varphi_2 - \varphi_2 \nabla^2 \varphi_1 \right] dV = \iint \left[\varphi_1 \nabla \varphi_2 - \varphi_2 \nabla \varphi_1 \right] dS \qquad (\text{E-1})$$

where $\partial/\partial n$ denotes differentiation along the outward normal to S.

Now, let $\Phi(\vec{R},t)$ be the velocity potential of the sound field in volume V of Fig. (E-1) which satisfies the wave equation:

$$\nabla^2 \Phi - \frac{1}{c^2} \frac{\partial^2 \Phi}{\partial t^2} = 0 \qquad (\text{E-2})$$

If the disturbance is monochromatic, Φ is of the form

$$\Phi(\vec{R},t) = \phi(\vec{R}) e^{i\omega t} \qquad (\text{E-3})$$

where $\phi(\vec{R})$ is a function of position only.

Since Φ satisfies Eq. (E-1), $\phi(\vec{R})$ satisfies

$$(\nabla^2 + k^2) \phi(\vec{R}) = 0 \qquad in \quad V(\vec{R})$$

$$(\text{E-4})$$

The free space Green's function $G|\vec{R}-\vec{R}_0|$, where $\vec{R}_0$ locates the source points and $\vec{R}$ locates the field points is the solution for a system excited by a point source type of forcing function. Hence $G|\vec{R}-\vec{R}_0|$ is the field at an observer point $\vec{R}$ caused by a unit point source at $\vec{R}_0$. It follows that the required Green's function is the solution of the inhomogeneous Helmholtz equation

$$\nabla^2 G + k^2 G = -\delta(|\vec{R}-\vec{R}_0|)$$

$$(\text{E-5})$$

for a unit point source at $\vec{R}_0$ whose general solution for three dimensional space is

$$G|\vec{R}-\vec{R}_0| = \frac{e^{-ik|\vec{R}-\vec{R}_0|}}{4\pi|\vec{R}-\vec{R}_0|}$$

$$(\text{E-6})$$

This function depends only on the scalar distance between the source point and the field point. One lets φ_1 correspond to $\phi(\vec{R})$ and φ_2 to $G(|\vec{R}-\vec{R}_0|)$ and writes Eq. (E-1) as

$$\iiint (\phi \nabla^2 G - G \nabla^2 \phi) \, dV = \iint (\phi \frac{\partial G}{\partial n} - G \frac{\partial \phi}{\partial n}) \, dS$$

$$(\text{E-7})$$

From eqs. (E-4) and (E-5), follows

$$\nabla^2 \phi(\vec{R}_0) = -k^2 \phi(\vec{R}_0) \qquad (\text{E-8})$$

$$\nabla^2 G(|\vec{R}-\vec{R}_0|) = -k^2 G(|\vec{R}-\vec{R}_0|) - \delta(|\vec{R}-\vec{R}_0|) \qquad (\text{E-9})$$

Substituting Eqs. (E-8) and (E-9) into the volume integral of Eq. (E-7), Eq. (E-7) then becomes

$$-\iiint \phi(\vec{R}_0)\,\delta(|\vec{R}-\vec{R}_0|)\,dV(\vec{R}_0) = \iint_{\Sigma}\left[\phi(\vec{R}_0)\frac{\partial G}{\partial n} - G\frac{\partial \phi(\vec{R}_0)}{\partial n}\right]dS$$

$$(\text{E-10})$$

From the diffraction geometry of Fig. (E-1), the surface of integration Σ is composed of an integral over S_1 plus integrals over S_0 and S_2. Here surface S_1 is taken to coincide with the surface boundary of the diffracting obstacle, and Helmholtz equation is assumed to be valid everywhere outside S_1. The point source is excluded from the volume of integration by surrounding it by a small sphere S_0 centered on the source. The surface integration over S_2 will tend to zero as the surface is displaced to infinity while the Sommerfeld condition is satisfied (Section 7.1). Hence the surface integral in Eq. (E-10) is restricted to S_0 and S_1 only.

Using a relation for the delta function

$$\nabla^2 \frac{1}{|\vec{R}-\vec{R}_0|} = -4\pi\,\delta(|\vec{R}-\vec{R}_0|)$$

$$(\text{E-11})$$

E - 3

The volume integral of Eq. (E-10) can be written as

$$I = \iiint \left[\frac{1}{4\pi}\,\phi(\vec{R}_0)\,\nabla^2 \frac{1}{|\vec{R}-\vec{R}_0|}\right]dV(\vec{R}_0)$$

$$(\text{E-12})$$

Since $\nabla^2 \dfrac{1}{|\vec{R}-\vec{R}_0|} = 0$ where $|\vec{R}-\vec{R}_0|$ is finite, therefore the volume integral is zero if $\vec{R}$ is not within V. For the case if $\vec{R}$ is within V, $|\vec{R}-\vec{R}_0|^{-1}$ becomes infinite as $\vec{R}\to\vec{R}_0$. We can exclude the point located by $\vec{R}$ by surrounding it with a small sphere of radius ϵ, and volume V_ϵ (Fig. E-2). Hence $\phi(\vec{R}_0)$ is essentially equal to $\phi(\vec{R})$ by virtue of their small separating distance ϵ. In view of the above, Eq.(E-12) now becomes

$$I = \frac{\phi(\vec{R})}{4\pi} \iiint_{V_\epsilon} \nabla^2 \frac{1}{|\vec{R}-\vec{R}_0|}\,dV(\vec{R}_0)$$

$$(\text{E-13})$$

The Laplacian of $|\vec{R}-\vec{R}_0|^{-n}$ is the same regardless of whether it operates on the source points or the field points.

That is,

$$\nabla^2 \frac{1}{|\vec{R}-\vec{R}_0|^n} = \nabla_0^2 \frac{1}{|\vec{R}-\vec{R}_0|^n}$$

We may write Eq. (E-13) as

$$I = \frac{\phi(\vec{R})}{4\pi} \iiint_{V_\epsilon} \nabla_0^2 \frac{1}{|\vec{R}-\vec{R}_0|}\,dV(\vec{R}_0)$$

$$(\text{E-14})$$

E - 4

Applying the divergence theorem, we have

$$I = \frac{\phi(\vec{R})}{4\pi} \iint_{A_\epsilon} \nabla_0 \left(\frac{1}{|\vec{R}-\vec{R}_0|} \right) \cdot dS(\vec{R}_0)$$

(E-15)

Now since

$$\nabla_0 \frac{1}{|\vec{R}-\vec{R}_0|} = \frac{\hat{r}}{|\vec{R}-\vec{R}_0|^2}$$

(E-16)

where $\hat{r}$ is a unit vector in the direction of $\vec{R}-\vec{R}_0$, Eq. (E-15) then becomes

$$I = \frac{\phi(\vec{R})}{4\pi} \iint_{A_\epsilon} \frac{\hat{r}}{|\vec{R}-\vec{R}_0|^2} \cdot \hat{n} \, dS(\vec{R}_0)$$

(E-17)

where $\hat{n}$ is the outward normal of S.

From the definition of the solid angle $d\Omega$, we have

$$d\Omega = \frac{\hat{r} \cdot \hat{n}}{|\vec{R}-\vec{R}_0|^2} \, dS$$

(E-18)

Eq. (E-17) thus becomes

$$I = -\frac{\phi(\vec{R})}{4\pi} \iint d\Omega$$

(E-19)

The right hand side of Eq. (E-19) is the solid angle subtended at R by surface A_ϵ . Since the solid angle subtended by a surface surrounding a point is always 4π , we have

$$I = \frac{-\phi(\vec{R})}{4\pi} \cdot 4\pi$$

(E-20)

$$= -\phi(\vec{R})$$

On the other hand, if $\vec{R}$ is allowed to approach the boundary of V, the solid angle subtended by A_ϵ on the surface of V is only 2π (Fig. E-3). Thus, the volume integral in Eq.(E-10) has the value of

$$\iiint \phi(\vec{R}_0) \, \delta(|\vec{R}-\vec{R}_0|) \, dV(\vec{R}_0) = -\phi(\vec{R}) \qquad \vec{R} \text{ in } V \qquad \text{(E-21a)}$$

$$= 0 \qquad \vec{R} \text{ outside } V \qquad \text{(E-21b)}$$

$$= \frac{-\phi(\vec{R})}{2} \qquad \vec{R} \text{ on boundary of } V \qquad \text{(E-21c)}$$

Substitution of Eqs. (E-21) into the left hand side of Eq. (E-10), and noting that the surface integral over S_0 is ϕ_i, i.e. the free field contribution, it follows that the potential at a point $P(\vec{R})$ lying on the surface is given by

$$\frac{\phi(p)}{2} = \phi_i(p) + \iint \left\{ \phi(q) \frac{\partial G(p,q)}{\partial n} - G(p,q) \frac{\partial \phi(q)}{\partial n} \right\} dS$$

(E-22)

where $\partial/\partial n$ denotes differentiation along the outward normal to S (see Fig. E-1) . Equation (E-22) is the required integral equation.
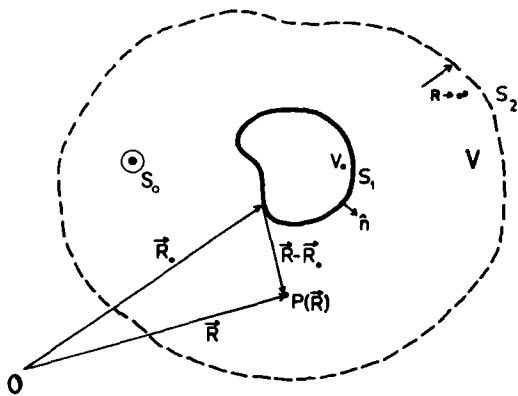
FIG. E-1 DEFINITION OF SOURCE AND FIELD VARIABLES

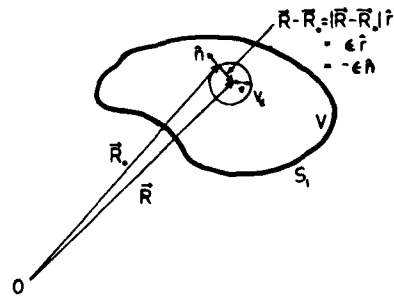FIG. E-2 EXCLUDING FIELD POINT $\vec{R}$ FROM VOLUME V WITH A SMALL SPHERE
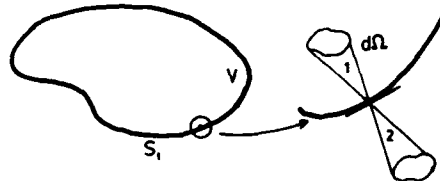

FIG. E-3 FOR A SMOOTH SURFACE, A TYPICAL ELEMENT CAN BE APPROXIMATED BY A TANGENT PLANE. PORTION 2 OF $d\Omega$ SUBTENDED BY A POINT LYING ON THE SURFACE IS EXTERNAL TO THE SURFACE AND DOES NOT CONTRIBUTE TO THE TOTAL VALUE OF $\iint d\Omega$. HENCE THE SOLID ANGLE SUBTENDED BY A SURFACE SURROUNDING A POINT ON ITS SURFACE IS 2π.

EVALUATION OF THE JACOBIAN $\partial\theta/\partial\alpha$

To evaluate $\oint \frac{e^{-ikR(\theta)}}{R(\theta)}d\theta$ in terms of a local coordinate system with α as the variable of integration (Fig. F-1), one must evaluate the Jacobian of the transformation $\partial\theta/\partial\alpha$. Let $q(x_0, y_0)$ be the origin of the local coordinate system attached to the element (i.e. 'q' is also taken as the centroid of the element). This origin can be specified in terms of the cylindrical coordinate (ρ_0, θ_0).

Due to the lack of symmetry, the Jacobian $\partial\theta/\partial\alpha$ (required to change the variable of integration) is not constant over different portions of the element's perimeter: sides 1, 2, 3 and 4.

From the cosine law, ρ can be expressed as (Fig. F-1)

$$\rho = (\ell^2 + \rho_0^2 - 2\,\rho_0\ell\cos\beta\,)^{\frac{1}{2}}$$

hence $$\frac{\partial\rho}{\partial\alpha} = \frac{1}{\rho}\left[\ell\frac{\partial\ell}{\partial\alpha} - \rho_0(\cos\beta\frac{\partial\ell}{\partial\alpha} - \ell\sin\beta\frac{\partial\beta}{\partial\alpha})\right] \qquad (F-2)$$

Now, for side 1, we have (Fig. F-1)

$$\rho \sin\theta = y_0 + d$$

then $$\frac{\partial\ell}{\partial\alpha}\sin\theta + \rho\cos\theta\frac{\partial\theta}{\partial\alpha} = 0 \qquad (F-3)$$

Hence, by (F-3), we have $$\frac{\partial\theta}{\partial\alpha} = \frac{-\partial\ell}{\partial\alpha}\frac{\tan\theta}{\rho} \qquad (F-4)$$

Thus to evaluate the Jacobian $\partial\theta/\partial\alpha$, we must know $\partial\ell/\partial\alpha$, tan θ and ρ along the perimeter of an element.

Tan θ can be found using:

$$\rho\cos\theta = x_0 - \ell\sin(\alpha - \pi/2)$$

$$\therefore \cos\theta = \frac{x_0 + \ell\cos\alpha}{\rho}$$

So that $$\tan\theta = \frac{y_0 + d}{x_0 + d\cot\alpha}$$

Now, $\partial\ell/\partial\alpha$ can be evaluated by using Eq. (F-2). The various terms are as follows:

$$\ell\frac{\partial\ell}{\partial\alpha} = (d\csc\alpha)(-d\csc\alpha\cot\alpha)$$

$$= \frac{-d^2\cos\alpha}{\sin^3\alpha}$$

$$\cos = \cos((\pi - \theta) + \theta_0)\cdot(-d\csc\alpha\cot\alpha)$$

$$= d\left[\frac{\cos\theta_0\cos^2\alpha}{\sin^2\alpha} + \frac{\sin\theta_0\cos\alpha}{\sin\alpha}\right]$$

$$\ell\sin\beta\frac{\partial\beta}{\partial\alpha} = -(d\csc\alpha)(\sin\alpha\cos\theta_0 - \cos\alpha\sin\theta_0)$$

$$= d(-\cos\theta_0 + \cot\alpha\sin\theta_0)$$

For side (2), we have (Fig. F-1)

$$\ell \cos \theta = x_0 - d$$

$$\therefore \frac{\partial \theta}{\partial \alpha} = \frac{\partial \ell}{\partial \alpha} \frac{1}{\ell \tan \theta}$$

also,

$$\ell \sin \theta = y_0 + \ell \sin(\pi - \alpha)$$

$$\therefore \tan \theta = \frac{y_0 + d \tan \alpha}{x_0 - d}$$

The various terms as required by $\partial\ell/\partial\alpha$ (Eq. F-2) over this portion of the line intergral are as follows:

$$\ell \frac{\partial \ell}{\partial \alpha} = (-d \sec \alpha)(-d \sec \alpha \tan \alpha)$$
$$= d^2 \sin \alpha / \cos^3 \alpha$$

$$\cos \beta \frac{\partial \ell}{\partial \alpha} = -(\cos \alpha \cos \theta_0 + \sin \theta_0 \sin \alpha)(-\ell \sec \alpha \tan \alpha)$$
$$= d(\tan \alpha \cos \theta_0 + \sin \theta_0 \tan^2 \alpha)$$

$$\ell \sin \alpha \frac{\partial \beta}{\partial \alpha} = d(\sec \alpha)(-\cos \alpha \sin \theta_0 + \sin \alpha \cos \theta_0)$$
$$= d(\cos \theta_0 \tan \alpha - \sin \theta_0)$$

F-3

In an analogous manner, one can show that the various terms required to evaluate the Jacobian $\partial\theta/\partial\alpha$ over the remaining 2 sides are as follows:

For side 3,

$$\frac{\partial \theta}{\partial \alpha} = -\frac{\partial \ell}{\partial \alpha} \frac{\tan \theta}{\ell} \quad , \quad \tan \theta = \frac{y_0 - d}{x - d \cot \alpha}$$

and

$$\ell \frac{\partial \ell}{\partial \alpha} = (-d \csc \alpha)(d \csc \alpha \cot \alpha)$$
$$= -d^2 \cos \alpha \csc^3 \alpha$$

$$\cos \beta \frac{\partial \ell}{\partial \alpha} = -d(\csc \alpha \cot \alpha)(\cos \alpha \cos \theta_0 + \sin \theta_0 \sin \alpha)$$
$$= -d(\cot^2 \alpha \cos \theta_0 + \cot \alpha \sin \theta_0)$$

$$\ell \sin \alpha \frac{\partial \beta}{\partial \alpha} = d \csc \alpha(\sin \alpha \cos \theta_0 - \cos \alpha \sin \theta_0)$$
$$= d(\cos \theta_0 - \sin \theta_0 \cot \alpha)$$

For side 4

$$\frac{\partial \theta}{\partial \alpha} = \frac{1}{\ell \tan \theta} \frac{\partial \ell}{\partial \alpha} \quad ; \quad \tan \theta = \frac{y_0 + d \tan \alpha}{x_0 + d}$$

and

$$\ell \frac{\partial \ell}{\partial \alpha} = \frac{d}{\cos \alpha} \, d \sec \alpha \tan \alpha$$
$$= \frac{d^2 \sin^2 \alpha}{\cos^3 \alpha}$$

$$\cos \beta \frac{\partial \ell}{\partial \beta} = -d \sec \alpha \tan \alpha(\cos \alpha \cos \theta_0 + \sin \alpha \sin \theta_0)$$
$$= -d(\tan \alpha \cos \theta_0 + \tan^2 \alpha \sin \theta_0)$$

and $$\ell \sin \alpha \frac{\partial \beta}{\partial \alpha} = d \sec \alpha(\cos \alpha \sin \theta_0 - \sin \alpha \cos \theta_0)$$
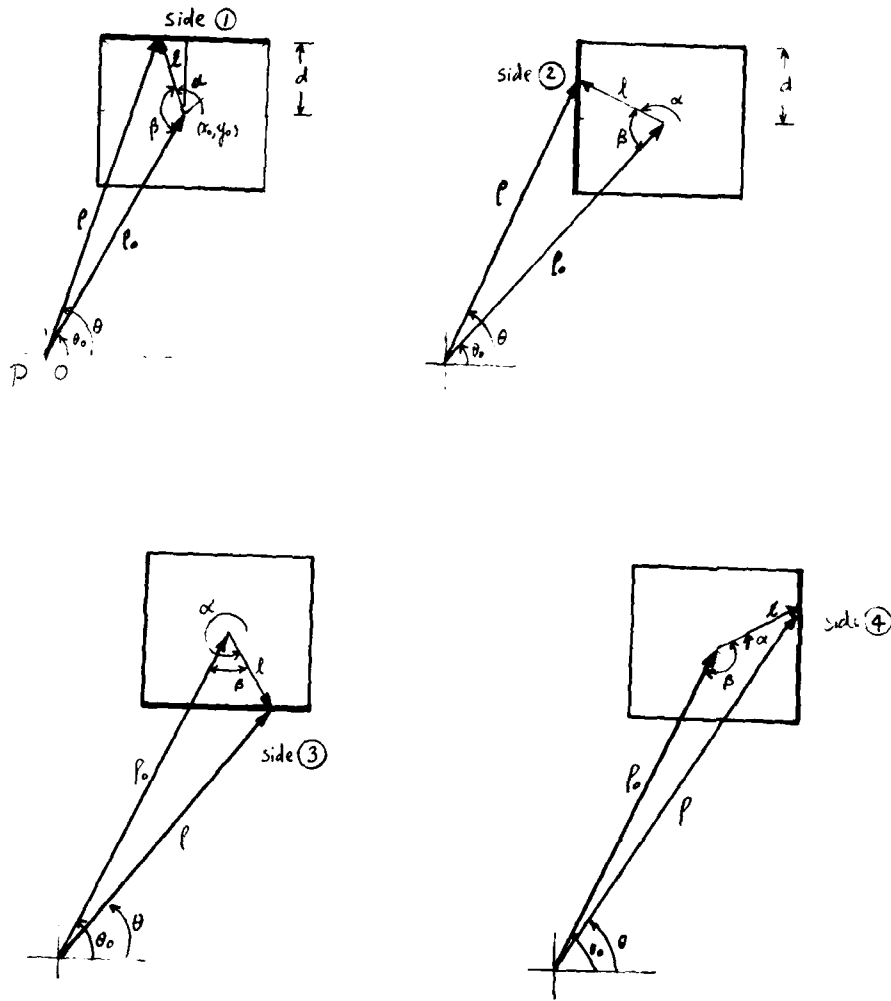$$= d(\sin \theta_0 - \tan \alpha \cos \theta_0)$$

F-4

FIG. F-1   GEOMETRICAL QUANTITIES USED IN THE LINE INTEGRAL OVER
THE PERIMETER OF AN ELEMENT

APPENDIX G

COMPUTER LISTING #1

```
         C
         C
         C     EXACT SOLUTION FOR FINITE STRAIGHTEDGED BARRIER
         C
    1          COMMON/CONST/PI,FK,LAMBDA
    2          COMMON/XLIMIT/ XV
    3          REAL NR,NS,C,LAMBDA,NR,NG
    4          COMPLEX TAT1,TAT2,TERM1,TERM2,TDA,C2
    5          PI=4.*ATAN(1.)
    6          TF=72.
    7          TK=(5.*(TF-32.)/9.)+273.
    8          C=SQRT(1.4*3085.4*TK)
    9          NR=64.0
   10          CA=12.
   11          NC=2.25
   12          XV=75.
   13          WRITE (6,25)
   14     25   FORMAT (1H1,/,1X,'STRAIGHT EDGE SHIELD OF LENGTH 16 D',/)
   15          F=8000.
   16          LAMBDA=C*12./F
   17          FK=2.*PI/LAMBDA
   18          THETA=80.
   19          DO 50 I=1,2
   20          THETAR=THETA*PI/180.
   21          WRITE (6,21) THETA
   22     21   FORMAT (1X,'THETA = ',F5.1)
   23          WRITE (6,13) F
   24     13   FORMAT    (1X,'FREQ =',F5.0,1X,'HZ',// )
   25          WX=5.0
   26          DO 60 NL=1,2
   27          NS=WX*0.75
   28          WRITE (6,15) WX
   29     15   FORMAT (1X,'X/D =',1X,F4.1)
   30          IF(THETA.LE.79.) GO TO 91
   31          SA=SQRT(NC**2+(CA -NS)**2)
   32          WX=CA-NS
   33          RG=NR*COS(THETAR)
   34          RQ=NR*SIN(THETAR)
   35          PH=RO-NC
   36          SG=RO-NS
   37          PA=CA-NO
   38          CR=SQRT(PB**2+Q**2)
   39          AR=SQRT(PA**2+P3**2)
   40          SR=SQRT(SQ**2+SO**2)
   41          PHIO=ATAN2(NC,WX)
   42          PHI=2.*PI-ATAN2(PB,PA)
   43          PHIO2=ATAN(NC/NS)
   44          IF (NG.LE.0.) PHI2=3.*PI/2.0
   45          IF (NG.LE.0.) GO TO 101
   46          PHI2=2.*PI-ATAN(PR/NO)
   47    101   CS=SQRT(NS*NS+NC*NC)
   48          GO TO 92
   49     91   AV=2.25
   50          SA=SQRT(AV*AV+(CA-NS)**2)
   51          AO=AR*COS(THETAR)-CA
   52          BO=NR*SIN(THETAR)-AV
   53          AR=SQRT(AO*AO+BO*BO)
   54          SM=CA-NS
   55          SR=SQRT((SM+AO)**2+(AV+BO)**2)
   56          PHIO=ATAN(AV/S4)
   57          PHI=PI+ATAN(BO/AO)
   58          CQ=CA+AO
   59          PHI2=2.*PI-ATAN(BO/CO)
   60          PHIO2=ATAN(NC/NS)
   61          CS=SQRT(NS*NS+NC*NC)
   62          SR=SQRT(CO*CO+BO*BO)
   63     92   CALL HANKEL (PHI,PHIO,SA,AB,SB,TAT1)
   64          CALL HANKEL (PHI2,PHIO2,CS,CB,SB,TAT2)
   65          TDA=TAT1+TAT2
   66          RTEM=CABS(TDA)
   67          NR=-20.*ALOG10(RTEM)
   68          WRITE (6,16) WX,TDA
   69     16   FORMAT (1X,'X/D =',1X,F4.1,3X,'  NK =',F10.6,1X,' + J',1X,F10.6)
   70          WRITE (6,17) RTEM,NR
   71     17   FORMAT (1X,'ATTENUATION FOR FINITE SHIELD WITH TWO EDGES =',2X,
                 '/NR/ =',F10.6,2X,'  =',F5.2,1X,'DB',//)
   72          WX=12.0
   73     60   CONTINUE
   74          THETA=THETA+10.0
   75     50   CONTINUE
   76          STOP
   77          END

   78          SUBROUTINE HANKEL (PHI,PHIO,SA,AB,SB,DAS)
   79          COMMON/CONST/ PI,FK,LAMBDA
   80          COMMON/XLIMIT/ XV
   81          REAL MNBSJ1
   82          REAL LAMBDA,NR
   83          COMPLEX RNRS1,RNIS1,RNRS2,RNIS2,DAR,DAI,TDAR,TDAI,DA
   84          COMPLEX C2,TERM1,TERM2,DAS
   85          Z1=PHIO*180./PI
   86          Z2=PHI*180./PI
   87          ZR=PHI-PHIO
   88          Z1=PHI+PHIO
   89          R=SQRT((SA*SA)+(AB*AB)-(2.*AB*SA*COS(ZR)))
   90          PPRIM=SQRT((SA*SA)+(AB*AB)-(2.*AB*SA*COS(Z1)))
   91          R1=SA*AB
   92          R1R=R1-R
   93          R1RP=R1-PPRIM
   94          A=COS(ZR/2.0)
   95          B=COS(Z1/2.0)
   96          TAUR=SQRT(FK*R1R)
   97          TAURP=SQRT(FK*R1RP)
   98          IF (A.LT.0.0) TAUR=-TAUR
   99          IF (E.LT.0.0) TAURP=-TAURP
  100          R1N=2.*R1/LAMBDA
  101          2NN=2.*R/LAMBDA
  102          FR=PI\-4.
  103          WRITE (6,18) Z1,Z2,FRN
  104     18   FORMAT (2X,'PHIO = ',F6.2,2X,'PHI = ',F6.2,6X,'FRESNEL NUMBER =',
                 1X,F5.2)
  105          TDAR=CMPLX(0.0,0.0)
  106          TDAI=CMPLX(0.0,0.0)
  107          ST=0.01
```

```
108        X1=-TAUR
109        X2=-TAUR-DM
110   20   W1=X1*X1+FK*R
111        W2=X2*X2+FK*RPRIM
112        G1=SQRT(X1*X1+2.*FK*R)
113        G2=SQRT(X2*X2+2.*FK*RPRIM)
114        DRJ1=-VMBSJ1(W1,IER1)
115        DIJ1=-VMBSJ1(W2,IER2)
116        CALL RESY(X1,1,DRY1,IER3)
117        CALL RESY(X2,1,DIY1,IER4)
118        DRJ1=DRJ1/G1
119        DIJ1=DIJ1/G2
120        DRY1=DRY1/G1
121        DIY1=DIY1/G2
122        RNRS1=CMPLX(DRJ1,DRY1)
123        RNIS1=CMPLX(DIJ1,DIY1)
124        X1=X1+ST
125        X2=X2+ST
126        W1=X1*X1+FK*R
127        W2=X2*X2+FK*RPRIM
128        G1=SQRT(X1*X1+2.*FK*R)
129        G2=SQRT(X2*X2+2.*FK*RPRIM)
130        DRJ2=VMBSJ1(W1,IER5)
131        DIJ2=VMBSJ1(W2,IER6)
132        CALL RESY(X1,1,DRY2,IER7)
133        CALL RESY(X2,1,DIY2,IER8)
134        DRJ2=DRJ2/G1
135        DIJ2=DIJ2/G2
136        DRY2=DRY2/G1
137        DIY2=DIY2/G2
138        RNRS2=CMPLX(DRJ2,DRY2)
139        RNIS2=CMPLX(DIJ2,DIY2)
140        DAR=(RNRS1+RNRS2)/2.0
141        DAI=(RNIS1+RNIS2)/2.0
142        TDAR=TDAR+DAR
143        TDAI=TDAI+DAI
144        IF (X1.GT.X5) GO TO 100
145        GO TO 20
146  100   TDAR=TDAR*ST
147        TDAI=TDAI*ST
148        DA=TDAR+TDAI
149        C1=FK*R
150        C2=CMPLX(0.0,-C1)
151        TERM1=CMPLX(0.0,-C1)
152        TERM2=CEXP(C2)
153        DAS=TERM1*TERM2*DA
154        RTFV=CABS(DAS)
155        ARF=20.*ALCG10(RTFV)
156        WRITE (6,501) TDAR
157  501   FORMAT (2X,'HANKEL(REAL SOURCE)',1X,F10.6,1X,'+ J',1X,F10.6)
158        WRITE (6,502) TDAI
159  502   FORMAT (2X,'HANKEL(IMAGE SOURCE)',1X,F10.6,1X,'+ J',1X,F10.6)
160        WRITE (6,16) DA
161   16   FORMAT (3X,'DIFFRACTED FIELD FOR ONE EDGE = ',F10.6,' + J ',F10.6)
162        WRITE (6,17) DAS,NR
163   17   FORMAT (3X,'ATTENUATION =',1X,F10.6,' + J ',F10.6,' = ',
              F6.2,1X,'DB')
164        RETURN
165        END
```

G-3

```
                                      SJOBW
         C
         C
         C          SOUND FIELD AROUND A RECTANGULAR PLATE BY INTEGRAL EQUATION METHOD
         C
     1              REAL NR
     2              COMPLEX TF,DIRFLD,C61,C65,C67,C62,TERM61,TERM63,CB2,CB3,DF
     3              COMPLEX C22,TERM21,C73,TERM22,E,VG,ST,TDA
     4              REAL KA(24)
     5              DIMENSION E(24,24),VD(24)
     6              DIMENSION VVG(24)
     7              COMMON/RCUTS/T(4),W(4),B
     8              COMMON/CONST/ PI,FK
     9              COMMON/PARM/ S,D
    10              COMMON/VALUE/ TDA
    11              COMMON/SIDE/ H1,H2,RHCSQ,COW,PIG,T3
    12              PI=4.*ATAN(1.)
    13              FK=18.84
    14              B=45.*PI/180.
    15              T(1)=0.33998104
    16              T(2)=0.86113631
    17              T(3)=-T(1)
    18              T(4)=-T(2)
    19              W(1)=0.65214516
    20              W(2)=0.34785485
    21              W(3)=W(1)
    22              W(4)=W(2)
    23              YW=0.1
    24              HL=0.15
    25              X0=0.125
    26              Y0=0.075
    27              DELTA=0.05
    28              D=DELTA/2.0
    29              S=DELTA**2
    30              CALL KERNEL (ST)
    31              XS=0.0
    32              YS=0.0
    33              ZS=0.5
    34              I=1
    35              XP=XO
    36              YP=YO
    37              ZP=0.0
    38              J=1
    39              XQ=XC
    40              YQ=YO
    41              KC=1
    42              DO 220 LL=1,4
    43              DO 110 KK=1,4
    44              IF (KC.EQ.1) GO TO 5
    45              XQ=XP
    46              YC=YP+DELTA
    47              IF (YQ.GT.Y1) XQ=XQ-DELTA
    48              IF (YQ.GT.Y1) YC=YO
    49              IF (XQ.LT.PL) GO TO 25
    50              J=J+1
```

G-4

```
51          GO TO 10
52      5   IF (I-J) 1,2,1
53      2   E(I,J)=ST
54          GO TO 3
55      1   J=J+1
56      10  TDA=CMPLX(0.0,0.0)
57          RHOSQ=(XQ-XP)**2+(YQ-YP)**2
58          T3=SQRT(RHOSQ)
59          H1=XQ-XP
60          H2=YQ-YP
61          FISH=SQRT(H1**2+H2**2)
62          COW=H1/FISH
63          PIG=H2/FISH
64          CALL KERNE1
65          CALL KERNE2
66          CALL KERNE3
67          CALL KERNE4
68          E(I,J)=TDA
69          E(J,I)=-TDA
70      3   YQ=YQ+DELTA
71          IF (YQ-YY) 1,4,4
72      4   AXA=XQ+DELTA
73          IF (AXA.LT.PL) GO TO 20
74          XQ=AXA
75          YQ=YO
76          GO TO 1
77      20  CONTINUE
78          RS=SQRT((XP-XS)**2+(YP-YS)**2+(ZP-ZS)**2)
79          C21=-FK*RS
80          C22=CMPLX(0.0,C21)
81          TERM21=CEXP(C22)/(4.*PI*RS)
82          C23=CMPLX(0.0,FK)
83          TERM22=(C23+1./RS)
84          TERM23=(ZP-ZS)/RS
85          VQ(I)=TERM21*TERM22*TERM23
86          I=I+1
87          YP=YP+DELTA
88          KC=2
89      110 CONTINUE
90          XP=XP+DELTA
91          YP=YO
92      220 CONTINUE
93          DO 25 IX=1,24
94          E(IX,IX)=ST
95      25  CONTINUE
96          WRITE (6,31) ((I,J,E(I,J),J=1,24),I=1,24)
97      31  FORMAT (3(1I7,1I3,1X,1I3,3X,F10.6,2X,F10.6))
98          N=24
99          IA=24
100         M=1
101         IB=24
102         IJOB=0
103         CALL LEQT1C (E,N,IA,VQ,M,IB,IJOB,WA,IER)
104         DO 50 I=1,24
105         VVQ(I)=CABS(VQ(I))
106     50  CONTINUE
107         WRITE (6,12)
108     12  FORMAT (///,1X,'SURFACE POTENTIAL DISTRIBUTION ON RIGID RECTANGULAR
109         PLATE AT EACH CALCULATIONAL POINT')
            WRITE (6,13)
```

```
110     13  FORMAT (1X,'FIRST POINT AT LOWER RIGHT CORNER,LAST POINT AT UPPER
            LEFT CORNER, FACING POINT SOURCE'///)
111         WRITE (6,11) ( VQ(I),VVQ(I), I=1,24)
112     11  FORMAT (2(1X,'('F9.5,' + J '.F9.5,')',' =',F7.5))
113         WRITE (6,18)
114     18  FORMAT (1H1,1X,'DIFFRACTION BY A RECTANGULAR SCREEN, MAGNITUDES OF
            TOTAL FIELD ARE THE RATIO  TO THE DIRECT SOUND AT EACH POINT'///)
115         PHIR=0.0
116         RR=0.31
117         DO 77 I7=1,10
118         PF=CMPLX(0.0,0.0)
119         PHI=PHIR*PI/180.
120         XR=RR*SIN(PHI)
121         YR=0.0
122         ZR=RR*COS(PHI)
123         RSP=SQRT((XR-XS)**2+(YR-YS)**2+(ZR-ZS)**2)
124         C60=-FK*RSP
125         C61=CMPLX(0.0,C60)
126         DIRFLD=CEXP(C61)/(4.*PI*RSP)
127         XQ=XO
128         YQ=YO
129         ZQ=0.0
130         I=1
131         DO 221 LL=1,6
132         DO 111 KK=1,4
133         RQR=SQRT((XR-XQ)**2+(YR-YQ)**2+(ZR-ZQ)**2)
134         C64=-FK*RQR
135         C65=CMPLX(0.0,C64)
136         C67=CEXP(C65)/(4.*PI*RQR)
137         C62 =CMPLX(0.0,FK)
138         C63=1./RQR
139         TERM61=(C62+C63)
140         TERM62=(ZR-ZQ)/RQR
141         TERM63=VQ(I)*C67*TERM61*TERM62
142         DF=DF+TERM63*S
143         I=I+1
144         YQ=YQ+DELTA
145     111 CONTINUE
146         XQ=XQ+DELTA
147         YQ=YO
148     221 CONTINUE
149         C89=CABS(DF)
150         TF=DF+DIRFLD
151         CH1= FK*RSP
152         CR2=CMPLX(0.0,C51)
153         CR3=RSP*CEXP(C62)*TF*4.*PI
154         RTEM=CABS(CR3)
155         NR=-20.*ALOG10(RTEM)
156         WRITE (6,17) PHIR,DF,C89
157     17  FORMAT ( /,1X,'ANGLE =',1X,F5.1,3X,'DIFFRACTED FIELD ',2X,F10.6,
            ' + J',1X,F10.6,2X,'=',1X,F10.6)
158         WRITE (6,16) C83,RTEM,NR
159     16  FORMAT (22X,'TOTAL FIELD ',2X,F10.6,    ' + J' ,1X,F10.6,2X,'=',
            1X,F10.6,5X,'=',F8.2,1X,'DB')
160         PHIR=PHIR+20.
161     77  CONTINUE
162         STOP
163         END

164         SUBROUTINE KERNEL (ST)
```

```
165        COMPLEX C,F,TOT,SIGMA,C6,ST
166        COMMON/CONST/ PI,FK
167        COMMON/ROOTS/T(4),W(4),B
168        COMMON/PARS/ S,D
169        DIMENSION TOT(4)
170        DO 10 I=1,4
171        R =PI*(0.25*T(I)+0.5)
172        A=-FK*D/SIN(R)
173        C=CMPLX(0.,0.,A)
174        F=SIN(R)*CEXP(C)/D
175        TOT(I)=W(I)*F
176   10   CONTINUE
177        SIGMA=H*4.*(TOT(1)+TOT(2)+TOT(3)+TOT(4))
178        C5=2.*PI*FK
179        C6=CMPLX(0.,0.,C5)
180        ST=-(SIGMA+C6)/(4.*PI)
181        RETURN
182        END

183        SUBROUTINE KERNE1
184        COMPLEX SIGMA,TOT,TDA
185        COMPLEX TINTG
186        DIMENSION TOT(4)
187        COMMON/CONST/ PI,FK
188        COMMON/ROOTS/T(4),W(4),B
189        COMMON/VALUE/ TDA
190        COMMON/FACTOR/ RHO,DTH
191        COMMON/TRIG/ CO,SI,TA
192        DO 10 I=1,4
193        R=PI*(0.25*T(I)+0.5)
194        SI=1./SIN(R)
195        CO=COS(R)
196        CALL EVAL1
197        TOT(I)=W(I)*TINTG(RHO,DTH)
198   10   CONTINUE
199        SIGMA=R*(TOT(1)+TOT(2)+TOT(3)+TOT(4))
200        TDA=TDA+SIGMA
201        RETURN
202        END

203        SUBROUTINE KERNE2
204        COMPLEX TINTG
205        COMPLEX SIGMA,TOT,TDA
206        DIMENSION TOT(4)
207        COMMON/CONST/ PI,FK
208        COMMON/ROOTS/T(4),W(4),B
209        COMMON/FACTOR/ RHO,DTH
210        COMMON/VALUE/ TDA
211        COMMON/TRIG/ CO,SI,TA
212        DO 10 I=1,4
213        R=PI*(0.25*T(I)+1.0)
214        CO=1./COS(R)
215        SI=SIN(R)
216        TA=TAN(R)
217        CALL EVAL2
218        TOT(I)=W(I)*TINTG(RHO,DTH)
219   10   CONTINUE
220        SIGMA=R*(TOT(1)+TOT(2)+TOT(3)+TOT(4))
221        TDA=TDA+SIGMA
222        RETURN
```

```
223        END
224        SUBROUTINE KERNE3
225        COMPLEX TINTG
226        COMPLEX SIGMA,TOT,TDA
227        DIMENSION TOT(4)
228        COMMON/CONST/ PI,FK
229        COMMON/ROOTS/T(4),W(4),B
230        COMMON/FACTOR/ RHO,DTH
231        COMMON/VALUE/ TDA
232        COMMON/TRIG/ CO,SI,TA
233        DO 10 I=1,4
234        R=PI*(0.25*T(I)+1.5)
235        CO=COS(R)
236        SI=1./SIN(R)
237        CALL EVAL3
238        TOT(I)=W(I)*TINTG(RHO,DTH)
239   10   CONTINUE
240        SIGMA=R*(TOT(1)+TOT(2)+TOT(3)+TOT(4))
241        TDA=TDA+SIGMA
242        RETURN
243        END

244        SUBROUTINE KERNE4
245        COMPLEX SIGMA,TOT,TDA
246        COMPLEX TINTG
247        DIMENSION TOT(4)
248        COMMON/CONST/ PI,FK
249        COMMON/ROOTS/T(4),W(4),B
250        COMMON/FACTOR/ RHO,DTH
251        COMMON/VALUE/ TDA
252        COMMON/TRIG/ CO,SI,TA
253        DO 10 I=1,4
254        R=PI*0.25*T(I)
255        CO=1./COS(R)
256        SI=SIN(R)
257        TA=TAN(R)
258        CALL EVAL4
259        TOT(I)=W(I)*TINTG(RHO,DTH)
260   10   CONTINUE
261        SIGMA=R*(TOT(1)+TOT(2)+TOT(3)+TOT(4))
262        TDA=TDA+SIGMA
263        RETURN
264        END

265        COMPLEX FUNCTION TINTG(RHO,DTH)
266        COMMON/CONST/ PI,FK
267        COMPLEX C2,C3
268        C1=-FK*RHO
269        C2=CMPLX(0.,0.,C1)
270        C3=CEXP(C2)
271        TINTG=DTH*C3/(4.*PI*RHO)
272        RETURN
273        END

274        SUBROUTINE EVAL1
275        COMMON/SIDE/ H1,H2,RHOSQ,COA,PIO,TS
276        COMMON/PARS/ S,D
277        COMMON/FACTOR/ RHO,DTH
278        COMMON/TRIG/ CO,SI,TA
```

```
279        A1=H1+D*CO*SI
280        IF (ABS(A1).LT.1.0E-15) GO TO 2
281        TT1=-D*D*CO*SI**3
282        TT2=D*(COW*CO**2*SI**2+PIG*CO*SI)
283        TT3=D*(PIG*CO*SI-COW)
284        T4=D**2*SI**2
285        T12=2.*T3*D*(COW*CO*SI+PIG)
286        RHO=SQRT((T4+RHOSQ+T12))
287        DTH=-(H2+D)*(TT1-T3*(TT2-TT3))/(A1*RHO**2)
288        GO TO 3
289    2   IF (H2) 4,6,6
290    6   RHO= T3+D
291        DTH=D/RHO
292        GO TO 3
293    4   RHO= T3-D
294        DTH=-D/RHO
295    3   RETURN
296        END

297        SUBROUTINE EVAL2
298        COMMON/SIDE/ H1,H2,RHOSQ,COW,PIG,T3
299        COMMON/PARM/ SW,D
300        COMMON/FACTOR/ RHO,DTH
301        COMMON/TRIG/ CO,SI,TA
302        A2=H2-D*TA
303        IF (ABS(A2).LT.1.0E-15) GO TO 2
304        TT1=D*D*SI*CC**3
305        TT2=D*(TA*COW+PIG*TA**2)
306        TT3=D*(COW*TA-PIG)
307        T4=D*D*CO**2
308        T12=2.* T3*D*(COW+TA*PIG)
309        RHO=SQRT(T4+RHOSQ-T12)
310        DTH=(H1-D)*(TT1- T3*(TT2-TT3))/(A2*RHO**2)
311        GO TO 3
312    2   IF (H1) 4,6,6
313    6   RHO= T3-D
314        DTH=-D/RHO
315        GO TO 3
316    4   RHO= T3+D
317        DTH=D/RHO
318    3   RETURN
319        END

320        SUBROUTINE EVAL3
321        COMMON/SIDE/ H1,H2,RHOSQ,COW,PIG,T3
322        COMMON/FACTOR/ RHO,DTH
323        COMMON/PARM/ SW,D
324        COMMON/TRIG/ CO,SI,TA
325        A3=H1-D*CO*SI
326        IF (ABS(A3).LT.1.0E-15) GO TO 2
327        TT1=-D*D*CO*SI**3
328        TT2=-D*(COW*CO**2*SI**2+PIG*CO*SI)
329        TT3=D*(COW-PIG*CO*SI)
330        T4=D*D*SI**2
331        T12=-2.*T3*D*(COW*CO*SI+PIG)
332        RHO=SQRT(T4+RHOSQ+T12)
333        DTH=-(H2-D)*(TT1-T3*(TT2-TT3))/(A3*RHO**2)
334        GO TO 3
335    2   IF (H2) 4,6,6
336    6   RHO=T3-D
```

```
337        DTH=-D/RHO
338        GO TO 3
339    4   RHO=T3+D
340        DTH=D/RHO
341    3   RETURN
342        END

343        SUBROUTINE EVAL4
344        COMMON/SIDE/ H1,H2,RHOSQ,COW,PIG,T3
345        COMMON/PARM/ SW,D
346        COMMON/FACTOR/ RHO,DTH
347        COMMON/TRIG/ CO,SI,TA
348        A4=H2+D*TA
349        IF (ABS(A4).LT.1.0E-15) GO TO 2
350        TT1=D*D*CO**2
351        T12=2.*T3*D*(COW+TA*PIG)
352        RHO=SQRT(T4+RHOSQ+T12)
353        TT1=D*SI*CO**3
354        TT3=D*(PIG-TA*COW)
355        TT2=-D*(TA*COW+PIG*TA**2)
356        DTH=(H1+D)*(TT1-T4*(TT2-TT3))/(A4*RHO**2)
357        GO TO 4
358    2   IF (H1) 4,6,6
359    6   RHO=T3
360        DTH=D/RHO
361        GO TO 3
362    4   RHO=T3+D
363        DTH=-D/RHO
364    3   RETURN
365        END
```

APPENDIX G

COMPUTER LISTING #3

```
C      INTEGRAL EQUATION METHOD FOR DIFFRACTION OF SOUND WAVES BY HALF ROUND
C      SCOOP SHIELDS
C
  1         REAL  AK,LAMBDA,NJD
  2         COMPLEX C2,TERM1,C27,TERM21,C23,TERM22,E,VJ,SUM
  3         COMPLEX TF,DIRFLU,C61,C65,C57,C62,TERM51,TERM63,C62,C65,DF
  4         COMPLEX TCT,TERM,TERM3,TDA,H,SK
  5         DIMENSION F(225,225),R(225,225),VJ(225),AE(225),WA(225)
  6         COMMON/PARM/ PI,FK,T(6),W(6),RS
  7         PI=4.*ATAN(1.)
  8         D=0.75
  9         TF=67.
 10         TK=(5.*(TF-32.)/9.)+273.
 11         C=SQRT(1.4*3085.*H*TK)
 12         F=1500.
 13         LAMBDA=C*12./F
 14         FK=2.*PI/LAMBDA
 15         DTD=12.
 16         DZ=0.8
 17         NXP=15
 18         NYP=15
 19         NEL=225
 20         DTH=PI*DTD/180.
 21         RS=3.75
 22         ZM=12.
 23         GR=DTH*DZ/4.0
 24         NP=6
 25         T(1)=0.93246951
 26         T(2)=0.66120939
 27         T(3)=0.23861919
 28         T(4)=-T(1)
 29         T(5)=-T(2)
 30         T(6)=-T(3)
 31         W(1)=0.17132449
 32         W(2)=0.36076157
 33         W(3)=0.46791393
 34         W(4)=W(1)
 35         W(5)=W(2)
 36         W(6)=W(3)
 37         THO=DTH/2.0
 38         ZO=DZ/2.0
 39         I=1
 40         THP=THO
 41         ZP=ZO
 42         J=1
 43         THQ=THO
 44         ZQ=ZO
 45         CALL KEPNEL (NP,SK,DTH,DZ)
 46         KC=1
 47         DO 220 LL=1,NXP
 48         DO 110 KK=1,NYP
 49         IF (KC.EQ.1) GO TO 5
 50         THQ=THP
 51         ZQ=ZP+DZ
 52         IF (ZQ.GT.ZM) THQ=THQ+DTH
 53         IF (ZQ.GT.ZM) ZQ=ZO
 54         IF (THQ.GT.PI) GO TO 20
 55         J=J+1
 56         GO TO 10
 57    5    IF (I-J) 1,3,1
 58    1    J=J+1
 59   10    SUM=CMPLX(0.0,0.0)
 60         DO 30 J3=1,NP
 61         H=DTH*T(J3)/2.0+THQ
 62         A1=COS(THP-H)
 63         DO 40 J4=1,NP
 64         G=DZ*T(J4)/2.0+ZQ
 65         R=SQRT(2.*RS**2*(1.-A1)+(G-ZP)**2)
 66         C1=FK*R
 67         CX=-C1
 68         C2=CMPLX(0.0,CX)
 69         TERM1=3.*(1.-C2)-C1**2
 70         TERM2=(RS**3)*(1.-2.*A1+A1**2)/(R**2)
 71         TERM3=RS*(1.-C2)*A1
 72         TERM=CEXP(C2)*(TERM1*TERM2+TERM3)/(4.*PI*R**3)
 73         TCT=W(J3)*W(J4)*TERM
 74         SUM=SUM+TCT
 75   40    CONTINUE
 76   30    CONTINUE
 77         E(I,J)=GR*SUM
 78         E(J,I)=E(I,J)
 79    3    ZQ=ZQ+DZ
 80         IF (ZQ-ZM) 1,4,4
 81    4    ATA=THQ+DTH
 82         IF (ATA.GT.PI) GO TO 20
 83         THQ=ATA
 84         ZQ=ZO
 85         GO TO 1
 86   20    CONTINUE
 87         I=I+1
 88         ZP=ZP+DZ
 89         KC=2
 90   110   CONTINUE
 91         THP=THP+DTH
 92         ZP=ZO
 93   220   CONTINUE
 94         DO 25 IX=1,NEL
 95         E(IX,IX)=SK
 96   25    CONTINUE
 97         DO 21 I=1,NEL
 98         DO 22 J=1,NEL
 99         R(I,J)=CMPLX(0.0,0.0)
100   22    CONTINUE
101   21    CONTINUE
102         DO 23 ID=1,NEL
103         R(ID,ID)=CMPLX(1.0,0.0)
104   23    CONTINUE
105         N=NEL
106         IA=NEL
107         M=N
108         IB=NEL
109         IJOB=0
110         CALL LEQT1C (E,N,IA,R,M,IB,IJOB,WA,IER)
```

```
111        NJF=15.
112        DO 70 IJC=1,15
113        XS=0.0
114        YS=0.0
115        ZS=NJF*I
116        THP=THC
117        ZP=Z0
118        I=1
119        DO 429 L=1=1,NXP
120        XP=RS*CUS(THP)
121        YP=RS*SIN(THP)
122        DO 428 L+2=1,NYP
123        RPS=SQRT((XP-XS)**2+(YP-YS)**2+(ZP-ZS)**2)
124        C55=RPS*SQRT(XP**2+YP**2)
125        C21=-FK*RPS
126        C22=CMPLX(0.0,C21)
127        TER721=CEXP(C22)/(4.*PI*RPS)
128        C23=CMPLX(0.0,FK)
129        TER722=(C23+1./RPS)
130        TERV23=(XP*(XP-XS)+YP*(YP-YS))/C55
131        VC(I)=-TERV21*TE*(22*TERV23
132        I=I+1
133        ZP=ZP+DZ
134   428  CONTINUE
135        THP=THP+DTH
136        ZP=Z0
137   429  CONTINUE
138        WRITE (6,999) F,LAMBDA,FK
139   999  FORMAT (1H1,1X,'FREQ =',F6.0,1X,'HZ',3X,'WAVELENGTH =',F6.2,
             1X,'IN.',4X,'WAVE NUMBER =',F6.2//)
140        WRITE (6,546) WJJ
141   546  FORMAT (2X,'X/J =',F6.2,/)
142        K=1
143        DO 15 I1=1,NEL
144        E(I1,K)=(0.0,0.0)
145        DO 32 J1=1,NEL
146        F(I1,K)=E(I1,K)+ R(I1,J1)*VC(J1)
147   32   CONTINUE
148   15   CONTINUE
149        DO 50 IC=1,NEL
150        AF(IC)=CABS(F(IC,K))
151   50   CONTINUE
152        WRITE (6,666)
153   666  FORMAT (///,1X,' SURFACE POTENTIAL DISTRIBUTION',//)
154        WRITE (6,11)  (E(I,1),AF(I),I=1,NEL)
155   11   FORMAT (3(1X,F5.5,2X,F5.5,2X,F7.5,2X))
156        PHI=40.
157        WRITE (6,701) PHID
158   701  FORMAT (///,1X,' FIELD POINT AT',F5.0,1X,' DEGREE WRT JET AXIS')
159        PHI=PHID*PI/180.
160        XR=0.0
161        YR=64.*SIN(PHI)
162        ZR=64.*COS(PHI)+6.0
163        RSR=SQRT((XR-XS)**2+(YR-YS)**2+(ZR-ZS)**2)
164        C60=-FK*RSR
165        C61=CMPLX(0.0,C60)
166        CIRFLD=CEXP(C61)/(4.*PI*RSR)
167        DF=CMPLX(0.0,0.0)
168        S=RS*DTH*DZ
169        THC=THC
```

```
170        ZP=ZP
171        I=1
172        DO 41 L1=1,XP
173        DO 42 L2=1,YP
174        SUMDF=CMPLX(0.0,0.0)
175        DO 555 J=1, P
176        HDF=THC*T((JS)/2.)+I-C
177        X=RS*COS(HDF)
178        Y=RS*SIN(HDF)
179        DO 556 JJ=1,XP
180        DHF=DZ*T((JJ)/2.)+Zu
181        RP=SQRT((X-XS)**2+(Y-YS)**2+(Z-ZS)**2)
182        C66=-FK*RP
183        C47=CMPLX(0.0,C66)
184        C47=CEXP(C47)/(4.*PI*RP)
185        C62=CMPLX(0.0,FK)
186        C63=1./RP
187        C70=RP*SQRT(X**2+Y**2)
188        TF=C62+C63
189        TER62=(X*(X-XS)+Y*(Y-YS))/C70
190        TK=C63*C47*TF*SLOTH**2/2*RS
191        TCTDF=CEXP(C61)*(J)*TF*C66
192        SUMDF=SUMDF+TCTDF
193   556  CONTINUE
194   555  CONTINUE
195        DFDF=SUMDF*E(I,1)
196        I=I+1
197        ZP=Z+DZ
198   42   CONTINUE
199        THC=THC+DTH
200        ZP=Z0
201   41   CONTINUE
202        DF=DF*S
203        CR=CABS(DF)
204        TF=CIRFLD
205        C41=FK*RSR
206        C42=CMPLX(0.0,C41)
207        CR=C55*C5*(C-2)*TF*F4.*PI
208        DTF=CABS(C-R)
209        SW=-ZL*AF*C12*TR*T
210        WRITE (6,17)  DDF,FCR
211   17   FORMAT ( /,1X,' X/J  =',1X,F5.5,3X,'DIFFRACTED  FIELD ',1X,F5.5,7X
             ,'+ J',1X,F5.5,'REAL FIELD',1X,F5.5//)
212        WRITE (6,16)  CR,DTF
213   16   FORMAT ( ///,1X,'TOTAL FIELD ',1X,F5.5,7X,'+ J',1X,F5.5,7X,'+
             1X,F5.5,7X,F5.5,'REAL',2X,F5.5//)
214        WRITE (6,44)  CR,DTF
215   44   FORMAT (///,1X,'DIRECT FIELD ',1X,F5.5,7X,F5.5,7X,'+ J',1X,F5.5,
             2X,F5.5//)
216        WJJ=WJJ+1.
217   7    CONTINUE
218        STOP
219        END

220        SUBROUTINE KERNEL (CR=XS,ZT,S,Z)
221        COMPLEX (ZR=Z / P)=F=PI)=T(I)=1=1=X
222        COMPLEX SUMDF,TF,CR,A
223        COMPLEX C,RP,SIGNA
224        TF=C  FLT(I,0,0,1)
225        SUMDF=CMPLX(0.0,0.0)
```

```
226        D1=SWZ/2.0
227        D2=RS*SWT/2.0
228        CK1=PI/2.0
229        TH1=ATAN(D1/D2)
230        B1=TH1/2.0
231        B2=(CK1-TH1)/2.0
232        DO 10 I=1,NP
233        H=(TH1*T(I)+TH1)/2.0
234        CH=COS(H)
235        A=-FK*D2/CH
236        C=CMPLX(0.0,A)
237        F=CH*CEXP(C)/D1
238        TOT=W(I)*F
239        SUM=SUM+TOT
240   10   CONTINUE
241        TDA=TDA+B1*SUM
242        SUM=CMPLX(0.0,0.0)
243        TH2=CK1-TH1
244        TH3=CK1+TH1
245        DO 11 I=1,NP
246        H=(TH2*T(I)+TH3)/2.0
247        SH=SIN(H)
248        A=-FK*D1/SH
249        C=CMPLX(0.0,A)
250        F=SH*CEXP(C)/D1
251        TOT=W(I)*F
252        SUM=SUM+TOT
253   11   CONTINUE
254        TDA=TDA+B2*SUM
255        C5=2.*PI*FK
256        C6=CMPLX(0.0,C5)
257        SK=-(4.*TDA*C6)/(4.*PI)
258        WRITE (6,13) SK
259   13   FORMAT (1X,'KERNEL =',1X,E14.7,2X,E14.7)
260        RETURN
261        END
```

END